Magnetic order and magnetic phase transitions in triangular or depleted periodic Anderson lattices

Studies within the framework of dynamical mean-field theory powered by hybridization expansion continuous-time quantum Monte Carlo

Dissertation

with the aim of achieving a doctoral degree at the

Faculty of Mathematics, Informatics and Natural Sciences
Department of Physics
University of Hamburg

submitted by

Maximilian Wolfgang Aulbach

Hamburg | 2021

This work was typeset in LaTeX, figures were created by matplotlib, Ti*k*Z and Ipe.

Gutachter der Dissertation:	Prof. Dr. Michael Potthoff Prof. Dr. Alexander Lichtenstein
Zusammensetzung der Prüfungskommission:	Prof. Dr. Michael Potthoff Prof. Dr. Alexander Lichtenstein Prof. Dr. Daniela Pfannkuche PD Dr. Elena Vedmedenko Prof. Dr. Wolfgang Hansen
Vorsitzender der Prüfungskommission:	Prof. Dr. Daniela Pfannkuche
Datum der Disputation:	29.03.2021
Vorsitzender Fach-Promotionsausschusses PHYSIK:	Prof. Dr. Wolfgang Hansen
Leiter des Fachbereichs PHYSIK:	Prof. Dr. Günter Hans Walter Sigl
Dekan der Fakultät MIN:	Prof. Dr. Heinrich Graener

Für mein Kathrinchen

Abstract

A site-selective extension of the dynamical mean-field approach is proposed and implemented. The implementation supposes remaining single impurity problems to be solved numerically exact by means of a continuous-time quantum Monte Carlo (CT-QMC) solver which is based on the hybridization expansion. It is then successfully used to study site dependent magnetic phenomena in the periodic Anderson model (PAM) on two very different lattice geometries. In a first scenario, the PAM is considered on the triangular lattice. To study the competition between Kondo screening and indirect magnetic exchange, this geometrically frustrated model is systematically scanned from the weak- to the strong-coupling regime for a wide range of fillings n. The magnetic phase diagram is derived in terms of the site-selective dynamical mean-field approach by self-consistent mapping onto three independent single-impurity models corresponding to the three correlated f orbitals in the unit cell. At half-filling, the system turns out to be a non-magnetic Kondo insulator for all considered interaction strengths $U > 0$ which immediately develops into a non-magnetic metallic Kondo-singlet phase for fillings slightly below half-filling. On the other hand, indirect magnetic exchange between the f moments results in antiferromagnetic order at lower fillings. The antiferromagnetic and the Kondo-singlet phases are separated in the U-n phase diagram by an extended region of partial Kondo screening, i.e., a phase where the magnetic moment at one site in the unit cell is Kondo screened while the remaining two are coupled antiferromagnetically. At even lower fillings the system crosses over from a local-moment to a mixed-valence regime where the minimization of the kinetic energy in a strongly correlated system gives rise to a metallic and partially polarized ferromagnetic state. In a second scenario, the finite-temperature properties of an Anderson lattice with regularly depleted impurities are investigated. The physics of this model is ruled by two different magnetic exchange mechanisms: Conventional Ruderman-Kittel-Kasuya-Yosida (RKKY) interaction at weak hybridization strength V and a novel inverse indirect magnetic exchange (IIME) at strong V, both favoring a ferromagnetic ground state. The stability of ferromagnetic order against thermal fluctuations is systematically studied by static mean-field theory for an effective low-energy spin-only model emerging perturbatively in the strong-coupling limit as well as by dynamical mean-field theory (DMFT) for the full model. The Curie temperature is found at a maximum for a half-filled conduction band and at intermediate hybridization strengths in the crossover regime between RKKY and IIME.

Zusammenfassung

Eine Gitterplatz-selektive Erweiterung der dynamischen Molekularfeldtheorie (*englisch:* dynamical mean-field theory, DMFT) wird vorgeschlagen. Entsprechende Implementierung sieht eine numerisch exakte Lösung resultierender Einzelstörstellenprobleme durch einen in kontinuierlicher Zeit operierenden Quanten-Monte-Carlo-Algorithmus vor. Dieser basiert auf der störungstheoretischen Reihenentwicklung der Hybridisierung. Das geschilderte methodische Konstrukt wird erfolgreich zur Untersuchung von Gitterplatz-abhängigen magnetischen Phänomenen im periodischen Anderson-Modell auf zwei unterschiedlichen Gittergeometrien herangezogen. In einem ersten Szenario wird eine dreieckige Gitterstruktur betrachtet. Um den Konkurrenzkampf zwischen Kondo-Abschirmung und indirektem magnetischen Austausch zu untersuchen, wird das geometrischer Frustration ausgesetzte Modell systematisch innerhalb einer großen Bandbreite verschiedener Füllungen n vom Bereich der schwachen bis hin zur starken magnetischen Kopplung untersucht. Das zugehörige magnetische Phasendiagramm wird, im Sinne der Gitterplatz-selektiven DMFT, durch eine selbstkonsistente Abbildung der drei in der Einheitszelle enthaltenen korrelierten f-Orbitale auf drei voneinander unabhängige Einzelstörstellenmodelle ermittelt. Bei Halbfüllung entpuppt sich das System für alle betrachteten Wechselwirkungen $U > 0$ als amagnetischer Kondo-Isolator, welcher für Füllungen leicht unterhalb der Halbfüllung sofort in eine Phase amagnetischer Kondo-Singuletts übergeht. Dementgegen resultiert für kleinere Füllungen ein indirekter magnetischer Austausch antiferromagnetischer Ordnung zwischen den magnetischen f-Momenten. Die Phasen antiferromagnetischer Ordnung und der Kondo-Singuletts werden im U-n Phasendiagramm durch einen ausgedehnten Bereich partieller Kondo-Abschirmung separiert. Letztere bezeichnet eine Phase, in welcher pro Einheitszelle das magnetische Moment eines Gitterplatzes durch den Kondo-Effekt abgeschirmt wird, während die verbleibenden beiden magnetischen Momente antiferromagnetisch miteinander koppeln. Bei noch niedrigeren Füllungen geht das System von einem Regime der lokalen magnetischen Momente in ein Regime gemischter Valenzen über. Hier führt die Minimierung der kinetischen Energie innerhalb eines stark korrelierten Systems zu einem partiell polarisierten ferromagnetischen Zustand. In einem zweiten Szenario werden die Eigenschaften des hinsichtlich der Störstellen homogen ausgedünnten Anderson Gitters bei endlicher Temperatur untersucht. Die Physik dieses Modells wird durch zwei verschiedene magnetische Austausch-Mechanismen geprägt: Die konventionelle Ruderman-Kittel-Kasuya-Yosida (RKKY) Wechselwirkung bei schwacher und einen neuartigen inversen indirekten magnetischen Austausch bei starker Hybridisierung V. Beide Austausch-Mechanismen favorisieren einen ferromagnetischen Grundzustand. Die Stabilität der ferromagnetischen Ordnung wird hinsichtlich thermischer Fluktuationen untersucht: Im Rahmen der statischen Molekularfeldtheorie in Bezug auf ein störungstheoretisch im Limes starker magnetischer Kopplung auftretendes, effektives niederenergetisches Spin-Modell, mittels DMFT für das voll umfängliche Modell. Die maximale Curie Temperatur stellt sich bei halb gefülltem Leitungsband und bei mittlerer Hybridisierungsstärke innerhalb des Übergangs zwischen RKKY und inverser indirekter magnetischer Austausch-Wechselwirkung ein.

Contents

Acronyms

AFM antiferromagnetic

AIM Anderson impurity model

BSS Blankenbecler-Scalapino-Sugar

CT-AUX continuous-time auxiliary field

CT-HYB continuous-time hybridization expansion

CT-INT continuous-time interaction expansion

CT-QMC continuous-time quantum Monte Carlo

DMFT dynamical mean-field theory

DMRG density matrix renormalization group

DOS density of states

FM ferromagnetic

HF Hartree-Fock

IIME inverse indirect magnetic exchange

KI Kondo insulator

KIM Kondo impurity model

KLM Kondo lattice model

KS Kondo singlet

MC Monte Carlo

MCMC Markov chain Monte Carlo

MPI Message Passing Interface

NRG numerical renormalization group

PAM periodic Anderson model

PKS partial Kondo screening

PM paramagnetic

QMC quantum Monte Carlo

RKKY Ruderman-Kittel-Kasuya-Yosida

sdDMFT site-dependent dynamical mean-field theory

SIAM single-impurity Anderson model

VMPS variational matrix product states

1. Introduction & motivation

The phenomenon of magnetism attracts human interest since ancient times. The first in western civilization who is known to analytically wonder about magnetism was Thales of Miletus. The famous philosopher, mathematician and astronomer of the ancient Greece believed that lodestone, a naturally magnetized piece of the mineral magnetite, attracts iron because it has a soul [Ari10].

Nowadays, the understanding—and with it the more or less abstract models—to theoretically describe magnetic phenomena, of course have drastically changed: Most technical applications mainly concentrate on and successfully deal with electromagnetism [Ida15] entirely described in terms of classical magnetostatics and electrodynamics [Jac98]. These classical field theories that are completely tailored around Maxwell's equations forbid the existence of magnetic monopoles but instead reduce the origin of magnetism to the necessary existence of a magnetic moment which in turn is induced by an electrical ring current—that is by the motion of electrical charge on a closed loop trajectory. A phenomenological fact which is also valid vice versa and that belongs to the conceptual basement of electrical engineering [KMR13]. In order to really understand the macroscopic magnetic behavior of materials like lodestone however, one has to properly investigate right those events that take place on the microscopic level of such structures. In this scenery, energy typically scales in magnitudes of Planck's constant wherefore classical approaches to some decisive extend fail and thus have to give way to corrections in terms of quantum [Sak94; Bel06] or even quantum field theories [FW03; AS10; BF04]. The origin of magnetism, namely the necessary existence of an electrical ring current here to some extend still holds. The most elementary magnetic moment might considered to be induced by the electronic spin, a purely quantum theoretical self-rotation associated to a quantized angular momentum of the single electron, hence its elementary portion of charge. Thereby, the quantization of this spin-angular-momentum occurs in magnitudes of the Bohr magneton.

By applying this to atoms, molecules or solids, one has to be aware of the following: While principally every spinning electron induces a magnetic moment, two moments induced by two electrons that only differ in the spin quantum number screen each other and thus vanish for the outside world of the hosting electronic orbital. Consequently, an elementary magnetic moment can be "felt" as such by its surroundings in the outer world, e.g. in a solid, only if the associated electron has no counterpart with equal quantum numbers apart from the spin quantum number. In accordance with Hund's rules (see e.g. [BJ03]) this always holds in the case of odd-filled electronic orbitals. The filling of electronic orbitals depends on energetic aspects which are usually defined by constellations of parameters of the system under investigation.

Now, proposed that the given energetic circumstances initiate the system to inhibit local mag-

netic moments on the microscopic level, those still have to arrange some principal order among each other to let the system show up as a magnet by means of appropriate detectors in the macrocosm. In that sense a macroscopic magnetic permanence may be explained as a consequence of a microscopic *collective phenomena*—hence may be categorized as a *collective magnetism*.

This statement however, raises significant questions: Firstly, for what reasons at all do local magnetic moments principally happen to form out? Secondly, why and how should those order? A model which originally was designed to fundamentally provide a theoretical base to study and finally get answers to both questions, but meanwhile has turned out to be a multi-purpose model in regard to the investigation, simulation and explanation of versatile physical phenomena is the periodic Anderson model [TSU97].

In momentum space, the periodic Anderson model (PAM) generally describes a band of conduction electrons, often also just denoted as sea or bath of electrons, hybridizing with a narrow band of correlated electrons. This very special constellation of highly localized and in this specific case thus correlated electrons on the one hand, hybridizing with free electrons on the other hand bares physics beyond that of local magnetic moments of high interest. By means of Fermi liquid theory [PN66] the correlated electrons theoretically can be represented by quasi-particles of masses up to a thousand times heavier than the known electron mass wherefore those electrons may be categorized as heavy electrons. Correspondingly, the conduction electrons are considered to be light electrons in this terminology. In that sense, the PAM also served as the model of choice to describe heavy-fermion materials realized in crystals [Fis+86; TSU97] or in quantum simulations [Neu+07; WA14b]. Furthermore, the charge fluctuations on the correlated orbitals of the PAM in conjunction with strong spin-orbit coupling naturally leads to the concept of a topological Kondo insulator [Dze+10; WA14a] which has argued to be realized in SmB_6 [Wol+13; Min+14].

In a corresponding real-space representation, aforementioned bands of the PAM transform into a lattice of concrete sites that each host a correlated and an uncorrelated electronic orbital. Here, electrons are allowed to freely move through the lattice because of an installed simple hopping between the uncorrelated orbitals of the concrete sites. Furthermore, there is a hybridization in this representation, too, which allows for an electron-exchange between the different orbital types. As electrons are not allowed to directly hop between different correlated orbitals, in that sense, electrons in the correlated orbitals are in fact localized, while electrons in the uncorrelated orbitals are not.

By analogy to the band-characteristics in momentum space representation, the correlated orbitals are generally considered to be narrower in space as the uncorrelated ones. Therefore local correlation effectively occurs in the case of electronic double-occupancy of a concrete correlated orbital due to a non-negligible local Coulomb repulsion that costs the system an additional amount of energy. By that, for a given well-defined Anderson model in equilibrium with a finite hybridization, it is the strength of the Coulomb repulsion that primarily regulates whether an electronic double-occupancy of local correlated orbitals is energetically favorable for the system or not. A fact that drastically affects the formation of magnetic moments in the correlated orbitals for already stressed out reasons: If a narrow orbital is doubly occupied by electrons, the associated spin-induced magnetic moments form a singlet state, hence screen each other and no result-

ing magnetic moment is felt by the world around. Apart from that, if the Coulomb repulsion is chosen strong enough to deny electronic double-occupancy of correlated orbitals, these remain singly occupied equipping the system with non-screened local magnetic moments. In the end, the formation of local magnetic moments surely does not only depend on the Coulomb repulsion but more on the whole set of already mentioned model parameters as the hybridization, the orbital energies and last but not least the temperature.

The necessary conditions in which a local moment formation takes place in particular have been studied in terms of the Anderson impurity model (AIM) in [And61]. In contrast to the PAM, the AIM only considers one single correlated orbital that hybridizes with a sea of free electrons. Initially it was proposed by nobel laureate Phil W. Anderson in order to be able to theoretically describe the relevant physics of an probably magnetic impurity ion like Ce which is nested inside a homogeneous metallic host material like Fe. Therefore, Anderson models are categorized as impurity models.

Thorough examinations of impurity models exposed to different sets of parameters allowed for the discovery and classification of several energetic regimes associated with typical characteristics. Of special interest here, is the so-called *local moment regime*. In this special regime every correlated orbital hosts one single electron with its unscreened magnetic moment. It sets the stage for the occurrence of an itinerant magnetic exchange mechanism in terms of Ruderman-Kittel-Kasuya-Yosida interaction [RK54; Kas56; Yos57]—an interaction between local magnetic moments of different sites which evolves indirectly via the host material and typically leads to an alternating arrangement of next-neighboring local magnetic moments in opposite directions. By that, a theoretically explainable antiferromagnetic order is established by means of an indirect non-local exchange mechanism. A common and essential question to be posed now is, how stable this order may be against competing phenomena. A purely local effect that in itself is already observable in the AIM but in terms of the PAM works against magnetic order is known as the Kondo effect [Kon64]. Proposed the temperature of the system is decreased under a specific critical temperature, the electronic spin that induces a local magnetic moment enters a singlet state with one or more spins of the host material, the Kondo singlet state. As a drastic consequence the local magnetic moment is screened by a tight so-called Kondo cloud of conduction electrons and thus is excluded from taking part in a magnetic long range order.

As RKKY exchange and the Kondo effect are ruled by respectively different energy scales the PAM is confronted with an energetic rival between both phenomena. A rival that inescapably manifests a parameter-driven quantum phase transition whose corresponding phase diagram is known as the famous phase diagram of Doniach [Don77; Löh+07]. It shows a phase of antiferromagnetic order due to the itinerant exchange and separated from that a paramagnetic phase of Kondo singlets—in terms of Fermi liquid theory an unordered heavy-fermion phase—in which local magnetic moments still exist but are screened by means of the Kondo effect. As already emphasized, the physics behind the Doniach phase diagram entirely takes place in the local moment regime of the Anderson lattice, thus usually at strong Coulomb repulsion. In this case Anderson models may be approximated by more simpler Kondo impurity models. Those are effective low-energy models of the Anderson-type impurity models in terms of a canonical transformation [SW66]. By that, the crucial formal difference between Anderson and Kondo models lies in the interpretation of the formed local magnetic moments: Here, the Kondo models come around

as spin-type models and charge fluctuations between the correlated and uncorrelated orbitals are suppressed. Therefore, the Anderson lattice has richer physics than the Kondo-lattice model because it still allows for real charge fluctuations between un- and correlated impurity orbitals.

Besides the already mentioned bare parameters like the Coulomb repulsion or the hybridization strength, the physics of local magnetic moments in terms of the Anderson lattice drastically depends on the choice of the geometry of this lattice. A triangular Anderson lattice tuned into its local-moment regime may act as a model of a geometrically frustrated magnet. While frustrated magnets are subjects of contemporary research *per se* [Bal10], also some heavy-fermion materials, such as CePdAl, are synthesized on frustrated geometries [Oya+08]. By confronting the PAM to geometrical frustration, even in energetic regimes where the absence of a Kondo effect is ensured, the then unscreened local magnetic moments may not establish a total antiferromagnetic order typically favored by means of the RKKY interaction anymore. Ideally the internal structure of the PAM principally grants for a way out of this unfavorable situation: A site-selective Kondo effect that alleviates the frustration thus allowing the remnant spins to order magnetically via the RKKY interaction. Thereby geometric frustration extends the energetic rival between Kondo effect and RKKY interaction by another energy scale in the problem associated with the release of frustration via the just mentioned mechanism known as partial Kondo screening [Mot+10]. A site-dependent screening like this can occur spontaneously or can reflect chemically different environments in compounds with large unit cells. The mechanism of partial Kondo screening has attracted considerable attention in the past: Back in 1991 Ballou, Lacroix, and Nunez Regueiro published results of their investigations of frustration-induced vanishing of magnetic moments in $R\mathrm{Mn}_2$ systems by means of a model they derived from the Hubbard Hamiltonian [BLN91]. Then, Benlagra, Fritz, and Vojta reported in 2011 on their studies on competitive versus cooperative Kondo screening in Kondo lattices with nonequivalent local moments [BFV11]. Of special interest in the context of magnetic phases in the geometrically frustrated PAM were two publications of Hayami, Udagawa, and Motome [HUM11; HUM12] out of the years 2011 and 2012: Both provide magnetic phase diagrams of the ground-state model at zero temperature, numerically calculated by means of static mean-field approaches. This naturally poses the question, whether it is principally possible to find and stabilize phases of PKS also beyond a static mean-field approximation in terms of a dynamical mean-field approach, hence by means of dynamical mean-field theory (DMFT).

Even the simplest most common models of quantum many-particle systems represent full quantum many-body problems, which implies one is blamed to work inside a describing Hilbert space of exponentially growing dimension with respect to a linearly increasing number of lattice sites. Consequently analytical solutions become rare and can principally only be obtained for very small systems or in terms of special limits of underlying parameter regimes that often do not contain, show or feedback the physics of interest such as phase transitions. In order to treat the full model within time-scales significantly shorter than the average human lifetime one therefore depends on strong numerical aid in form of powerful approximation schemes. In the case of strongly correlated models one additionally has to handle the difficulty of choosing approximations in a way that the physical impact induced by the electron-electron interaction remain conserved. While static mean-field theory evidently fails in regard to this requirement a dynamical mean-field approximation—as per construction—serves well on this demand.

Generally, the DMFT [MV89; Geo+96] is a comprehensive non-perturbative and thermodynamically consistent numerical method that was especially developed to provide an approximate treatment of correlated electronic lattice models such as the PAM of preferably high dimension. Thereby the original model conceptually is self-consistently mapped on, thus reduced to an effective single impurity model which is then left to be solved by an appropriate impurity solver. Like its static counterpart, the DMFT becomes exact in the limit of infinite dimension $D \to \infty$ and is methodically based on the locality of the systems self-energy in that limit (c.f. section 4.2).

The dynamical mean-field approach has successfully been applied to calculations of the PAM: The first notable publication in that spirit was the examination of the symmetric PAM in infinite dimensions with an essentially exact quantum Monte Carlo (QMC) method [Jar95]. Furthermore, the paramagnetic ground state of the PAM was studied by DMFT and the usage of a numerical renormalization group (NRG) solver [PBJ00].

DMFT neglects the feedback of non-local, e.g. magnetic correlations, on the local self-energy and the local one-particle Green's function but correctly accounts for all local correlations. This represents a decisive step beyond the static mean-field approach. In order to hunt for the PKS phase in the triangular Anderson lattice, a variant of the DMFT has to be applied, which treats the different correlated orbitals in the suitably chosen unit cell independently, similar to a real-space DMFT approach [PN97]. We will show that the competition between RKKY coupling and Kondo screening, supplemented by lattice frustration leads to a remarkably rich phase diagram including a PKS phase emerging in the local-moment regime at the border between paramagnetic heavy-fermion and magnetically ordered phases.

As already mentioned above, by means of DMFT, this technically is only possible by the usage of a stable and well-suited impurity solver. On demand of this, we choose a segment variant of the continuous-time hybridization expansion (CT-HYB) [Wer+06; WM06] algorithm out of the family of continuous-time quantum Monte Carlo impurity solvers [Gul+11]. Methodically, this algorithm provides Monte Carlo (MC) estimators of physical observables by means of the sampling of the grand canonical partition function of the given impurity model, here the PAM. In particular, the sampling is based on a diagrammatic expansion of stochastically controlled order applied to the hybridization part of the PAM. Per construction this method works numerically exact and offers the technically advantageous opportunity to solve single-impurity problems directly in terms of Matsubara frequencies instead of imaginary times. It is predestined as the impurity solver of choice to solve complex impurity problems at strong coupling and with the full Coulomb repulsion [Ass14], especially in the framework of DMFT [WM07; Wer+08; Par+13; WA13; WA14a].

The described numerical apparatus of DMFT combined with the CT-HYB segment code turns out to be very flexible in regard to the used lattice geometry. This invites for the examination of another Anderson lattice besides the triangular one. Of special interest here, is the depleted PAM. To be more specific, a periodic Anderson lattice thinned out in a regular manner with regard to the correlated impurity orbitals. The depleted Anderson lattice model has been considered beforehand to describe artificial Kondo systems realized as ultracold atoms trapped in optical lattices [SHP14]. It is related to two-dimensional superlattices consisting of periodic arrangements of correlated-electron- and non-interacting layers [PTK13]—thus may be used to

describe systems of magnetic atoms on non-magnetic metallic surfaces where a manipulation of the adatom geometry and a precise mapping of magnetic couplings is accessible to scanning-tunneling techniques on an atomic scale [ES90; HLH06; Wie09; Kha+11; Kha+12].

From a general point of view, the depleted PAM may offer a deeper insight into the physics of magnetic order of correlated orbitals coupled indirectly by conduction electrons. Ground-state calculations of the depleted Kondo lattice model (KLM) and the PAM in the local-moment regime at Zero temperature by means of variational matrix product states (VMPS) and DMFT have coincidentally shown surprising results [SGP12]. The magnetic moments of the remaining correlated impurity orbitals in terms of RKKY couple ferromagnetically for rather weak magnetic coupling between those and the corresponding magnetic moments of the surrounding electron due to the RKKY interaction. This however drastically changes towards strong couplings, where the Coulomb repulsion and the local hybridization strength getting much stronger than the nearest-neighbor conducting-electron hopping. Here, on every site that still hosts a correlated impurity orbital a Kondo singlet forms out. As a direct consequence, the mentioned ferromagnetic coupling between magnetic moments on the remaining correlated orbitals globally vanishes. Instead, the magnetic moments of the free bath orbitals hosted on sites that only consist out of one uncorrelated orbital each, show a ferromagnetic coupling. A coupling that turned out to be mediated via the Kondo singlets and thus was named as an inverse indirect magnetic exchange (IIME) [STP13]. By means of perturbation theory in regard to an effective Hamiltonian in the strong-coupling limit, the IIME could be identified as a perturbative effect of fourth order [TSP14].

In further studies, the effective Hamiltonian has been successfully used for temperature-dependent static mean-field calculations of the depleted PAM in one up to three dimensions, showing qualitatively satisfying the crossover from conventional RKKY to the novel IIME and amongst further results identifying a flat band at the Fermi energy of the system [TSP15]. For one reason, those studies promised a rather stable thermodynamic behavior of the ferromagnetic coupling due to RKKY as well as IIME. For another reason, the existence of a flat band due to Stoner's criterion, suppose the depleted Anderson lattice to behave extremely susceptible to ferromagnetic order. Therefore, a high critical temperature of the model system is expected. A fact, that possibly bares the chance to be able to experimentally verify the IIME by means of already mentioned ultracold atoms which are trapped in optical lattices [LSA12].

However, like in our topic before, both predictions of the effective mean-field approach need to be verified beyond this approximation with respect to accuracy. In regard to thermodynamical stability of the ferromagnetic coupling this ideally should be done for a three dimensional model in order to overcome the theorem of Mermin and Wagner [MW66]. Thus, a possible verification of the mean-field results at finite temperature and in dimensions higher than two, conceptually depends on a method that is suited for a thermodynamical application towards the strong coupling limit in several dimensions while being less approximative than the effective mean-field approach. Methodologically non-trivial requirements, that principally could and can not be fulfilled by the VMPS approach. The VMPS [Sch11], a sophisticated technical realization of the density matrix renormalization group (DMRG) [Sch05; PE] out from the ranks of tensor networks [Orú14] indeed is applicable for calculations at finite temperature but for technical reasons is restricted to one dimensional problems [Sch13].

A method that does fulfill the above mentioned requirements however is a DMFT approach that distinguishes between different lattice sites to match the lattice dilution. This comes full circle with a repetitive demand for our previously explained setup of site-dependent dynamical mean-field theory (sdDMFT) implying a CT-HYB segment code impurity solver adapted to the concerns of the diluted Anderson lattice. In that spirit, we will calculate several transitions from ferromagnetic to paramagnetic phases in order to get the corresponding critical temperatures for different hybridization strengths. For calculations in three dimensions in expecting a "RKKY-to-IIME crossover" these temperatures then should follow the rivaling energy scales of RKKY for weak and of IIME towards strong hybridizations. Consequently, a maximum of the critical temperature is expected at intermediate hybridization strength in the crossover regime between RKKY interaction and IIME. Apart from that, respective DMFT results can be compared to those available by means of the effective mean-field approach.

1.1. Outline of the thesis

The topics of this thesis as motivated above are thematically organized into concrete chapters.

In that sense chapters 2 and 3 provide the foundation of theoretical background information and knowledge that is required in and often will be referenced to by the subsequent chapters. In chapter 2 we give a compact presentation of those models of many-body systems commonly used and treated within theoretical many-particle physics but additionally conceptionally located around the PAM. Here, our focus particularly lies on the construction and discussion of representing Hamilton operators, hence more on the technical formulation of models as on the implied physics. Nevertheless we present some physical insights of interest for the subsequent chapters of the thesis. With the PAM and relative impurity models at hand, we are able to focus on the physics of local magnetic moments in chapter 3 including a discussion from the formation up to the Doniach phase diagram and an outlook on further influences that disturb magnetic order.

Chapters 4 and 5 entirely report on the methods and the numerical setup which was used to produce the physical results and insights presented in the subsequent chapters 6 and 7. In particular, chapter 4 is on mean-field theory in general, on DMFT in special and on sdDMFT in very special. The following chapter 5 gives a very detailed kind of review of the general Markov chain Monte Carlo (MCMC) methods as used in statistical physics and the very special segment variant of the CT-HYB approach as a member of the family of CT-QMC impurity solvers.

Chapters 6 and 7 contain the actual physical results we want to communicate by means of this thesis. In chapter 6 we present our sdDMFT-studies on the $D = 2$ -dimensional PAM on the triangular lattice in regard to emerging magnetic phases, mainly that of a PKS. This chapter also contains a detailed methodical preparation by means of the site-selective approach. This is followed by chapter 7 which implies the investigations of a minimally periodically diluted PAM on a $D = 1$, square $D = 2$ and a cubic $D = 3$-dimensional lattice structure. All of them are treated by means of a mean-field approach on an perturbatively derived effective Hamiltonian as well as in the framework of sdDMFT in regard to the full original Hamiltonian.

Finally in chapter 8 we provide conclusions and an outlook. Those traditionally and effectively contain a summary of the preceding parts of the thesis thereby focussing on the physical as well as technical conclusions. Furthermore we give some outlook on emergent questions and provide proposals for further steps of research in the context of the studies presented within chapters 6 and 7.

This thesis also bares an appendix which directly follows chapter 8. It contains remarks on mathematical notation, the Matsubara formalism and different representations of the partition function.

1.2. Units

For convenience and to fit to common conventions (see e.g. [EK16]) throughout this work units are chosen such that

$$\hbar = k_\mathrm{B} = 1\,, \tag{1.1}$$

where $\hbar$ is the *Planck constant* in its *reduced variant* and k_B is the *Boltzmann constant*. By that the very often used parameter $\beta = 1/k_\mathrm{B}T$, originally known from the formulation of the Boltzmann distribution (see e.g. [BB09]), simply reduces to the inverse temperature $1/T$.

2. Model Hamiltonians and physical insights

Like for all quantum systems, the first step in order to be able to theoretically treat quantum many-body systems in a qualitative as well as quantitative way is to map such systems—or at least the features of current interest—on a suitable model. In terms of a formal quantum theoretical and in the end mathematical treatment this is synonymous to the formulation of a suitable, hence applicable Hamilton operator that corresponds to the initial model and also includes its actual features. In that spirit, the present chapter sketches the formulation, manipulation or just extraction of Hamiltonians that cover the formal description of all many-body models which in some sense will show up as useful or even essential for the understanding of the upcoming chapters. Additionally, some remarks on physical insights that result out of the structure of the full Hamiltonians or alternatively in regard to some special parameter-limits will be given. As such, depending on the reader's familiarity with theoretical many-body physics, this chapter was carefully designed to serve as a reviewing refresher as well as a compact introduction on the subject. In the general context of this thesis, as already stressed out in the introduction on page 1 and the following, clearly the most important model to be treated is the periodic Anderson model (PAM). We will do so in section 2.3. Nevertheless, to be able to argue in a wider context, it seemed reasonable to additionally introduce relative models. Listed in a loose order, those are the Kondo impurity models in section 2.4 as well as the Hubbard model in section 2.2 and actually the Heisenberg model in section 2.5, even though the latter one will be presented in a rather poor fashion due to its minor importance for the core topics of this thesis. As a clean starting point for a formally reasonable development of the corresponding model Hamiltonians, the formulation of a *general* many-body Hamiltonian was chosen and presented in section 2.1. Like it has become usual in many-body theory, the formal language of choice will be the second quantization like it is for example introduced or reviewed in a very pedagogical sense in [NO98; BF04; AS10]. This however, besides only a few exceptions, will be applied even beyond this chapter for the rest of the thesis. As it reports on physical phenomena of purely electronic systems, one should recall that as a direct consequence, it will be constantly sufficient to restrict formalism to its fermionic flavor.

2.1. General formulation of many-body systems

As just mentioned above, in common quantum theory the physics of a quantum system is described by a so-called Hamilton operator. In a very general sense, such a *Hamiltonian* at first sight arises as the sum of two parts: One part which represents the total kinetic energy T_{tot} and a second part that stands for the total potential energy V_{tot}. This fact also holds for many-body

Hamiltonians. Traditionally, for models like those of interest here, T_{tot} is identified as an *one-particle* operator while V_{tot} is assumed to be of a *two-particle* nature. In second quantization, both operators may comfortably be formulated using typical *creation* and *annihilation operators*.

In that sense, let a_α be an arbitrary fermionic single-particle annihilation operator that annihilates a particle in the state indexed by α. Its *hermitian adjoint*[1] $a_\alpha^\dagger$ is called the corresponding fermionic single-particle creation operator that creates a particle in the state indexed by α, respectively. Typically, as elaborately shown in [NO98], those operators fulfill the following anti-commutation relations:

$$[a_\alpha^\dagger, a_\beta^\dagger]_+ = [a_\alpha, a_\beta]_+ = 0\,, \tag{2.1}$$

$$[a_\alpha, a_\beta^\dagger]_+ = \delta_{\alpha\beta}\,. \tag{2.2}$$

where the common notation of anti-commutators as defined by eq. (A.6) and the Kronecker's delta $\delta_{\alpha\beta}$ defined within eq. (A.1) were used. From that, one directly derives

$$(a_\beta)^2 = (a_\beta^\dagger)^2 = 0\,, \tag{2.3}$$

what reflects the *Pauli exclusion principle*[2] within the formalism of second quantization. With these operators at hand, finally a *general Hamiltonian* in second quantization may be formulated like

$$H = \underbrace{\sum_{\alpha\nu} T_{\alpha\nu} a_\alpha^\dagger a_\nu}_{T_{\text{tot}}} + \underbrace{\frac{1}{2} \sum_{\alpha\beta\gamma\delta} V_{\alpha\beta\gamma\delta} a_\alpha^\dagger a_\beta^\dagger a_\gamma a_\delta}_{V_{\text{tot}}}\,, \tag{2.4}$$

where the indices $\alpha, \beta, \gamma, \delta$ and ν represent multi-indices that may collect severe quantum numbers like spin-projection and orbital as well as site indices. In addition $T_{\alpha\nu}$ marks the elements of a general *hopping matrix* whose entries feedback the kinetic energy gained by the system as a result of the linked electronic motion i.e. *hopping*. $V_{\alpha\beta\gamma\delta}$ represents the strength of *pairwise interactions* of electrons that were in the electronic states $|\gamma\rangle$ and $|\delta\rangle$ before and in $|\alpha\rangle$ and $|\beta\rangle$ after the interaction taking place. In this context, one rather speaks of the kinetic term as of the *hopping term* and of the potential term as of the *interaction term*.

By the usage of multi-indices the Hamiltonian written in eq. (2.4) may be used to describe models of practically arbitrary complexity. Yet, for the purposes this thesis wants to communicate, in addition to the already indicated restriction to fermionic formalism, it will be sufficient to exclusively focus on electronic single-band models whose corresponding Hamiltonians are diagonal in regard to the projections of electronic spins.

[1] As might be for example looked up in [Bel06], generally, the operator a is *hermitian* if for its *hermitian adjoint* $a^\dagger$ the equation $a^\dagger \overset{!}{=} a^{-1}$ holds, where per definition $a^\dagger$ is identified as the *complex conjugated transposed* of a, hence $a^\dagger := (a^*)^\mathsf{T}$.

[2] One should find information on the famous *Pauli exclusion principle* in any serious textbook on quantum mechanics. We tend to refer to [Sak94] as our textbooks of choice.

Furthermore, note that while so far the symbol V was used to mark a potential to be conform to the traditional notation of classical and quantum field theory,[3] in the following potentials will be marked by U what fits to the common notation in many-body physics.[4]

2.2. The Hubbard Model

The structure of the general many-body Hamilton operator shown in eq. (2.4) directly expresses the fact that the behavior of interacting electrons in correlated systems is ruled by the competition between kinetic and impulsive potential energy. The easiest lattice model that is able to properly describe this competition is the single-band Hubbard model [Hub63]. Its model Hamiltonian in real-space representation may be formally derived from eq. (2.4) by applying the following three steps:

1. Each multi-index is reduced to a combination of site indices i, j that are short notation for corresponding real-space vectors $\mathbf{r}_i, \mathbf{r}_j$ which mark the locations of discrete lattice sites in real-space and an additional spin-projection index $\sigma = \uparrow, \downarrow$. In particular:

$$\alpha = \delta \to i, \sigma \quad , \quad \beta = \gamma \to i, -\sigma \quad \text{and} \quad \nu \to j, \sigma \, .$$

2. According to that, in order to stick with the usual notation, the electronic operators are renamed from a to c and the general hopping matrix $T_{\alpha\nu}$, now T_{ij}, is changed to t_{ij} which regarding its entries is defined as

$$t_{ij} = \begin{cases} -t & \forall i, j \, : \, |\mathbf{r}_i - \mathbf{r}_j| = a \text{ with lattice constant } a \, , \\ \varepsilon_0 & \forall i, j \, : \, i = j \, , \\ 0 & \text{else} \, . \end{cases} \tag{2.5}$$

3. In a last step the complicated interaction $V_{\alpha\beta\gamma\delta}$ is replaced by a constant, hence index-independent U, the so-called *Hubbard U*.

With that, the Hamiltonian of the single-band Hubbard model in second quantization finally reads

$$H_{\text{Hub}} = \sum_{ij\sigma} t_{ij} c^\dagger_{i\sigma} c_{j\sigma} + \frac{U}{2} \sum_{i\sigma} c^\dagger_{i\sigma} c_{i\sigma} c^\dagger_{i-\sigma} c_{i-\sigma} \, , \tag{2.6}$$

where the formally favored *normal order*[1] [NO98] of creation and annihilation operators inside the interaction term has been broken up[2] in support of the introduction of *particle number operators* that, back in general notation, are defined as:

$$n^{(a)}_\nu = a^\dagger_\nu a_\nu \, . \tag{2.7}$$

[3] For demonstration, you may want to compare notation with that used in [Sch12] and [Mag04].

[4] At this place, the main concern of doing so is to prevent a confusion with the hybridization V that will be introduced later within this chapter.

In this spirit the Hamiltonian (2.6) can alternatively be written as

$$H_{\mathrm{Hub}} = -t \sum_{\langle i,j \rangle} \sum_{\sigma} c^{\dagger}_{i\sigma} c_{j\sigma} + \varepsilon_0 \sum_{i\sigma} n^{(c)}_{i\sigma} + \frac{U}{2} \sum_{i\sigma} n^{(c)}_{i\sigma} n^{(c)}_{i-\sigma} \,, \tag{2.8}$$

where $\sum_{\langle i,j \rangle}$ represents the sum over all next-neighboring sites marked by the indices i and j. As it poses no formal problem, in the following usually $\varepsilon_0 = 0$ will be set for convenience.

Starting from its *atomic limit* at $t = 0$, the single-band Hubbard model may be seen as a model lattice of hydrogen atoms or, to be more precise, of single spin-degenerate *Wannier orbitals* per identical hydrogen atom i.e. discrete lattice site. With increasing $t > 0$ those orbitals progressively overlap. This bares a *tight-binding* character of the model which was already taken into account formally by the next-neighbor inter-site hopping of electrons in the definition of t_{ij} (2.5) inside the Hamilton (2.6) and equivalently by the sum $\sum_{\langle i,j \rangle}$ in the alternative formulation of H_{Hub} in terms of eq. (2.8). Through electron-hopping between next-neighboring sites that is conformal to Pauli's exclusion principle (c.f. the footnote on page 10), the system can reduce its kinetic energy by $-t$ per hop. In contradiction to this, the system gains an energy U per doubly occupied Wannier orbital, i.e. site, as the result of an electron-electron Coulomb repulsion that is assumed to be very local due to the narrow nature of the Wannier orbital and the screening by surrounding interfering electrons. This is explained in a more detailed and especially visualized fashion in fig. 2.1.

In this context the above mentioned model-internal competition between kinetic and impulsive potential energy may be reformulated as competition between itinerancy and localization. It is reflected by the value of U/t or—for a very precisely formulated model in terms of its lattice geometry—of U/W, where $W \propto t$ is the width of the single band. As discussed in [Lec11] with an increasing value of U/t the single-band Hubbard model passes through a metal-insulator transition which is indicated by a splitting of the local spectral function into a lower and upper Hubbard band. In the case of the half-filled lattice, this transition at $U \gg t$ results in a so-called *Mott insulator* [Mot68]. For energetic reasons this insulator is characterized by an electronic single-occupancy of all lattice sites whereas the separated electronic spins located on next-neighboring sites show an anti-parallel orientation. This observation indicates the Mott insulator as an antiferromagnetic insulator [Geb97; BB06]. In this special constellation of parameters, the single-band Hubbard model may be correctly described by a Heisenberg Hamiltonian (c.f. section 2.5 on page page 20 ff.) with antiferromagnetic coupling constant $J = 4t^2/U > 0$ [Faz99].

In regard to magnetic phenomena the single-band Hubbard model generally is predestined to study effects concerning *band magnetism* [NR09] but is structurally not suited to describe the physics of local magnetic moments. This motivates the introduction of so-called *magnetic impurity models* like *Anderson* as well as *Kondo models* in the following sections. For more information on the Hubbard model beyond the scope of facts presented so far the interested reader is referred to the monographs [Ess+05] and [Geb97] as well as the excellent and already cited review by Lechermann [Lec11] and additional references on the topic therein.

[1] That is in a sequence of operators all creation operators are positioned to the left of all annihilation operators.

[2] This was done using the anticommutation relations given by eqs. (2.1) and (2.2) thereby leading to a total sign $(-1) \cdot (-1) = +1$.

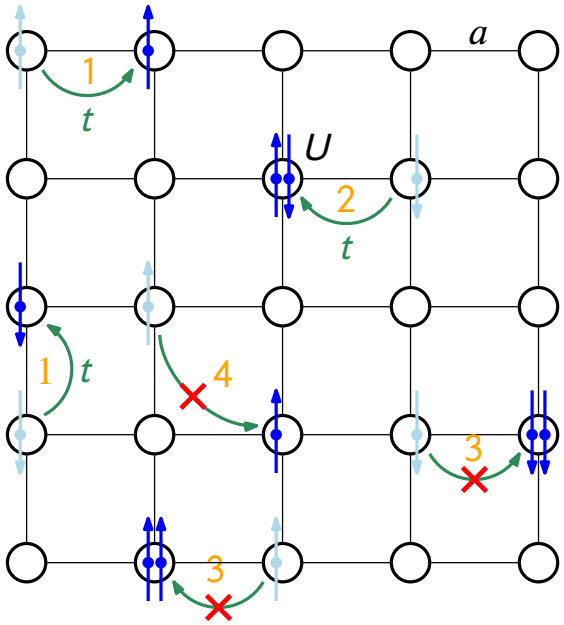

Figure 2.1.: Visualization of the $D = 2$-dimensional single-band Hubbard model. Electrons with spin projections $\uparrow, \downarrow$ (blue arrowed dots) may hop (green arrows) between discrete sites that host one spin-degenerate electronic orbital (black circles) each and form a square lattice. Here, black lines mark the shortest distance between next-neighbouring sites which is equal to the lattice constant a. Each regular hop (1) reduces the energy of the system per $-t$ while some hops are forbidden (red crosses) due to Pauli's exclusion principle (3) or due to the model restriction to next-neighbour hops (4). If a site becomes doubly occupied the system has to pay the energy U of an emerging local repulsion (2).

2.3. Anderson models

In the zoo of many-particle models, the *Anderson models* belong to the category of *impurity models*. Those are primarily constructed to study the physical behavior of local magnetic moments whereupon the Anderson models are even suitable to study the formation of those. In more detail, Anderson models describe the prominent problematic scenario of electronic systems of discrete, *possibly* magnetic impurity atoms that are nested inside a metallic host material. Primarily, as will be discussed in more depth below, the s- and p-orbitals of the host as well as impurity ions melt together to a "broad" conduction band often also called bath of electrons. On top, every impurity ion provides an active "narrow" shell to the system that may exchange electrons with the existing conduction band due to *hybridization* between energetically degenerate orbitals. As a formal consequence, corresponding Anderson-type Hamiltonians arise as the sum of three parts

$$H_{\mathrm{And}} = H_{\mathrm{band}} + H_{\mathrm{imp}} + H_{\mathrm{hyb}}\,, \tag{2.9}$$

where H_{band} describes the single conduction band, H_{imp} the physics of the active additional impurity orbitals and H_{hyb} represents the hybridization part of H_{And}. The simplest versions of all three parts will be presented and explained based on the example of the PAM in more detail in

the following.

As already mentioned, the single conduction band is formed by smeared out atomic *s*- or *p*-orbitals. Those orbitals are extended in space in such a way that Coulomb-type interactions between conduction electrons may be neglected. Formally this is sufficiently described by an effective non-interactive model Hamiltonian that may be derived from the single-band Hubbard model as introduced in the previous section 2.2 on page 11 and the following: In the so-called *Fermi gas* limit $U \to 0$ the interaction term of H_{Hub} (2.8) vanishes and H_{band} forms as

$$\lim_{U\to 0} H_{\mathrm{Hub}} \Big|_{\varepsilon_0=0} = H_{\mathrm{band}} = -t \sum_{\langle i,j\rangle} \sum_{\sigma} c^{\dagger}_{i\sigma} c_{j\sigma} = \sum_{\mathbf{k}\sigma} \varepsilon_{\mathbf{k}} c^{\dagger}_{\mathbf{k}\sigma} c_{\mathbf{k}\sigma} \,. \tag{2.10}$$

Here, the right side of the last equation represents H_{band} in momentum space, where $c^{\dagger}_{\mathbf{k}\sigma}$ creates and $c_{\mathbf{k}\sigma}$ annihilates an electron with momentum $\mathbf{k}$ and spin projection $\sigma = \uparrow, \downarrow$. Those annihilation and creation operators directly follow from appropriate Fourier, hence *unitary*[5] transformations of the corresponding real-space operators $c^{\dagger}_{i\sigma}$ and $c_{j\sigma}$. By respecting the condition that electronic hopping is only allowed between next-neighboring sites on the real-space lattice, for a hyper-cubic D-dimensional model $\varepsilon_{\mathbf{k}}$ is identified as

$$\varepsilon_{\mathbf{k}} = -2t \sum_{i}^{D} \cos k_i a \,, \tag{2.11}$$

with the lattice constant a and k_i marking the i-th component of a D-dimensional wave vector $\mathbf{k}$. The electronic eigenstates of this model are identified as *Bloch states*. In that sense, H_{band} indeed represents a single cosine-like band—so far declared in a more sloppy fashion just as conduction band—of *Bloch electrons* whose energy eigenvalues are given by an electronic dispersion relation $\varepsilon_{\mathbf{k}}$. Note here that in literature the band of uncorrelated conduction electrons often is also referred to as *bath* of electrons and in analogy the associated atoms as *bath sites*.

In a next step in order to derive the full PAM [TSU97], every bath site is extended with an additional single spin-degenerate orbital of an electronic energy level ε_f. In real materials those orbitals equal active d- or f-levels that are narrow in a spacial context. Therefore, emerging Coulomb repulsions between two possibly occupying electrons become important and may not be neglected anymore. Instead, Coulomb correlations are taken into account by an on-orbital—in a somehow imprecise formulation called on-site—Hubbard interaction U. In the following, electrons that occupy correlated impurity orbitals are conventionally indicated as f-electrons.

In regard to the derivation of the full model Hamiltonian the formal treatment of locally correlated impurity orbitals consequently manifests into an additional sum of two operator parts: One part H_f that describes the total on-site energy of the f-electrons, and a second part H_{int} that marks the local electronic interaction of the f-electrons in cases where the correlated impurity

[5] Assuming $\mathcal{U}$ to be the linear transformation operator and $\mathcal{U}^{\dagger}$ the linear operator of the corresponding back-transformation then the transformation is said to be *unitary* if $\mathcal{U}$ is an unitary operator, hence if $\mathcal{U}^{\dagger} = \mathcal{U}^{-1}$ (c.f. [Bel06]).

orbitals are doubly occupied. Thus, the local Hamiltonian reads:

$$H_{\mathrm{imp}} = \underbrace{\varepsilon_f \sum_{i\sigma} f^\dagger_{i\sigma} f_{i\sigma}}_{H_f} + \underbrace{\frac{U}{2} \sum_{i\sigma} n^{(f)}_{i\sigma} n^{(f)}_{i-\sigma}}_{H_{\mathrm{int}}} . \tag{2.12}$$

Here, by analogy to the conduction electrons in eq. (2.10), $f^\dagger_\sigma$ creates and f_σ annihilates an electron with spin projection $\sigma = \uparrow, \downarrow$ inside the correlated impurity orbital that belongs to the concrete lattice site positioned at $\mathbf{r}_i$. Obviously, the notation of H_{int} makes usage of the particle number operators for f-electrons whose general structure was defined by eq. (2.7). Those give back the number of electrons with spin projection σ that occupy the appropriate impurity state. Thereby, $n^{(f)}_\sigma$ clearly can return only one of its two eigenvalues—namely 0 and 1—depending on which of the states represented by eq. (3.1) it operates on. In this context, each particle number operator inside H_{int} as described by means of eq. (2.12) feeds back the existence or the absence of a local spin-resolved charge density inside the indicated narrow f-orbital. For that reason one often constitutes interactions described by products of the reduced form

$$n^{(f)}_\sigma \cdot n^{(f)}_{-\sigma} \tag{2.13}$$

as of density-density type.

A so far still missing interplay between f and c electrons is now installed in terms of a hybridization term H_{hyb} that allows for a hopping of electrons between f- and c-levels and vice versa. This term may be formulated like

$$H_{\mathrm{hyb}} = \sum_{ij\sigma} \left(V_{ij} c^\dagger_{i\sigma} f_{j\sigma} + V^*_{ji} f^\dagger_{j\sigma} c_{i\sigma} \right) , \tag{2.14}$$

where V_{ij} marks the hybridization strength. Physically a hybridization of f-states is expected as a consequence of spatial overlaps between f- and c-orbitals in association with an energetic degeneration of f- and c-states. In that sense, V_{ij} is a measure for the just mentioned spatial orbital-overlaps. Mathematically however, V_{ij} marks the off-diagonal element of a hybridization matrix $\mathbf{V}$ that—like the electronic two-body interaction in eq. (2.4)—could be of almost arbitrary complexity, e.g. also σ-dependent or of complex nature or both. Again, just like setting the interaction to U, it is sufficient here to stick with a constant V for convenience.

In summary, a complete Hamiltonian of the simplest version of the PAM is given by

$$\begin{aligned} H_{\mathrm{PAM}} = \overbrace{-t \sum_{\langle i,j \rangle} \sum_\sigma c^\dagger_{i\sigma} c_{j\sigma}}^{H_{\mathrm{band}}\ (2.10)} + \overbrace{\varepsilon_f \sum_{i\sigma} f^\dagger_{i\sigma} f_{i\sigma} + \frac{U}{2} \sum_{i\sigma} n^{(f)}_{i\sigma} n^{(f)}_{i-\sigma}}^{H_{\mathrm{imp}}\ (2.12)} + \\ + \underbrace{\sum_{ij\sigma} \left(V_{ij} c^\dagger_{i\sigma} f_{j\sigma} + V^*_{ji} f^\dagger_{j\sigma} c_{i\sigma} \right)}_{H_{\mathrm{hyb}}\ (2.14)} . \end{aligned} \tag{2.15}$$

A graphical visualization of the corresponding model in the case of a diagonal $\mathbf{V}$ with elements $V_{ij} = \delta_{ij} V$ in $D = 1$-dimension regarding electronic inter-orbital hops and exchanges is shown in fig. 2.2.

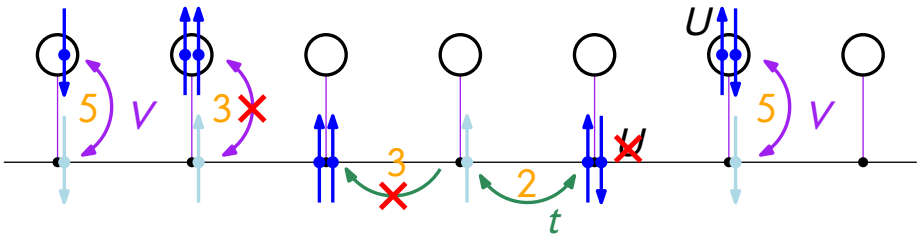

Figure 2.2.: Visualization of the $D = 1$-dimensional periodic Anderson model with diagonal hybridization by means of fig. 2.1 on page 13: Spin-degenerate *uncorrelated* electronic orbitals (black dots) hybridize with corresponding *correlated* orbitals (black circles) due to a diagonal hybridization (magenta lines). Depending on the filling, electrons with spin projections $\uparrow, \downarrow$ (blue arrowed dots) may hop freely (green arrows) along the shortest distance between discrete *uncorrelated* electronic orbitals (black lines). Alternatively there may occur electronic exchanges between corresponding correlated and uncorrelated orbitals by means of the diagonal hybridization of strength $V_{ij} = \delta_{ij} V$ (magenta arrows). Typical possible moves in that sense are (2) and (5), while movements (3) violate Pauli's exclusion principle. Electronic double occupancy of correlated orbitals (5) costs the system an energy U (5), while remains for free in the case of uncorrelated orbitals (2).

For reasons of argumentation it is often fruitful to treat the PAM in a mixed representation, where the bath parts are presented in momentum i.e. *reciprocal space* while the impurity parts of H_{PAM} are written in real-space representation like in eq. (2.16). By remembering the right side of eq. (2.10) on page 14, consequently this reads

$$H_{\mathrm{PAM}} = \overbrace{\sum_{\mathbf{k}\sigma} \varepsilon_{\mathbf{k}} c^{\dagger}_{\mathbf{k}\sigma} c_{\mathbf{k}\sigma}}^{H_{\mathrm{band}}\ (2.9)} + \overbrace{\varepsilon_f \sum_{i\sigma} f^{\dagger}_{i\sigma} f_{i\sigma} + \frac{U}{2} \sum_{i\sigma} n^{(f)}_{i\sigma} n^{(f)}_{i-\sigma} + \underbrace{+ \sum_{i\mathbf{k}\sigma} \left(V_{i\mathbf{k}} \mathrm{e}^{-\mathrm{i}\mathbf{k}\mathbf{r}_i} c^{\dagger}_{\mathbf{k}\sigma} f_{i\sigma} + V^{*}_{i\mathbf{k}} \mathrm{e}^{\mathrm{i}\mathbf{k}\mathbf{r}_i} f^{\dagger}_{i\sigma} c_{\mathbf{k}\sigma} \right)}_{H_{\mathrm{hyb}}}}^{H_{\mathrm{imp}}}, \tag{2.16}$$

where, when starting form a H_{hyb} in momentum space, the exponential functions and the sum over index i arise from the Fourier transformation of the f-electron operators from $\mathbf{k}$-space into real-space.

While a very diluted model may be seen as a cluster of single-impurity models, in a very dense array of impurities also the orbitals of the impurity sites show up as a flat and—for already mentioned reasons—narrow band of correlated f-electrons at energy ε_f. In the presence of a $V \neq 0$ the c- and f-band hybridize, thereby forming two bands that are separated by a band gap. In terms of *Fermi liquid theory* [PN66] those *hybridization bands* host quasi-particles that obey effective masses much larger than the usual electron mass and therefore are identified as so-called

heavy bands [AI10; Amu+15; Col02]. Particularly for the free case, where $U = 0$, this may be shown at little expense. Here, the PAM as described by H_{PAM} (2.15) reduces to a simple two-band tight-binding model with hybridization as the corresponding free Hamilton may be diagonalized by introducing appropriate hybridized quasi-particle operators. This in turn soon leads to a quasi-particle spectrum of two bands

$$E_{\mathbf{k}\pm} = \frac{1}{2}\left[\varepsilon_{\mathbf{k}} + \varepsilon_f \pm \sqrt{\left(\varepsilon_{\mathbf{k}} - \varepsilon_f\right)^2 + 4V^2}\right], \tag{2.17}$$

the lower and upper hybridization bands [TSU97]. A calculated example in one dimension is shown in fig. 2.3. As a result, the dense PAM has been successfully used as model of choice for studying heavy fermions [Fis+86; Neu+07; WA14b].

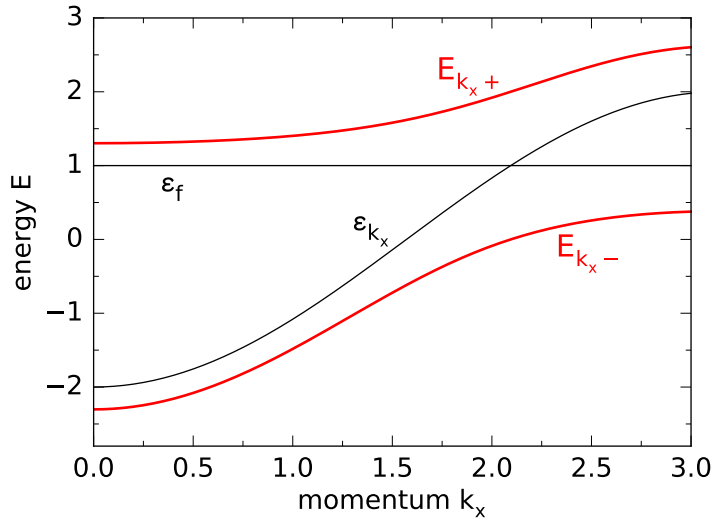

Figure 2.3.: Lower and upper hybridized bands E_{k_x-} and E_{k_x+} (red lines) in the free periodic Anderson model resulting from a one-dimensional consideration of the quasi-particle spectrum given by eq. (2.17). For the calculation the x-component ε_{k_x} of the cosine-like dispersion $\varepsilon_{\mathbf{k}}$ of eq. (2.11) with a hopping $t = 1$ was assumed for $L = 500$ bath sites at $\varepsilon_f = V = 1$.

Conceptually as well as historically the PAM follows as the "natural extension" [Hew93] of the Anderson impurity model (AIM), also known as single-impurity Anderson model (SIAM) [And61]. Like its name propagates, this model is nothing else than a PAM with only one single impurity site. Thus, with the knowledge of eq. (2.16) the full Hamiltonian of the AIM in momentum space is just given by:

$$H_{\mathrm{AIM}} = \underbrace{\sum_{\mathbf{k}\sigma} \varepsilon_{\mathbf{k}} c^\dagger_{\mathbf{k}\sigma} c_{\mathbf{k}\sigma}}_{H_{\mathrm{band}}\ (2.10)} + \underbrace{\varepsilon_f \sum_{\sigma} f^\dagger_\sigma f_\sigma + \frac{U}{2} n^{(f)}_\sigma n^{(f)}_{-\sigma}}_{H_{\mathrm{imp}}} + \underbrace{\sum_{\mathbf{k}\sigma} \left(V_{\mathbf{k}} c^\dagger_{\mathbf{k}\sigma} f_\sigma + V^*_{\mathbf{k}} f^\dagger_\sigma c_{\mathbf{k}\sigma}\right)}_{H_{\mathrm{hyb}}}. \tag{2.18}$$

Typically the AIM was and is used to study the formation of a local magnetic moment inside the

correlated orbital of the impurity site (c.f. section 3.1, page 24 ff.) and thus in a general context opens the gate to enter a deeper understanding of the physics of local magnetic moments.

As Anderson models include itinerant c-electrons as well as strictly localized f-electrons, in literature these models are also categorized as *hybrid models*, see e.g. [AI10].

2.4. Kondo impurity models

Similar to the single-band Hubbard model that may be replaced by the Heisenberg model in the limit $U \to \infty$ also the AIM may be partially replaced by a spin-type model in the limit

$$U \to \infty\,, \quad V = \text{const.} \tag{2.19}$$

that constitutes a low-energy limit of the AIM. Because of the infinitely large Coulomb repulsion within this limit the impurity site characteristically is singly occupied, hence it is

$$n^{(f)} = \sum_{\sigma} n_{\sigma}^{(f)} = n_{\uparrow}^{(f)} + n_{\downarrow}^{(f)} = 1\,, \tag{2.20}$$

whereat charge fluctuations between the conduction band and the impurity site are suppressed or at least become of purely virtual nature. What then remains is a single spin on the impurity site that magnetically couples to the spins of the host material. This allows for the construction of an effective low-energy model of the AIM which is known as the Kondo impurity model (KIM) with its corresponding Hamiltonian H_{KIM} [Kon64]. Here, in comparison to the Hamiltonian of the AIM written out as H_{AIM} (2.18) on page 17, the band part H_{band} is left untouched whereas H_{imp} and H_{hyb} are replaced by an effective *Heisenberg Hamiltonian* H_{HB} that only covers the spin-spin interaction between locally correlated impurity and conduction band spins. Altogether this leads to the famous Kondo Hamiltonian which is formulated as

$$H_{\mathrm{KIM}} = \underbrace{\sum_{\mathbf{k}\sigma} \varepsilon_{\mathbf{k}} c_{\mathbf{k}\sigma}^{\dagger} c_{\mathbf{k}\sigma}}_{H_{\mathrm{band}}} + \underbrace{J_{\mathrm{K}}\, \mathbf{s}_{\mathrm{host}} \cdot \mathbf{S}_f}_{H_{\mathrm{HB}}}\,, \tag{2.21}$$

where for now $\mathbf{s}_{\mathrm{host}}$ denotes the spin density formed by the conduction electrons at the impurity site [Lec11] and $\mathbf{S}_f$ is the localized quantum mechanical spin of magnitude $S = 1/2$ on the correlated orbital of the impurity site [SN02]. A more precise definition of the spin operators will be given below. Conceptually, the KIM is the model of choice to study for the so-called *Kondo effect* as will be discussed in section 3.2 on page 27 and the following.

An existent mathematical derivation of the AIM to the KIM implies a canonical transformation of H_{AIM} (2.18) proposed by Schrieffer and Wolff [SW66] where the extraction of the low-energy ($n^{(f)} = 1$)-subspace leads to H_{KIM} (2.21). As a main result of this transformation the coupling is determined as

$$J_{\mathrm{K}} = 2V^2 \frac{U}{\varepsilon_f(\varepsilon_f + U)} = 2V^2 \left(\frac{1}{\varepsilon_f + U} + \frac{1}{-\varepsilon_f} \right) > 0\,. \tag{2.22}$$

Similar to the hybridization strength V, also the coupling J can be principally $\mathbf{k}$-dependent. Without risking a formal mistake this will be neglected for simplification. In accordance to common conventions we will define a magnetic coupling as *ferromagnetic* if the associated coupling constant $J < 0$ and consequently as *antiferromagnetic* if $J > 0$. Thus, as $J_\mathrm{K} > 0$, the spin-spin coupling inside the KIM is identified as antiferromagnetic. In direct relation to that, the spin-spin coupling just presented in eq. (2.22) is identified as an antiferromagnetic coupling in consistence with the literature like e.g. [Faz99]. Further notable in this context is the so-called *symmetric* AIM that is realized for

$$\varepsilon_f = -\frac{U}{2}\,. \tag{2.23}$$

For this case the mathematical structure of the coupling simplifies to

$$J_\mathrm{K} = \frac{8V^2}{U}\,, \tag{2.24}$$

what implies $J_\mathrm{K} \to 0$ in the limit (2.19). Generally, the set of those constellations of model-parameters that allow for a *Schrieffer-Wolff transformation* of the AIM towards the KIM define the so-called *Kondo regime* of the former one.

The aforementioned argumentation for a single-impurity model also holds for a lattice of correlated impurities, i.e. the PAM as presented in section 2.3 on page 13 ff. and for low energies in fact results in the Kondo lattice model (KLM). The corresponding Hamilton operator of this model then reads

$$H_\mathrm{KLM} = \sum_{\mathbf{k}\sigma} c^\dagger_{\mathbf{k}\sigma} c_{\mathbf{k}\sigma} + J_\mathrm{K} \sum_{\mathbf{k}\mathbf{k}'i} \mathrm{e}^{-\mathrm{i}(\mathbf{k}'-\mathbf{k})\mathbf{R}_i}\, \mathbf{S}_i \cdot \mathbf{s}_{\mathbf{k}'\mathbf{k}}\,. \tag{2.25}$$

In this version again, as in the case of the H_hyb as part of H_PAM (2.16), the Heisenberg term is given in mixed representation. In particular, the spin operators contained in the Heisenberg term read

$$\mathbf{s}_{\mathbf{k}'\mathbf{k}} = \frac{1}{2}\sum_{\sigma'\sigma} c^\dagger_{\mathbf{k}'\sigma'} \sigma_{\sigma'\sigma} c_{\mathbf{k}\sigma}\,, \tag{2.26}$$

$$\mathbf{S}_i = \frac{1}{2}\sum_{\sigma'\sigma} f^\dagger i\sigma' \sigma_{\sigma'\sigma} f_{i\sigma}\,. \tag{2.27}$$

While eq. (2.26) describes the structure of spin-density operators of the conduction band, eq. (2.27) defines the spin operators of the localized spins of magnitude $S = 1/2$. In both equations $\sigma = (\sigma_x, \sigma_y, \sigma_z)^T$ marks the vector of *Pauli matrices*.[6]

In the sense of the Schrieffer-Wolff transformation that maps the AIM onto the KIM it was explicitly shown by Sinjukow and Nolting inside [SN02] that H_KLM (2.25) can be obtained out of H_PAM (2.16) for any finite $J_\mathrm{K} > 0$ in an appropriate limit

$$\varepsilon_f = -\frac{U}{2} \quad \text{and} \quad U \longrightarrow \infty\,, \quad V \longrightarrow \infty \quad \text{with} \quad \frac{V^2}{U} \longrightarrow \text{const.}\,, \tag{2.28}$$

which is referred to as *extended Kondo limit* and firstly was defined in [MO95]. As the comparison between the first equality inside the limit (2.28) and eq. (2.23) shows, the extended Kondo

[6] For the explicit definitions of the *Pauli matrices*, again see e.g. [Sak94].

limit already implies the condition for symmetric Anderson models. In accordance to the results of an existing Schrieffer-Wolff transformation between the symmetric AIM and KIM as shown above, the mapping between the PAM and the KLM as derived within [SN02], if existing in the limit (2.28), also yields a coupling constant J_K like that given by eq. (2.24).

Like for the PAM crucial physical properties of the KLM depend on the density of the impurity lattice [Col15a; Col02; Hew93]. In that sense, the electronic density of states (DOS) of a KLM with a dense lattice of impurity sites shows a gap inside the Kondo resonance that in turn leads to a macroscopically detectable insulating state. This qualifies the KLM to serve as a model for studying the physics of so-called *Kondo insulators* [Wer15].

2.5. The Heisenberg model

Like the Kondo impurity models presented in section 2.4 on page 18 ff. are the effective low-energy models of the Anderson impurity models introduced in section 2.3 on page 18 and the following, the Heisenberg model is the effective low-energy model of the Hubbard model that was presented in section 2.2 starting on page 11. For the reasons already explained there in short, in the limit $U \to \infty$, where at low energies only spin excitations take place, the half-filled single-band Hubbard model described by H_{Hub} eq. (2.6) on page 11 may be replaced by the antiferromagnetic Heisenberg model. The corresponding model Hamiltonian, which is a pure SU(2) spin-rotation symmetric spin-type Hamiltonian, is generally formulated as

$$H_{\mathrm{HB}} = -\sum_{ij} J_{ij}\, \mathbf{S}_i \cdot \mathbf{S}_j \,. \tag{2.29}$$

It describes local spins on discrete sites at positions like $\mathbf{r}_i$ and $\mathbf{r}_j$, represented by spin-operators $\mathbf{S}_i$ and $\mathbf{S}_j$ that are coupled among each other with strength J_{ij}. According to eq. (2.27) on page 19 concerning the KLM, the spin operators are defined as

$$\mathbf{S}_i = \frac{1}{2} \sum_{\sigma\sigma'} c^\dagger_{i\sigma} \sigma_{\sigma\sigma'} c_{i\sigma'} \,. \tag{2.30}$$

Consistently $\sigma = (\sigma_x, \sigma_y, \sigma_z)^T$ marks a vector of *Pauli matrices*. For a more detailed discussion of the structural as well as algebraic characteristics of the spin operators and in particularly of the anticommutation relations of their components among each other see the appropriate chapter of [NR09]. We want to conclude this section with the remark that the reduction of the full spin operators in eq. (2.29) to corresponding z-components in the fashion of

$$\mathbf{S}_i \to S^z_i = \pm 1 \tag{2.31}$$

leads to the relative but much simpler model category of the *Ising models* [NR09] not to be further discussed in this context.

2.6. Summary & outlook

After a short recapitulation of their general formulation, in this chapter a selection of common models of many-body systems that are in some sense needed for the further conceptual development of this thesis was presented. Thereby the main focus was laid on the development of associated Hamilton operators. In that sense, besides the—for our further concerns most necessary—presentation of the Anderson impurity models, namely the PAM and its little brother, the AIM, their corresponding effective low-energy models, the Kondo impurity models inclusively their Hamiltonians were discussed in a short and compact manner. The same applies for the single-band Hubbard model and its effective low-energy model, the Heisenberg model. By that, the conceptual foundation stone was laid to study the physics of local magnetic moments and magnetic order. Studies of that kind by means of the single impurity as well as the lattice Anderson and Kondo models will be the main content of the following chapter.

3. Local magnetic moments and magnetic order

On top of the background information on lattice and especially lattice impurity models presented in chapter 2 on page 9 ff. this chapter concentrates on the physics and order of local magnetic moments as well as on its formal description.

- The *existence* or the *formation* of *local magnetic moments*,
- a *coupling mechanism* favoring a certain alignment of the moments, e.g. ferro- or antiferromagnetically, and
- the *stability* of long-range magnetic order against different types of thermal or quantum fluctuations and against competing ordering phenomena.

This poses the motivation for the outline of this chapter that implies the more detailed discussion of all three aspects mentioned above in terms of exemplary phenomena.

We begin with the formation of local magnetic moments in section 3.1. Thereby, basically the simplest model, thus the model of choice, that allows for the study of the entire physics of the forming of and interaction among local magnetic moments is the periodic Anderson model (PAM) as it was introduced in section 2.3 on page page 13 and the following. In all present cases within this thesis, a local magnetic moment is assumed as the result of precession of an unscreened single spin inside an odd filled active and per definition correlated orbital of a localized impurity atom.

However, the exclusive study of the formation of such a local magnetic moment in a metallic host traditionally is left to be demonstrated on the corresponding single impurity model, the Anderson impurity model (AIM) which was also presented in section 2.3. If there exist local magnetic moments on all present impurity sites of an Anderson impurity model it is, for reasons of a clearer demonstration, appropriate to switch to the Kondo models we already know from section 2.4 on page 18 and the following. While the Kondo lattice model (KLM) is most adequate for the discussion of coupling mechanisms between local magnetic moments like the *itinerant exchange* that lead to magnetic order, the *Kondo effect* which is a purely local effect that negatively affects the stability of magnetic order is best studied on the stage of the Kondo impurity model (KIM). A resulting rival between both phenomena manifests in the famous *Doniach phase diagram* [Don77] of the KLM that gives an overview in which energy scales which phenomena is dominating. This is the scope of section 3.2.

Finally in section 3.3, it will be explained how the ability of a system to evolve magnetic order

is influenced by the mixture of temperature and model dimension on the one hand and by the lattice geometry on the other hand. While the former exactly is managed by highlighting the statements of the *Mermin-Wagner theorem* [MW66], the latter is impressively discussed in the context of *geometrical frustration*.

3.1. The formation of local magnetic moments

As already mentioned, the formation of local magnetic moments was first studied by means of the AIM in [And61]. The corresponding model Hamiltonian H_{AIM} was already introduced by eq. (2.18) in section 2.3 as H_{AIM}. As it was explained there, the AIM describes a single impurity atom that is nested inside a sea of Bloch electrons whose states form a single conduction band. In particular, the impurity atom is described by a single spin-degenerate electronic level with energy ε_f that bares a local Coulomb repulsion U if it is occupied by two electrons of opposite spin-projection σ. By that, each f-level provides four electronic states

$$|0\rangle, \quad |\uparrow\rangle, \quad |\downarrow\rangle, \quad |\uparrow\downarrow\rangle, \tag{3.1}$$

namely one unoccupied or empty state, two degenerate singly occupied states and a doubly occupied one. Conduction band and impurity level may exchange electrons due to a hybridization of strength V.

For the discussion of the formation of local magnetic moments we first concentrate on the impurity site. In the occupation number representation the states presented in (3.1) form a complete orthonormal base that easily diagonalizes the impurity part H_{imp} of H_{AIM} (2.18). According to these states this offers the four energy eigenvalues

$$E_0 = 0, \quad E_\uparrow = E_\downarrow = E_1 = \varepsilon_f, \quad E_{\uparrow\downarrow} = E_2 = 2\varepsilon_f + U\,. \tag{3.2}$$

The thereby arising doubly degenerate energy-levels $E_\uparrow$ and $E_\downarrow$ are a *Kramers doublet* as a direct result of *Kramers theorem*,[1] sometimes also called *Kramers degeneracy* due to the *time-reversal invariance*[2] of H_{AIM} (2.18) [Yos96].

As already stated in the entry of this chapter, in the context of this work and the primary underlying impurity models, local magnetic moments are just assumed as the unscreened precession of single spins with spin projection σ inside odd filled active orbitals of the localized impurity atoms. By that out of the four electronic states provided by the impurity orbital (3.1) clearly $|\uparrow\rangle$ and $|\downarrow\rangle$ are identified as magnetic while $|0\rangle$ and $|\uparrow\downarrow\rangle$ are non-magnetic. Recalling the corresponding energies (3.2) one easily may verify that the impurity atom has an electronic excitation spectrum of two sharp energy values, namely ε_f if the impurity orbital is empty and $\varepsilon_f + U$ if a second electron of suitable spin-projection is added to an already singly-occupied, hence half-filled impurity orbital. Therefore, one expects the impurity atom in a magnetic state $|\uparrow\rangle$ or $|\downarrow\rangle$

[1] Kramers theorem states that in a system containing an odd number of electrons at least two-fold degeneracy must remain in the absence of a magnetic field [Blu01]. For a proof see [Sch08].
[2] For time reversal invariance and especially Kramers degeneracy, see also [Sak94].

if the energetic condition

$$\varepsilon_f < \varepsilon_\mathrm{F} < \varepsilon_f + U \tag{3.3}$$

where ε_F marks the *Fermi level*[1] that divides occupied states with energies smaller than ε_F from unoccupied states whose energies lie above ε_F, is fulfilled, as the unoccupied state $|0\rangle$ as well as the doubly occupied state $|\uparrow\downarrow\rangle$ become energetically unfavorable within this scenario.

So far, our considerations only covered the atomic limit of H_AIM (2.18) that is realized for $V = 0$ as in this case H_hyb vanishes and the local impurity is decoupled from the host material. Leaving this limit by driving V to a finite value, the above mentioned hybridization of the f-states takes place and the former sharp excitation levels of the impurity ion at ε_f and $\varepsilon_f + U$ broaden to resonances whose widths $\Gamma(\varepsilon_f)$ and $\Gamma(\varepsilon_f + U)$ depend on the hybridization strength and the free density of states (DOS) of the conduction band electrons

$$\rho(\varepsilon) = \sum_{\mathbf{k}} \delta\left(\varepsilon - \varepsilon_{\mathbf{k}}\right) \tag{3.4}$$

at the energy of the excitation level. In general, one finds

$$\Gamma(\varepsilon) = \pi V^2 \rho(\varepsilon)\,. \tag{3.5}$$

In the thermodynamic limit, the $\varepsilon_{\mathbf{k}}$ become continuous [GM12], hence for a large host lattice at least very dense which is why the transition of an electron from the f-orbital into the conduction band may approximately be seen as a transition rate from a bounded state into a continuum. Therefore, by considering the hybridization strength V as perturbation parameter, eq. (3.5) may be derived using *Fermi's golden rule*, hence by means of time-dependent perturbation theory in first order (compare to [Sak94]). This resonance-broadening however leads to the problem that if U is too small or more precisely

$$U < \frac{1}{2}\left[\Gamma(\varepsilon_f) + \Gamma(\varepsilon_f + U)\right], \tag{3.6}$$

the two resonances merge and any prediction on the formation of magnetic moments fail. Therefore in the full AIM, U needs to be just large enough to still keep the two resonances distinguishable. To face this additional requirement, the conditions concerning the atomic limit given by eq. (3.3) have to be extended in order to favor the formation of local moments. This is done in the following way:

$$\varepsilon_f + \frac{\Gamma(\varepsilon_f)}{2} < \varepsilon_\mathrm{F} < \varepsilon_f + U - \frac{\Gamma(\varepsilon_f + U)}{2}\,. \tag{3.7}$$

If these inequalities are fulfilled, the impurity for energetic reasons should be favorably in one of its two singly-occupied magnetic states. Hence, the AIM is in its so-called *local moment regime*. The conditions (3.7) are also known as the *Kondo limit* of the AIM in which it may be safely replaced by the KIM as already known from section 2.4.

By further changes of the parameter values and a subsequent rearrangement of inequalities to meet the prevailing energetic situations, one may scan through even more parameter regimes

[1] We for now use intentionally the somehow vague expression "Fermi level" instead of "Fermi energy" as we want our discussions to hold even in the case of finite temperatures T. The "Fermi energy", however, strictly is only defined for $T = 0$.

of the AIM. While the condition (3.7) implies that the Fermi level ε_F does not lie within any of the two resonances there exist possible cases for which this is true. Given such cases, the system is in its *mixed-valence* or alternatively *intermediate-valence regime* that is characterized through strong charge fluctuations between impurity and conduction band orbitals. In addition to that, there remain two more regimes, both of them non-magnetic: The first one is realized if

$$\varepsilon_f - \frac{\Gamma(\varepsilon_f)}{2} > \varepsilon_\mathrm{F}\,. \tag{3.8}$$

Then the impurity is expected to be in the non-occupied state what is sometimes called the *empty orbital regime*. The second one emerges if the condition

$$\varepsilon_f + U + \frac{\Gamma(\varepsilon_f + U)}{2} < \varepsilon_\mathrm{F} \tag{3.9}$$

holds. In this scenario, the f-orbital should be doubly-occupied. A graphical interpretation of the most important facts discussed so far on this score is shown in fig. 3.1.

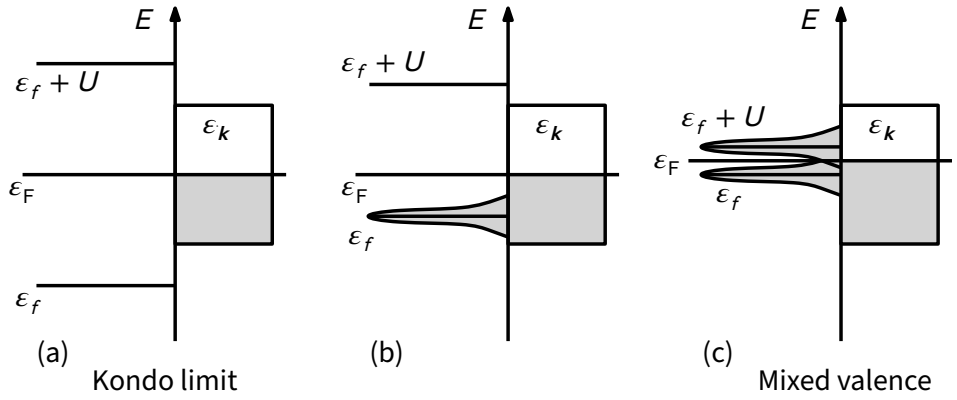

Figure 3.1.: Energy level scheme of a localized orbital with resonances at ε_f and $\varepsilon_f + U$ and a conduction band with energies $\varepsilon_\mathbf{k}$ like described by the AIM. The local excitation levels are broadened due to a hybridization if there exists a level of the same energy in the conduction band. All levels with energies above the Fermi-level ε_F are occupied (continuous and local broadened occupied levels are filled light gray). Clearly the constellations (a) and (b) result in magnetic states, whereas (c) is non-magnetic since the local orbital becomes doubly-occupied. Furthermore (a) shows the Kondo-limit, whereas (c) shows a total mixed-valence constellation as both local orbital resonances overlap with the Fermi-level at ε_F. In (c) also both energy levels of the local orbital overlap due to a small U by means of eq. (3.6). Inspired by [TSU97].

What remains at this place is a more precise definition of the Fermi level ε_F in regard to the model Hamiltonians that were discussed so far and those that will be in the following. A proper definition of ε_F relies on the chosen statistical ensemble one wishes to consider the underlying models in. Usually one is concerned to investigate many-particle systems under varying energies but with a fixed average number of particles. Thus, the statistical ensemble of choice is the *grand canonical ensemble* where the average particle number is fixed by an introduced *chemical potential* μ which then automatically plays the role of the Fermi level, hence $\varepsilon_\mathrm{F} \sim \mu$. Already defined

Hamilton operators H may easily be transferred to the grand canonical ensemble by applying the substitution

$$H \to \mathcal{H} = H - \mu N\,, \tag{3.10}$$

where $\mathcal{H}$ marks the Hamilton operator in the grand canonical ensemble and N is the total particle number operator of the corresponding system.[2] For the case of H_{AIM} (2.18) it is

$$N_{\mathrm{aim}} = \sum_{\mathbf{k}\sigma} n^{(c)}_{\mathbf{k}\sigma} + \sum_{\sigma} n^{(f)}_{\sigma} = \sum_{\mathbf{k}\sigma} c^{\dagger}_{\mathbf{k}\sigma} c_{\mathbf{k}\sigma} + \sum_{\sigma} f^{\dagger}_{\sigma} f_{\sigma}\,,$$

where particle number operators in the sense of eq. (2.7) were used. Consequently, for the Anderson impurity models defined by H_{PAM} (2.16) and H_{AIM} (2.18) this implies:

$$\varepsilon_{\mathbf{k}} \to (\varepsilon_{\mathbf{k}} - \mu)\,, \quad \varepsilon_f \to (\varepsilon_f - \mu)\,.$$

By that, for assumed small excitation energies, $\varepsilon_{\mathbf{k}}$ varies around μ whereas $(\varepsilon_{\mathbf{k}} - \mu)$ varies around 0 [BF04]. So, in this assumption the Kondo limit (3.7) may be formulated in an alternative, more comfortable way as

$$\varepsilon_f \ll \varepsilon_{\mathbf{k}} \ll \varepsilon_f + U\,, \quad |\varepsilon_f - \varepsilon_{\mathbf{k}}|,\, |\varepsilon_f + U - \varepsilon_{\mathbf{k}}| \gg \Gamma_{\mathrm{eff}}\,, \quad \varepsilon_{\mathbf{k}} \approx \mu\,, \tag{3.11}$$

where Γ_{eff} simply is assumed as the level broadening (3.4) at the Fermi level [TSU97], hence

$$\Gamma_{\mathrm{eff}} = \Gamma(\mu)\,.$$

3.2. Kondo effect, itinerant exchange and the Doniach phase diagram

Having provided appropriate models to do so, finally it is time to have a closer look on the Kondo effect [Kon64] and the itinerant exchange that is usually known as the Ruderman-Kittel-Kasuya-Yosida (RKKY) [RK54; Kas56; Yos57] interaction—whereas to stay correct one has to mention that the itinerant exchange arises as the result of the RKKY interaction. The competition between the Kondo effect and the RKKY interaction then is reflected within the famous Doniach phase diagram [Don77].

Even though the physics of the Kondo effect are included in both, the AIM and the PAM presented in section 2.3, while the order of magnetic moments through the RKKY interaction clearly only is included in the latter one as technically at least two magnetic moments at different sites are used to be able to explain an order between local magnetic moments, it is easier to study those phenomena as well as their competition within the simpler Kondo impurity models introduced in section 2.4.

So let's start with having a closer look on the itinerant exchange, hence the RKKY interaction by means of the KLM. In theory there exist several different magnetic exchange mechanisms

[2] The other way round one may argue that previously defined Hamiltonians were just considered at $\mu = \varepsilon_{\mathrm{F}} = 0$. For the argumentation of the generalized Schrieffer-Wolff transformation in [SN02], cited and summarized in section 2.4 this actually was true.

(see e.g. [Koc12; NR09; Blu01; Yos96]). The first one might think of, is a *direct exchange* which is based on a spatial overlap integral between the wave functions of two magnetic states. This clearly is impossible within our model since the PAM and consequently also the KLM lack of any direct coupling between f-electronic states of different impurity sites. In contrast, what is conceivable is an indirect coupling between the magnetic moments of different impurity sites that is mediated by the conduction electrons inside the host material resulting in an *indirect exchange* to which category of exchange mechanisms also the itinerant exchange is assigned to. In the special case of the itinerant exchange a localized magnetic impurity ion spin-polarizes the conduction electrons. This polarization then couples to the magnetic moment of a neighboring impurity site. Or to be more precise in terms of the KLM being defined by H_{KLM} (2.25) the local spin on an arbitrary impurity site, let's say on the site at $\mathbf{r}_i$, $\mathbf{S}_i$, typically couples antiferromagnetically to the spin density of the conduction electrons that are localized near to the impurity site. This induces so-called *Friedel oscillations* in the density of the conduction electron spins. Now, the local spin $\mathbf{S}_j$ on a second impurity site at $\mathbf{r}_j$ may couple to this oscillations what results in an effective magnetic exchange interaction between the two local magnetic moments. Formally this is described by the RKKY interaction which itself is the result of a perturbation calculation. One thereby considers the coupling between the local spin $\mathbf{S}_i$ and the conduction electrons that equates to the Heisenberg part H_{HB} of eq. (2.25) as perturbation of the unpolarized ground state of the conduction electrons. The full calculation up to second order which can be entirely found in [NR09] then leads to an effective Hamiltonian H_{RKKY} that is also of a Heisenberg nature but represents a coupling between the local spins $\mathbf{S}_i$ and $\mathbf{S}_j$:

$$H_{\mathrm{RKKY}} = \sum_{ij} J_{\mathrm{RKKY},ij}\, \mathbf{S}_i \cdot \mathbf{S}_j \,. \tag{3.12}$$

While this Hamiltonian is of very simple structure, the *coupling constant* J_{RKKY} is not, as

$$J_{\mathrm{RKKY},ij} \sim J_{\mathrm{K}}^2 \frac{\left(n^{(c)}\right)^2}{\varepsilon_{\mathrm{F}}} F\left(2k_{\mathrm{F}} r_{ij}\right) , \tag{3.13}$$

where $n^{(c)}$ is the conduction-electron density, k_{F} marks the absolute of the *Fermi wavevector* and $r_{ij} = |\mathbf{r}_i - \mathbf{r}_j|$ stands for the distance between the two local spins at $\mathbf{r}_i$ and $\mathbf{r}_j$. Due to the function

$$F(x) = \frac{\sin(x) - x\cos(x)}{x^4} , \tag{3.14}$$

the coupling constant J_{RKKY} gets the behavior of a damped oscillation whose wavelength is of the magnitude of π/k_{F} and that originates from the *Friedel oscillations* already mentioned above.

By that, as a result of the eqs. (3.13) and (3.14), the coupling induced by the RKKY interaction can either be of ferro- or antiferromagnetic nature depending on the distance r_{ij} and thus the underlying model lattice which in the end maps the microscopic setup of the corresponding real material. A schematic visualization of all that is provided by fig. 3.2. It remains to note here that on the one hand, for large distances r_{ij} the RKKY interaction behaves like

$$J_{\mathrm{RKKY},ij} \sim \frac{1}{r_{ij}^3} , \tag{3.15}$$

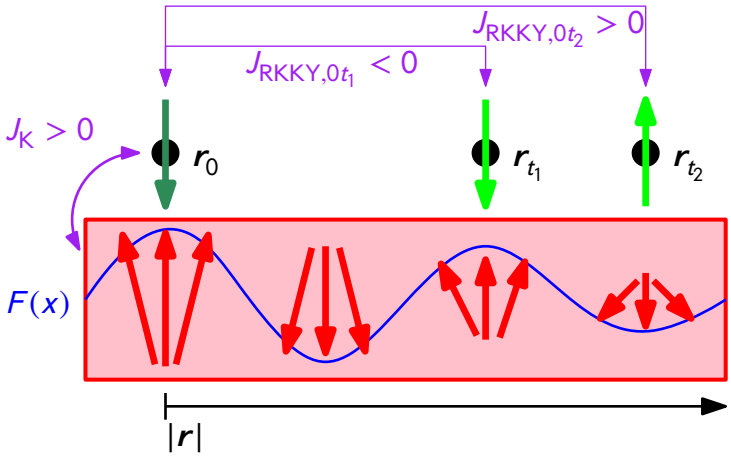

Figure 3.2.: Schematic visualization of the RKKY interaction by means of the $D = 1$-dimensional two impurity Kondo lattice model. A local spin (dark green arrow) at discrete site (black dot) $\mathbf{r}_0$ couples antiferromagnetically with $J_\mathrm{K} > 0$ to the spins of the nearest Bloch electrons of the host material (red box) what induces a spin-polarization (red arrows) whose damped oscillatory dispersion is mediated by $F(x)$ given by eq. (3.14) (blue line). Depending on its position i.e. the distance $|\mathbf{r}|$ to the initial spin at $\mathbf{r}_0$ a local spin on a second discrete test site (light green arrow on black dot) may couple anti- at $\mathbf{r}_{t_2}$ or ferromagnetically at $\mathbf{r}_{t_1}$ respectively with effective indirect couplings $J_{\mathrm{RKKY},0t_1} < 0$ and $J_{\mathrm{RKKY},0t_2} > 0$.

while on the other hand, the fact that it is

$$J_{\mathrm{RKKY},ij} \sim J_\mathrm{K}^2 \tag{3.16}$$

reflects that the RKKY interaction is a second-order effect. A different indirect magnetic coupling mechanism, the so-called inverse indirect magnetic exchange (IIME) will be the main topic of chapter chapter 7 on page 95 and the following. The understanding of the IIME however, apart from the knowledge on the RKKY, also presumes some at least basic knowledge on the Kondo effect.

Depending on the energetic situation, instead of mediating an interaction between different local spins, the conduction electrons near the local spins may also just screen the magnetic moments. This is respectively realized by the formation of a spin singlet out of a local spin and, depending on the coupling strength J_K, one or more spins of the conduction electrons near to the impurity site. This is indicated as the *Kondo effect* [Kon64] and is shown in fig. 3.3. Theoretically, in a perfect *strong-coupling* limit the *Kondo-singlet* is formed out of one impurity spin and exactly one spin of a conduction electron. With decreasing coupling J_K, the impurity spin is screened by more and more conduction electrons which form the so-called *Kondo cloud* [Aff09]. This all happens below a material-specific *Kondo temperature*

$$T_\mathrm{K} \sim \exp -\frac{1}{J_\mathrm{K}\rho(\varepsilon_\mathrm{F})} \tag{3.17}$$

which therefore sets the energy scale of the Kondo effect. In appropriate real materials this effect is responsible for a temperature-dependent minima of the resistivity. As the Kondo-clouds

act as scattering centers inside the conduction band the mobility of the free electrons around is disturbed. Macroscopically this manifests in a rather untypical increasing resistivity of the host material when the decreasing temperature sinks below T_K. Local magnetic moments that are screened in terms of the Kondo effect are invisible for and thus may not take part in the RKKY interaction. Hence the Kondo effect constrains or even totally destroys the magnetic long-range order tendencies resulting out of itinerant exchange.

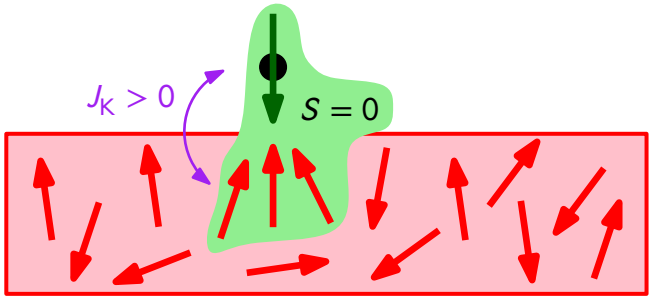

Figure 3.3.: Schematic visualization of the Kondo effect by means of the $D = 1$-dimensional Kondo impurity model. A local spin (dark green arrow) at a discrete site (black dot) and some of the spins of near Bloch electrons (red arrows) of a host material (red box) form a (green) Kondo cloud with total spin $S = 0$. Hence, the local spin is screened for the remaining host electrons that do not participate in the Kondo cloud.

As the RKKY interaction follows a different energy scale, both phenomena rival each other depending on the energy of the system. A theoretical study of this rival was the main content of the famous work of Doniach [Don77]. He expected the physics within the KLM to be dominated by two energy scales, namely that of the Kondo effect, and that of the RKKY interaction. While the scale of the former is given by the binding energy of a local Kondo-singlet that equals T_K, the latter is given by the binding energy of a spin-singlet which is formed by two different antiferromagnetically coupled local spins. This leads to

$$T_{RKKY} \sim J_K^2 \rho(\varepsilon_F)\,. \tag{3.18}$$

In that sense, depending on the value of $J_K\rho(\varepsilon_F)$, the formation of local Kondo-singlets ($T_K > T_{RKKY}$) or antiferromagnetic coupling ($T_{RKKY} > T_K$) is favored. Graphically this results in the famous $T[J_K\rho(\varepsilon_F)]$ *Doniach phase diagram* which is shown in fig. 3.4. Here, at weak $J_K\rho(\varepsilon_F)$, where $T_{RKKY} > T_K$, an antiferromagnetic (AFM) phase occurs as an antiferromagnetic coupling between local impurity spins is dominating due to the RKKY interaction. The AFM phase breaks down at a critical value of $J_K\rho(\varepsilon_F)$ resulting out of the crossing energy scales T_{RKKY} and T_K. For stronger $J_K\rho(\varepsilon_F)$, the regime $T_{RKKY} < T_K$ is characterized by a heavy Fermi liquid phase due to the formation of local Kondo singlets (KS). This phenomena in turn destroys the magnetic order due to the RKKY mechanism which has become energetically unfavorable in regard to the current parameter regime.

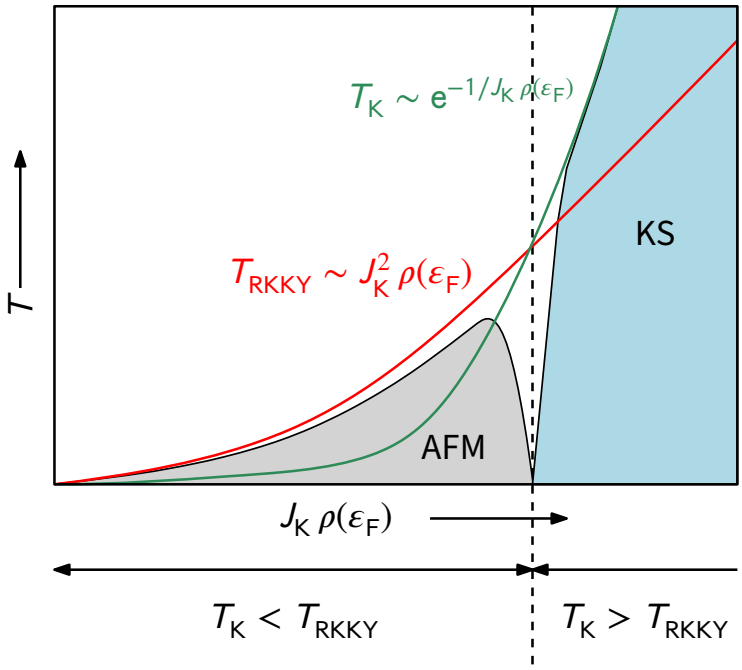

Figure 3.4.: Sketch of the $T[J_K\rho(\varepsilon_F)]$ Doniach phase diagram for the Kondo lattice model for an antiferromagnetic $J_{RKKY} > 0$ as a result of the energetic rival between the Kondo effect that energetically scales with T_K (green) and the RKKY interaction represented by T_{RKKY} (red) [Don77]. For further discussion, see section 3.2. Inspired by [Col02; Löh+07; Col15a].

3.3. Further influences

Magnetic long-range order strongly depends on the characteristics of the underlying lattice model as well as on the temperature T. For example, there exists a very important theorem that makes a strong statement on the arising of magnetic order in magnetically isotropic models at finite temperatures in regard to the model dimensionality. It is known as the Mermin-Wagner theorem. Another interesting phenomena in this context is the failure of magnetic order due to geometrically frustration that, like its name indicates, goes back on the lattice geometry. As both aspects will play important roles within our studies in chapters 6 and 7, they will be presented in more detail in the following.

3.3.1. The Mermin-Wagner theorem

Originally, the Mermin-Wagner theorem [MW66] is an exact result for the Heisenberg model presented in section 2.5. It states that the spontaneous magnetization $m_s(T)$ of the D dimensional Heisenberg model at temperature T due to the presence of an external homogeneous magnetic field $\mathbf{B} = B\mathbf{e}_z \neq 0$ vanishes in the limit $B \to 0$ for finite T and $D < 3$. Mathematically speaking

it is:

$$(\forall\, T \neq 0)\ (\forall\, D < 3): \quad m_{\mathrm{s}}(T) = \lim_{B \to 0} m(T, B) = 0\,. \tag{3.19}$$

In short one may formulate this just as:

> *In one and two dimensions, the isotropic Heisenberg model does not show any spontaneous magnetization at finite temperature.*

This theorem is best proven by setting up an appropriate Bogoliubov inequality in terms of the Heisenberg Hamiltonian H_{HB} given by (2.29) and the spin operators it contains. In a first step a tedious calculation implies the evaluation of this inequality by parts. In a subsequent step the spontaneous magnetization m at $T > 0$ is estimated in dependence of D for the isotropic model, i.e. the model in the absence of any external magnetic field, hence $\mathbf{B} = 0$. This finally yields eq. (3.19) [NR09].

Alternatively, the physical statements of the Mermin-Wagner theorem may be derived via the theory of magnons, i.e. bosonic quasi-particles that describe states of collective excitations in magnetic systems. Here, $m \to 0$ holds for the same parameter constellations regarding T and D like those written above as the number of excited spin-waves i.e. magnons diverges for these cases [Blu01].

Aside from the Heisenberg model the Mermin-Wagner theorem is also valid for a huge class of other magnetically isotropic models like explicitly the PAM (c.f. section 2.3) and its effective low-energy model the KLM (c.f. section 2.4) [GN01].

In a more general sense the statement of the Mermin-Wagner theorem may be reformulated in the context of magnetic phase transitions [Zin07]. Those are based on critical phenomena and therefore are driven by a spontaneous temperature-dependent breaking of the symmetry of the underlying model Hamiltonian. In preparation for our studies of the depleted Anderson lattice in chapter 7 on page 95 ff. we want to take the chance here to shortly and qualitatively discuss the transition from a ferromagnetic (FM) to a paramagnetic (PM) phase for an example [Coe10]. As illustrated in fig. 3.5 starting from high temperatures there exists a phase microscopically characterized by the existence of disordered magnetic moments. Macroscopically this phase is therefore classified as paramagnetic phase.

With decreasing temperature T the system will reach its critical temperature, the *Curie temperature* [GRH91], at T_{C} where suddenly a ferromagnetic order of the magnetic moments sets in. This is characterized by a spontaneous magnetization m of finite magnitude towards $T = 0$ (see labeled green line in fig. 3.5) which in a general sense plays the role of the *order parameter* or *generator* of the phase transition. It typically is Zero in the disordered but symmetric and non-Zero in the ordered but symmetry-broken phase. Just as a marginal note and also in preparation for chapter 7 remember the following: Apart from the temperature-development of the magnetization m, the critical temperature T_{C} is also fixed through the zero point of the inverse susceptibility χ^{-1} that only occurs in the disordered paramagnetic phase (see labeled blue line in fig. 3.5) according to the Curie-Weiss law [Kit05].

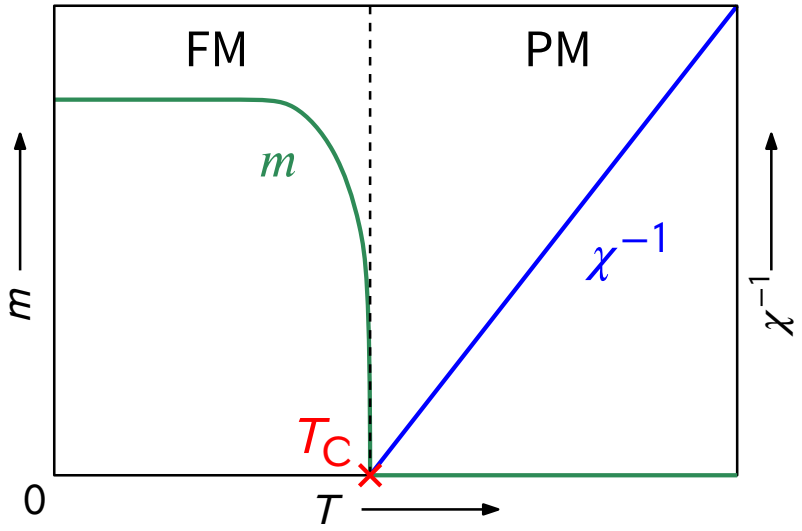

Figure 3.5.: Schematic visualization of a transition from a ferromagnetic to a paramagnetic phase at the critical temperature T_C (red cross) indicated by a magnetization m (green line). Additionally the temperature-development of the magnetic susceptibility χ^{-1} is shown (blue line). See section 3.3.1 for further explanation and discussion.

After this example, we finally give the general statement of the Mermin-Wagner theorem:

> *At dimensions $D = 1, 2$ and finite temperatures $T > 0$ the existence of a long-range order that goes ahead with the spontaneous breaking of a continuous symmetry is not possible.*

Back to our example this would forbid the formation of ferromagnetic order for systems of dimensions $D < 3$.

3.3.2. Geometrical frustration

In *frustrated magnetic systems* the localized magnetic moments, or spins, interact through competing exchange interactions that cannot be simultaneously satisfied [Bal10]. For an example, consider a pure spin-type model like the Heisenberg model as described in section 2.5 on page 20 and the following in $D = 2$ dimensions. Consider further the existence of spin-to-spin exchange interactions that favor an antiferromagnetic coupling between spins on next-neighboring concrete lattice sites. In the case of installing this model on a simple square lattice, there is no confusion on how the spins should arrange an antiferromagnetic coupling among each other (see the left side of fig. 3.6). A circumstance that is ensured by the *bipartite* structure of the square lattice.

> *Generally, we define a lattice as of bipartite structure if it could be divided into two sublattices A and B in such a way that each next-neighboring site of A belongs to B and vice*

versa.

As it is further graphically illustrated on the left side of fig. 3.6, in the scenario of considering the above introduced toy-model on a square lattice, exactly this original lattice can be divided into two equivalent sublattices: One that consists out of those sites that host spins of spin-projection ↑, let's call it A, and a second sublattice whose sites will be labeled with B while only hosting spins with spin-projection ↓. This bipartite structure ensures the mutual compensation of spins of different spin-projection, i.e. orientation.

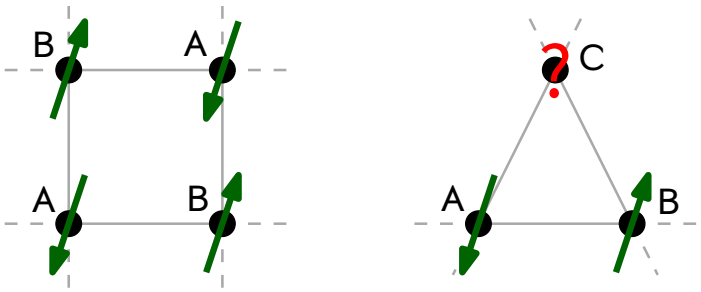

Figure 3.6.: Graphical demonstration of geometrical frustration by a simple spin type model. Local spins (green arrows) at discrete sites (black dots with sublattice labels) are supposed to couple antiferromagnetically. *Left*: on a square lattice. On this bipartite lattice out of A- and B-sublattices, spins of next-neighboring sites compensate in terms of the antiferromagnetic coupling. *Right*: same scenario on a triangular lattice. The spin on the "C"-site can not fit into the coupling scheme—it remains geometrically frustrated. See section 3.3.2 for further discussion.

However, this harmonic constellation drastically changes when the model is considered on a triangular lattice geometry. Here, one would divide the original lattice into three equivalent sublattices A, B, C thereby leaving the bipartite lattice structure. Consequently, if the spins of the A and B sites are oriented as before, hence couple antiferromagnetically, the spins residing on the remaining C sites are unable fit into the coupling scheme. The considered exchange interactions just cannot be saturated completely on C sites, i.e. neither a spin-projection ↑ nor ↓. Generally, the phenomenon of geometrical frustration occurs in frustrated lattice models of uncompensated spins. Physically, this typically leads to competing groundstates where either a specific magnetic order or a spin liquid phase can emerge [ZW15; SB17; HE88].

While we used spins and a spin-type model for reasons of simplification above facts also hold for well-formed local magnetic moments in regard to Anderson models. This is an important conclusion concerning the oncoming chapter 6 (page 75 ff.) on our studies of the PAM on the triangular lattice.

3.4. Summary & outlook

In this chapter some background information on the physics of local magnetic moments was given. The formation and necessary conditions for it to happen were discussed in regard to the parameter regime considered models were tuned into. Particularly, we focused on suitable models already known from the the preceding chapter 2 on page 9 and the following. Having understood how to drive those models into their local moment regimes, the impacts of the resulting magnetic moments on a non-magnetic environment were examined. These appeared as the Kondo effect and an indirect exchange mechanism known as the Ruderman-Kittel-Kasuya-Yosida (RKKY) interaction, both obeying different energy scales. From a resulting energetic rival between those phenomena followed the Doniach phase diagram whereby two main phases were identified: An antiferromagnetic phase as the direct consequence of dominating indirect exchange on the one hand and a heavy Fermi liquid phase of suppressed magnetic order induced by the screening of local magnetic moments in terms of the Kondo effect on the other hand. The last section of the chapter provided a short presentation of two further circumstances that heavily influence the occurrence of magnetic order: Firstly the Mermin-Wagner theorem which denies magnetic long range order at all for systems of lower dimension than $D = 3$ at finite temperature. Secondly the phenomena of geometrical frustration where due to problematic geometrical constellations the aspired scheme of magnetic order cannot be fulfilled for all magnetic moments simultaneously.

By that, the conceptual foundations should be laid out for entering the chapters 4 and 5 on the numerical setup and implied methods that were used for gaining the physical results presented later on in chapters 6 and 7.

4. Site-dependent dynamical mean-field theory

This chapter deals with the numerical framework of our studies whose results will be presented in chapter 6, page 75 ff. and chapter 7, page 95 and the following. As one already knows from the introduction on page 1 ff. this framework is formed by a site-dependent dynamical mean-field approach that internally necessarily endeavors an impurity solver based on the continuous-time hybridization expansion method. This solver will be explicitly presented and discussed in very detail in chapter 5 on page 49 and the following. As already pointed out in the introduction as well, the big methodical challenge to overcome when theoretically and qualitatively dealing with systems of correlated electrons like those introduced and shortly revised in the former chapters 2 and 3 is the handling of correlations mimicked through interaction terms inside this models. As the determination of analytically as well as numerically exact solutions of the full, especially the correlated lattice models in speech is impossible or at least very difficult mostly due to the interaction terms, one has to develop more or less sophisticated approximations for those model parts in order to get some theoretical insights. A very well established and powerful approximation scheme thereby is provided by mean-field theories, where in regard to applications to many-body problems it has become usual to differ between a standard or *static* and a somehow *dynamical* variant of the underlying approximation. Both variants are non-perturbative, hence perturbatively controllable as well as thermodynamically consistent theories that, for very different methodical reasons, determine exact or at least very reliable results for systems of very high dimension in a self-consistent manner but, as will be explained below, extremely differ in their technical scopes of application and their capabilities in regard to the strength of the present correlations.

In section 4.1 we start with a short review of the general mean-field idea. Then we will focus on its dynamical variant, originally specifically tailored to calculate strongly correlated electronic systems in section 4.2. Typically the dynamical mean-field theory (DMFT) can treat correlated models of a single-site homogeneity. In order to examine models merged of sublattices hence of a unit cell homogeneity, whereas the sites inside each unit cell show different physics one has to adapt, hence extend the resolution of the standard dynamical mean-field approach appropriately. Accordingly, in section 4.3, we propose a suitable site-selective extension of the standard DMFT as it is necessarily required for our purposes in chapters 6 and 7, starting on page 75.

The site-selective mean field approach as described in Section 4.3, especially the self-consistency equations therein were implemented in Fortran 90 from scratch in preparation for this thesis and our corresponding publications [AAP15; ATP15].

4.1. The general mean-field idea and static mean-field theory

In very general, a typical many-particle system consists of a large number of particles that interact among each other leading to a complex correlated motion. The mean-field idea is to consider each single particle to interact with an effective external field that is an averaged replacement of the interactions with as well as among the remaining particles. Like it is schematically visualized in fig. 4.1, a complex many-body problem is approximately reduced or better say *mapped* onto an *effective* one-body problem. The latter then usually is left to be solved *self-consistently* what turns out to be equivalent to the determination of a solution characterized by a minimal *free energy*[1] of the system [BF04]. Mathematically this is known as *Bogoliubov variation* [Kuz15], a special variational principle that provides a systematic way of deriving the mean-field theory (MFT) for a given microscopic Hamiltonian H and thus represents the formal basis for standard MFT [Yeo92]. It develops around a *Bogoliubov inequality*[2] which states that

$$\mathcal{F} \leq \Phi = \mathcal{F}_0 + \langle H - H_0 \rangle_0 \,, \tag{4.1}$$

where, besides the true free energy of the system $\mathcal{F}$, H_0 marks a trial Hamiltonian depending on a parameter h_0 with corresponding free energy $\mathcal{F}_0$, and $\langle \bullet \rangle_0$ denotes a thermal average taken in the ensemble defined by H_0. Resulting from that, the mean-field free energy $\mathcal{F}_{\mathrm{MF}}$ is defined by minimizing Φ with respect to the variational parameter h_0

$$\mathcal{F}_{\mathrm{MF}} = \min_{h_0} \{\Phi\} \,. \tag{4.2}$$

For a given choice of H_0, which for technical reasons usually tends to a non-interacting Hamiltonian, this procedure provides the best possible approximation to $\mathcal{F}$ as Ineq. (4.1) insists that the mean-field free energy $\mathcal{F}_{\mathrm{MF}}$ never falls below the true free energy.[3]

To get back to the initial problem of approximating interactions in a first step one claims the interaction part of an underlying Hamiltonian as

$$H_{\mathrm{int}} = AB \,, \tag{4.3}$$

hence a product of two operators A and B. In static MFT those original and true operators are then replaced by their average, again noted by $\langle \bullet \rangle$, plus the difference between their real value and their average. We therefore write

$$A = \langle A \rangle + (A - \langle A \rangle) \tag{4.4}$$

and analogously for B and put it into eq. (4.3). After some algebra this leads to

$$H_{\mathrm{int}} = A\langle B \rangle + \langle A \rangle B - \langle A \rangle \langle B \rangle + (A - \langle A \rangle)(B - \langle B \rangle) \,. \tag{4.5}$$

[1] The *free energy* is a thermodynamical potential which describes the energy of a system in thermal equilibrium with its environment at a given temperature T. For further details have a look at e.g. [Fer56].
[2] For the interested reader, a formal proof of Ineq. (4.1) may be found in [Cal85].
[3] This is analogous to the variational principle in quantum mechanics. Again, see e.g. [Sak94].

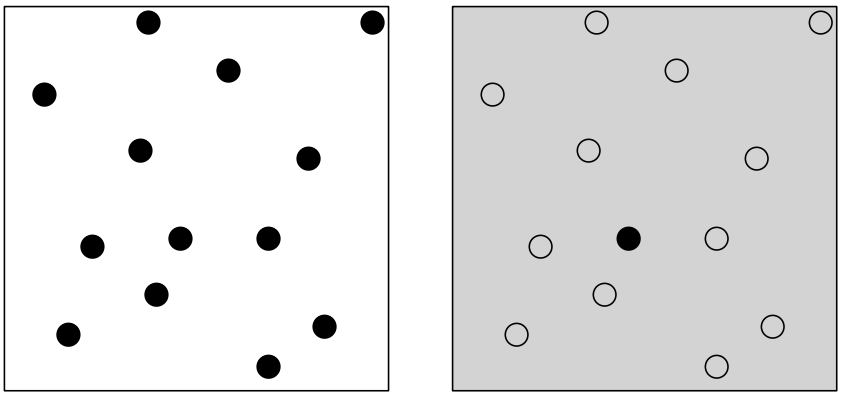

Figure 4.1.: Schematic visualization of the mean-field idea. The full many-particle problem (*left*) is replaced by an effective one-particle problem (*right*): a reference particle interacts with a surrounding mean-field that approximates all remaining particles and spatial interactions. Inspired by [BF04].

The actual mean-field approximation then is to treat the difference between an operator and its average, hence its fluctuation about its average what in a static theory is a spatial fluctuation, as a very small correction. As to eq. (4.4) this means

$$A - \langle A \rangle \approx 0\,, \tag{4.6}$$

what physically becomes true for very dense systems, i.e. systems with high coordination numbers and therefore usually of high dimension D, as in an infinitely high compact system there is just no space left for spatial fluctuations. Thus, the static mean-field approximation (4.6) becomes exact in the limit $D \to \infty$ while being sensitive for spatial fluctuations [Vol11]. By applying eq. (4.6) and its analog for B the last term in eq. (4.5) becomes negligible in terms of static MFT what results in a mean-field expression of the original interaction part of the Hamilton (4.3) that we write as

$$H_{\text{int}}^{\text{MF}} = A\langle B \rangle + \langle A \rangle B - \langle A \rangle \langle B \rangle\,. \tag{4.7}$$

At this stage one may notice what was already stated more generally above: Within MFT the original two-body problem AB mainly was broken down to a sum of one-body terms that in each case consist out of one operator multiplied by the mean-field, i.e. the thermal average, of the remaining operator of different kind. The general impact of the static mean-field approximation becomes clear by comparing the thermal averages of the initial operator H_{int} (4.3) and $H_{\text{int}}^{\text{MF}}$ (4.7):

$$\langle H_{\text{int}} \rangle = \langle AB \rangle \quad \longleftrightarrow \quad \langle H_{\text{int}}^{\text{MF}} \rangle = \langle A \rangle \langle B \rangle\,. \tag{4.8}$$

Thus, within static MFT the average of the originally occurring interaction is just factorized. From a mathematical point of view this only holds in cases where A and B are *uncorrelated*. Hence static MFT becomes a very brave approximation for systems whose physical properties are ruled by stronger correlations and thus may totally fail in providing reliable physical insights of such systems or, to be more concrete, in describing physical phenomena that arise due to strong electronic correlations. This can be traced back to the static character of the theory wherefore it behaves totally insensitive for dynamical correlations.

To sum up, one may note that the static MFT should provide reliable approximations of high dimensional, rather weakly correlated many-body systems, whereas it may fail for strongly correlated systems and/or systems of low dimension.

4.2. The dynamical mean-field approach and its approximations

The key for a better approximation of even strong electronic correlations beyond a static mean-field approach is to fully take into account dynamical instead of spatial quantum fluctuations. For the special case of correlated many-particle lattice models this, while in return totally neglecting spatial correlations, is realized by the comprehensive approximation scheme of dynamical mean-field theory (DMFT) [MV89; Geo+96]. Here, instead of trying to solve the given correlated lattice model in terms of its full dynamics as a whole, what usually is impossible, in imitation of its static counterpart just presented in section 4.1, the basic idea of the dynamical mean-field approach is to pick out one effective single site or unit cell of a correlated lattice model and to dynamically solve its local correlations embedded in a fictitious tight-binding model that effectively replaces the remnant interacting lattice [And12].

Formally, this is usually treated within the formalism of many-body Green's functions, where electronic correlations are encoded into *electronic self-energies* that reflect the influence of electronic correlations on the propagators, hence the Green's functions. While there also exists a dynamical mean-field approach for approximating the dynamics of correlated lattice systems in *thermal non-equilibrium* [SM02; Aok+14], for studies in *thermal equilibrium* at finite temperatures $T > 0$, as it was the case in the projects presented in chapter 6 and chapter 7, quantum dynamics are respected in terms of the *Matsubara formalism* that, as well as the corresponding Green's functions, was described and referred to in appendix A.2 on page 122 and the following. Within this formalism, the idea of DMFT manifests as follows: The local dynamics of the effective lattice site chosen inside the DMFT are formally described by the $\mathbf{k}$-averaged and consequently $\mathbf{k}$-independent lattice Green's function $G_{\mathrm{lat},\mathbf{k}}(\mathrm{i}\omega_n)$, referred to as the local Green's function $G_{\mathrm{loc}}(\mathrm{i}\omega_n)$. Within DMFT however this function is expressed by the local Green's function of an appropriate single-impurity problem $G_{\mathrm{imp}}(\mathrm{i}\omega_n)$. To sum up, for a lattice of L lattice sites, that is

$$\frac{1}{L}\sum_{\mathbf{k}} G_{\mathrm{lat},\mathbf{k}}(\mathrm{i}\omega_n) = G_{\mathrm{loc}}(\mathrm{i}\omega_n) \equiv G_{\mathrm{imp}}(\mathrm{i}\omega_n)\,, \tag{4.9}$$

where for now indices like spin-projection or further quantum numbers were suppressed for simplification. As we are not expecting any kind of translational or spin symmetry-breaking this will not lead to any implications in regard to the following discussion.

As $G_{\mathrm{imp}}(\mathrm{i}\omega_n)$ usually does not initially fit to the lattice problem to be solved it needs to be adapted *self-consistently* to the given $G_{\mathrm{loc}}(\mathrm{i}\omega_n)$ by iterations. In this context as visualized in fig. 4.2 the DMFT may also be described as *self-consistent mapping* of the full lattice problem on a suitable single impurity model.[4] What again conceptually seems to be a familiar receipt in regard to the

[4] From this point of view on the DMFT a possibility of deriving this mapping is provided by the so-called *cavity method* which is shown in [Geo+96; VBK12] and especially [Li08].

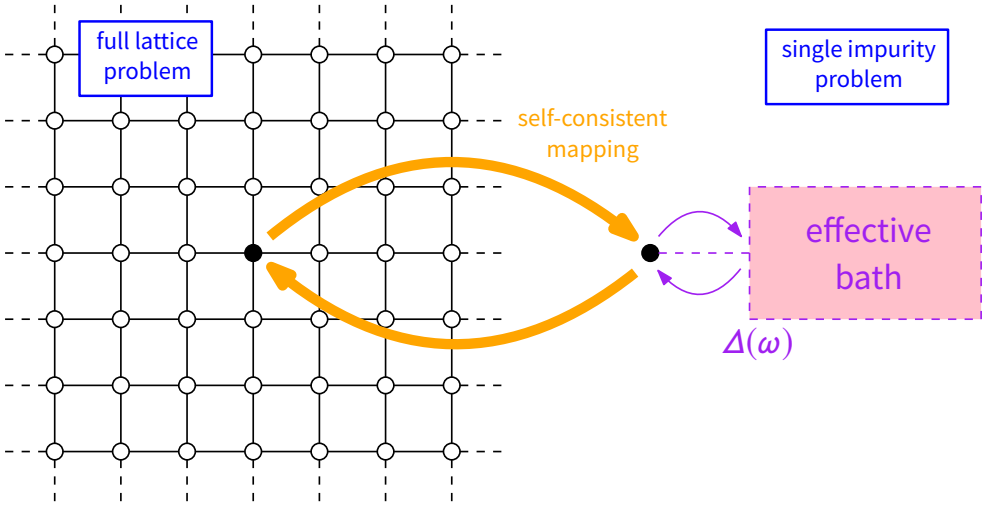

Figure 4.2.: Schematic visualization of the dynamical mean-field approach. The dynamics of a full correlated lattice model is self-consistently mapped onto a suitable single-impurity model whose dynamics are effectively described by a hybridization function $\Delta(\omega)$ which acts as the *dynamical mean-field*. Inspired by [Geo14].

static MFT crucially differs from that in the nature of the approximation of electronic interactions: While these in the static mean-field approach directly fall victim to the approximation as a consequence of factorization, within the DMFT the already mentioned reduction of a correlated lattice onto a still correlated single-impurity model, that even though solvable, still remains a full many-body problem, conserves a full, yet untouched electronic interaction which possibly bares the physics of strong electronic correlations. Characteristically for the DMFT in this context is the fact that the remaining single-impurity problem necessarily has to be solved by an appropriate *impurity solver*[5] like the CT-HYB that will be presented in more detail in chapter 5 on page 49 and the following. Therefore the DMFT is often categorized as *methodical framework*.

In order to appropriately realize the necessary self-consistency equation according to Eq. (4.9) the main approximation of DMFT has to be applied. This is to neglect the momentum dependence of the electronic self-energy of the lattice problem and to additionally approximate it by the single-particle impurity self-energy, hence

$$\Sigma_{\mathrm{lat},\mathbf{k}}(\mathrm{i}\omega_n) = \Sigma_{\mathrm{lat}}(\mathrm{i}\omega_n) \approx \Sigma_{\mathrm{imp}}(\mathrm{i}\omega_n)\,. \tag{4.10}$$

Equivalently, in real space representation one states

$$\Sigma_{ij}(\mathrm{i}\omega_n) \approx \Sigma_{\mathrm{imp}}(\mathrm{i}\omega_n)\,\delta_{ij}\,, \tag{4.11}$$

hence considers the lattice self-energy as purely local i.e. diagonal, where the remaining diagonal elements are simply replaced by the electronic self-energy of the single impurity problem.

These assumptions do not appear out of nothing but have a real physical background as they, and consequently the whole dynamical mean-field approach as such, become true in the limit of

[5] For an overview on common impurity solvers used within the framework of DMFT, also see [VBK12] and references therein.

infinite lattice dimension D. Originally this was proven by Metzner and Vollhardt in [MV89] for the Hubbard model [Hub63] as introduced in its single-band version in section 2.2 on page 11 and the following. The limit $D \to \infty$ however is *not trivial* for this model as the hopping t inside the Hamiltonian H_{Hub} (2.8) has to be scaled properly in the fashion

$$t = \frac{\tilde{t}}{\sqrt{2D}}, \quad \tilde{t} = \text{const.}, \tag{4.12}$$

in order to prevent the density of states (DOS) to become arbitrarily broad and featureless—from a different point of view, to ensure a correct conservation of all terms of the Hubbard Hamiltonian H_{Hub} (2.8) when D is increased [MV89; Vol10]. In contrast to that, the *trivial* limit would lead to a vanishing of the interaction term contained in H_{Hub} (2.8) and consequently to a vanishing of the competition between kinetic and potential energy, hence itinerancy and locality of the electrons that should be properly described by the Hubbard model (again see section 2.2, page 11 ff.). As the study of this competition however is the main target of the DMFT, the scaling (4.12) is not only unpreventable for physical reasons but turns out to be the key for all approximative assumptions of the dynamical mean-field approach.

As exposed in [VBK12] and further references therein, the scaling (4.12) of the hopping t in the limit $D \to \infty$ tremendously simplifies in the investigation of Hubbard-type lattice models and is equivalently derivable in momentum as well as in real space representations. Particularly in the latter, it evolves to a scaling of the dynamic free single-particle Green's function of the Hubbard model, hence the bare propagator, regardless of its representation in imaginary times or Matsubara frequencies, like

$$G^0_{ij} \sim \mathcal{O}\left(D^{-\frac{\|\mathbf{r}_i - \mathbf{r}_j\|}{2}}\right), \tag{4.13}$$

where $\|\mathbf{r}_i - \mathbf{r}_j\|$ is the *Manhattan distance* between two discrete sites of a possibly hyper-cubic lattice at real-space positions marked by $\mathbf{r}_i$ and $\mathbf{r}_j$. In a perturbation expansion of the Hubbard model in infinite dimension in terms of U, hence a *weak coupling* expansion, this property (4.13) implies the collapse of all connected, irreducible Feynman diagrams in the position space. Consequently, the full irreducible self-energy becomes a purely local [MV89] but still dynamic [Mül89a] quantity. Furthermore, the remaining, non-collapsed perturbation theory diagrams in the perturbation expansion of the full irreducible self-energy by comparison turns out to be the identical with that of the single-impurity Anderson model (SIAM) [Pru08]. Thus, both assumptions contained in eq. (4.11) are provable to be correct in the limit $D \to \infty$. In this context we additionally refer to [Kol11].

Now, everything is ready to formulate suitable self-consistency equations in the spirit of DMFT. For demonstration purposes we will stay with the single-band Hubbard model. Here, by using the model's equation of motion one may derive the *free lattice Green's function* as

$$G_{0,\mathbf{k}}(\mathrm{i}\omega_n) = \frac{1}{\mathrm{i}\omega_n - \varepsilon_{\mathbf{k}} + \mu}. \tag{4.14}$$

In combination with the *lattice Dyson equation*

$$\Sigma_{\mathrm{lat},\mathbf{k}}(\mathrm{i}\omega_n) = G_{0,\mathbf{k}}(\mathrm{i}\omega_n)^{-1} - G_{\mathrm{lat},\mathbf{k}}(\mathrm{i}\omega_n)^{-1} \tag{4.15}$$

that defines the *lattice self-energy* $\Sigma_{\text{lat},\mathbf{k}}$, the *dynamical interacting lattice Green's function* is obtained as

$$G_{\text{lat},\mathbf{k}}(\mathrm{i}\omega_n) = \frac{1}{\mathrm{i}\omega_n - \varepsilon_{\mathbf{k}} + \mu - \Sigma_{\text{lat},\mathbf{k}}(\mathrm{i}\omega_n)}\,. \tag{4.16}$$

Within the DMFT self-consistency cycle the single-band Hubbard model is reduced to the Anderson impurity model (AIM) as it was introduced in section 2.3 on page 13 and the following, whereas its electronic dynamics are fully described by the corresponding *local impurity Green's function* that in turn may be derived as

$$G_{\text{imp}}(\mathrm{i}\omega_n) = \frac{1}{\mathrm{i}\omega_n - \varepsilon_f + \mu - \Sigma_{\text{imp}}(\mathrm{i}\omega_n) - \Delta(\mathrm{i}\omega_n)}\,. \tag{4.17}$$

Similar to the steps above for the single-band Hubbard model, this equation algebraically directly results out of the *impurity Dyson equation* given by

$$\Sigma_{\text{imp}}(\mathrm{i}\omega_n) = \mathcal{G}_0(\mathrm{i}\omega_n)^{-1} - G_{\text{imp}}(\mathrm{i}\omega_n)^{-1} \tag{4.18}$$

that defines the self-energy of the impurity problem Σ_{imp} out of $G_{\text{imp}}(\mathrm{i}\omega_n)$ and the *free impurity Green's function*

$$\mathcal{G}_0(\mathrm{i}\omega_n) = \frac{1}{\mathrm{i}\omega_n - \varepsilon_f + \mu - \Delta(\mathrm{i}\omega_n)} \tag{4.19}$$

which in the context of DMFT plays the role of the *effective bare propagator*.

Both functions, $G_{\text{imp}}(\mathrm{i}\omega_n)$ (4.17) as well as $\mathcal{G}_0(\mathrm{i}\omega_n)$ (4.19), depend on the hybridization function $\Delta(\mathrm{i}\omega_n)$ that effectively describes the dynamics of the electronic bath including its electronic exchange with the impurity site. In terms of the Hamilton H_{AIM} (2.18) as defined on page 17 this special and physically important function is identified as

$$\Delta(\mathrm{i}\omega_n) = \sum_{\mathbf{k}} \frac{V^2}{\mathrm{i}\omega_n - \varepsilon_{\mathbf{k}} + \mu} = \int \mathrm{d}\varepsilon\, \frac{-\mathrm{Im}\Delta(\varepsilon)/\pi}{\mathrm{i}\omega_n - \varepsilon}\,. \tag{4.20}$$

As in particular

$$-\,\mathrm{Im}\left[\Delta(\varepsilon)\right] = \pi V^2 \sum_{\mathbf{k}} \delta\left(\varepsilon - \varepsilon_{\mathbf{k}}\right) = \Gamma(\varepsilon)\,, \tag{4.21}$$

the hybridization function is directly related to the hybridization-induced broadening of the impurity excitation levels $\Gamma(\varepsilon)$ given by eqs. (3.4) and (3.5) as already discussed in the context of the formation of local magnetic moments in section 3.1, page 24 ff., by means of the AIM.

Finally we are prepared to formulate a self-consistency equation in regard to the *dynamic* local Green's function of the single impurity problem $G_{\text{imp}}(\mathrm{i}\omega_n)$ Eq. (4.9) [Geo14]: In a first step we write out eq. (4.9) in terms of eq. (4.16) and apply the DMFT approximation (4.10). We get

$$G_{\text{imp}}(\mathrm{i}\omega_n) = G_{\text{loc}}(\mathrm{i}\omega_n) = \frac{1}{L}\sum_{\mathbf{k}} G_{\text{lat},\mathbf{k}}(\mathrm{i}\omega_n) \approx \sum_{\mathbf{k}} \frac{1}{\mathrm{i}\omega_n - \varepsilon_{\mathbf{k}} + \mu - \Sigma_{\text{imp}}(\mathrm{i}\omega_n)}\,. \tag{4.22}$$

The additional extraction of $\Sigma_{\text{imp}}(\mathrm{i}\omega_n)$ in terms of the impurity Dyson equation (4.18) and eq. (4.19) finally yields:

$$G_{\text{imp}}(\mathrm{i}\omega_n) = \frac{1}{L}\sum_{\mathbf{k}} \frac{1}{G_{\text{imp}}(\mathrm{i}\omega_n)^{-1} + \Delta(\mathrm{i}\omega_n) - \varepsilon_{\mathbf{k}} - \varepsilon_f}\,. \tag{4.23}$$

Due to the impact of eq. (4.19) this equation also is remarkably strongly dominated by the hybridization function $\Delta(\mathrm{i}\omega_n)$ which for physical reasons has to be, since in the end it is $\Delta(\mathrm{i}\omega_n)$ and not $G_{\mathrm{imp}}(\mathrm{i}\omega_n)$ that plays the important role of the *dynamical mean-field* as a central magnitude of the dynamical mean-field approach. Therefore, especially if one uses quantum Monte Carlo (QMC) algorithms inside the framework of DMFT (c.f. chapter 5 page 49 ff.), in order to solve the remaining single impurity problem it is more convenient to directly formulate a system of self-consistency equations by solving eq. (4.23) for the hybridization function, resulting in

$$\Delta(\mathrm{i}\omega_n) = \mathrm{i}\omega_n - \varepsilon_f + \mu - \Sigma_{\mathrm{imp}}(\mathrm{i}\omega_n) - \frac{1}{G_{\mathrm{loc}}(\mathrm{i}\omega_n)}\,, \tag{4.24}$$

where $G_{\mathrm{loc}}(\mathrm{i}\omega_n)$ follows the approximation in eq. (4.22). By that, principally a full algorithmic *self-consistency cycle* may be realized. To do so, one would start with an initial guess of Σ_{imp} in order to calculate $G_{\mathrm{loc}}(\mathrm{i}\omega_n)$ (4.22) and with it $\Delta(\mathrm{i}\omega_n)$ according to eq. (4.24). Now the job of an appropriate single impurity solver would be to extract a new Σ_{imp} out of the given single impurity model $\Delta(\mathrm{i}\omega_n)$. A job which finalizes the first iteration step. Further steps have to follow unless a comparison of the "old" and "new" self-energies turns out positive.

What still needs to be mentioned are the not entirely positive consequences as immediate results out of the strictly local character of the DMFT. While due to its theoretical base, the dynamical mean-field approach treats local effects like the Kondo effect as described in section 3.2 exactly, one has to tolerate an approximate treatment of the non-local effects e.g. like those of the Ruderman-Kittel-Kasuya-Yosida (RKKY) interaction. This is due to the fact that within DMFT the previously criticized factorization of electronic correlations in terms of static MFT, c.f. section 4.1 on page 38 ff., emerges comparably but is shifted up to two-particle and higher correlation functions [And12]. In this context, one particularly has to expect problems in regard to the correct representation of phenomena based on a long-range order like c.f. long-wavelength magnetic excitations, known as magnons or, more generally, of non-local two-particle correlations. From a perturbative point of view, those higher correlations do not contribute, thus simply do not feedback to the expansion of the local single-particle self-energy mentioned above and therefore are not recognized by means of DMFT.

Consequently, a well-known artifact of the dynamical mean-field approach arises in form of its insensitiveness towards the statements of the Mermin-Wagner theorem that already was the topic of section 3.3.1. This fact plays an enormous role concerning the performed DMFT-studies of magnetic phase transitions which are the main content of chapter 6 on page 75 ff. and chapter 7 on page 95 and the following.

4.3. Site-dependent extension of the dynamical mean-field approach

In the preceding section 4.2 we worked out the DMFT self-consistency equations with the single-band Hubbard model (c.f. section 2.2, page 11 ff.) in mind, hence a model that is homogeneous in regard to its throughout correlated sites. Consequently, until now, we have been focussing on the so-called *single-site* dynamical mean-field theory.

Generally this *standard variant* of the dynamical mean-field approach treats every impurity site of the model to be equally solved, hence is only reasonably applicable for systems or many-body problems that are considered as homogeneous in terms of the physics of every single site. For our purposes however, as already motivated in the Introduction, page 1 ff., in chapters 6 and 7 we will be confronted with periodic Anderson models in which the physics of interest occurs among single member sites of pragmatically clever chosen, i.e. defined unit cells. Therefore we need an extended dynamical mean-field approach that principally shifts the methodical treatment of single sites towards unit cells while additionally site-selectively respecting the unit-cell-internal sites in the necessary self-consistent mapping. Thus this required site-dependent dynamical mean-field theory (sdDMFT) methodically should be categorized somewhere in between the single-site and the real-space DMFT [PN97].

Before becoming more specific in this attempt, we first leave behind the single-band Hubbard model in favor of the PAM as the model of our interest. In order to fit our just mentioned requirements, we write out the real-space Hamiltonian in an extended fashion compared to that given by eq. (2.15) on page 15. Formally this is achieved by appropriately extending the set of used indices yielding:

$$\begin{aligned} H = &\sum_{\mathbf{r}\mathbf{r}'}\sum_{\alpha\alpha'}\sum_{\sigma} c^{\dagger}_{\mathbf{r}\alpha\sigma} t_{\alpha\alpha'}(\mathbf{r}-\mathbf{r}') c_{\mathbf{r}'\alpha'\sigma} \\ &+ V\sum_{\mathbf{r}\alpha\sigma}\left(c^{\dagger}_{\mathbf{r}\alpha\sigma} f_{\mathbf{r}\alpha\sigma} + f^{\dagger}_{\mathbf{r}\alpha\sigma} c_{\mathbf{r}\alpha\sigma}\right) \\ &+ \varepsilon_f \sum_{\mathbf{r}\alpha\sigma} f^{\dagger}_{\mathbf{r}\alpha\sigma} f_{\mathbf{r}\alpha\sigma} \\ &+ \frac{U}{2}\sum_{\mathbf{r}\alpha\sigma} f^{\dagger}_{\mathbf{r}\alpha\sigma} f_{\mathbf{r}\alpha\sigma} f^{\dagger}_{\mathbf{r}\alpha-\sigma} f_{\mathbf{r}\alpha-\sigma}\,. \end{aligned} \tag{4.25}$$

Here, $\mathbf{r}$ runs over the position vectors to the different unit cells, α concretely refers to the sites within a unit cell, and σ is the spin projection as usual. $c^{\dagger}_{\mathbf{r}\alpha\sigma}$ ($f^{\dagger}_{\mathbf{r}\alpha\sigma}$) creates an electron in the c (f) orbital with quantum numbers $\mathbf{r}, \alpha, \sigma$. Again, conduction electrons are assumed to hop between nearest-neighboring sites, i.e., the hopping amplitude $t_{\alpha\alpha'}(\mathbf{r}-\mathbf{r}') = t \neq 0$ if $\mathbf{r}, \alpha$ and $\mathbf{r}', \alpha'$ are nearest neighbors. Furthermore, also as usual, V is the local hybridization strength, and U is the strength of the Hubbard-type local interaction on the f orbitals. The one-particle energy of the f orbitals is ε_f and for the c orbitals $\varepsilon_c \equiv t_{\alpha\alpha}(0)$.

Based on this notation let's focus on the self-energy once more: As reported in the previous section 4.2 on page 40 and the following, DMFT assumes the self-energy on the f orbitals to be local, hence

$$\Sigma_{\mathbf{r}\alpha\sigma,\mathbf{r}'\alpha'\sigma'}(\mathrm{i}\omega_n) = \delta_{\mathbf{r},\mathbf{r}'}\delta_{\alpha\alpha'}\Sigma_{\sigma\sigma'}(\mathrm{i}\omega_n)\,,$$

and maps the lattice problem onto an effective single-impurity Anderson model with one-particle parameters or, equivalently, with a hybridization function $\Delta_{\sigma\sigma'}(\mathrm{i}\omega_n)$ that is determined from the local element of the lattice Green's function $G_{\mathrm{loc},\sigma\sigma'}(\mathrm{i}\omega_n)$ via the DMFT self-consistency condition. This implicitly assumes that the dynamical mean-field $\Delta_{\sigma\sigma'}(\mathrm{i}\omega_n)$ is homogeneous. Consequently, only homogeneous phases of the DMFT equations can be found in this way.

In contrast to that, in the real-space DMFT approach the self-energy is still assumed as completely

local but inhomogeneous solutions of arbitrary complexity are allowed by keeping the full spatial dependence of the local self-energy:

$$\Sigma_{\mathbf{r}\alpha\sigma,\mathbf{r}'\alpha'\sigma'}(\mathrm{i}\omega_n) = \delta_{\mathbf{r},\mathbf{r}'}\delta_{\alpha\alpha'}\Sigma_{\mathbf{r}\alpha;\sigma\sigma'}(\mathrm{i}\omega_n)\,.$$

In this context, a sdDMFT may be constructed by assuming that the local self-energy has possibly different elements on the different sites in a unit cell that is larger than a primitive cell. Otherwise, the self-energy is taken as homogeneous:

$$\Sigma_{\mathbf{r}\alpha\sigma,\mathbf{r}'\alpha'\sigma'}(\mathrm{i}\omega_n) = \delta_{\mathbf{r},\mathbf{r}'}\delta_{\alpha\alpha'}\delta_{\sigma\sigma'}\Sigma_{\alpha\sigma}(\mathrm{i}\omega_n)\,. \tag{4.26}$$

It is important to generally state here, that throughout our studies, we will restrict ourselves to collinear magnetic phases for simplicity. Therefore we consider a possibly spin-dependent but spin-diagonal self-energy.

Obviously the site-dependent extension has to affect the DMFT self-consistency equations previously defined by means of eqs. (4.22) and (4.24). The exploitation of the remaining translational symmetry tightly followed by the Fourier transformation of the one-particle term of the Hamiltonian (4.25), especially including the hopping parameters $\mathbf{t}$ yields a $\mathbf{k}$-dependent hopping matrix $\varepsilon_{\mathbf{k}}$ of the dimension $\dim = n \times n$, where wave vectors $\mathbf{k}$ are considered in the reduced Brillouin zone and where n is the number of orbitals per chosen unit cell.

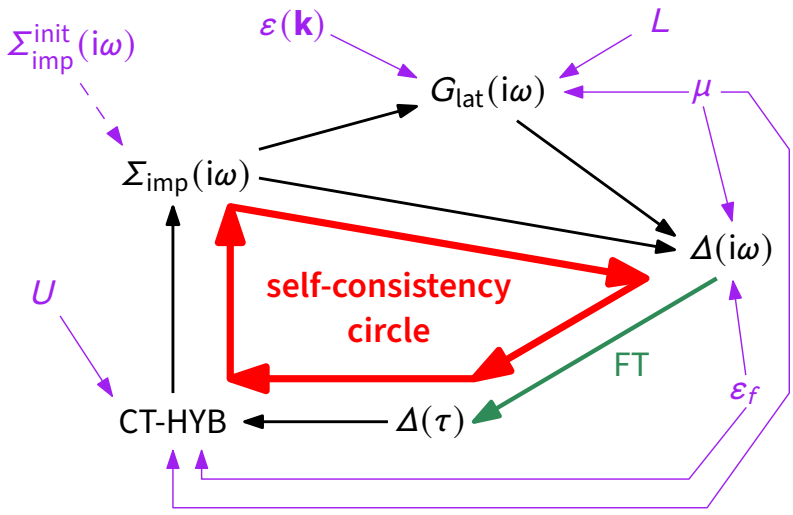

Figure 4.3.: Schematic visualization of the DMFT-self-consistency cycle (closed loop of red arrows) by means of our sdDMFT ansatz, implying the usage of the CT-HYB algorithm as single-impurity solver. Static system parameters (purple symbols) are repeatedly used for the cyclic self-consistent re-calculations of the dynamical functions and by the CT-HYB—compare to chapter 5—(black symbols). The green arrow reflects the Fourier transform from $\Delta(\mathrm{i}\omega)$ to $\Delta(\tau)$ as expected from the CT-HYB. For further explanation and discussion see text in section 4.3.

As visualized in fig. 4.3 by that, and with a guess for the local but now site-dependent f self-energy $\Sigma_{\alpha\sigma}(\mathrm{i}\omega_n)$ the DMFT self-consistency cycle can be started by calculating the elements of the local but in contrast to eq. (4.22) site-selectively extended lattice Green's function via

$$G_{\mathrm{loc},\gamma\delta,\sigma}(\mathrm{i}\omega_n) = \frac{1}{L}\sum_{\mathbf{k}\in\mathrm{BZ}}\left[\frac{1}{\mathrm{i}\omega_n + \mu - \varepsilon_{\mathbf{k}} - \mathbf{\Sigma}_\sigma(\mathrm{i}\omega_n)}\right]_{\gamma\delta}, \tag{4.27}$$

where γ, δ run over the n orbitals in the unit cell and where the $n \times n$-matrix $\mathbf{\Sigma}_\sigma(\mathrm{i}\omega_n)$ is diagonal and non-zero on the f orbitals only. μ still marks the chemical potential that is used to fix the total particle density, while from the extended point of view L runs over the model's unit cells instead of its lattice sites. Methodically equal to the descriptions in section 4.2, the local Green's function is then used to determine the hybridization functions of the single-impurity Anderson models (α) as

$$\Delta_{\alpha\sigma}(\mathrm{i}\omega_n) = \mathrm{i}\omega_n - \varepsilon_f + \mu - \Sigma_{\alpha\sigma}(\mathrm{i}\omega_n) - \frac{1}{G_{\mathrm{loc},\alpha\alpha,\sigma}(\mathrm{i}\omega_n)}. \tag{4.28}$$

Having defined the impurity models this way one principally proceeds further according to section 4.2: The self-consistency cycle is closed by calculating the self-energy $\Sigma_{\alpha\sigma}(\mathrm{i}\omega_n)$ *for each* impurity model independently by means of an appropriate impurity solver. As already stated repeatedly, in our case this is the CT-HYB impurity solver based on the segment code algorithm. This continuous-time quantum Monte Carlo (CT-QMC) approach will be the topic of the following chapter 5. As we will see there, besides the static system parameters ε_f, μ and the impurity onsite correlation U, the CT-HYB approach generally expects the input of a time-dependent hybridization function $\Delta_{\alpha\sigma}(\tau)$. The site-dependent dynamical-mean field approach as discussed here, however *per se* provides a hybridization function in terms of eq. (4.28), hence in the space of Matsubara frequencies $\mathrm{i}\omega_n$. For technical reasons this is only possible for a finite number of frequencies

$$n = 0, 1, \ldots, n_\omega \ll \infty.$$

Nevertheless, one in the end has to carry out a Fourier transform in the spirit of that given by eq. (A.17) for imaginary-time Matsubara Green's functions

$$\Delta_{\alpha\sigma}(\tau) = \sum_{n=-\infty}^{\infty} \mathrm{e}^{-\mathrm{i}\omega_n\tau}\Delta_{\alpha\sigma}(\mathrm{i}\omega_n). \tag{4.29}$$

In the knowledge of the high frequency behavior of the hybridization function as of order $\mathcal{O}(1/\mathrm{i}\omega_n)$, we can expand $\Delta(\mathrm{i}\omega_n) \sim \xi/(\mathrm{i}\omega_n)$ in this limit. Proposed, this behavior is already reached by means of the calculated hybridization function at ω_{n_ω}, the expansion coefficient ξ can be derived numerically as $\xi = \lim_{n=0\to n_\omega} \mathrm{i}\omega_n\Delta(\mathrm{i}\omega_n)$. Then, in particular by gaining from the relationship between the indices of fermionic Matsubara frequencies illustrated in eq. (A.19), one can state

$$\Delta(\tau) = \underbrace{\frac{2}{\beta}\,\mathrm{Re}\left[\sum_{n=0}^{n_\omega} \mathrm{e}^{-\mathrm{i}\omega_n\tau}\left(\Delta(\mathrm{i}\omega_n) - \frac{\xi}{\mathrm{i}\omega_n}\right)\right]}_{\text{calculated}} + \underbrace{\frac{1}{\beta}\sum_{n=-\infty}^{\infty} \mathrm{e}^{-\mathrm{i}\omega_n\tau}\frac{\xi}{\mathrm{i}\omega_n}}_{\text{analytical}}, \tag{4.30}$$

where we have dropped indices for convenience. Here, the determination of $\Delta(\tau)$ is split into a calculated and an analytical part. While the prior can be determined directly out of the numerical

data provided by the numerical setup, the latter one can be identified as $-\xi/2$ [Com07] in terms of an evaluation of fermionic Matsubara sums [BF04; AS10; Mah00]. In the context of eq. (4.30), the analytical part is categorized as the *analytical tail* of the calculated part.

This practice is of course not restricted to $\Delta(\tau)$ but instead is generically applicable for functions that show the same high frequency behavior, e.g. the τ-dependent correspondent elements of the site-selectively extended lattice Green's function $G_{\mathrm{loc},\gamma\delta,\sigma}(\mathrm{i}\omega_n)$ (4.27), to stay with the above mentioned Fourier transform eq. (A.17). By that, in combination with a generalized relation (A.13), it is furthermore possible to derive single occupation numbers of the orbitals in consideration.

4.4. Summary

From a general point of view, this chapter provided the fundamentals of different mean-field theories—namely the general and the dynamical plus its site-dependent extension—used in equilibrium many-body physics. As the main benefit we want to point out the derivation of a site-selectively extended self-consistency circle by means of a sdDMFT in section 4.3, especially fig. 4.3 and eqs. (4.22) and (4.24). By that, we have constructed and presented the framework of our numerical setup that will soon be put into action in chapters 6 and 7. There, we will also concretize the practical derivation of the hopping matrix $\varepsilon_{\mathbf{k}}$ by means of specific models build on concrete lattice geometries. But before doing so we will have to care about the theory and methodology of the used and already repeatedly announced (see the purple parameters in fig. 4.3) impurity solver, hence the CT-HYB algorithm in its segment-picture variant. This will be done properly in the following chapter 5.

5. The continuous-time hybridization expansion algorithm

In the previous chapter 4 mean-field theories up to the site-dependent dynamical mean-field theory approach were discussed. It was emphasized there, that dynamical mean-field theory (DMFT) in general breaks down a correlated many-body to a single-impurity problem which is then left to be solved by an appropriate impurity solver. So far, we repeatedly mentioned the continuous-time hybridization expansion (CT-HYB) continuous-time quantum Monte Carlo (CT-QMC) method as our method of choice to act as impurity solver inside our sdDMFT implementation but factually, it was only regarded as a working "black box" so far. This chapter fills this content-related gap by giving a detailed report on the technical inside and the methodical as well as formal background of this black box: a segment variant of the CT-HYB algorithm.

In preparation of this thesis we implemented a working CT-HYB code in the segment variant in Fortran 90 from scratch, using both, Intel and GNU Fortran compilers. The code was parallelized by means of the Message Parsing Interface (MPI). This was done for two reasons:

1. To be able to design the numerical setup in very detail and

2. simply in order to understand the underlying algorithm in depth.

Besides for simulations presented in chapters 6 and 7 the resulting code was also used by Peschke to produce physical results for his master thesis [Pes14]. The whole implementation process required half of the time needed for getting the scientific results reported on within this thesis and thus our CT-HYB code itself represents one of the main results of this thesis. These facts are reflected by the rather wider scope of this chapter.

We open the chapter with a short review of the Monte Carlo (MC) method in solid state physics in section 5.1.1, thereby also caring about the fermionic sign problem (see section 5.1.2) before moving on to the CT-QMC approach in section 5.1.3.

We then carry out the CT-HYB typical expansion of the hybridization function of the impurity model to be solved in section 5.2. This expansion is essential for the derivation of the stochastic process of the CT-HYB. Before this is discussed for the segment variant in section 5.4 a discussion of the general Markov chain Monte Carlo (MCMC) sampling by means of the well-known Metropolis algorithm is provided by section 5.3. We close the chapter with an explanation and overview of the measurements of observables that are performed within our CT-HYB approach in section 5.5—especially that of the impurity self-energy as needed to close the dynamical mean-

field self-consistency circle as described in section 4.3 on page 47 and the following.

5.1. Introduction and general aspects

The CT-HYB [Wer+06; WM06] algorithm, besides the continuous-time interaction expansion (CT-INT) [RSL05] and the continuous-time auxiliary field (CT-AUX) [RHJ99; RHJ98; Gul+08] approaches, belongs to the prominent family of thermodynamic, numerically exact impurity solvers that methodically rely on the so-called CT-QMC method [Gul+11]. In essence, those algorithms are methodically based on a MCMC integration [GRS96; MNR12] which generally is a numerical approach to stochastically evaluate preferably multidimensional integrals under heavy usage of pseudo random numbers.

5.1.1. The Monte Carlo method in solid state physics

Similar to the typical and general area of application in statistical physics [BH10; LB14; Kra06], in particular regard to quantum Monte Carlo (QMC) simulations of solids, MCMC approaches are used to stochastically provide an estimation inclusive a corresponding more or less reliable error of expectation values in respect to high-dimensional configuration spaces [Fou+01].

More formal, in denoting a particular configuration space of all configurations c by Ω, the expectation value of an observable A, usually marked by $\langle A \rangle$, is given by the average of A in configuration c, that is $A(c)$, over all configurations $c \in \Omega$ with respect to their statistical weight $p(c)$. Hence,

$$\langle A \rangle_p = \frac{1}{Z} \sum_{c \in \Omega} A(c) p(c) \,, \quad Z = \sum_{c \in \Omega} p(c) \,, \tag{5.1}$$

with the crucial quantity Z, known as one of the central magnitudes of statistical physics, the *partition function*. Thereby, to match the common definitions of probability theory (e.g. see [GS97; Kle08]), the implied normed distribution

$$\frac{p(c)}{Z} =: P(c) \tag{5.2}$$

clearly has to fulfill the two conditions

$$\sum_{c \in \Omega} P(c) = 1 \,, \tag{5.3}$$

$$\forall\, c \in \Omega \,:\, P(c) \geq 0 \,. \tag{5.4}$$

In practice however, the problem in determining $\langle A \rangle_p$ in terms of eq. (5.1) lies in the fact that the sums in eq. (5.1)—and consequently also the normed distribution given by (5.2)—as such are usually not executable in total. On the contrary, one at least is able to calculate $A(c_i)$ for

discrete configurations $\{c_i\}$ while additionally the corresponding weights $\{p(c_i)\}$ may be determined. Resulting from these facts given, the primary ansatz of the MC method manifests in the approximation of the exact average by a representative sample mean in the fashion of

$$\langle A\rangle_p \approx \langle A\rangle_{\mathrm{MC},p} = \frac{1}{M}\sum_{i=1}^{M} A(c_i)\,, \tag{5.5}$$

where the configurations $\{c_i \,:\, i = 1,\dots,M\}$ are sampled according to $P(c)$, hence arise as a sequence of the possible outcomes of random variables $\{C_i(\Omega,P)\}$ defined on Ω and $P(c)$. Interestingly, the convergence of $\langle A\rangle_{\mathrm{MC},p}$ to $\langle A\rangle_p$ in the limit $M\to\infty$ is stochastically ensured by the *empirical law of large numbers* [Fou+01] which may be looked up in [Gro13] or [RF94]. Moreover, in this context, the $\{A(C_i)\}$ as functions of $\{C_i\}$ are also identified as random variables and thus the *central limit theorem* [Cah13] predicts the distribution of $\langle A\rangle_{\mathrm{MC},p}$ to *converge in probability* [Fel68] to a *normal distribution* with mean $\langle A\rangle_p$ and variance

$$\sigma^2_{\langle A\rangle} = \frac{\sigma^2_A}{M}\,, \tag{5.6}$$

provided that the $\{A(c_i)\}$ are *statistically independent*, that is *uncorrelated*. Typically the variance σ^2_A of the $\{A(c_i)\}$ is unknown and therefore has to be appropriately estimated itself. Since the basic sample is the sample over configurations $\{c_i \,:\, i = 1,\dots,N\}$ and not over functions $\{A(c_i)\}$ the naive usage of the corresponding *sample variance* as it is usually taught by basic data analysis [Bra14; Bon13] leads to a *biased*, hence wrong imagination of the error of the simulation for the general but common case of $A(c)$ representing a non-linear function of c. Thus, to avoid the performance of *standard error propagation* [Tay97] and the numerically cumbersome evaluation of associated partial derivatives, one has to use advanced re-sampling methods like the *bootstrap method* or a special case of it known as the *jackknife analysis* [Efr82; Bon13], which will be our choice here.

This special re-sampling scheme is based on forming jackknife blocks of data out of the sampled dataset at hand and the subsequent utilization of the corresponding averages of those blocks as input of the error analysis. Thereby each jackknife block results out of the original data set by removing or leaving out one configuration respectively. By that, the average of the ith jackknife block reads

$$A_{\mathrm{J},i} \equiv \frac{1}{M-1}\left[\sum_{j=1}^{M} A(c_j) - A(c_i)\right]^2\,, \tag{5.7}$$

implying that the total value of the average of all jackknife blocks is equal to that of the standard Monte Carlo estimate defined by eq. (5.5). Correspondingly, as it is explicitly shown in [You12], the corrected, unbiased jackknife variance of the $\{A_i\}$ that estimates σ^2_A of eq. (5.6) best, manifests as[1]

$$\sigma^2_{\mathrm{J},A} = (M-1)\sum_{n=1}^{M}\left[A_{\mathrm{J},n} - \frac{1}{M}\sum_{n=1}^{N} A_{\mathrm{J},n}\right]^2 \approx \sigma^2_A\,. \tag{5.8}$$

[1] Note here that, apart from the referenced literature above, this estimate is written down in eq. (5.8) with already

The typical error-scaling of MC processes certainly may already have been revealed from eq. (5.6): The error in terms of the number of sampled configurations M scales as $\sigma_{\langle A\rangle} \propto 1/\sqrt{M}$ and thus remarkably stays independent of the dimension D of the configuration space a Monte Carlo simulation runs through or equivalently, from a more general point of view, of a likewise simulated integral.

It is due to this fact that the MC integration is the method of choice for evaluating integrals of high or even infinite dimension D, as errors originating from standard numerical integration approaches like e.g. Newton-Cotes formulae [DR84; Pre+07] in terms of the number of evaluation points show a convergence behavior that drastically slows down with increasing dimension and hence often simply become inapplicable to solve multidimensional problems[2] [Wei00; Kat09]. Against this very basic methodical background, when discussing quantum Monte Carlo simulations of fermionic systems, it is unavoidable to address the more special so-called negative sign problem. This will be done in the following.

5.1.2. Dealing with the negative sign problem

In performing QMC simulations of fermionic impurity models one might be confronted with the *negative sign problem*. That is the QMC process internally may encounter configurations c that exhibit statistical weights $p(c) < 0$ of negative sign what in turn goes back to the anticommutation relations between fermionic operators like those shown in eq. (2.1). Generally the existence of a solution is highly questionable as in terms of *computational complexity* [Hig15; GBL08; Ner16; Cor+09] those problems were categorized as NP hard, hence as *non-deterministic hard*, thereby implying that a generic solution of the negative sign problem remains non-existent until the set P of problems which are solvable in polynomial computational time was proven to be equal to the set of NP problems that only can be verified in polynomial time, hence NP ≡ P [TW05]. It is therefore recommended to switch to a sampling with respect to $|p(c)|$, hence the absolute value of $p(c)$, instead of $p(c)$ itself and to additionally reweigh the observable averages i.e. measurements $\langle A\rangle_p$ and $\langle A\rangle_{\mathrm{MC},p}$ originally given by eqs. (5.1) and (5.5) in terms of

$$\langle A\rangle_{|p|} = \frac{\sum_c A(c)\frac{p(c)}{|p(c)|}|p(c)|}{\sum_c \frac{p(c)}{|p(c)|}|p(c)|} = \frac{\sum_c A(c)s(c)|p(c)|}{\sum_c s(c)|p(c)|} \approx \langle A\rangle_{\mathrm{MC},|p|} = \frac{\sum_{i=1}^M s(c_i)A(c_i)}{\sum_{i=1}^M s(c_i)}\,, \tag{5.9}$$

corrected pre-factors. In detail, for each analysis method ♠ one would initially consider the defined standard variance

$$s^2_{\spadesuit,A} = \frac{1}{N}\sum_{n=1}^{N}\left[A_{\spadesuit,n} - \sum_{n=1}^{N} A_{\spadesuit,n}\right]^2$$

and subsequently multiply a correction C to the pre-factors leading to the corrected estimate of the respective variance

$$\tilde{\sigma}^2_{\spadesuit,g} = C s^2_{\spadesuit,g}\,.$$

See e.g. [LP16] for details.

[2] To be fair in this context, one has to mention that traditional methods serve highly trustful *deterministic* errors, whereas by using MC integration approaches one has to pay the price of receiving errors of solely *probabilistic* nature.

where generally $s(x) = p(x)/|p(x)| = \mathrm{sgn}[p(c)]$ is identified as the sign function and therefore reflects the sign of $p(x)$. Although this enables for QMC simulations of sign-problematic systems, one has to pay the price of a weakened statistics as can be directly seen from the r.h.s. of eq. (5.9). As a direct consequence of the scaling of the MC error as manifested by eq. (5.6), this may lead to a catastrophic performance of the underlying MC process in regard to the computational time that is required to provide measurements of a desired fixed accuracy. With that in mind, we finally will turn our attention to the continuous-time quantum Monte Carlo.

5.1.3. The Continuous-time quantum Monte Carlo approach

Focusing on the continuous-time variant, the generalities on QMC approaches presented so far become special inasmuch as CT-QMC simulation relies on an expansion of the partition function Z into a series of diagrams and the stochastic sampling of precisely these diagrams. Therefore, the CT-QMC also is classified as a *diagrammatic* MC method. As for a given expansion order the stochastic sampling principally cares of all emerging diagrams additionally the CT-QMC approach is considered as *numerically exact*.

While formerly conventional auxiliary-field QMC methods like the Blankenbecler-Scalapino-Sugar (BSS) [BSS81] or the Hirsch-Fye [HF86; Blü11] algorithm are based on a time-discrete sampling that methodically implies a *Hubbard-Stratonovich transformation* in a technically necessary combination with a *Trotter decomposition* that in turn results in a systematic time discretization error [Ass02; AE08], the great benefit of the invention of CT-QMC was to be able to sample in the limit of a vanishing time-discretization, hence in a continuous-time fashion. In other words this might be described as a stochastically controlled perturbation expansion of the partition function that actually serves the average perturbation order as an important MC measurement. According to their nomenclature established within [Gul+11] the CT-INT algorithm and the CT-AUX approach, at what the latter may be factually seen as a continuous-time, hence optimal implementation of the famous time-discrete auxiliary-field Hirsch-Fye algorithm, are based on expansions of Z in powers of the interaction U, whereas consequentially the CT-HYB solver relies on an expansion of Z in powers of the impurity-bath hybridization V.

However, with the experience of a mapping between both approaches, the CT-AUX was found to be a special variant of the more general CT-INT method [MMJ09]. While in this context the CT-HYB method remains unique, there exist two versions of this algorithm that significantly differ in regard to the categories of solvable models, the sampling procedure and the scaling: A general version, also called *matrix code* that is able to solve impurity models implying general-type interactions and a more special *segment code* that on the one hand only may deal with impurity models whose interaction is of density-density character, but on the other hand relies on a more efficient sampling scheme and may measure, hence serve the single-particle impurity self-energy highly efficiently in terms of Matsubara frequencies in a direct, solver-internal way, what will be explained in more detail in section 5.5 on page 71.

This last mentioned quality is an unbeatable advantage of the segment code in regard to the usage as impurity solver inside a DMFT cycle, where one usually operates in the space of Matsubara

frequencies. Another reason why in practice one should always prefer the usage of the segment variant to that of the matrix code lies in the scaling concerning the given system size N: Regardless of a possible negative sign problem, the complexity of the segment code shows a *polynomial* scaling, whereas the matrix code scales *exponentially* in this scope.

To stay with the scaling, but in a more general context again, one has to mention that the simulation in continuous time unfortunately also has its drawback: The computational time of CT-QMC algorithms scales like $\mathcal{O}(N_{\mathrm{imp}}^3\beta^3)$ in regard of the inverse temperature β and the number of impurities N_{imp} contained in the impurity problem to be solved. From this viewpoint, discrete-time auxiliary-field QMC methods [AE08] win the game as they may show a scaling of $\mathcal{O}(N_{\mathrm{imp}}^3\beta)$ that is at least linear in β [Ass14; IT15]. Therefore, the usage of CT-QMC methods is quite suboptimal for solving impurity lattice models. This fact clearly resolves the question, why those approaches are usually used as single-impurity solvers within the framework of DMFT and not solely as cluster solvers.

In the role of a single-impurity solver however, the already mentioned fact that the CT-HYB solver is based on an expansion of the partition function Z in powers of the impurity-bath hybridization V gives this approach an essential character of a sheer insensitivity to high magnitudes of the on-site interaction U. Therefore the CT-HYB algorithm is very well suited to simulate and solve impurity models inside the local-moment regime that usually is reached for rather high interactions (c.f. section 3.1, page 24 ff.). As our studies which are presented in chapters 6 and 7 purely concentrate on models that strictly imply only interactions of density-density character it was no question to choose the CT-HYB segment code variant as impurity solver inside our framework of sdDMFT for our concerns. In the following section we will concentrate on the mentioned hybridization expansion that forms the methodical base of the continuous-time hybridization expansion approach.

5.2. The hybridization expansion

As repeatedly stated, the fundamental basement of the CT-HYB approach is a clever expansion of the partition function of the impurity model to be solved. For the purpose of deriving this expansion in more detail, it is best to represent the partition function as a *fermionic functional integral*. In this context, a formal refresher on this topic is provided in appendix A.3 on page 124 and the following.

By choosing this formal way, generally the full derivation of the CT-HYB-typical hybridization expansion would begin with the full grand canonical partition function $\mathcal{Z}_{\mathrm{AIM}}$ of the Anderson impurity model (AIM) (c.f. section 2.3, page 13 ff.) in terms of eq. (A.21). Thereby, inside the corresponding action as generally defined by eq. (A.24), of course one would use the imaginary-time dependent version of the Hamiltonian H_{AIM} (2.18) that additionally was quantum-statistically shifted into the grand canonical ensemble by applying the substitution (3.10).

However, by using the CT-HYB approach as impurity solver in terms of the framework of DMFT,

we will take a context-compatible shortcut. From the DMFT—per construction—one is confronted with an effective impurity model to solve, whose action reads

$$\mathcal{S} = -\int_0^\beta \mathrm{d}\tau \int_0^\beta \mathrm{d}\tau' \sum_\sigma \bar{f}_\sigma(\tau)\, \mathcal{G}_0^{-1}(\tau-\tau')\, f_\sigma(\tau') + \frac{U}{2}\int_0^\beta \mathrm{d}\tau \sum_\sigma \bar{f}_\sigma(\tau) f_\sigma(\tau) \bar{f}_{-\sigma}(\tau) f_{-\sigma}(\tau)\,, \tag{5.10}$$

with the non-interacting imaginary-time dependent f-electron Green's function [Ass14]

$$\mathcal{G}_{0\sigma}^{-1}(\tau-\tau') = -\delta(\tau-\tau')\left[\frac{\partial}{\partial\tau} + \varepsilon_f\right] + \Delta_\sigma(\tau-\tau') \tag{5.11}$$

which in the context of the dynamical mean-field approach is the Fourier transform of the effective bare propagator $\mathcal{G}_{0\sigma}(\mathrm{i}\omega_n)$ (4.19) and therefore consequently $\Delta_\sigma(\tau-\tau')$ is the imaginary-time dependent Fourier transform of the Matsubara hybridization function $\Delta_\sigma(\mathrm{i}\omega_n)$ (4.20) of the fictitious electronic bath (c.f. section 4.2 on page 40 ff.). In this representation of $\mathcal{S}$ all bath degrees of freedom that initially were contained in the mixed hybridization part have been already integrated out by means of *Grassmann Gaussian integration* yielding a separate part $\mathcal{Z}_{\mathrm{host}}$ of the total partition function $\mathcal{Z}_{\mathrm{AIM}}$ which is of no further interest in regard to our concerns. Consequently, the action $\mathcal{S}$ (5.10) does not contain c-fields anymore but is left with the τ-dependent conjugated Grassmann numbers $\bar{f}_\sigma(\tau)$ and $f_\sigma(\tau)$ that eventually represent the impurity electrons.

From here, an appropriate reformulation of $\mathcal{S}$ (A.24) in the knowledge of eq. (5.11) leads to

$$\begin{aligned}
\mathcal{S} &= \int_0^\beta \mathrm{d}\tau \int_0^\beta \mathrm{d}\tau' \sum_\sigma \bar{f}_\sigma(\tau)\, \delta(\tau-\tau')\left[\frac{\partial}{\partial\tau} + \varepsilon_f\right] f_\sigma(\tau') \\
&\quad + \frac{U}{2}\int_0^\beta \mathrm{d}\tau \sum_\sigma \bar{f}_\sigma(\tau) f_\sigma(\tau) \bar{f}_{-\sigma}(\tau) f_{-\sigma}(\tau) \\
&\quad + \int_0^\beta \mathrm{d}\tau \int_0^\beta \mathrm{d}\tau' \sum_\sigma \bar{f}_\sigma(\tau)\, \Delta_\sigma(\tau-\tau')\, f_\sigma(\tau') \\
&= \mathcal{S}_{\mathrm{imp}} + \int_0^\beta \mathrm{d}\tau \int_0^\beta \mathrm{d}\tau' \sum_\sigma \bar{f}_\sigma(\tau)\, \Delta_\sigma(\tau-\tau')\, f_\sigma(\tau') \\
&= \mathcal{S}_{\mathrm{imp}} + \mathcal{S}_{\mathrm{hyb}}\,.
\end{aligned}$$

We use this to appropriately write out the partition function:

$$\begin{aligned}
\mathcal{Z}_{\mathrm{AIM}} &= \mathcal{Z}_{\mathrm{host}} \cdot \int \mathrm{D}[\bar{f}(\tau), f(\tau')]\, \mathrm{e}^{-\mathcal{S}_{\mathrm{imp}} - \mathcal{S}_{\mathrm{hyb}}} \\
&= \mathcal{Z}_{\mathrm{host}} \cdot \int \mathrm{D}[\bar{f}(\tau), f(\tau')]\, \mathrm{e}^{-\mathcal{S}_{\mathrm{imp}}[\bar{f}(\tau), f(\tau')]} \cdot\ \mathrm{e}^{-\mathcal{S}_{\mathrm{hyb}}}\,.
\end{aligned} \tag{5.12}$$

Now, factually the actual hybridization expansion happens in terms of a Taylor expansion of $\mathrm{e}^{-\mathcal{S}_{\mathrm{hyb}}}$. Particularly for actions whose hybridization parts are diagonal in regard to the spin flavor

σ, like it is the case here, one may not only perform one Taylor expansion of the whole construct but is allowed to carry out one expansion *per* spin channel as follows:[3]

$$\begin{aligned}
\mathrm{e}^{-\mathcal{S}_{\mathrm{hyb}}} &= \exp\left[-\sum_{\sigma}\int_0^\beta \mathrm{d}\tau \int_0^\beta \mathrm{d}\tau' \; \bar{f}_\sigma(\tau)\Delta_\sigma(\tau,\tau')f_\sigma(\tau')\right] \\
&= \prod_{\sigma}\exp\left[-\int_0^\beta \mathrm{d}\tau\,\mathrm{d}\tau' \; \bar{f}_\sigma(\tau)\Delta_\sigma(\tau,\tau')f_\sigma(\tau')\right] \\
&= \prod_{\sigma}\sum_{k_\sigma=0}^{\infty}\frac{(-1)^{k_\sigma}}{k_\sigma!}\left[\int_0^\beta \mathrm{d}\tau \int_0^\beta \mathrm{d}\tau' \; \bar{f}_\sigma(\tau)\Delta_\sigma(\tau,\tau')f_\sigma(\tau')\right]^{k_\sigma} \\
&= \prod_{\sigma}\sum_{k_\sigma=0}^{\infty}\frac{(-1)^{k_\sigma}}{k_\sigma!}\int_0^\beta \mathrm{d}\tau_{1_\sigma}\cdots\mathrm{d}\tau_{k_\sigma}\int_0^\beta \mathrm{d}\tau'_{1_\sigma}\cdots\mathrm{d}\tau'_{k_\sigma}\; \bar{f}_\sigma(\tau_{1_\sigma})f_\sigma(\tau'_{1_\sigma})\cdots \\
&\qquad \cdots \bar{f}_\sigma(\tau_{k_\sigma})f_\sigma(\tau'_{k_\sigma})\,\Delta_\sigma(\tau_{1_\sigma},\tau'_{1_\sigma})\cdots\Delta_\sigma(\tau_{k_\sigma},\tau'_{k_\sigma})\,.
\end{aligned}$$

Here, one may want to exploit the fact that the conjugated Grassmann variables $\bar{f}_\sigma$ and f_σ of the same spin index σ behave like anti-commuting numbers [Cah13] and thus

$$\bar{f}_\sigma(\tau)f_\sigma(\tau')\Delta_\sigma(\tau-\tau') = -f_\sigma(\tau')\bar{f}_\sigma(\tau)\Delta_\sigma(\tau-\tau')$$

holds. Therefore, for every expansion order per spin channel k_σ, commuting all k_σ pairs of conjugated Grassmann variables that belong together yields a sign for the case of odd k_σ and thus kills the alternating global sign of the Taylor expansion, resulting in

$$\begin{aligned}
\mathrm{e}^{-\mathcal{S}_{\mathrm{hyb}}} = \prod_{\sigma}\sum_{k_\sigma=0}^{\infty}\frac{1}{k_\sigma!}\int_0^\beta \mathrm{d}\tau_{1_\sigma}\cdots\mathrm{d}\tau_{k_\sigma}\int_0^\beta \mathrm{d}\tau'_{1_\sigma}\cdots\mathrm{d}\tau'_{k_\sigma}\; f_\sigma(\tau'_{1_\sigma})\bar{f}_\sigma(\tau_{1_\sigma})\cdots \\
\cdots f_\sigma(\tau'_{k_\sigma})\bar{f}_\sigma(\tau_{k_\sigma})\,\Delta_\sigma(\tau_{1_\sigma},\tau'_{1_\sigma})\cdots\Delta_\sigma(\tau_{k_\sigma},\tau'_{k_\sigma})\,.
\end{aligned}$$

The big trick in the further proceeding which prevents a possible sign problem in the later MC sampling of $\mathcal{Z}_{\mathrm{AIM}}$ lies in the collection of all possible $\Delta_\sigma(\tau,\tau')$ into a determinant per spin channel. This was the main statement and progress of Werner et al. in [Wer+06]. This may appropriately be achieved by the insertion of a factor $k_\sigma!/k_\sigma! = 1$ and the subsequent interpretation of the nominator as $k_\sigma!$ different possible permutations P out of the group of permutations of k_σ elements S_{k_σ} in regard to imaginary times τ' as arguments of the Grassmann numbers f_σ. Thus

$$\begin{aligned}
\mathrm{e}^{-\mathcal{S}_{\mathrm{hyb}}} &= \prod_{\sigma}\sum_{k_\sigma=0}^{\infty}\frac{1}{k_\sigma!}\frac{k_\sigma!}{k_\sigma!}\int_0^\beta \mathrm{d}\tau_{1_\sigma}\cdots\mathrm{d}\tau_{k_\sigma}\int_0^\beta \mathrm{d}\tau'_{1_\sigma}\cdots\mathrm{d}\tau'_{k_\sigma}\; f_\sigma(\tau'_{1_\sigma})\bar{f}_\sigma(\tau_{1_\sigma})\cdots \\
&\qquad \cdots f_\sigma(\tau'_{k_\sigma})\bar{f}_\sigma(\tau_{k_\sigma})\,\Delta_\sigma(\tau_{1_\sigma},\tau'_{1_\sigma})\cdots\Delta_\sigma(\tau_{k_\sigma},\tau'_{k_\sigma}) \\
&= \prod_{\sigma}\sum_{k_\sigma=0}^{\infty}\frac{1}{k_\sigma!}\frac{1}{k_\sigma!}\sum_{P\in\mathsf{S}_{k_\sigma}}(-1)^P\int_0^\beta \mathrm{d}\tau_{1_\sigma}\cdots\mathrm{d}\tau_{k_\sigma}\int_0^\beta \mathrm{d}\tau'_{1_\sigma}\cdots\mathrm{d}\tau'_{k_\sigma}\; f_\sigma(\tau'_{P(1_\sigma)})\bar{f}_\sigma(\tau_{1_\sigma})\cdots \\
&\qquad \cdots f_\sigma(\tau'_{P(k_\sigma)})\bar{f}_\sigma(\tau_{k_\sigma})\,\Delta_\sigma(\tau_{1_\sigma},\tau'_{1_\sigma})\cdots\Delta_\sigma(\tau_{k_\sigma},\tau'_{k_\sigma})\,,
\end{aligned}$$

[3] For a general derivation that includes the non-spin-diagonal case, have a look at [Ass14].

where additionally a factor $(-1)^P$ was spent in order to correctly pay respect to the anti-commuting property of the Grassmann algebra. To formally get back the original order of those $\{\tau_{P(i)} : i = 1_\sigma, \dots, k_\sigma\}$ one simply renames the relevant indices in such a way that one returns to the initial indication. This in turn affects the indices of the integration measures and the hybridization functions. Consequently, one obtains

$$\mathrm{e}^{-\mathcal{S}_{\mathrm{hyb}}} = \prod_\sigma \sum_{k_\sigma=0}^{\infty} \frac{1}{k_\sigma!}\frac{1}{k_\sigma!} \sum_{P\in \mathsf{S}_{k_\sigma}} (-1)^P \int_0^\beta \mathrm{d}\tau_{1_\sigma} \cdots \mathrm{d}\tau_{k_\sigma} \int_0^\beta \mathrm{d}\tau'_{P(1_\sigma)} \cdots \mathrm{d}\tau'_{P(k_\sigma)}\; f_\sigma(\tau'_{1_\sigma})\bar{f}_\sigma(\tau_{1_\sigma}) \cdots \\ \cdots f_\sigma(\tau'_{k_\sigma})\bar{f}_\sigma(\tau_{k_\sigma})\, \Delta_\sigma(\tau_{1_\sigma}, \tau'_{P(1_\sigma)}) \cdots \Delta_\sigma(\tau_{k_\sigma}, \tau'_{P(k_\sigma)}) \,.$$

As the integration variables are allowed to be reordered again without consequences, the permutation-induced sign only concerns the τ'-arguments of the hybridization functions and thus may be shuffled into the integral what yields

$$\mathrm{e}^{-\mathcal{S}_{\mathrm{hyb}}} = \prod_\sigma \sum_{k_\sigma=0}^{\infty} \frac{1}{k_\sigma!}\frac{1}{k_\sigma!} \int_0^\beta \mathrm{d}\tau_{1_\sigma} \cdots \mathrm{d}\tau_{k_\sigma} \int_0^\beta \mathrm{d}\tau'_{1_\sigma} \cdots \mathrm{d}\tau'_{k_\sigma}\; f_\sigma(\tau'_{1_\sigma})\bar{f}_\sigma(\tau_{1_\sigma}) \cdots \\ \cdots f_\sigma(\tau'_{k_\sigma})\bar{f}_\sigma(\tau_{k_\sigma}) \sum_{P\in \mathsf{S}_{k_\sigma}} (-1)^P \Delta_\sigma(\tau_{1_\sigma}, \tau'_{P(1_\sigma)}) \cdots \Delta_\sigma(\tau_{k_\sigma}, \tau'_{P(k_\sigma)}) \,.$$

According to the explicit representation of determinants, which in literature is also known as the Leibniz formula[4], one is allowed to further write

$$\sum_{P\in \mathsf{S}_{k_\sigma}} (-1)^P \Delta_\sigma(\tau_{1_\sigma}, \tau'_{P(1_\sigma)}) \cdots \Delta_\sigma(\tau_{k_\sigma}, \tau'_{P(k_\sigma)}) = \det \begin{vmatrix} \Delta_{\sigma\tau_{1_\sigma}\tau'_{1_\sigma}} & \dots & \Delta_{\sigma\tau_{1_\sigma}\tau'_{k_\sigma}} \\ \vdots & \ddots & \vdots \\ \Delta_{\sigma\tau_{k_\sigma}\tau'_{1_\sigma}} & \dots & \Delta_{\sigma\tau_{k_\sigma}\tau'_{k_\sigma}} \end{vmatrix} =: \det \mathbf{\Delta}_\sigma \,. \tag{5.13}$$

Thus, after the performed expansion, the initial partition function by means of eq. (5.12) now reads:

$$\mathcal{Z}_{\mathrm{AIM}} = \mathcal{Z}_{\mathrm{host}} \cdot \int \mathrm{D}[\bar{f}(\tau), f(\tau')]\, \mathrm{e}^{-\mathcal{S}_{\mathrm{hyb}}} \prod_\sigma \sum_{k_\sigma=0}^{\infty} \frac{1}{k_\sigma!}\frac{1}{k_\sigma!} \int_0^\beta \mathrm{d}\tau_{1_\sigma} \cdots \mathrm{d}\tau_{k_\sigma} \\ \times \int_0^\beta \mathrm{d}\tau'_{1_\sigma} \cdots \mathrm{d}\tau'_{k_\sigma}\; f_\sigma(\tau'_{1_\sigma})\bar{f}_\sigma(\tau_{1_\sigma}) \cdots f_\sigma(\tau'_{k_\sigma})\bar{f}_\sigma(\tau_{k_\sigma})\, \det \mathbf{\Delta}_\sigma \,. \tag{5.14}$$

While in principle one is done with the tricky hybridization expansion of $\mathcal{Z}_{\mathrm{AIM}}$ by means of eq. (5.14) at this point, for further application it is necessary to escape from the pure abstract Grassmann representation into the numerically reasonably treatable notation in terms of modified Heisenberg operators (c.f. appendix A.2, page 122 ff. and appendix A.3, page 124 ff.). An attempt elegantly attainable by identifying a thermal impurity average in the style of eq. (A.25) written on page 125 collecting all Grassmann numbers $\bar{f}, f$ still contained in $\mathcal{Z}_{\mathrm{AIM}}$ (5.14). Prac-

[4] For a complete derivation see e.g. [Jän08] or [LM15].

tically doing so effectively yields

$$\frac{\mathcal{Z}_{\mathrm{AIM}}}{\mathcal{Z}_{\mathrm{imp}}} = \mathcal{Z}_{\mathrm{host}} \cdot \prod_{\sigma} \sum_{k_\sigma=0}^{\infty} \frac{1}{k_\sigma!} \frac{1}{k_\sigma!} \int_0^\beta \mathrm{d}\tau_{1_\sigma} \cdots \mathrm{d}\tau_{k_\sigma} \\ \times \int_0^\beta \mathrm{d}\tau'_{1_\sigma} \cdots \mathrm{d}\tau'_{k_\sigma} \left\langle f_\sigma(\tau'_{1_\sigma}) \bar{f}_\sigma(\tau_{1_\sigma}) \cdots f_\sigma(\tau'_{k_\sigma}) \bar{f}_\sigma(\tau_{k_\sigma}) \right\rangle_{\mathrm{imp}} \det \mathbf{\Delta}_\sigma \,. \tag{5.15}$$

Due to relation (A.27) the just introduced impurity average over Grassmann numbers $f, \bar{f}$ in the fashion of eq. (A.26) may be replaced by an equivalent formulation in terms of a time-ordered trace over corresponding fermionic Heisenberg operators $f, f^\dagger$. By doing so, eq. (5.15) simply mutates to

$$\frac{\mathcal{Z}_{\mathrm{AIM}}}{\mathcal{Z}_{\mathrm{imp}}} = \mathcal{Z}_{\mathrm{host}} \cdot \prod_{\sigma} \sum_{k_\sigma=0}^{\infty} \int_0^\beta \mathrm{d}\tau_{1_\sigma} \cdots \int_0^{\tau_{k_\sigma-1}} \mathrm{d}\tau_{k_\sigma} \int_0^\beta \mathrm{d}\tau'_{1_\sigma} \cdots \int_0^{\tau'_{k_\sigma-1}} \mathrm{d}\tau'_{k_\sigma} \\ \times \left\langle f_\sigma(\tau'_{1_\sigma}) f^\dagger_\sigma(\tau_{1_\sigma}) \cdots f_\sigma(\tau'_{k_\sigma}) f^\dagger_\sigma(\tau_{k_\sigma}) \right\rangle_{\mathrm{imp}} \det \mathbf{\Delta}_\sigma \,, \tag{5.16}$$

where, as a matter of taste, the factors $1/(k_\sigma!) \cdot 1/(k_\sigma!)$ were absorbed into an explicit time ordering of corresponding annihilation and creation operators per spin-channel σ by manipulation of the integration limits of the associated imaginary times in an appropriate manner [BF04].

By that, the expanded representation of the partition function given by eq. (5.16) finally poses the base of the CT-HYB sampling that will be discussed in the following section and especially in section 5.4, page 65 ff. with regard to the segment picture.

5.3. General sampling procedure

In section 5.1.1 it was already mentioned that CT-QMC solvers and therefore also the CT-HYB algorithm internally rely on a sampling of the expanded partition function which technically is realized in terms of Markov chain Monte Carlo (MCMC). The pure functioning and especially the efficiency of such a stochastic approach is heavily associated with its special internal sampling procedure. Before diving into the sampling procedure that was tailored for the segment variant of the CT-HYB approach we will give some general remarks on MCMC sampling and the correct error analysis of correlated data.

5.3.1. Markov chain Monte Carlo

In general, like all Monte Carlo sampling methods, also the more special Markov chain Monte Carlo approach is for sampling M configurations $\{c_i\}$ according to a given $P(c)$ with the objective of efficiently providing MC estimates. For simplicity regardless of any negative sign problems,

by recapitulating eq. (5.5) on page 51, we remember those estimates as

$$\langle A\rangle_p \approx \langle A\rangle_{\mathrm{MC},p} = \frac{1}{M}\sum_{i=1}^{M} A(c_i)\,.$$

The underlying sampling according to $P(c)$ usually is technically realized by a sampling technique called *importance sampling* that relies on a finite discrete-time *Markov chain* [KS83; Häg02], hence on a special *Markov process* without memory that, again for simplicity, lives in a finite configuration space and evolves discretely in the internal process time t_{MC}. Generally, a Markov chain creates a sequence of random variables $C(\Omega, P_{t_{\mathrm{MC}}})$ whose outcomes are influenced by a time-dependent weight function $P_{t_{\mathrm{MC}}}(c)$. Therefore, in order to realize a qualitatively good sample it is crucial to manage that for large times $t_{\mathrm{MC}} \to \infty$ the time-dependent weight converges to the given one, hence

$$\lim_{t_{\mathrm{MC}}\to\infty} P_{t_{\mathrm{MC}}}(c) = P(c)\,. \tag{5.17}$$

Then, in this limit one expects the Markov chain to produce a sequence of configurations $\{c_i : i = 1,\dots,M\}$, in the terminology of Markov processes also called *states* of a *state space* Ω, that arise with a frequency according to $P(c)$. Thus, starting at an arbitrary state $c_{t_{\mathrm{MC}}=0}$ at time $t_{\mathrm{MC}} = 0$, characteristically the Markov chain evolves stepwise in terms of *updates* without memory, wherefore the conditional probability of arriving at state c_{m+1} at time $t_{\mathrm{MC}} = m+1$ given the state c_m at time $t_{\mathrm{MC}} = m$ arises as

$$P(c_{m+1}|c_m) = T_{c_{m+1},c_m}\,. \tag{5.18}$$

Here, T_{c_{m+1},c_m} is the element of a *transition matrix* $\mathbf{T}$ that generally contains all transition probabilities from one *state* of the Markov chain to another. This matrix rules the time evolution of $P_{t_{\mathrm{MC}}}(c)$ in the following way:

$$\mathbf{P}_t = \mathbf{T}\mathbf{P}_{t-1}\,, \tag{5.19}$$

where $\mathbf{P}_t$ is a probability vector formed out of all probabilities $\{P_t(c_i)\}$ of all discrete configurations $\{c_i \in \Omega\}$ at process time $t_{\mathrm{MC}} = t$. According to [TO15], within this notation, the limit (5.17) reads

$$\lim_{t_{\mathrm{MC}}\to\infty} \mathbf{P}_{\mathbf{t}_{\mathrm{MC}}} = \mathbf{P}\,, \tag{5.20}$$

where $\mathbf{P}$ has to be the *stationary solution* that obeys the equation

$$\mathbf{T}\mathbf{P} = \mathbf{P}\,. \tag{5.21}$$

It is known from the theory of Markov chains, as e.g. discussed in [Nor98; Häg02; GS97; Mey01], that, independently of the initial configuration, a corresponding process converges exponentially fast to a *unique* stationary solution in terms of the process time if the transition matrix $\mathbf{T}$ is *stochastic*, that is

$$\forall i,j \in \Omega : T_{ij} \geq 0\,, \quad \forall j \in \Omega : \sum_i T_{ij} = 1\,, \tag{5.22}$$

and *regular*, hence

$$\exists l\, \forall i,j \in \Omega : [\mathbf{T}^l]_{ij} > 0\,. \tag{5.23}$$

This follows as a direct result of the then estimable sets of eigenvectors and -values of $\mathbf{T}$ which mathematically is ensured by the statements of the *Perron-Frobenius theorem* [Geo11; Gan99;

Mey01] on matrices that fulfill the characteristics required above by eq. (5.22) and eq. (5.23). Furthermore a stationary solution $\mathbf{P}$ as in the limit (5.20) sufficiently exists in terms of an asymptotic average over time of state probabilities as

$$\mathbf{P} = \lim_{M\to\infty} \frac{1}{M} \sum_{n=1}^{M} \mathbf{T}^n \,, \tag{5.24}$$

if the condition of regularity (5.23) is weakened to the demand of an *ergodic* transition matrix $\mathbf{T}$ which in concrete terms means

$$\forall i, j \in \Omega \, \exists l \, : \, [\mathbf{T}^l]_{ij} > 0 \,. \tag{5.25}$$

It is fruitful to note here that the stationarity condition (5.21) in regard of two arbitrary states $i, j \in \Omega$ may be written component-by-component as

$$\sum_i T_{ji} P(c_i) = P(c_j) \,. \tag{5.26}$$

This condition is always fulfilled in the case of *detailed balance* also known as *reversibility*. Here, it is

$$T_{ji}\, P(c_i) = T_{ij}\, P(c_j) \quad \Longleftrightarrow \quad T_{ji} \frac{p(c_i)}{Z} = T_{ij} \frac{p(c_j)}{Z} \,, \tag{5.27}$$

whereby eq. (5.26) directly is obtained by summing both sides of the left-hand side of eq. (5.27) over i in compliance with the statements made inside eq. (5.22). Spectacularly eq. (5.27) also holds for probabilities $p(c_i)$, $p(c_j)$ that are not normed explicitly, as Z may be dropped out of the right equation.

5.3.2. Metropolis sampling and algorithm

In directly reconnecting to the preceding section it still is up to the MC process to simulate a Markov chain whose stationary solution, hence distribution effectively coincides with that of the target distribution in eq. (5.1) by an appropriate construction of the process-underlying transition matrix $\mathbf{T}$. This construction is the real art when applying MCMC approaches. Principally, there are many ways to do so, a generic functional derivation of the problem is worked out in [Ass14]. We will follow a well-known way by implementing the so-called *Metropolis sampling*.

Here, the transition matrix is defined by

$$T_{ij} = \begin{cases} q_{ij} a_{ij}, & \text{if } i \neq j \,, \\ 1 - \sum_{k\neq j} q_{kj} a_{kj}, & \text{if } i = j \,, \end{cases} \tag{5.28}$$

where q marks a proposal probability and a stands for an acceptance probability of a move, i.e. update in the Markov chain [RK07]. While a transition matrix $\mathbf{T}$ resulting out of eq. (5.28) obviously is stochastic according to eq. (5.22), its ergodic character depends on suitable update schemes and

resultant proposal probabilities. To additionally guarantee stationarity one adapts the detailed balance condition (5.27) according to eq. (5.28) what in focussing on the case $i \neq j$ yields[5]

$$q_{ji}\, a_{ji}\, P(c_i) = q_{ij}\, a_{ij}\, P(c_j) \quad \Longleftrightarrow \quad q_{ji}\, a_{ji}\, \frac{p(c_i)}{Z} = q_{ij}\, a_{ij}\, \frac{p(c_j)}{Z}\,. \tag{5.29}$$

By that, one of many possibilities in order to construct a suitable transition matrix is to achieve the acceptance probabilities via

$$a_{ji} = \min\left[1, \frac{q_{ij} P(c_j)}{q_{ji} P(c_i)}\right], \quad i \neq j\,. \tag{5.30}$$

This choice then finally leads to the famous *Metropolis Hastings algorithm* [Met+53; Has70] as visualized by means of fig. 5.1 and to be explained in the following:

A random number r out of the interval $[0, 1]$ is compared to the acceptance probability of a Markov step a_{ji} (5.30).

For performing our CT-HYB simulations, we used `Fortran` implementations of two different pseudo random number generators: The one published by Marsaglia and Zaman in [MZ91] and that proposed by Matsumoto and Nishimura in [MN98] also known as the *Mersenne Twister*.

If $r < a_{ji}$ the corresponding transition from configuration $c_{t_{\mathrm{MC}}=n} = c_i$ to $c_{t_{\mathrm{MC}}=n+1} = c_j$ is accepted and the Markov chain moves on to the proposed, i.e. new configuration. Else the transition is rejected and the new configuration in regard to the MC time t_{MC} is identical to the former one, namely $c_{t_{\mathrm{MC}}=n} = c_{t_{\mathrm{MC}}=n+1} = c_i$. Once processes of this algorithm have converged to the given distribution of $P(c)$ of c after a so-called *thermalization time period*, an ongoing generation of valid and correctly distributed configurations $c \in \Omega$ with progressing process time t_{MC} is established. In this context, in regard to common implementation schemes, it makes sense to note that MCMC approaches excellently allow for *parallel computing*.

In our codes, we used an *open source* variant of the well-known Message Passing Interface (MPI) for that purpose. Further information may be found in e.g. [GLS14; Gro+14; Ben+15] and references therein.

Here, instead of simulating one long Markov chain, one runs more shorter MCMC processes. Of course, the parallel Markov chains may not become shorter than the above mentioned thermalization period of the process in order to get converged, reliable MC estimates. In such a parallel implementation, the otherwise independently processed single MCMC runs only meet for collecting, averaging over and equally re-distributing the respectively sampled measurements (see section 5.5 on page 71 below) by an algorithmically predetermined master process. In this scenario it is important to initialize the several parallel MCMC simulations with advantageously chosen *seeds* i.e. natural numbers that indicate the starting points or vectors of the used random

[5] For simplicity we only consider cases where the old configuration differs from the proposed one as later, in the CT-HYB algorithm only this case will be sampled anyway.

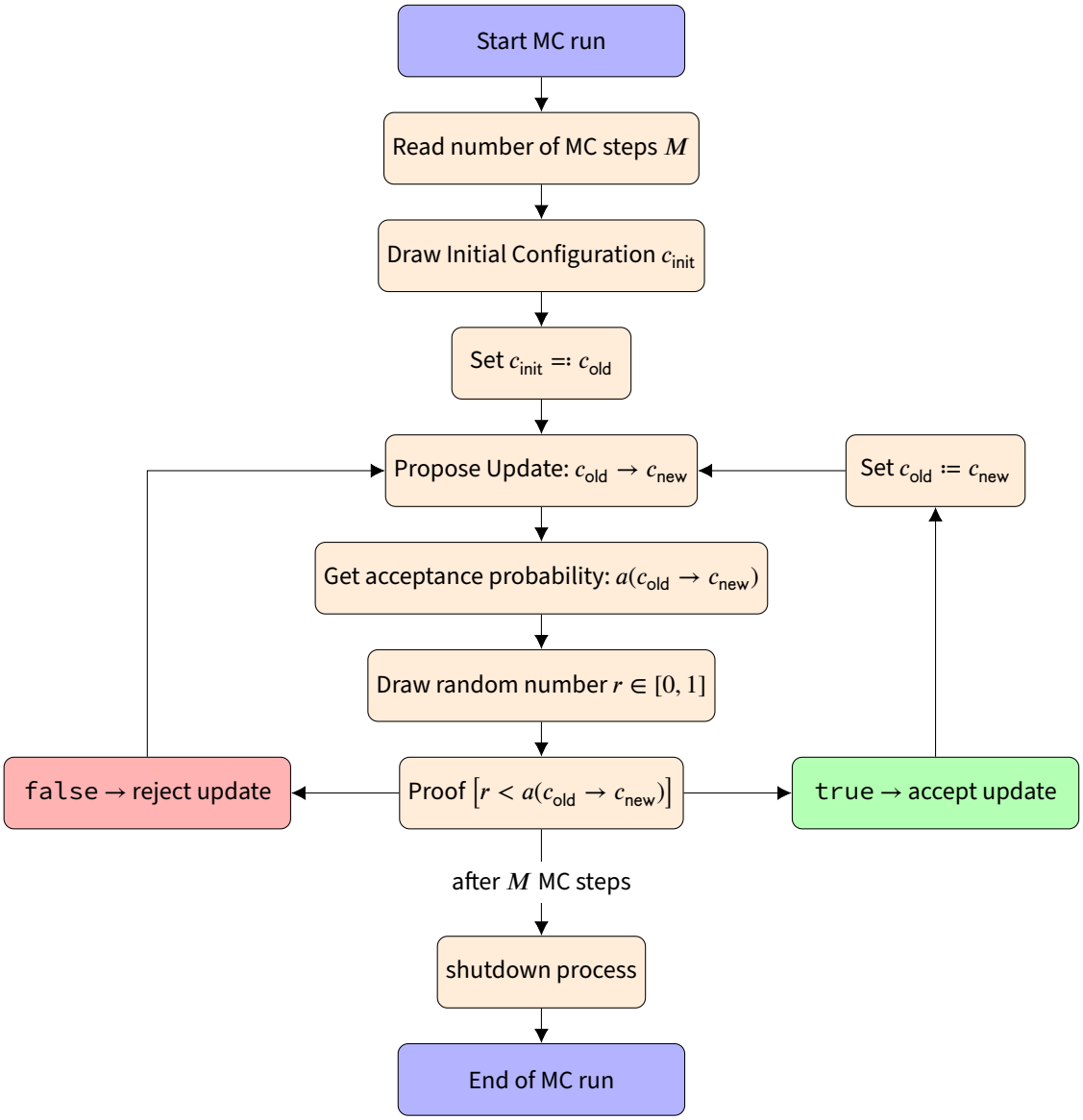

Figure 5.1.: Flowchart of a simple Markov chain Monte Carlo process which is based on the Metropolis-Hastings algorithm as explained in section 5.3.2.

number generator. Parallelization empowers MCMC implementations to run on supercomputers and drastically reduces the risk of getting the Markov chain trapped in one of many local maxima of $P(c)$. Disregard of the latter aspect bares the possibility of problematic systematical errors in regard to the production of reliable MC estimates.

5.3.3. Advanced error analysis of correlated data

In section 5.1, page 51 ff., the variance of a MC simulation could be derived by the central limit theorem, thus implicitly stating an infinite number of statistically independent, i.e. uncorrelated sampled configurations. However, one practically never will be able to sample an infinite amount of configurations, but instead one may gain acceptable results by just sampling a sufficiently large number of configurations M (see below). Furthermore, especially when applying the MCMC method as described in the preceding section, the configurations that are sequentially sampled in form of a Markov chain definitively show a strong pairwise correlation just because the probability of drawing configuration c_{n+1} at time $t_{\mathrm{MC}} = n + 1$ per definition of the Markovian process arises as the conditional probability of having sampled configuration c_n at time $t_{\mathrm{MC}} = n$ (c.f. eq. (5.18) on page 59). This might lead to an understatement of the error, hence the derived error appears smaller than the "real" one what lets the MCMC estimate occur as of higher accurateness as it is. This in turn is a dangerous trap and not reconcilable with correct and careful scientific work. Therefore, in addition to the cherry-pick of the right estimate of the sample-variance in terms of the Jackknife analysis as described in section 5.1, one has to apply further methodical steps to get the entire estimated error reliable again.

Actually the degree of correlation between two configurations out of the sample is indicated through the so-called *autocorrelation*, yet in terms of the process time through the corresponding *autocorrelation time* t_{AC}. Indeed there exist formulas to derive the autocorrelation [Jan02; Ass14] but doing this constantly during a MCMC run is practically neither comfortable nor beneficial in regard to the performance of the running process.

An easily implementable scheme in order to weaken correlation effects among configurations is to average not over every individually sampled configuration but only over each *sweep*, that is every q-th [Bac11]. This however neither shows whether the step width of measurements q still meets the autocorrelation time t_{AC}, nor whether enough data has been sampled or not in order to be able to perform a reliable error analysis. A much better approach, even combinable to the one just mentioned, constitutes the so-called *rebinning analysis*. Here, to follow up the text passage on average and corresponding variance estimation on page 51 of section 5.1, even before performing the jackknife analysis on the given but this time considered as correlated dataset $\{A(c_i) : i \in 1, \dots, M\}$ of M elements is rearranged into continuous, non-overlapping blocks of data, also called *bins*, each of them containing k elements, where clearly $k \in \{1, \dots, M\}$. Therefore it is $M = kM_{\mathrm{B}}$, while k is referred to as *bin size*. By that, one is able to take the M_{B} blocks as initial position for a jackknife analysis as described in 5.1.1 on page 50 ff. [Jan02; You12].

Hence, the formula for a reliable estimate of the MC error up to now given by eq. (5.8) under this circumstances transforms to a somehow final version that is—again already equipped with

corrected pre-factors—given by

$$\sigma_{\langle A\rangle} = \frac{\sigma_A}{\sqrt{M}} \approx \frac{\sigma_{\mathrm{JB},A}}{\sqrt{M_\mathrm{B}}} = \sqrt{\frac{M_\mathrm{B}-1}{M_\mathrm{B}} \sum_{n=1}^{M_\mathrm{B}} \left(A_{\mathrm{JB},n} - \sum_{n=1}^{M_\mathrm{B}} \frac{1}{M_\mathrm{B}} A_{\mathrm{JB},n} \right)^2}\,, \tag{5.31}$$

with the n-th jackknife block average

$$A_{\mathrm{JB},n} = \frac{\sum_i^M A_i - k A_{\mathrm{B},n}}{M-k}\,, \quad n \in \{1,\ldots,M_\mathrm{B}\}\,, \tag{5.32}$$

that now implies bin block averages in the fashion of the average of the n-th bin block given by

$$A_{\mathrm{B},n} \equiv \frac{1}{k} \sum_{i=1}^{k} A_{(n-1)k+i}\,, \quad n \in \{1,\ldots,M_\mathrm{B}\}\,. \tag{5.33}$$

Throughout eqs. (5.31) to (5.33) we have used once more abbreviations in general terms of $A(c_X) = A_X$.

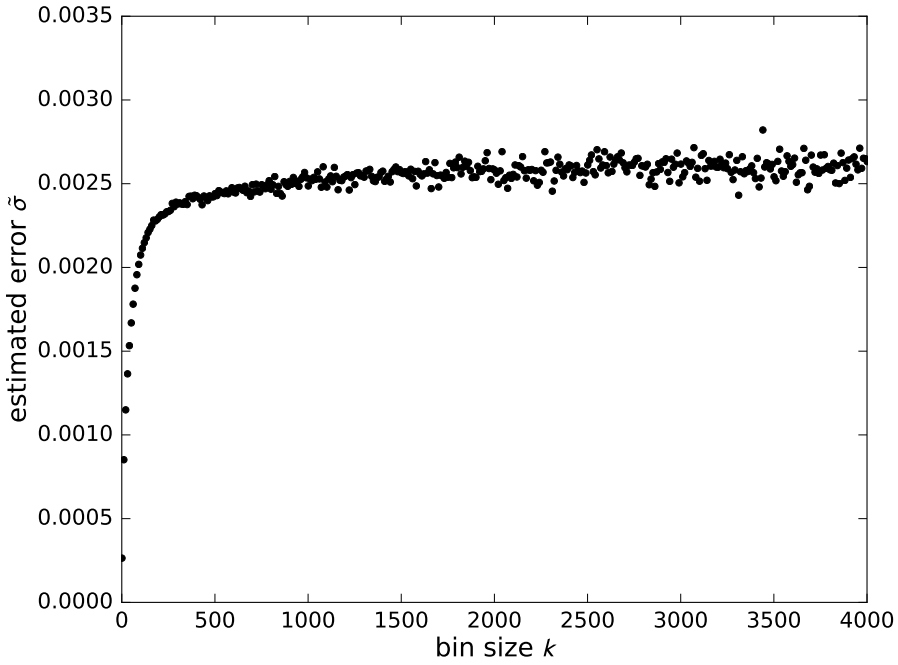

Figure 5.2.: Typical result of an error analysis by *rebinning* (c.f. figure 6 of [Jan02]). For too small block lengths i.e. bin sizes k the error $\tilde{\sigma}$ misleadingly is estimated too small. As the block length k is increased $\tilde{\sigma}$ converges to its true and confidential value. If no convergence could be reached, the underlying sample i.e. data set does not contain enough data [Jan02].

The essence of performing a rebinning analysis now lies in the variation of the bin size k. By continuously scanning through increasing values k one may plot the error estimate $\sigma_{\langle A\rangle}$ in dependence of k. Now, as it is shown in fig. 5.2, if the number of sampled configurations M taken

into account was large enough, the error should converge to its true value. Otherwise, for given data sets of poor usable content, the error estimate would show a divergent trend. Assuming enough useable data, once having found a M_B with corresponding k for which the error is converged one is left with an uncorrelated data set of M_B bin averages $\{A_{\mathrm{B},n} : n = 1, \dots, M_\mathrm{B}\}$ in terms of eq. (5.33).

One should note here that none of the advanced error estimation and analysis schemes change the value of the total average. This means: Independently of averaging over jackknife or binning blocks or a combination of both of a given data set $\{A_n\}$, it is obvious that the resulting total average is of the identical value as the standard average given by eq. (5.5) on page 51. Furthermore, one should be aware that for generality as well as simplicity the negative sign problem and its impact on the formulation of MC estimates, hence averages were ignored here but of course have to be taken into account in a real implementation of a MC simulation of fermionic systems.

All MC estimates presented within this thesis were sensitively encountered in regard to possibly arising sign problems, while additionally all resulting errors were carefully determined in terms of eq. (5.31) and the underlying procedures of error analysis.

By that we close this section, thus the general part of this chapter to get into the CT-HYB sampling.

5.4. Sampling in segments—the segment picture

Having reviewed more general aspects of the Markov chain Monte Carlo sampling procedure in section 5.3 and the necessary advanced error estimation related thereto in section 5.3.3, we now will—in a manner which is tight to [Gul08; Wer11]—refocus on the CT-HYB. Concretely, this is on the very special internal sampling methodology of its segment approach which is applicable for solving single-impurity problems with local on-site correlations of density-density character. To be able to do so, we first need to remember the already expanded partition function that concluded section 5.2 on page 58 in form of eq. (5.16). This implies to stay further with the single-impurity single spin-degenerate orbital Anderson model for simplified but of course absolutely adequate demonstration purposes. In that sense, we write out the just mentioned expanded partition function in a slightly adapted notation: With regard to the products over all spin-channels σ and the impurity average written out as trace in the fashion of eq. (A.26) it reads:

$$\begin{aligned}\frac{\mathcal{Z}_\mathrm{AIM}}{\mathcal{Z}_\mathrm{imp}} = \mathcal{Z}_\mathrm{host} \cdot \sum_{k_\sigma=0}^{\infty} \int_0^\beta \prod_\sigma \mathrm{d}\tau_{1_\sigma} \cdots \int_0^{\tau_{k_\sigma-1}} \prod_\sigma \mathrm{d}\tau_{k_\sigma} \int_0^\beta \prod_\sigma \mathrm{d}\tau'_{1_\sigma} \cdots \int_0^{\tau'_{k_\sigma-1}} \prod_\sigma \mathrm{d}\tau'_{k_\sigma} \\ \times \mathrm{Tr}\left[\mathrm{e}^{-\beta\mathcal{H}_\mathrm{imp}} \cdot T_\tau \prod_\sigma f_\sigma(\tau'_{1_\sigma}) f^\dagger_\sigma(\tau_{1_\sigma}) \cdots f_\sigma(\tau'_{k_\sigma}) f^\dagger_\sigma(\tau_{k_\sigma}) \right] \prod_\sigma \det \mathbf{\Delta}_\sigma \,. \end{aligned} \tag{5.34}$$

Now, our goal is to sample this partition function by means of MCMC. Therefore, it is necessary to define an appropriate configuration space to be able to rewrite $\mathcal{Z}_\mathrm{AIM}$ as sum over implied configurations c according to their statistical weight $p(c)$, hence $\mathcal{Z}_\mathrm{AIM} = \sum_{k_\sigma} p(c_{k_\sigma})$, in accordance

to the right side of eq. (5.1) that was given on page 50. By that, the configurations may be visited according to their contribution to $\mathcal{Z}_{\mathrm{AIM}}$ by means of Metropolis sampling (c.f. section 5.3.2, page 60 ff.), provided that there exists a clear definition of both, the configurations c and their corresponding statistical weights $p(c)$. We will care about both in the following.

5.4.1. Configuration space and statistical weights

In the context above, it is the fact that the models we want to study only imply density-density interactions which gives birth to the *segment picture*: As those models particularly with the evolution of time do not mix spin-channels inside the hybridization part, it is possible to construct configurations c as alternating sequences of time-ordered creator-annihilator-pairs called *segments* and time-ordered annihilator-creator-pairs called *antisegments* of the same spin-index σ. While the prior describe occupied, the latter represent unoccupied intervals of the time line between zero and β of the respectively observed identical spin-channel of the impurity orbital. Hence, a suitable corresponding configuration space in regard to an arbitrary but concrete spin-flavor σ is defined by

$$\mathcal{C}_\sigma : \{\{\mathrm{empty}_\sigma\}, \{\mathrm{full}_\sigma\}, \{(\tau_{1_\sigma}, \tau'_{1_\sigma})\}, \{(\tau_{1_\sigma}, \tau'_{1_\sigma}), (\tau_{2_\sigma}, \tau'_{2_\sigma})\}, \ldots\}, \tag{5.35}$$

where every continuous variable out of the interval $[0, \beta)$, namely $\{\tau_i\}$ ($\{\tau'_i\}$) with $i \in \{1_\sigma, \ldots, k_\sigma\}$, is associated with a creator $f^\dagger_\sigma$ (an annihilator f_σ) of an electron with spin-index σ inside the impurity orbital. Additionally—without any loss of generality—we want to assume the imaginary times enclosed by curly brackets to be time-ordered among each other. Therefore, arising τ-τ'-pairs explicitly mark segments whereas antisegments are implied implicitly except for the case of the *fully* occupied impurity orbital. Together with the configuration of the totally *empty*, i.e. unoccupied impurity orbital, this special configuration represents the unperturbed "ground state" at perturbation order zero. The full configuration space in terms of the segment picture, however, builds up from eq. (5.35) as the union over all spin-flavors the underlying model provides. By that, together with eq. (5.34) we may determine the statistical weight of a concrete configuration c as

$$\begin{aligned} p(c) = \mathcal{Z}_{\mathrm{host}} \cdot \mathrm{Tr}\left[\mathrm{e}^{-\beta \mathcal{H}_{\mathrm{imp}}} \cdot T_\tau \prod_\sigma f_\sigma(\tau'_{1_\sigma}) f^\dagger_\sigma(\tau_{1_\sigma}) \cdots f_\sigma(\tau'_{k_\sigma}) f^\dagger_\sigma(\tau_{k_\sigma}) \right] \\ \prod_\sigma \det \mathbf{\Delta}_\sigma(\mathrm{d}\tau)^{2k_\sigma} . \end{aligned} \tag{5.36}$$

Here, it is principally the trace over a time-ordered product of creation and annihilation operators of f-electrons, the mathematical formulation of an *impurity average* $W_{\mathrm{imp}}(c)$, that poses a numerical challenge. In the case of the matrix code, e.g. see [Hau07], one tries to overcome this by exploiting symmetries contained in the resulting matrix to be traced or even by shooting at the problem by means of a Krylov approach [LW09]. On the contrary, in terms of the segment picture—and this poses one of its advantages in usability as well as performance—this part of

the statistical weight (5.36) in the case of our model of choice simply reduces to

$$W_{\mathrm{imp}}(c) = \mathrm{Tr}\left[\mathrm{e}^{-\beta\mathcal{H}_{\mathrm{imp}}} \cdot T_\tau \prod_{\sigma=\uparrow,\downarrow} f_\sigma(\tau'_{1_\sigma}) f^\dagger_\sigma(\tau_{1_\sigma}) \cdots f_\sigma(\tau'_{k_\sigma}) f^\dagger_\sigma(\tau_{k_\sigma}) \right]$$
$$= s\mathrm{e}^{-(\varepsilon_f-\mu)(L_\uparrow+L_\downarrow)-(2\varepsilon_f+U)O_{\uparrow\downarrow}}, \tag{5.37}$$

where L_σ represents the total length of occupied times in the two spin-channels $\sigma = \uparrow, \downarrow$, $O_{\uparrow\downarrow}$ marks overlapping densities, each correctly weighted by means of the eigenvalue of the associated state in accordance to eqs. (3.1) and (3.2) on page 24. The prefactor s is a permutation sign. Practically it explicitly fixes upcoming signs due to so-called possibly sampled "wrapping" or "winding" segments that pass the transition from β back to 0 as concretely is the case for the segment marked by (τ_7, τ_2) in fig. 5.3 on page 67. A segment which is ill-defined with regard to time order as the annihilator time happens earlier than the creator time but is defined as correct segment in terms of the segment code. The necessary fix then simply lies in the controlled absorbing of the defected time-order due to this known artifact by spending the sign s to the affected configuration.

For illustration, an exemplary calculation of the impurity average for the configuration visualized

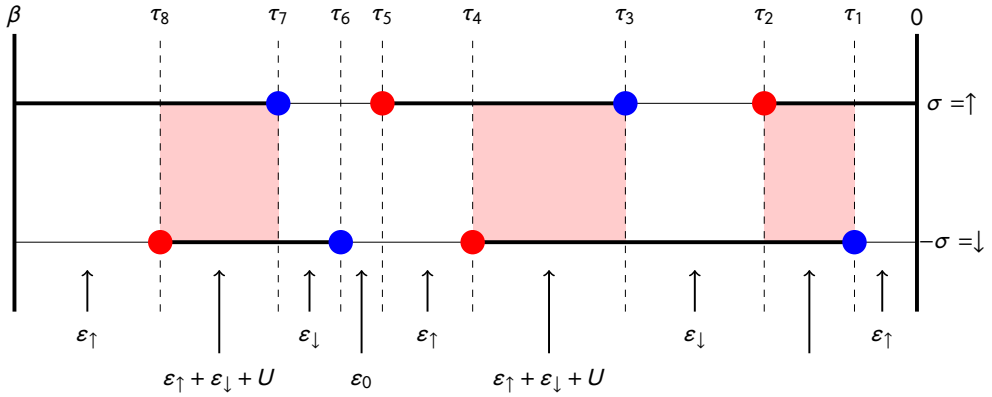

Figure 5.3.: Concrete example of a physically realistic configuration, which could have been generated by our implemented segment-CT-HYB code for the case of a spin-degenerate correlated single impurity orbital. Pairs of fermionic creators (blue bullets) and annihilators (red bullets) form so-called segments of occupied time-slices (fat black lines) between zero and β, never mixing time lines of different spin channels, here: $\sigma = \uparrow$ and $-\sigma = \downarrow$. Overlapping occupied time-slices between the two spin-channels are marked by light-red areas. For every time segment the occupation-dependent energy levels $\varepsilon_0, \varepsilon_\uparrow, \varepsilon_\downarrow$ or $\varepsilon_\uparrow + \varepsilon\downarrow + U$ are denoted below. The segment marked by τ_7 and τ_2 is identified as winding or wrapping segment. For further and an entire discussion, see text of section 5.3.

by fig. 5.3 according to eq. (5.37) is carried out as follows:

$$\begin{aligned}
\left|W_{\text{imp}}(c)\right| &= \mathrm{e}^{-\varepsilon_\uparrow(\tau_1-0)} \cdot \mathrm{e}^{-(\varepsilon_\uparrow+\varepsilon_\downarrow+U)(\tau_2-\tau_1)} \cdot \mathrm{e}^{-\varepsilon_\downarrow(\tau_3-\tau_2)} \cdot \mathrm{e}^{-(\varepsilon_\uparrow+\varepsilon_\downarrow+U)(\tau_4-\tau_3)} \cdot \mathrm{e}^{-\varepsilon_\uparrow(\tau_5-\tau 4)} \\
&\quad \times \mathrm{e}^{-\varepsilon_0(\tau_6-\tau_5)} \cdot \mathrm{e}^{-\varepsilon_\downarrow(\tau_7-\tau_6)} \cdot \mathrm{e}^{-(\varepsilon_\uparrow+\varepsilon_\downarrow+U)(\tau_8-\tau_7)} \cdot \mathrm{e}^{-\varepsilon_\uparrow(\beta-\tau_8)} \\
&= \mathrm{e}^{-\varepsilon_0(\tau_6-\tau_5)} \cdot \mathrm{e}^{-\varepsilon_\uparrow(\beta-\tau_8+\tau_8-\tau_7+\tau_5-\tau_4+\tau_4-\tau_3+\tau_2-\tau_1+\tau_1-0)} \\
&\quad \times \mathrm{e}^{-\varepsilon_\downarrow(\tau_8-\tau_7+\tau_7-\tau_6+\tau_4-\tau_3+\tau_3-\tau_2+\tau_2-\tau_1)} \cdot \mathrm{e}^{-U(\tau_8-\tau_7+\tau_4-\tau_3+\tau_2-\tau_1)} \\
&= \mathrm{e}^{-\varepsilon_\uparrow(\beta-\tau_7+\tau_5-\tau_3+\tau_2-0)} \cdot \mathrm{e}^{-\varepsilon_\downarrow(\tau_8-\tau_6+\tau_4-\tau_1)} \cdot \mathrm{e}^{-U(\tau_8-\tau_7+\tau_4-\tau_3+\tau_2-\tau_1)} \\
&= \mathrm{e}^{-(\varepsilon_\uparrow \cdot L_\uparrow + \varepsilon_\downarrow L_\downarrow + U \cdot O_{\uparrow\downarrow})},
\end{aligned}$$

where for our chosen model

$$\varepsilon_\uparrow = \varepsilon_\downarrow = \varepsilon_f - \mu$$

respectively. Because of the included wrapping segment, in a running process, one would drop the absolute value $|\ldots|$ by setting $s = -1$ according to eq. (5.37). Besides the local average of a configuration also the determinant of hybridization functions may be visualized. This occurs in terms of hybridization diagrams that show all possible hybridization lines between the start and the end times of segments of a given configuration. A possible example for the perturbation order $k = 3$ is shown in fig. 5.4. With that in mind one is finally able to define sampling updates to visit configurations according to their importance.

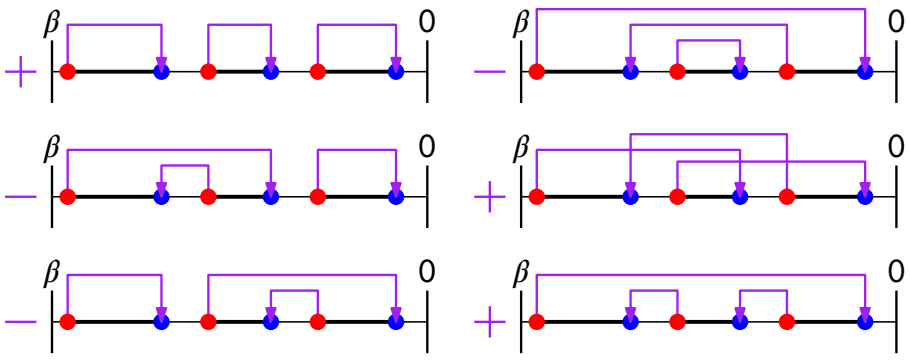

Figure 5.4.: Visualization of *hybridization diagrams* associated to a concrete configuration out of the CT-HYB-sampling for a given spin flavor. Hybridization lines (purple arrows) result from pairwise connecting of creator-annihilator-pairs (red and blue dots) that in a time-ordered sequence define the segments of a concrete configuration within the CT-HYB segment picture. At the given perturbation order $k = 3$ there exist $k! = 6$ different *hybridization diagrams* shown besides corresponding signs respectively. By means of the CT-HYB sampling, these signs *per construction* are absorbed within the determinant of all hybridization functions. Adopted from [HPW12].

5.4.2. Updates

Basically, a working and therefore necessarily ergodic segment variant of the CT-HYB algorithm internally has to imply the following four basic update types:

- The **adding of a segment**,
- the **removing of a segment**,
- the **adding of an antisegment** and
- the **removing of an antisegment**.

This is especially required to be able to sample from configuration "empty" to "full" (compare to eq. (5.35)) and vice versa. By suppressing the symmetric but always necessary dicing of the spin-flavor in terms of $1/\sigma$ the updates manifest as follows: In the case of **adding a segment (antisegment)**, first of all, we dice an imaginary time $\tau \in (0, \beta)$ of the proposed creator (annihilator). If τ lies on a segment (antisegment) created in previous update steps, the update is rejected immediately. If the new segment (antisegment) is possible to create, we have to dice a second imaginary time for the annihilator (creator) out of the interval $(0, l_{\max})$, where $l_{\max}$ is the time distance between the first diced time and the beginning time of the next already present segment (antisegment). As for **removing a segment (antisegment)**, we simply have to choose one segment (antisegment) out of the number of present segments (antisegments), this results in the following for- and backward proposals in the style of eqs. (5.29) and (5.30):

$$q_{c_{k_\sigma} \to c_{k_\sigma+1}} = \frac{\mathrm{d}\tau}{\beta} \cdot \frac{\mathrm{d}\tau}{l_{\max}}, \qquad q_{c_{k_\sigma}+1 \to c_{k_\sigma}} = \frac{1}{k_\sigma + 1}. \tag{5.38}$$

From that, we instantly derive the proposals for the case of *removing* a segment (antisegment) as

$$q_{c_{k_\sigma} \to c_{k_\sigma-1}} = \frac{1}{k_\sigma}, \qquad q_{c_{k_\sigma-1} \to c_{k_\sigma}} = \frac{\mathrm{d}\tau}{\beta} \cdot \frac{\mathrm{d}\tau}{l_{\max}}. \tag{5.39}$$

These proposal probabilities together with the statistical weight of a configuration as given by eq. (5.36) are then used to prepare ratios in the way as the following, which specifically results from eq. (5.38), hence when proposing to add a segment or antisegment:

$$\begin{aligned} &\frac{1}{k_\sigma + 1} \cdot \frac{\beta \cdot l_{\max}}{(\mathrm{d}\tau)^2} \cdot \frac{p(c_{k_\sigma+1})}{p(c_{k_\sigma})} \cdot \\ &= \frac{1}{k_\sigma + 1} \cdot \frac{\beta \cdot l_{\max}}{(\mathrm{d}\tau)^2} \cdot \mathrm{e}^{-(\varepsilon_f - \mu) l_{\mathrm{new}} - U o_{\mathrm{new}}} \cdot \frac{\boldsymbol{\Delta}_\sigma^{(k_\sigma+1)}}{\boldsymbol{\Delta}_\sigma^{(k_\sigma)}}. \end{aligned} \tag{5.40}$$

Here, the l_{new} denotes the length of the new segment while o_{new} is the possible overlap of the new segment with densities on the alternate spin-channel. For removing a segment or antisegment the ratio is constructed in an analogous manner. The ratios in the fashion of eq. (5.40) are then passed to eq. (5.30) as an argument in order to determine the respectively associated acceptance probabilities which in turn pass the stochastic decision of the process in terms of Metropolis sampling (c.f. section 5.3.2, page 61 ff.).

5.4.3. Smart det-ratios and fast matrix updates

As was seen in section 5.3, within the CT-HYB sampling procedure it is necessary to calculate statistical weights of drawn configurations which split up into a local average and a determinant of a matrix that implies the hybridization functions of all possible constellations of accompanying creation and annihilation times. It was also seen, the calculation of the local average, especially in terms of the segment code, is straight forward. The numerical calculation of the determinant, however may principally be done in two ways [Pre+07]:

1. In using standard techniques, usually based on LU-decomposition and therefore show a scaling of $\mathcal{O}(n^3)$ in complexity regarding the dimension n of the quadratic matrix.

2. In using smart det-ratios—as primarily only ratios of determinants are needed for the stochastic process in terms of eq. (5.40)—together with so-called *fast matrix updates* that only have to be performed if the corresponding proposed new configuration is accepted in terms of the Metropolis Hastings algorithm as shown in fig. 5.1 on page 62. As will be clarified below, in the worst case, this is performed in a time $\mathcal{O}(n^2)$ and therefore outperforms the previous method.

As one surely may expect perturbation orders of much higher values than $k = 3$ one clearly will implement approach number 2. In particular, this is based on storing and manipulating the inverse of $(\Delta)_{ij} = \mathbf{\Delta}$ that will be denoted by $\mathbf{\Delta}^{-1} =: \mathbf{M}$ in terms of the so-called *matrix determinant lemma* [Pre+07] and the Sherman-Morrison formula [Mey01]. In the end, by assuming $\mathbf{M}$ as an $(n-1)\times(n-1)$ matrix, in accordance to the appendix of [Hau07] one may find an efficient update formula in order to add a new n-th row and column each to obtain an updated $n \times n$ matrix M_{new} as the result of a twofold application of the Sherman-Morrison formula that reads

$$\mathbf{M}_{\text{new}} = \left(\begin{array}{ccc|c} & \mathbf{M} & & \begin{matrix}0\\0\\\vdots\end{matrix} \\ \hline 0 & 0 & \cdots & 0 \end{array}\right) + p \left(\begin{array}{c} L_{1n} \\ L_{2n} \\ \vdots \\ \hline -1 \end{array}\right) \otimes \left(\begin{array}{ccc|c} R_{n1}, & R_{n2}, & \cdots & -1 \end{array}\right), \tag{5.41}$$

where "⊗" marks an *outer product* and

$$L_{ij} = \sum_{l<n} M_{il}\Delta_{lj}\,, \quad R_{ij} = \sum_{l<n} \Delta_{il}M_{lj}\,.$$

Additionally p is given by

$$\frac{1}{p} = \Delta_{nn} - \sum_{l<n} \Delta_{nl}L_{ln} = \Delta_{nn} - \sum_{ll'<n} \Delta_{nl}M_{ll'}\Delta_{l'n}\,.$$

In staying with this terminology the matrix determinant lemma provides the ratio of determinants for *adding a row and a column* as:

$$\frac{\det \mathbf{M}}{\det \mathbf{M}_{\text{new}}} = \frac{1}{p} = \Delta_{nn} - \sum_{ll'<n} \Delta_{nl}M_{ll'}\Delta_{l'n}\,, \tag{5.42}$$

where one already has used the fact that $\det \mathbf{\Delta} = 1/\det \mathbf{\Delta}^{-1} =: 1/\mathbf{M}$.

Similarly, by again starting with a $n \times n$ matrix $\mathbf{M}$, in order to remove a row and a column, let's say the k-th one each, one finds the elements of the updated, reduced Matrix $\mathbf{M} = (M)_{ij}$ as

$$M_{ij}^{\text{new}} = M_{ij} - \frac{M_{ik} M_{kj}}{M_{kk}} \tag{5.43}$$

where in particular i and j do not need to run over index k. Consequently, the ratio of determinants for *removing a row and a column* just arises as:

$$\frac{\det M}{\det M_{\text{new}}} = M_{kk} \tag{5.44}$$

and thus is a $\mathcal{O}(1)$ operation as it only implies the reading of one single matrix element M_{kk}.

5.5. Measurements

As already reported in section 5.1, in the case of MC methods measurements are sequences of sampled or so-called *measured* values, yielding MC estimates of thermal averages of physical observables in the fashion of eq. (5.5) on page 51. This is the same for the CT-HYB algorithm. Some basic observables may directly be estimated out of the stochastic process. From the structure of the statistical weights of a sampled configuration as given by eq. (5.37) on page 67 follows for M total measurement steps:

- The average perturbation order per spin-channel k_σ as the MC average of the number of segments inside the σ-associated spin-channel:

$$\langle k_\sigma \rangle = \frac{1}{M} \sum_{i=1}^{M} k_\sigma \,. \tag{5.45}$$

  This obviously induces the estimate of the total perturbation order as

$$\langle k \rangle = \frac{1}{M} \sum_{i=1}^{M} \sum_{\sigma} k_\sigma \,. \tag{5.46}$$

- Besides, the estimate over the single-occupation

$$\langle n_\sigma \rangle = \frac{1}{M\beta} \sum_{i=1}^{M} L_\sigma \,, \tag{5.47}$$

  hence the MC average over all individually measured total segment lengths L_σ per spin channel σ.

- Finally, similar to the preceding point, the estimator of the double occupation

$$\langle n_\sigma n_{-\sigma} \rangle = \frac{1}{M\beta} \sum_{i=1}^{M} O_{\uparrow\downarrow} \,. \tag{5.48}$$

  That is the MC average of the total length of doubly occupied time-slices (compare to fig. 5.3 on page 67).

However, eventually, we need the CT-HYB to solve a proposed single impurity problem. In the spirit of our numerical framework as reported on in section 4.3 on page 44 and the following, hence in the context of DMFT this is achieved by calculating the self-energy of the impurity problem $\Sigma_{\mathrm{imp}\sigma}$—for the rest of this section just denoted by Σ_σ.

For our throughout assumed AIM with non-mixing spin channels and an impurity onsite interaction of density-density character this is comfortably achieved by means of so-called *improved estimators* initially proposed, described and fully derived in very detail by Hafermann, Patton, and Werner in [HPW12].

Here, the estimation of $\Sigma_{\mathrm{imp}\sigma}$ relies on an alternative impurity Dyson equation to that given by eq. (4.18) on page 43 originally proposed by Bulla, Hewson, and Pruschke in the context of numerical renormalization group (NRG) [BCP08; Bul12] calculations on the AIM [BHP98]:

$$\Sigma_\sigma(\mathrm{i}\omega_n) = U \frac{F_\sigma(\mathrm{i}\omega_n)}{G_\sigma(\mathrm{i}\omega_n)} \,, \tag{5.49}$$

where $F(\mathrm{i}\omega_n)$ is a higher correlation function that differs from G_σ only by a density of the alternative spin flavor $n_{-\sigma} = f^\dagger_{-\sigma}(\tau) f_{-\sigma}(\tau)$ according to eq. (2.7). So in addition to

$$G_{\sigma\sigma}(\tau - \tau') \equiv -\left\langle T_\tau f_\sigma(\tau) f^\dagger_\sigma(\tau') \right\rangle \tag{5.50}$$

out of eq. (A.11), we define

$$F_{\sigma\sigma}(\tau - \tau') \equiv -\left\langle T_\tau f_\sigma(\tau) f^\dagger_{-\sigma}(\tau) f_{-\sigma}(\tau) f^\dagger_\sigma(\tau') \right\rangle \,. \tag{5.51}$$

Now for convenience, the measurement of Σ_σ occurs via a general measurement of

$$(G\Sigma)_\sigma(\tau) = U F_\sigma(\tau) \tag{5.52}$$

and the division of $G_\sigma(\tau)$ afterwards. The estimator of $G_\sigma(\tau)$ was already proposed as

$$G_\sigma(\tau) = -\langle \frac{1}{\beta} \sum_{i,j=1}^{k_\sigma} \delta^-(\tau, \tau_i - \tau'_j) M_{ji} \rangle_{\mathrm{MC}} \tag{5.53}$$

in [Wer+06], confirmed in [Gul+11] and is pedagogically motivated and derived excellently in [Wer11]. Consequently, from eq. (5.50) and eq. (5.51) follows

$$F_\sigma(\tau) = -\langle \frac{1}{\beta} \sum_{i,j=1}^{k_\sigma} \delta^-(\tau, \tau_i - \tau'_j) M_{ji} n_{-\sigma}(\tau'_j) \rangle_{\mathrm{MC}} \,. \tag{5.54}$$

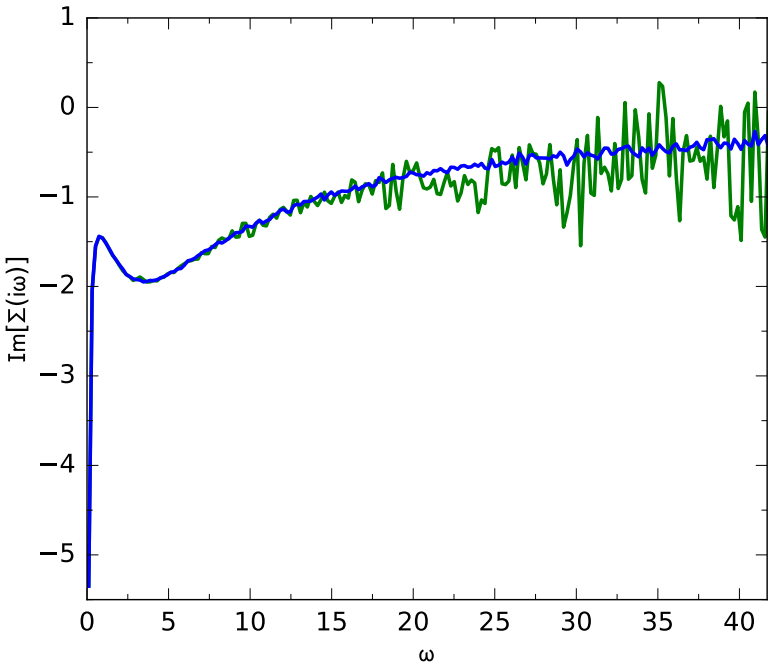

Figure 5.5.: Impressive example of the improved estimator of the impurity self-energy by comparing the imaginary parts of two differently calculated impurity self-energy estimates $\Sigma(i\omega)$ in dependence of the Matsubara frequencies ω. The one stemming from a simulation using improved estimators (blue line) clearly occurs smoother as that resulting one out of a calculation via standard Dyson equation (green line) for higher Matsubara frequencies. Of course, both simulations counted the same number of measurement and were based on identical initial seeds of random numbers, hence MC steps in regard to an equal sequence of sampled configurations.

Here, MC averages in terms of eq. (5.5), sampled according to eq. (5.34), were assumed, while M_{ji} are relevant elements of the matrix of inverse hybridization functions as introduced in section 5.4.3 on page 70 and the following. This stems from eq. (5.44), as the G-measurement (5.53) is based on the idea of measuring values of $G_\sigma(\tau)$ for every pair of (τ, τ') given by the current configuration of order k_σ by respectively cutting off hybridization lines as those shown in fig. 5.4. This turns out to be equivalent to the removing of recently one (τ, τ')-corresponding row and line of the matrix $\mathbf{M}$ for what comfortably eq. (5.44) has to be applied. The necessary usage of a clever "binning function"

$$\delta^-(\tau, \tau') \coloneqq \mathrm{sgn}(\tau')\delta(\tau - \tau' - \Theta(-\tau')\beta)\,, \tag{5.55}$$

where the sign function (A.4) was used, ensures that the continuous time values $(\tau_i - \tau'_j)$ of the configuration at hand may be binned into a preset discrete time-mesh of measured G or F values in τ.

As in terms of the "improved estimators" the impurity Dyson equation is solved and by that the impurity self-energy is directly produced inside the impurity solver, performed measurements may be directly Fourier transformed in one go at run time of the binning process.

Due to the fact that the measuring concept described here and used later on is based on the ratio (5.49), while standard impurity Dyson equation occurs as the difference of two measured quantities, one expects a more advantageous error propagation. For a concrete sampling example this is impressively demonstrated by means of fig. 5.5.

Generally, the usage of this measurement scheme however is not recommended for models beyond a Hubbard-type density-density interaction as is the case, here. More complicated interactions soon lead to unpleasant additional terms in above measurement formulas making them formally as well as computationally unattractive.

5.6. Summary & outlook

This chapter provided a mainly technical review of the common MCMC method as used in statistical as well as solid state physics in general and a very special extension of those, the CT-QMC approaches. After some general background information on this family of impurity solvers, we particularly went into detail with the so-called segment variant of the CT-HYB algorithm which already was repeatedly mentioned as our impurity solver of choice inside our numerical setup based on a sdDMFT framework in the previous chapter 4 on page 37 and the following. By that, we hope this chapter not only closed the thematic holes that were left from previous chapters but also—besides the cited standard references on the topic—may serve as fruitful literature or even an implementation guide for those who may be concerned with the usage or even the programming of such an algorithm. With the conclusion of this chapter we are now ready to focus on physical applications of our numerical apparatus in the following chapters 6 and 7.

6. Magnetic phases in the triangular Anderson lattice

Major parts of this chapter were already published as

> M. W. Aulbach, F. F. Assaad, and M. Potthoff. "Dynamical mean-field study of partial Kondo screening in the periodic Anderson model on the triangular lattice". In: *Phys. Rev. B* 92 (23 Dec. 2015), p. 235131. *Copyright (2015) by the American Physical Society. Reproduced with permission.*

All presented numerical results were simulated by means of our numerical setup as described in chapters 4 and 5, especially section 4.3 on page 37 and the following. Necessary calculations were entirely performed on clusters of the PHYSnet Rechenzentrum of the University of Hamburg and the SuperMUC super computer cluster of the Leibniz Rechenzentrum Munich.Support of these studies by the Deutsche Forschungsgemeinschaft within the Forschergruppe FOR 1346 (projects P1 and P8) and within the Sonderforschungsbereich SFB 668 (project A14) is gratefully acknowledged.

In this chapter we report on our studies of the periodic Anderson model (c.f. section 2.3, page 13 ff.) on the triangular and thus geometrically frustrated lattice. In accordance to the topics of the chapters 2 and 3 we focus our research on the competition between Kondo screening and indirect magnetic exchange . Principally, as already mentioned in the introduction on page 1 and the following, our main concern and motivator is the quest for a favorably stable partial Kondo screening (PKS) phase, substantiated in the following section 6.1, by means of dynamical mean-field theory. This is a first opportunity to apply our numerical setup as described in chapters 4 and 5 especially in section 4.3 on page 44 ff. in order to practically achieve the necessary self-consistent mapping onto three independent single-impurity models corresponding to the three correlated orbitals in the appropriately chosen unit cell. By that, with a model-adapted version as described in section 6.2, we systematically scan the geometrically frustrated Anderson lattice from the weak- to the strong-coupling regime for a wide range of fillings n. Relevant results are presented in section 6.3.1, discussed and concluded in section 6.4.

6.1. Introduction

In chapter 2 on page 9 ff. some essential lattice models and their corresponding Hamiltonians were reviewed. There, it was already emphasized that besides the bare parameters it is the lattice

geometry encoded into the hopping t that rules the physical behavior of a lattice model. Thus, in comparison to those on a let's say a square lattice, models on a triangular lattice structure show drastic differences. As a very prominent and likewise unpleasant example, the density of states (DOS) loses its comfortable symmetry (see fig. 6.5 on page 84) and resulting from that also very helpful predictions in regard to the preparation of half-filling as pointed out in eq. (2.23) on page 19 are not valid anymore. Furthermore and in terms of magnetic order of local magnetic moments, a triangular lattice geometry poses the problem of geometric frustration. This was already emphasized in section 3.3.2 on page 33 ff. by means of a simple antiferromagnetic spin-type model in $D = 2$ dimensions. There, against the background of the terminology of a bipartite lattice, a partitioning of sites into two equivalent sublattices A and B as per orientation of the corresponding spins succeeded for the case of the square lattice. For the case of the triangular lattice this however failed as to correctly describe the full lattice one needed to introduce a further, third equivalent sublattice C of sites whose spins remain unable to fit to the expected antiferromagnetic order already dictated by the A and B spins. Principally and correspondingly to the literature, it was concluded that the geometrical frustration arise as a phenomenon in lattice models of uncompensated spins.

This general model category, however, also implies impurity lattice models like the Kondo lattice model (KLM) (c.f. section 2.4, page 18 ff.) and the PAM (c.f. section 2.3, page 13 ff.), where for the latter one the term "spin" literally as well as conceptually has to be replaced by "local magnetic moment" as induced by the spin angular moment.

In section 3.2 on page 27 ff. we referred on the Doniach phase diagram as the result of a rival between the energy scales of the Kondo effect and the Ruderman-Kittel-Kasuya-Yosida (RKKY) exchange mechanism that occurs in the PAM and the KLM. A confrontation of these models to geometric frustration introduces another energy scale in the problem associated with the release of frustration via a mechanism of so-called partial Kondo screening [Mot+10]. Thus, under the right energetic circumstances a special magnetic state of the system can be reached which simply avoids the frustration. This is due to the fact that the sites of Anderson as well as Kondo lattices host two electronic orbitals each, what allows for a partial but periodic, hence a site-selective Kondo screening of local magnetic moments leaving the remnant magnetic moments for taking part in a magnetic order scheme without frustration. To be more concrete, let's assume the local magnetic moments on all C-sites to be screened by corresponding onsite bath electrons. As a result only the local magnetic moments formed up on A and B sites are still available for magnetic interactions in a RKKY-like manner. In regard to the lattice structure however, the A and B sites in an imagined absence of the C sites define a honeycomb lattice which clearly is a bipartide lattice. Consequently an antiferromagnetic coupling between local magnetic moments of next-neighboring A and B sites principally may occur without frustration. Away from the global view on the geometrically frustrated lattice in terms of the three sublattices, the principal physics of the PKS is compressed into a non-primitive unit cell which contains one concrete site of all three sublattices each. By that, the lattice physically becomes homogeneous in terms of those unit cells and therefore generally treatable by means of a site-selective dynamical mean-field approach as presented in section 4.3 on page 44 and the following. Therefore, we expect it to be feasible to study the PKS beyond the static mean-field approximation—an effort already practiced in the past [HUM11; HUM12].

To the end, we will not only manage to stabilize a PKS phase by means of DMFT. Moreover, we will show that our, for this purpose conveniently adapted numerical setup, as generally described further in section 4.3 on page 44 ff., could be used for the entire study of the competition between RKKY coupling and Kondo screening in the triangular Anderson lattice: We will draw a remarkably rich phase diagram including a PKS phase emerging in the local-moment regime at the border between paramagnetic heavy-fermion and magnetically ordered phases. This will be reported in detail in section 6.3 on page 79 and the following. In order to never get lost in the different phases, a graphical overview of all relevant emerging phases by means of the corresponding constellations of the orientation of magnetic moments per unit cell is provided by fig. 6.2 on page 81.

6.2. Model and methodical adaptations

The choice of the model principally should be already clear by means of section 4.3: An Anderson model (c.f. section 2.3, page 13 ff.) in real-space standard notation that besides the spin-channel σ offers opportunities, i.e. indices to concretely tune-in position $\mathbf{r}$ and internal site α of a unit cell as given by eq. (4.25) on page 45 and entirely described there. For a comfortable overview, we shall rewrite it at this place:

$$\begin{aligned} H = &\sum_{\mathbf{r}\mathbf{r}'}\sum_{\alpha\alpha'}\sum_{\sigma} c^{\dagger}_{\mathbf{r}\alpha\sigma} t_{\alpha\alpha'}(\mathbf{r}-\mathbf{r}') c_{\mathbf{r}'\alpha'\sigma} \\ &+ V\sum_{\mathbf{r}\alpha\sigma}\left(c^{\dagger}_{\mathbf{r}\alpha\sigma} f_{\mathbf{r}\alpha\sigma} + f^{\dagger}_{\mathbf{r}\alpha\sigma} c_{\mathbf{r}\alpha\sigma}\right) \\ &+ \varepsilon_f \sum_{\mathbf{r}\alpha\sigma} f^{\dagger}_{\mathbf{r}\alpha\sigma} f_{\mathbf{r}\alpha\sigma} \\ &+ \frac{U}{2}\sum_{\mathbf{r}\alpha\sigma} f^{\dagger}_{\mathbf{r}\alpha\sigma} f_{\mathbf{r}\alpha\sigma} f^{\dagger}_{\mathbf{r}\alpha-\sigma} f_{\mathbf{r}\alpha-\sigma} \,. \end{aligned}$$

We concretize our model to be studied here, conforming to that focused on in [HUM11; HUM12], hence focus on the $D = 2$-dimensional triangular lattice. Thereby, we consider a partitioning of the lattice into non-primitive unit cells containing three sites each, as principally shown in fig. 6.1 and already mentioned in the preceding section. As also emphasized repeatedly throughout this thesis, we restrict ourselves to non-mixing spin-channels of possible spin-projections $\sigma = \uparrow, \downarrow$.

To be able to simulate a PKS state at all, the internal sites of the priorly defined unit cells, have to be treated nonequivalent by means of our site-selective dynamical mean-field approach as derived in section 4.3 on page 44. The corresponding self-consistency cycle was constructed there by an appropriate arrangement of the eqs. (4.27) and (4.28).

The ansatz (4.26) back on page 46 for the self-energy $\Sigma_{\mathbf{r}\alpha\sigma,\mathbf{r}'\alpha'\sigma'}(\mathrm{i}\omega_n)$ in this case means that the periodic Anderson model is self-consistently mapped onto three independent impurity models with possibly spin-dependent but spin-diagonal one-particle parameters. The impurity models

can be solved independently but are coupled indirectly via the DMFT self-consistency equation. In particular, we do not impose any further condition on the spatial or spin dependence of $\Sigma_{\alpha\sigma}(\omega)$. Thereby, we can account for different phases, in particular for collinear magnetic phases,characterized by inhomogeneous order parameters within a unit cell.

In regard for the practical application of DMFT we need to determine the hopping matrix $\varepsilon(\mathbf{k})$ in consideration of the lattice geometry. According to the scheme sketched in section 4.3 on page 44 and the following, we get a 6×6 hopping matrix

$$\varepsilon(\mathbf{k}) = \begin{pmatrix} \varepsilon_f & 0 & 0 & V & 0 & 0 \\ 0 & \varepsilon_f & 0 & 0 & V & 0 \\ 0 & 0 & \varepsilon_f & 0 & 0 & V \\ V^* & 0 & 0 & \varepsilon_c & \varepsilon_{\mathrm{AB}}(\mathbf{k}) & \varepsilon_{\mathrm{AC}}(\mathbf{k}) \\ 0 & V^* & 0 & \varepsilon^*_{\mathrm{AB}}(\mathbf{k}) & \varepsilon_c & \varepsilon_{\mathrm{BC}}(\mathbf{k}) \\ 0 & 0 & V^* & \varepsilon^*_{\mathrm{AC}}(\mathbf{k}) & \varepsilon^*_{\mathrm{BC}}(\mathbf{k}) & \varepsilon_c \end{pmatrix} \tag{6.1}$$

for each wave vector $\mathbf{k}$ in the reduced Brillouin zone. We have

$$\begin{aligned} \varepsilon_{\mathrm{AB}}(\mathbf{k}) &= t \left[1 + 2\cos\left(k_y/2\right) \mathrm{e}^{-i\frac{\sqrt{3}}{2}k_x} \right], \\ \varepsilon_{\mathrm{AC}}(\mathbf{k}) &= t \left[1 + \mathrm{e}^{-\mathrm{i}\frac{\sqrt{3}}{2}k_x}\, \mathrm{e}^{-\mathrm{i}\frac{1}{2}k_y} + \mathrm{e}^{-\mathrm{i}k_y} \right], \\ \varepsilon_{\mathrm{BC}}(\mathbf{k}) &= t \left[1 + \mathrm{e}^{-ik_y} + \mathrm{e}^{\mathrm{i}\frac{\sqrt{3}}{2}k_x}\, \mathrm{e}^{-\mathrm{i}\frac{1}{2}k_y} \right], \end{aligned} \tag{6.2}$$

where the triangular lattice geometry evidently is entirely encoded in the pre-factors of the wave vector components k_x and k_y. These originally stem from the chosen set of translational vectors in real-space that translation-symmetrically point from one chosen reference unit cell (compare to fig. 6.1) to the next-neighboring unit cells around respectively.

With the hopping matrix $\varepsilon(\mathbf{k})$ (6.1), and with a guess for the local but site-dependent f self-energy $\Sigma_{\alpha\sigma}(\omega)$ (for $\alpha \in \{\mathrm{A}, \mathrm{B}, \mathrm{C}\}$) we can start the DMFT self-consistency cycle by calculating the elements of the local lattice Green's function via eq. (4.27) on page 47. We repeat it for or a quick lookup:

$$G_{\mathrm{loc},\gamma\delta,\sigma}(\mathrm{i}\omega_n) = \frac{1}{L} \sum_{\mathbf{k}\in\mathrm{BZ}} \left[\frac{1}{\mathrm{i}\omega_n + \mu - \varepsilon_{\mathbf{k}} - \mathbf{\Sigma}_\sigma(\mathrm{i}\omega_n)} \right]_{\gamma\delta}.$$

In this case, γ, δ run over the 6 orbitals in the unit cell. The 6×6-matrix $\mathbf{\Sigma}_\sigma(\omega)$ is diagonal and non-zero on the f orbitals only. The local Green's function is used to determine the hybridization functions $\Delta_{\alpha\sigma}$ of the three single-impurity Anderson modelsingle-impurity Anderson models (SIAMs) ($\alpha \in \{\mathrm{A}, \mathrm{B}, \mathrm{C}\}$) by means of eq. (4.28), we remember as

$$\Delta_{\alpha\sigma}(\omega) = \omega + \mu - \varepsilon_f - \Sigma_{\alpha\sigma}(\omega) - \frac{1}{G_{\mathrm{loc},\alpha\alpha,\sigma}(\omega)}.$$

The resulting formal expressions of three independent impurity models $\Delta_{\mathrm{A}\sigma}, \Delta_{\mathrm{B}\sigma}, \Delta_{\mathrm{C}\sigma}$, are used to initialize and run three independent instances of our segment code implementation of the continuous-time hybridization expansion (CT-HYB) algorithm (c.f. sections 5.4 and 5.5, page 65 ff.)

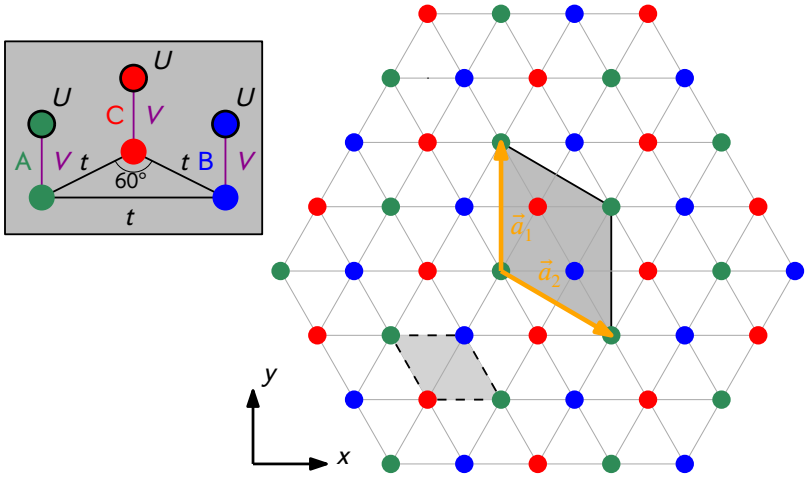

Figure 6.1.: Periodic Anderson model on the triangular lattice. *Right:* Primitive unit cell (light gray, dashed lines) and unit cell (gray, solid lines), spanned by the vectors $\mathbf{a}_1$ and $\mathbf{a}_2$, considered here. The latter contains three sites (A, B, C) treated independently within site-dependent dynamical mean-field theory. *Left:* For each site, a correlated (f) orbital with local interaction U couples to an uncorrelated conduction-electron (c) orbital via the hybridization of strength V. The nearest-neighbor hopping $t = 1$ between conduction-electron orbitals sets the energy scale. Figure as published in [AAP15]. *Copyright (2015) by the American Physical Society. Reproduced with permission.*

at finite but low temperatures T in order to obtain the self-energy $\Sigma_{\alpha\sigma}(\omega)$ for each impurity model independently.

As the interaction term of our model is entirely of the type density-density Hubbard-type interaction (c.f. eq. (2.13), page 15 ff.), we are save to sample the impurity self-energies by means of the improved estimators we reviewed in section 5.5 on page 71 and the following. As already pointed out there, this enables us to elegantly close the DMFT self-consistency cycle by extracting the required impurity self-energies $\Sigma_{\alpha\sigma}(i\omega_n)$ directly on the fermionic Matsubara frequencies $\mathrm{i}\omega_n$.

6.3. Results

By means of the suitably prepared methodical base focussed on in the preceding section 6.2, DMFT calculations have been performed for the model eq. (4.25) on page 45 with different chemical potentials μ to scan the interesting regime at and off half-filling $n = 1$ where n is explicitly given by

$$n = \frac{1}{6} \sum_{\alpha=\mathrm{A,B,C}} \sum_{\sigma=\uparrow,\downarrow} \left(n^{(f)}_{\alpha\sigma} + n^{(c)}_{\alpha\sigma} \right) \tag{6.3}$$

with $n^{(f)}_{\alpha\sigma} = \langle f^\dagger_{\mathbf{r}\alpha\sigma} f_{\mathbf{r}\alpha\sigma} \rangle$ and $n^{(c)}_{\alpha\sigma} = \langle c^\dagger_{\mathbf{r}\alpha\sigma} c_{\mathbf{r}\alpha\sigma} \rangle$, which can be determined out of the diagonal elements of G_{loc} (4.27), via relation (A.13) combined with a sum over Matsubara frequencies in

the style of eq. (4.30). The Hubbard interaction is scanned in the weak- to intermediate-coupling range $0 \leq U \leq 4$ where the energy scale is fixed throughout this chapter by the nearest-neighbor hopping $t = 1$. It is worth it to note that choosing $t > 0$ is convenient as this implies that the center of gravity of the total DOS as shown in fig. 6.5 on page 84 is located close to the lower band edge. Symmetry-broken magnetic phases are therefore expected to occur for fillings below half-filling. We furthermore fix the hybridization strength at $V = 1$ and choose $\varepsilon_f = -U/2$ for the on-site energy of the f orbitals. For strong U, this ensures that the occupancy of the f orbital at any site α in the unit cell is close to unity, i.e.,

$$n_\alpha^{(f)} \equiv \langle n_{\alpha\uparrow}^{(f)} \rangle + \langle n_{\alpha\downarrow}^{(f)} \rangle \approx 1 \,.$$

The on-site energy of conduction-electron orbitals fixes the energy zero: $\varepsilon_c = 0$.

Our main result is shown in fig. 6.3 on page 82: It is the phase diagram for the PAM on the triangular lattice as obtained by site-dependent dynamical mean-field theory (sdDMFT). To cover the relevant parameter region, we have performed $\sim$ 500 independent DMFT calculations for different U and μ in several massively parallel runs (see our comment on that in section 5.3.2 on page 60 ff.) with step sizes $\Delta U = 0.5$ and $\Delta\mu = 0.05$. We have considered the model, eq. (4.25), formally written out on page 45, on a lattice with 25×25 unit cells and periodic boundary conditions to perform the $\mathbf{k}$-sum in eq. (4.27) explicitly. This is sufficient to ensure that the results do not depend significantly on the system size as has been checked carefully. The gained self-consistent results are indicated as dots and symbols in fig. 6.3 in the U-n plane. About 200 iterations of the DMFT self-consistency cycle usually turned out to be sufficient for convergence. To allow for spontaneous breaking of the SU(2) spin-rotation symmetry, we explicitly treat the $\sigma = \uparrow$ and the $\sigma = \downarrow$ channels as independent of each other within the impurity solver—a segment variant of the CT-HYB algorithm presented in sections 5.4 and 5.5 on sections 5.4 and 5.5 and the following. Furthermore, the DMFT cycle is started with a spin-asymmetric Hartree-Fock-type initial self-energy. It turns out that magnetic phases, if present, are easily found and stabilized in this way. Within the present study we focus on magnetic phases with collinear moments for simplicity even though non-collinear magnetic phases may be expected in the case of the triangular lattice due to geometrical frustration. In fact, previous Hartree-Fock calculations at and off half-filling [HUM11; HUM12] suggest that a "classical" non-collinear 120° (c.f. fig. 6.2 on page 81) antiferromagnetic phase is realized in a certain range of the phase diagram. We expect that, by enforcing collinearity, the 120° phase is replaced by a collinear "↑, ↑, ↓" antiferromagnetic phase which has also been found within HF theory [HUM11; HUM12].

6.3.1. Phase diagram

Our determined phase diagram fig. 6.3 shows the occurrence of five different phases. The corresponding constellations of magnetic moments on the different orbitals of the chosen unit cell are shown in fig. 6.2 on page 81. Staring at fig. 6.3, at half-filling, the system is a non-magnetic Kondo insulator (KI) in the entire U range considered here. For fillings sightly off half-filling, the system stays non-magnetic but immediately becomes metallic. Above half-filling, this non-magnetic "Kondo singlet" phase is the only phase that has been found, at least up to $n = 1.1-1.2$.

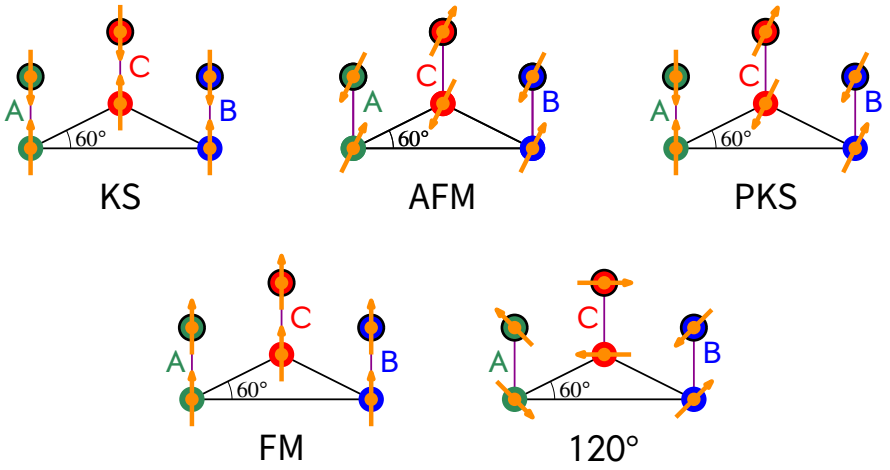

Figure 6.2.: Overview of the constellation and orientation of local magnetic moments inside a triangular unit cell in regard to different magnetic phases. Unit cell and site labels are shown in accordance to fig. 6.1 on page 79. For further discussion, see chapter 6, page 75 ff..

Below half-filling and for a sufficiently strong interaction $U > U_c \approx 2$, there are two different magnetic phases, an antiferromagnetic (AFM) and a phase with partial Kondo screening (PKS). The AFM phase is a collinear "↑, ↑, ↓" phase where the magnetic moments at two sites (say, A and B) in the unit cell are ferromagnetically aligned and of equal magnitude while the third moment is antiferromagnetically oriented to the former two with a magnitude such that the total magnetic moment in the unit cell is zero:

$$m_A^{(f)} + m_A^{(c)} = m_B^{(f)} + m_B^{(c)} \equiv m_0 > 0 \quad \text{and} \quad m_C^{(f)} + m_C^{(c)} = -2m_0 < 0\,.$$

Here,

$$m_\alpha^{(f)} \equiv n_{\alpha\uparrow}^{(f)} - n_{\alpha\downarrow}^{(f)} \quad \text{and} \quad m_\alpha^{(c)} \equiv n_{\alpha\uparrow}^{(c)} - n_{\alpha\downarrow}^{(c)}\,.$$

The PKS phase is characterized by one site (say A) with vanishing ordered magnetic moment, or almost vanishing moment (see discussion below), while the moment on the two remaining sites are of equal magnitude but antiferromagnetically aligned:

$$m_B^{(f)} + m_B^{(c)} \equiv m_0 = -(m_C^{(f)} + m_C^{(c)}) > 0\,.$$

The total moment in a unit cell is again zero. The AFM and the PKS phases appear in a certain filling range $n_{c1}(U) < n_{c2}(U)$ which increases in width with increasing U and which is roughly centered around $n \approx 0.9$. The PKS phase appears at weaker U as compared to the AFM phase and separates the latter from the non-magnetic KS phase for $n \to n_{c1}(U)$. At much lower fillings, there is also a ferromagnetic (FM) with a non-zero total magnetic moment per unit cell. This requires a significantly weaker critical interaction $U_c \approx 1.25$ as compared to AFM and PKS magnetic phases. The FM phase is realized in a rather narrow filling range, roughly centered around $n \approx 0.75$ for weak U and $n \approx 0.67$ for $U = 4$.

We expect that the phase diagram obtained for inverse temperature $\beta = 100$ and shown in fig. 6.3 on page 82 is close to the zero-temperature phase diagram. To estimate the remaining effects that

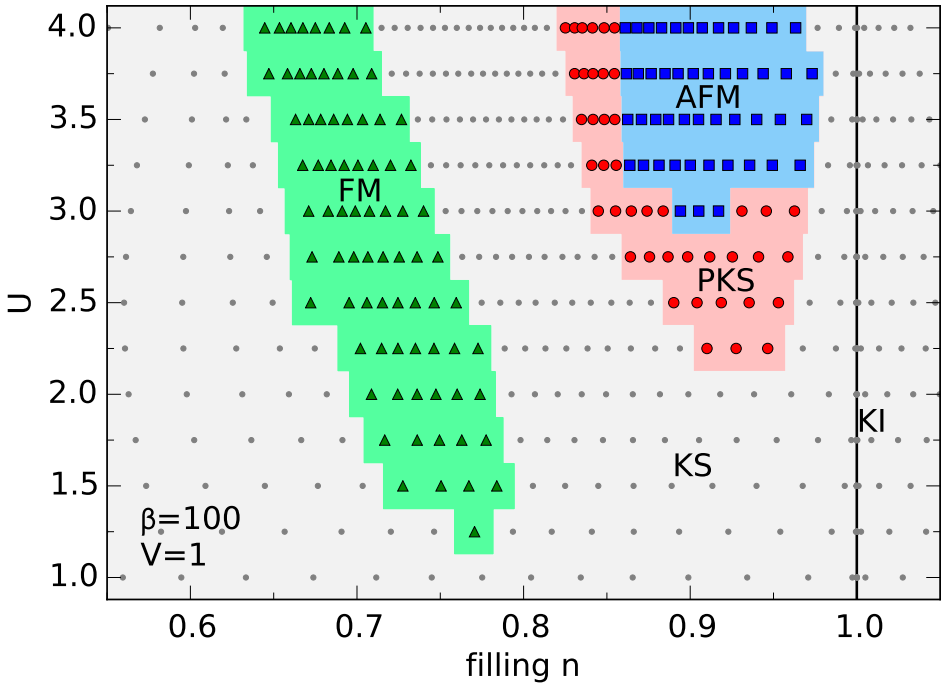

Figure 6.3.: U-vs.-n phase diagram of the Anderson model on the triangular lattice as obtained by site-dependent dynamical mean-field theory. Each point corresponds to a converged DMFT calculation using CT-QMC (CT-HYB, segment code) as a solver at $\beta = 100$. At half-filling $n = 1$ (solid line) the system is a Kondo insulator (KI) for all $U \geq 0$. Off half-filling, we find a metallic Kondo singlet state (KS, dots) as well as three different collinear magnetic phases: a partial Kondo-singlet phase (PKS, circles), an antiferromagnetic phase (AFM, squares) as well as a ferromagnetic phase (FM, triangles). Figure as published in [AAP15]. *Copyright (205) by the American Physical Society. Reproduced with permission.*

are due to a finite β, we have studied the parameter region close to the PKS phase for a somewhat higher temperature ($\beta = 70$). The results are shown in fig. 6.4 on page 83.

Comparing the phase diagrams for the different temperatures, there are no qualitative differences. Merely the extension of the AFM and the PKS phases in the U-n plane is somewhat reduced for $\beta = 70$, and the critical interaction increases a bit from $U_c \approx 2$ ($\beta = 100$) to $U_c \approx 2.5$ ($\beta = 70$).

6.3.2. Kondo insulator at half-filling

We start the discussion with the KI phase at half-filling. The insulating nature of this phase is easily verified by means of the charge susceptibility $\kappa = \partial n / \partial \mu$ which is found to vanish at half-filling for any $U \geq 0$. For $U = 0$ and half-filling the system is actually a simple band insulator: The chemical potential is located in the hybridization band gap which opens for any $V > 0$, see

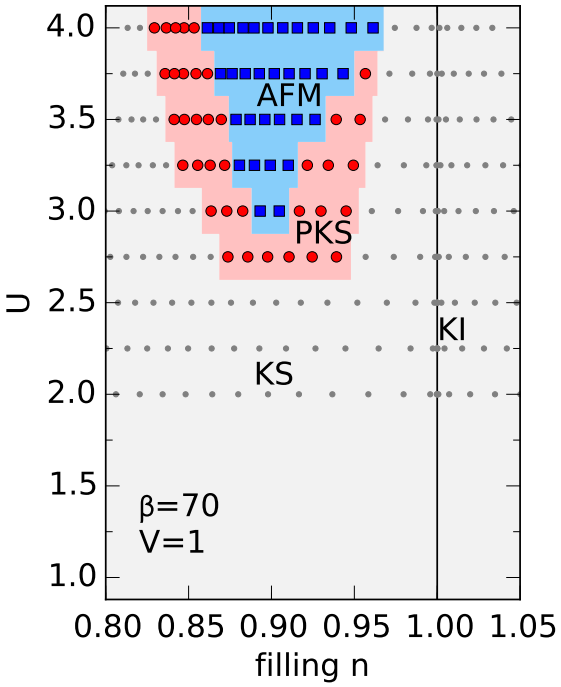

Figure 6.4.: U-vs.-n phase diagram as in fig. 6.3 but for $\beta = 70$ and in a smaller filling range including the antiferromagnetic (AFM) and partial Kondo screening (PKS) phases. Figure as printed within [AAP15]. *Copyright (2015) by the American Physical Society. Reproduced with permission.*

fig. 6.5 on page 84.

For the correlated system at $U = 2.5$, the charge gap Δ_c at half-filling can be read off from the μ range in which the charge susceptibility κ vanishes; see lower panel of fig. 6.6 on page 85 where μ is plotted as a function of the n.

The gap persists for all $U > 0$ and decreases with increasing U as is obvious when comparing with the charge gap for $U = 3.5$, for example, which can be read off from the lower panel in fig. 6.7 (note the different scales for μ in the two figures).

It is tempting to relate this decrease of the energy scale with increasing U to the decrease of the coupling constant $J = 8V^2/U$ in the effective low-energy Kondo lattice that is formally obtained by the Schrieffer-Wolf transformation [SW66] in the local-moment regime of the Anderson lattice model. Local magnetic moments, required for magnetic long-range order, are formed on the f orbitals due to a strongly repulsive Hubbard-U. One must be aware, however, that even for $U = 4$ there are still substantial charge fluctuations on the f orbitals. This is indicated, for example, by a $\sim 5\%$ deviation of the average f occupancy from unity at half-filling (see upper panels of figs. 6.6 and 6.7). Hence, the system is not fully in the local-moment limit. Nevertheless, we find an antiferromagnetic linear response of the conduction-electron magnetic moments when

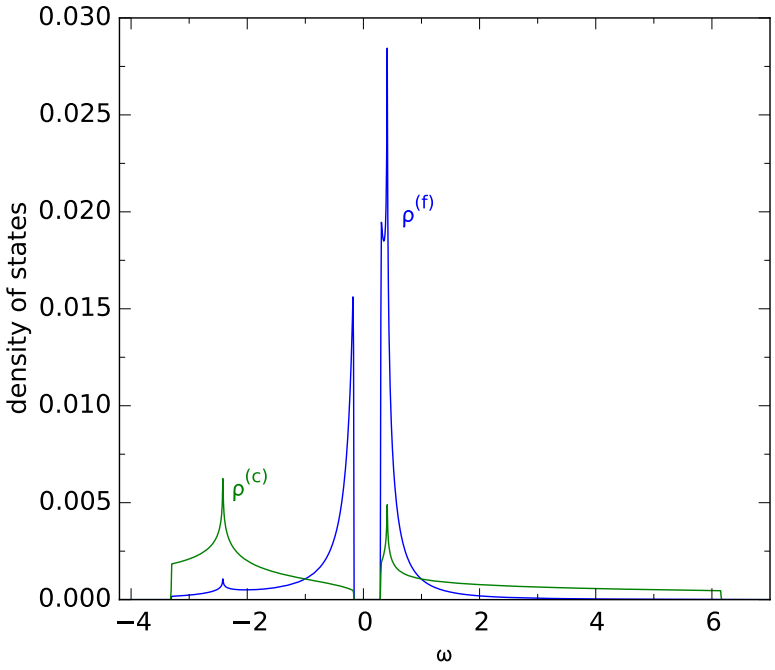

Figure 6.5.: f- and conduction-electron densities of states $\rho^{(f)}(\omega)$ and $\rho^{(c)}(\omega)$, respectively, for the non-interacting ($U = 0$) Anderson model on the triangular lattice. Energy units are fixed by the nearest-neighbor hopping $t = 1$. Further parameters: $V = 1$, $\varepsilon_c = \varepsilon_f = 0$. Centers of gravity are located at $\omega = 0$. Figure as printed within [AAP15]. *Copyright (2015) by the American Physical Society. Reproduced with permission.*

applying a homogeneous static magnetic field to the f electron spins. This indicates an antiferromagnetic ($J > 0$) coupling between the local f and c spins consistent with the local-moment picture provided by an effective Kondo lattice.

Deep in the local-moment regime (see section 3.1, page 24 ff.) for $U \to \infty$ at fixed V, the physics would be governed by a small energy scale, set by J, or even by $T_\mathrm{K} \propto e^{-W/J}$, which makes calculations at stronger U extremely difficult: In fact, we have not been able to stabilize a self-consistent solution of the DMFT equations at interaction strengths substantially stronger than $U = 4$.

Interestingly, there is no magnetic phase found at half-filling $n = 1$. This is opposed to static mean-field (HF) theory for the same model [HUM11] which generates a rather complex phase diagram which comprises different magnetic as well as insulating and metallic phases *at half-filling*. As the DMFT correctly accounts for local fluctuations beyond the static mean-field theory, we conclude that those local fluctuations are sufficient to destroy any magnetic order at $n = 1$ (and in the U range considered here).

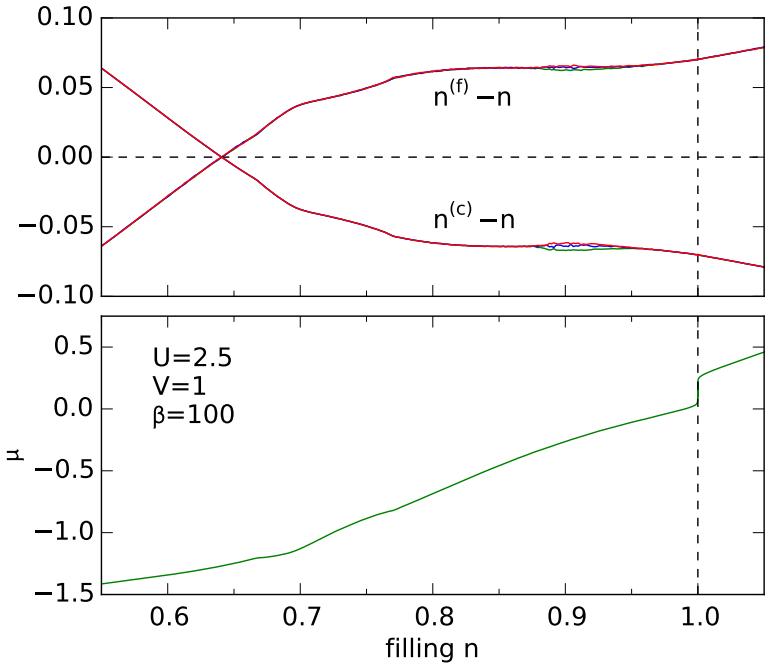

Figure 6.6.: *Upper panel:* Difference between the occupancy of the f (c) orbitals and the average filling, $n_\alpha^{(f)} - n$ ($n_\alpha^{(c)} - n$), as function of n. Results for different sites in the unit cell: A (green), B (blue), C (red). *Lower panel:* Chemical potential μ as function of n. Calculations for $U = 2.5$. Further parameters: $V = 1$, $\beta = 100$. Figure as printed within [AAP15]. *Copyright (2015) by the American Physical Society. Reproduced with permission.*

6.3.3. Metallic Kondo singlet phase

For fillings slightly off half-filling, the system becomes immediately metallic and has a finite charge compressibility $\kappa > 0$ (see lower panels of figs. 6.6 and 6.7). Actually κ turns out as non-zero for any filling. Opposed to previous HF calculations [HUM12], this implies that there is no instability towards phase separation.

The local correlations between f and c spins are strongly antiferromagnetic as indicated by a corresponding antiferromagnetic linear response. Still, there is no magnetic order for fillings $n \lesssim 1$. We refer to this paramagnetic metallic state with local antiferromagnetic correlations as a heavy-fermion or Kondo singlet state even if the local spin on the f orbitals,

$$\mathbf{S}_\alpha^{(f)} = \frac{1}{2} \sum_{\sigma\sigma'} f_{\alpha\sigma}^\dagger \sigma_{\sigma\sigma'} f_{\alpha\sigma'} \,,$$

cannot be seen as a rigid spin-$S = 1/2$ since the local f moment $\left(\boldsymbol{S}_\alpha^{(f)}\right)^2$ somewhat deviates from $S(S+1) = 3/4$.

The respective top panels of figs. 6.8 and 6.9 show the f orbital double occupancy relative to its

non-interacting value, i.e.,

$$D_\alpha \equiv \langle f^\dagger_{\alpha\uparrow} f_{\alpha\uparrow} f^\dagger_{\alpha\downarrow} f_{\alpha\downarrow} \rangle / (n^{(f)}_{\alpha\uparrow} n^{(f)}_{\alpha\downarrow}) \,.$$

While the double occupancy is suppressed considerably for fillings close to half-filling, it is still far from zero even at $U = 3.5$ (c.f. fig. 6.9), for example, where $D_\alpha \approx 0.45$. At $U = 2.5$ (c.f. fig. 6.8) we find D_α at a minimum for $n \approx 0.65$.

6.3.4. Antiferromagnetism

Magnetic phases first appear at fillings centered around $n \approx 0.92$ for $U = 2.5$ and for $U = 3.5$ (c.f. figs. 6.8 and 6.9). This is the filling range where the f occupancy is at or very close to unity and where, despite substantial charge fluctuations, the local-moment picture is most adequate. The magnetic coupling between the local moments must be provided by the *a priori* uncorrelated c orbitals, similar to the standard RKKY mechanism [RK54; Kas56; Yos57] that can be derived perturbatively in the Kondo lattice model (KLM) (see section 2.4, page 18 ff.and section 3.2, page 27 ff.).

On the triangular lattice, however, magnetic order induced by indirect antiferromagnetic exchange is frustrated. Except for a non-magnetic state, there are two obvious possible compromises to form a state with vanishing total magnetic moment in the unit cell, namely a state with 120° orientations between pairs of magnetic moments as well as a collinear $\uparrow, \uparrow, \downarrow$ phase. Apart from the PKS phase to be discussed below, the latter is the only plausible antiferromagnetic state if collinearity between the moments is enforced as is done here.

For $U = 3.5$ and with decreasing filling n the system undergoes a phase transition to the AFM phase at $n \approx 0.97$. Figure 6.9 demonstrates that this phase transition is continuous with the staggered magnetization m_0 (see definition above) as an order parameter that evolves from $m_0 = 0$ and increases with decreasing n in a continuous way. The magnetism is predominantly carried by the f moments with a maximum of $|m^{(f)}_B| \approx 0.6$ while the c orbitals are by about one order of magnitude less polarized (note the different scales in fig. 6.9). Note that the site-dependent moments are oriented antiparallel to the respective f moments.

Across the transition to the AFM phase there is hardly any change of the double occupancy $\langle f^\dagger_{\alpha\uparrow} f_{\alpha\uparrow} f^\dagger_{\alpha\downarrow} f_{\alpha\downarrow} \rangle$, i.e., the increase of D_α seen in fig. 6.9 (top panel) is mainly due to the polarization of the f orbital only. For the "$\downarrow$" site in the $\uparrow, \uparrow, \downarrow$ state this effect is a bit stronger as its magnetic moment has the higher absolute value. The fact that the double occupancy and thus the size of the local f moment is basically unaffected, favors a picture of magnetic ordering of preformed local moments and is consistent with an RKKY-like indirect exchange mechanism in the local-moment regime of the Anderson lattice.

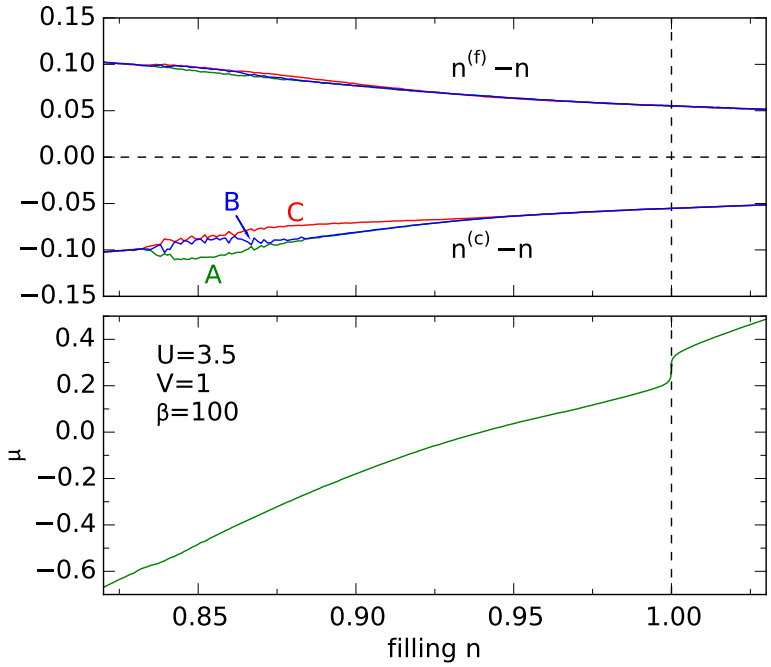

Figure 6.7.: The same as fig. 6.6 but for $U = 3.5$. Results for different sites in the unit cell: A (green), B (blue), C (red), as indicated. Figure as printed within [AAP15]. *Copyright (2015) by the American Physical Society. Reproduced with permission.*

6.3.5. Partial Kondo screening

With further decreasing n at $U = 3.5$ there is another second-order phase transition from the AFM state to a phase with partial Kondo screening (PKS) (see fig. 6.9). For $U = 2.5$ the PKS phase directly evolves from the KS through a second-order transition (see fig. 6.8). In both cases, a Kondo singlet formed at one site in the unit cell, say A, coexists with a non-local pair of antiferromagnetically coupled moments at the B and C sites. The total ordered moment in a unit cell is zero. Eventually, for fillings $n < n_{c1} \approx 0.88$ at $U = 2.5$ and for $n < n_{c1} \approx 0.82$ at $U = 3.5$, the system returns to a paramagnetic KS state in another continuous phase transition.

As compared to the AFM and also, at even lower fillings, to the FM phase, the numerical stabilization of a self-consistent PKS solution is most difficult, i.e., a large number of iterations (up to 200) is required. This also reflects itself in the remaining (nonphysical) noise on the PKS data seen in figs. 6.8 and 6.9. As a technical remark, let us mention that each DMFT run is completely independent from the preceding one and starts from the same initial guess for the self-energy which is taken as frequency independent and homogeneously spin-polarized. Due to this independency, the self-consistent values for the magnetic moments typically do not always form continuous functions of μ, because arbitrary permutations of the A, B, C sites in a unit cell and also a global sign change $\sigma \to -\sigma$ yield physically equivalent solutions of the DMFT equations. We have employed those symmetry operations *a posteriori* in scans with extremely small steps in

the chemical potential ($\Delta\mu = 0.007$) to generate functions as continuous as possible by means of least-square fits minimizing the parametric distance between pairs of consecutive self-consistent solutions.

The Kondo effect requires a locally antiferromagnetic effective coupling between the local f and c spins (c.f. section 2.4, page 18 ff.). This is clearly present: As mentioned above, the linear response of the c moments to a static magnetic field applied to the f electron spins is found as antiferromagnetic in paramagnetic phase close to the AFM and PKS phase. Furthermore, within the symmetry-broken PKS phase, the ordered moments $m_\alpha^{(f)}$ and $m_\alpha^{(c)}$ are antiferromagnetically aligned on the B and C sites. On the other hand, the robustness of the PKS phase, i.e., its extension in the $U - n$ plane, and also the presence of strong charge fluctuations, see the sizable double occupancy in figs. 6.8 and 6.9, suggest that the physics is non-universal and by no means ruled by a single Kondo scale T_K.

It is interesting to note that our data unambiguously show that there is no "perfect" partial Kondo screening. Namely, a slight polarization $m_A^{(f)} < 0$ and $m_A^{(c)} > 0$ of the local f and c spins on the A, i.e., on the Kondo site is clearly visible in figs. 6.8 and 6.9. The proximity to the pair of RKKY-like antiferromagnetically coupled moments, which explicitly breaks time-reversal symmetry, implies that there are admixtures of states with non-zero spin quantum number to the Kondo *singlet*. Assuming this admixture to be given by a single spin-triplet state for simplicity, the antiferromagnetic environment explains a coupling to the $M = 0$ component of the triplet. A finite polarization of the Kondo singlet, however, rather requires a coupling to the $M = \pm 1$ components and thus implies the additional breaking of the Z_2 symmetry of the antiferromagnetic state. This spontaneous symmetry breaking in the PKS phase is also visible in the magnitudes of the B- and C-site moments, namely $|m_C^{(f)}| > |m_B^{(f)}|$, and is present in the "↑, ↑, ↓" AFM state anyway.

Accompanying the ordering of the spin degrees of freedom, there is a also a (weak) charge ordering in the AFM and the PKS phase (see upper panels of figs. 6.6 and 6.7). There are two interesting observations: First, the deviation of the charge density from the average density is much stronger on the c orbitals as must be expected in the local-moment regime where charge fluctuations on the correlated f orbitals are very effectively suppressed. This effect is stronger for $U = 3.5$ and compared to $U = 2.5$. Second, within the PKS phase, there is a charge transfer from the "Kondo site" (A) to the "magnetic sites" (B, C): $n_\mathrm{A}^{(c)} < n_\mathrm{B,C}^{(c)}$ and $n_A^{(f)} < n_\mathrm{B,C}^{(f)}$. Due the Kondo effect, the local conduction-electron density of states at the A site will develop a dip, and spectral weight must be shifted above or below the Fermi energy. In the absence of particle-hole symmetry, this shift is asymmetric and changes the occupancy. The sign and the size of the resulting charge transfer, however, depend on the *details* of the band structure. Charge disproportionation was also found within the PKS (*partial disorder*) state that is obtained by means of the HF approach [HUM11; HUM12]. Opposed to our DMFT results, the charge transfer seen in the HF studies is much larger for the f as compared to the c orbitals. This must be seen as an artifact of the static mean-field approach which cannot account for local-moment formation.

As a function of U, the PKS phase is located between the KS and the AFM phase in the phase diagram. This can be understood by referring to the famous Doniach diagram [Don77] as reviewed in section 3.2 on page 27. In the KS phase at weaker U (stronger J) the Kondo effect dominates

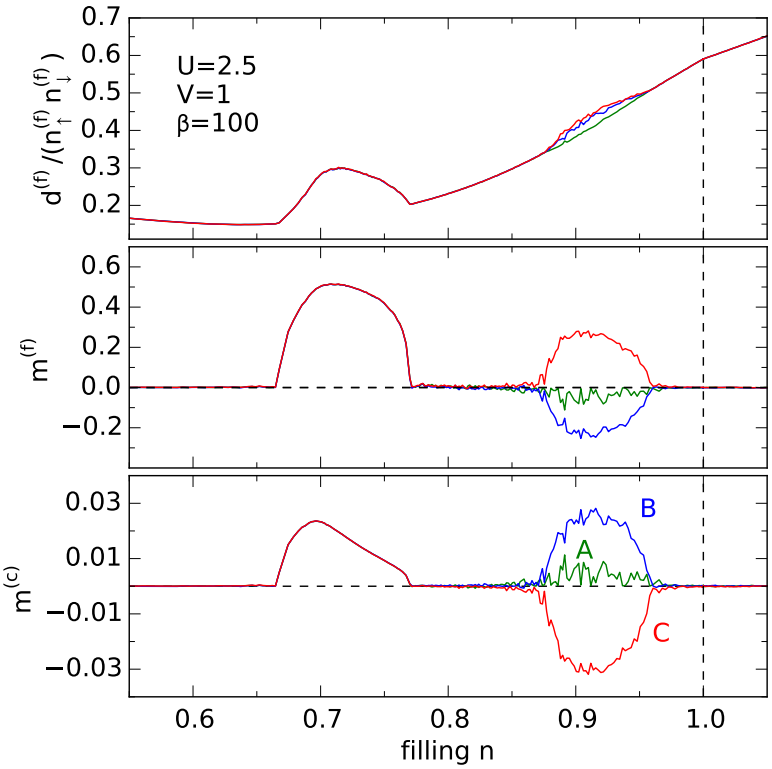

Figure 6.8.: *Top panel:* Filling dependence of the f-orbital double occupancy $d_\alpha^{(f)} = \langle f_{\alpha\uparrow}^\dagger f_{\alpha\uparrow} f_{\alpha\downarrow}^\dagger f_{\alpha\downarrow}\rangle$ (relative to its non-interacting value $n_{\alpha\uparrow}^{(f)} n_{\alpha\downarrow}^{(f)}$) for $U = 2.5$. Results for different sites A (green), B (blue), C (red) in the unit cell as indicated.
Middle and bottom panels: f and c ordered magnetic moments, $m_\alpha^{(f)}$ and $m_\alpha^{(c)}$ at the different sites in the unit cell for $U = 2.5$ as functions of n. Figure as printed within [AAP15]. *Copyright (2015) by the American Physical Society. Reproduced with permission.*

while for strong U (weak J) the RKKY interaction is dominant and results in magnetic order. The PKS state can be seen as a possible way to avoid geometrical frustration in the antiferromagnetically ordered state which is preferred if the formation of a Kondo singlet is less expensive than breaking up two frustrated magnetic bonds and forming a non-frustrated third one. As a compromise between indirect exchange, frustration and the Kondo effect, it appears between the KS and the AFM phase.

6.3.6. Ferromagnetism

At lower fillings around $n = 0.7$, depending slightly on U, the system develops homogeneous ferromagnetic (FM) order (see fig. 6.3). As can bee seen from fig. 6.8 for $U = 2.5$, the transition to this state is continuous at the lower as well as at the upper critical density. The ferromagnetic state is metallic with a finite compressibility (see fig. 6.6) and partially polarized with a maximum

ordered f moment of $m^{(f)} \approx 0.52$ at $n \approx 0.71$. The moment on the conduction-electron orbitals ($m^{(c)} \approx 0.02$) is more than an order of magnitude smaller and *ferromagnetically* aligned to the moment on the f orbitals.

Generally, there are several mechanisms that may cause metallic ferromagnetism [Mor85; Cap87; BDN01]: The main idea of the RKKY concept (c.f. section 3.2, page 27 ff.) consists in a magnetic coupling of well-formed local f moments in an effective KLM (see section 2.4, page 18 ff.) which is mediated by the conduction electrons and features ferromagnetic order if the effective RKKY coupling

$$J_{\mathrm{RKKY}}(\boldsymbol{q}) = -J^2 \chi_s(\boldsymbol{q}, \omega = 0)\,,$$

where χ_s is the conduction-electron spin susceptibility, is peaked at wave vector $\mathbf{q} = 0$. While the RKKY theory is a perturbative approach ($J \to 0$), the double-exchange mechanism [Zen51; Gen60; Koc12] applies to the strong-J regime of a Kondo lattice and predicts that a ferromagnetic ordering of the f moments minimizes the kinetic energy of the conduction electrons.

It is questionable, however, if those concepts apply here as there are strong charge fluctuations preventing the formation of well-defined f moments in our case. This is obvious from the sizable deviation of the f occupancy from unity (see fig. 6.6, $n^{(f)} \approx 0.8$ in the relevant filling range). Another clear indication that the system is no longer in a local-moment regime is the ferro- rather than antiferromagnetic coupling between f and c moments (see middle and lower panel of fig. 6.8 around $n = 0.7$). This is incompatible with an effective low-energy Kondo model.

It is interesting to note that this implies a filling-dependent crossover from the local-moment regime with a locally antiferromagnetic coupling between f and c moments (see $m_\alpha^{(f)}$ and $m_\alpha^{(c)}$ in fig. 6.8 in the PKS and AFM phases) to a mixed-valence regime. This can also be verified easily by studying the linear response in the paramagnetic phase separating the FM and the PKS phase in fig. 6.3: By applying a weak magnetic field to the f moments, one finds that the local coupling between f and c moments changes from antiferro- to ferromagnetic with decreasing filling.

At $U = 0$ the static off-diagonal f-c magnetic spin susceptibility can be computed easily in the entire filling range. Except for low fillings around and below $n \approx 0.25$, corresponding to the van Hove singularity of the density of states close to the lower band edge (see fig. 6.5), the local response is found as antiferromagnetic for $n < 1$. Above half-filling, the response turns to ferromagnetic and is at a maximum for $n \approx 1.2$ corresponding to the van Hove singularity at $\omega \approx 0.4$ (see fig. 6.5). We conclude that the FM phase cannot be understood as an instability of the Fermi sea in the weak-U regime. Just the opposite, the paramagnetic state from which the ferromagnetic phase evolves should be considered as strongly correlated. Already for $U = 2.5$, the double occupancy is strongly suppressed and D_α is in fact at a minimum for $n \approx 0.65$ (see fig. 6.8).

The importance of a strong asymmetry of the density of states for metallic ferromagnetism at strong and intermediate interaction strengths has been emphasized by DMFT studies of the single-band Hubbard model [Ulm98; Pot+98; Vol+99; PP09]. The key idea is that in a situation where double occupancies are effectively suppressed, the system does not gain much interaction energy from ferromagnetic ordering. Therefore, the appearance of ferromagnetism must be understood by referring to the (complicated) kinetic energy of the correlated paramagnetic

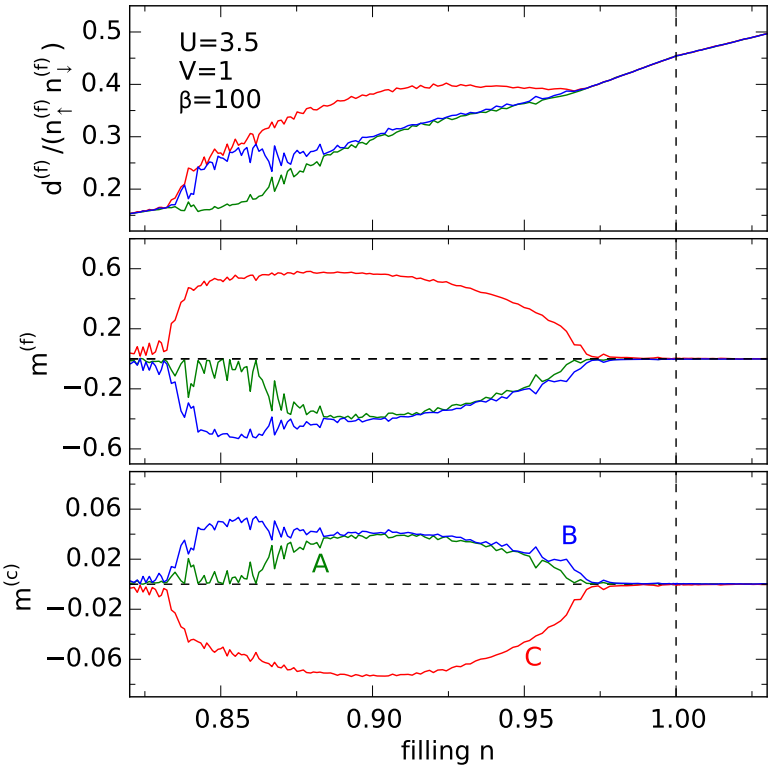

Figure 6.9.: The same as fig. 6.8 but for $U = 3.5$ and for a smaller filling range. Figure as printed within [AAP15]. *Copyright (2015) by the American Physical Society. Reproduced with permission.*

state from which it derives. Within DMFT this suggests that the *shape* of the non-interacting density of states becomes important. In fact, studying the impact of a shape-controlling parameter [Wah+98], ferromagnetism was demonstrated to be favored in cases with a highly *asymmetric* density of states, in a parameter range where the density of states is *high*, and at strong to intermediate interaction strengths.

We propose that a similar line of reasoning applies to the PAM in the considered parameter region: Even at $U = 2.5$ and all the more for stronger U, double occupancies are strongly suppressed, and the gain in kinetic energy obtained by ferromagnetic ordering is dictated by a strongly asymmetric partial f density of states. The filling range where ferromagnetism is likely to occur, is then indicated by a corresponding high density of states. Note that $n = 0.7$ corresponds to a non-interacting chemical potential of $\mu \approx -0.62$ which is already close to the van Hove singularity (at $\omega = -0.18$). Substantially higher fillings would be even more favorable for ferromagnetism, but here the crossover to the local-moment regime and the developing antiferromagnetic correlations overwrite the ferromagnetic tendencies.

This picture also explains why the FM phase shifts to lower fillings with increasing U in fig. 6.3: Stronger interactions favor ferromagnetism and extend the FM phase to a larger filling range as

is again well known from the single-band case [Wah+98]. This explains the decrease of the lower critical filling for the FM phase with increasing U. At the same time, however, an increasing U favors local-moment formation, and therefore the KS phase with antiferromagnetic correlations extends at the cost of the mixed-valence regime. This explains the decrease of the upper critical filling with increasing U.

Previous work [YS93; MW93; TJF97; DS98; MN00; BBG02] on ferromagnetism in the PAM has been done using different theoretical approaches and in largely different parameter regimes. Nevertheless, ferromagnetic order away from half-filling appears as a robust result. As basically all studies have exclusively been performed for bipartite lattices, a direct comparison with our results is not possible. There are, however, close similarities with the results of a DMFT study by Meyer and Nolting [MN00] which, for a Bethe lattice with infinite connectivity, demonstrates that ferromagnetism appears in the mixed-valence regime for a finite filling range. This study also points out a crossover from antiferro- to ferromagnetic coupling between f and c magnetic moments with decreasing filling, consistent with our findings, and suggests a mechanism based on an effective single-band model with strongly correlated and itinerant electrons—an idea that was formalized later on by Batista, Bonca, and Gubernatis [BBG02].

6.4. Conclusions

Our sdDMFT study of the magnetic phase diagram of the PAM on the triangular lattice has uncovered a surprisingly complex phenomenology which could be traced back to a competition between several physical mechanisms at work. In particular, the phase diagram is governed by:

- The *formation of local magnetic moments* on the f orbitals. Due to the non-bipartite structure of the triangular lattice, half-filling of the f orbitals is found for total fillings below half-filling, around $n \approx 0.9$, weakly depending on U. Here, the low-energy physics is well captured by an effective Kondo lattice although there are sizable f charge fluctuations for the weak- to intermediate-coupling regime considered here ($U \leq 4$). At somewhat lower fillings, there are still well-developed local f moments, but the charge fluctuations increase since the f electrons become itinerant.

- *Mixed-valence physics* with strong charge fluctuations on the f orbitals, even at stronger U, replaces the local-moment regime for lower fillings (roughly below $n \approx 0.75$, depending on U). The filling-dependent crossover from the local-moment to the mixed-valence regime is accompanied by a reversal of the effective local exchange between the local f and c spins from antiferromagnetic to ferromagnetic.

- An *RKKY-like indirect magnetic exchange* between the f magnetic moments induces antiferromagnetic order for sufficiently strong U within the local-moment regime. As we have enforced spin structures to be collinear, this results in an "↑, ↑, ↓" AFM phase on the triangular lattice which possibly mimics "classical" 120° AFM order.

- The *Kondo effect* competes with the indirect exchange in the spirit of the Doniach phase diagram as presented by means of fig. 3.4 on page 31. At low temperatures, besides magnetic ordering, the large entropy carried by the local-moment system can be removed by screening the f moment in a Kondo singlet with the conduction-electron spin degrees of freedom. With decreasing U, and prior to charge fluctuations becoming dominant, this Kondo singlet (KS) phase replaces the antiferromagnetic order. Kondo physics is also dominating for lower fillings around $n \approx 0.8$, depending slightly on U, as well as for fillings very close to and at half-filling. The hybridization band gap in the non-interacting density of states results in a band insulator at half-filling for $U = 0$ and develops into a correlated Kondo insulator with increasing U.

- *Geometrical frustration* affects the competition between Kondo screening and RKKY coupling. At the border between the AFM and KS phase, it becomes favorable to avoid frustration by partial Kondo screening of one f moment per unit cell. This allows the remnant moments to form an nonfrustrated RKKY-coupled collinear antiferromagnet. The PKS phase is metallic, and it supports a (weak) charge-density-wave ordering in addition, mainly on the c orbitals. Although it results from a compromise between Kondo screening, RKKY coupling and frustration, the PKS state has turned out to be surprisingly robust. It appears in an extended parameter range and does not need any anisotropic terms in the Hamiltonian [Mot+10]. Due to proximity to the time-reversal-symmetry-breaking RKKY-coupled remnant moments, the partial Kondo screening is imperfect resulting in a tiny magnetic moment on the f and, antiferromagnetically aligned, on the c orbital at the “Kondo site”.

- *Strong correlations among itinerant electrons* give rise to a metallic and partially polarized ferromagnetic phase in the mixed-valence regime. In this case, the non-bipartite lattice structure favors magnetic order as it produces a highly asymmetric non-interacting density of states which is known to crucially affect the kinetic-energy balance favoring ferromagnetism in a range of fillings with high density of states at the Fermi level and where antiferromagnetic correlations are subdominant. As a non-perturbative effect, this itinerant-electron ferromagnetism lacks a clear (simple) mechanism—even in a single-band Hubbard model.

By that we close the chapter on our studies of the triangular PAM thereby referencing to chapter 8 on page 117 ff. for some concluding remarks. In the next chapter, we will change the model geometry form triangular to depleted for DMFT calculations in regard to the crossover from conventional to inverse indirect magnetic exchange (IIME).

7. Magnetic order and exchange in the depleted periodic Anderson model

In the preceding chapter 6 we presented our site-dependent dynamical mean-field theory (sdDMFT) studies of the geometrical frustrated Anderson lattice by means of a triangular lattice structure. In this chapter we leave the triangular geometry for Anderson lattices with regularly depleted impurities of different dimension—cubic, square and one dimensional. Again, like in chapter 6, we are principally interested in the finite-temperature properties of such structures but for different reasons.

Major parts of this chapter were already published as

> M. W. Aulbach, I. Titvinidze, and M. Potthoff. "Crossover from conventional to inverse indirect magnetic exchange in the depleted Anderson lattice". In: *Phys. Rev. B* 91 (17 May 2015), p. 174420. *Copyright (2015) by the American Physical Society. Reproduced with permission.*

All presented numerical results were simulated by means of our numerical setup as described in chapters 4 and 5, especially section 4.3 on page 37 and the following. Necessary calculations were entirely performed on clusters of the PHYSnet Rechenzentrum of the University of Hamburg and the SuperMUC super computer cluster of the Leibniz Rechenzentrum MunichPresented results derived im terms of static mean-field theory (MFT) were kindly provided by our former colleague Irakli Titvenidze, while density matrix renormalization group (DMRG)/variational matrix product states (VMPS) data was made available by Andrej Schwabe. We gratefully thank both of them for this kind of assist. Support of our studies by the Deutsche Forschungsgemeinschaft within the SFB 668 (project A14), by the excellence cluster "The Hamburg Centre for Ultrafast Imaging – Structure, Dynamics and Control of Matter at the Atomic Scale" and by the SFB 925 (project B5) is gratefully acknowledged.

Like the partial Kondo screening (PKS) phase initially was the motivator for our studies of the triangular lattice, in regard to the depleted ones, we aim at experiencing the crossover from conventional to inverse indirect magnetic exchange (IIME) by means of our numerical setup—a site-selective dynamical mean-field approach as described in section 4.3, page 44 ff., combined with the continuous-time hybridization expansion (CT-HYB) segment code as reviewed in sections 5.4 and 5.5 on page 65 and the following. Thus, we try to stabilize this crossover between Ruderman-Kittel-Kasuya-Yosida (RKKY) (see section 3.2, page 27 ff.) interaction and IIME in terms of the dynamical mean-field approach by scanning from weak towards strong hybridization strengths V. We extend our studies to different model dimensions $D = 1$, $D = 2$ and $D = 3$, whereas for the

latter case we produce DMFT-results that are reliable in the spirit of the Mermin-Wagner theorem (c.f. section 3.3.1, page 31 ff.). Generated results are compared with those provided by a static mean-field approximation for an effective low-energy spin-only model emerging perturbatively in the strong-coupling limit. Independently, we will prove the theoretical prediction of the Curie temperature to be located at a maximum for a half-filled conduction band and at intermediate hybridization strengths in the crossover regime between RKKY and IIME.

All this is organized as follows: After a motivation (see section 7.1) we will directly proceed with the mean-field studies by means of the mentioned effective model in section 7.2. This sets the basement for a comparison with DMFT results emerging from the application of our numerical setup as described by section 4.3, page 44 and the following. Appropriate explanations and results are presented in section 7.3. The chapter is closed by a global summary in section 7.4.

7.1. Introduction

It was pointed out by Nozières some decades ago that the presence of a correlated impurity in an *a priori* uncorrelated metal introduces *effective* interactions among the conduction electrons [Noz74; NOZ76; NB80]. The range of these interactions decisively depends on the strength of the impurity-host coupling. Consider the case of an Anderson impurity model (AIM) that could alternatively to eq. (2.18) on page 17 be described by

$$\begin{aligned} H = &-t \sum_{\langle i,j\rangle} \sum_{\sigma=\uparrow,\downarrow} c^\dagger_{i\sigma} c_{j\sigma} + V \sum_{\sigma=\uparrow,\downarrow} \left(c^\dagger_{i_0\sigma} f_\sigma + \text{h.c.} \right) \\ &+ U(f^\dagger_\uparrow f_\uparrow - 1/2)(f^\dagger_\downarrow f_\downarrow - 1/2)\,, \end{aligned} \tag{7.1}$$

with annihilators $c_{i\sigma}, f_\sigma$ referring to local conduction-electron and impurity orbitals, respectively. For the case of a Hubbard interaction U and a local hybridization V much stronger than the nearest-neighbor conduction-electron hopping t, an effective Hamiltonian with an almost local interaction characterizing the low-energy physics of the conduction-electron system can be derived explicitly [TSP15]. This is achieved by means of degenerate fourth-order perturbation theory in the hopping terms which connect the neighboring conduction-electron sites to the site i_0 where the impurity is coupled to. To leading order, the effective model is given by

$$H_{\text{eff}} = -t \sum_{\langle i,j\rangle}^{i,j\neq i_0} \sum_{\sigma=\uparrow,\downarrow} c^\dagger_{i\sigma} c_{j\sigma} - \frac{z^2\alpha}{3} \mathbf{S}^2_{\text{bond}}\,, \tag{7.2}$$

where z is the coordination number of the lattice, where

$$\alpha = t^4 \frac{U^3 + 48UV^2}{24V^6} \tag{7.3}$$

is the effective interaction strength, and where $\mathbf{S}_{\text{bond}}$ is the spin-operator referring to the "bonding" symmetric linear superposition of the z orbitals neighboring i_0 (see [TSP15] for details).

There are three different energy scales to be considered:

- Local singlet formation at i_0 takes place on the high-energy scale $\sim U, V$. While this singlet may be called a local *Kondo* singlet, its binding energy scales linearly with V for strong V. This is opposed to the weak-coupling limit $V \to 0$ (with $U \gg t$ fixed) where it is exponentially small and where the low-energy physics is dictated by a single Kondo scale [Wil75; Hew93].

- On an energy scale $\sim t$, conduction electrons scatter at the local Kondo singlet. This scattering effect is already included at zeroth order in the perturbative expansion and is formally described by excluding the site i_0 from the summation in the first term of the effective Hamiltonian in eq. (7.2).

- The first non-trivial effect takes place at fourth order. An effective interaction among the conduction electrons in the immediate vicinity of the impurity emerges which is mediated by virtual excitations of the local Kondo singlet. This happens on the lowest energy scale given by the effective coupling constant α in the second term of eq. (7.2).

A fundamentally interesting question is whether the emergent *effective* interaction among the *a priori* uncorrelated conduction electrons can give rise to collective phenomena. This may be expected for a lattice variant of the model, i.e., for a system with a thermodynamically relevant concentration of impurities. The extreme case is a periodic Anderson model with a depleted system of "impurities" placed at every second site, i.e., on the B sites of a bipartite lattice consisting of sublattices A and B. Figure 7.1 displays an example for the $D = 3$ dimensional simple-cubic lattice. We consider a model with L sites ($L \to \infty$ in the thermodynamical limit) and $R = L/2$ impurities. The total number of electrons N satisfies $2R \leq N \leq 4R$ such that there are well-formed local Kondo singlets in the low-energy sector.

At fourth order, perturbation theory is essentially unchanged as compared to the impurity model eq. (7.1), since any local Kondo singlet, consisting of the correlated impurity coupled to an B-sublattice site, is surrounded by uncorrelated A-sublattice sites, and thus the same virtual processes lead to the same effective interaction. Therefore, the resulting effective Hamiltonian only involves A-sublattice sites and excess conduction electrons that are not absorbed in a local Kondo singlet. The hopping term becomes ineffective since the excess conduction electrons are confined between the local Kondo singlets surrounding each A site. Hence, we are left with a lattice model of A sites, made up by non-local spins $\mathbf{S}_{i,\mathrm{bond}}$ referring to the bonding orbital around each B site:

$$H_{\mathrm{eff}} = -\frac{z^2\alpha}{3}\sum_{i\in B}\mathbf{S}^2_{i,\mathrm{bond}}\,, \tag{7.4}$$

with

$$\mathbf{S}_{i,\mathrm{bond}} = (1/2)\sum_{\sigma\sigma'} b^\dagger_{i\sigma}\sigma_{\sigma\sigma'}b_{i\sigma'}\,,$$

where σ is the vector of Pauli matrices and where the creation operator of the bonding orbital around $i \in B$ is given by $b^\dagger_{i\sigma} = \sum_{j\in A}^{n.n.(i)} c^\dagger_{j\sigma}/\sqrt{z}$, i.e., the bonding one-particle orbital is the sym-

metric superposition of neighboring A-sublattice orbitals:

$$|\text{bond}\, i, \sigma\rangle = \sum_{j \in A}^{n.n.(i)} |j, \sigma\rangle / \sqrt{z} \qquad (i \in B)\,. \tag{7.5}$$

The effective spin-only model, given by eq. (7.4), is non-trivial as different non-local spins refer to overlapping orbitals and therefore do not commute. There is not much known about this model:

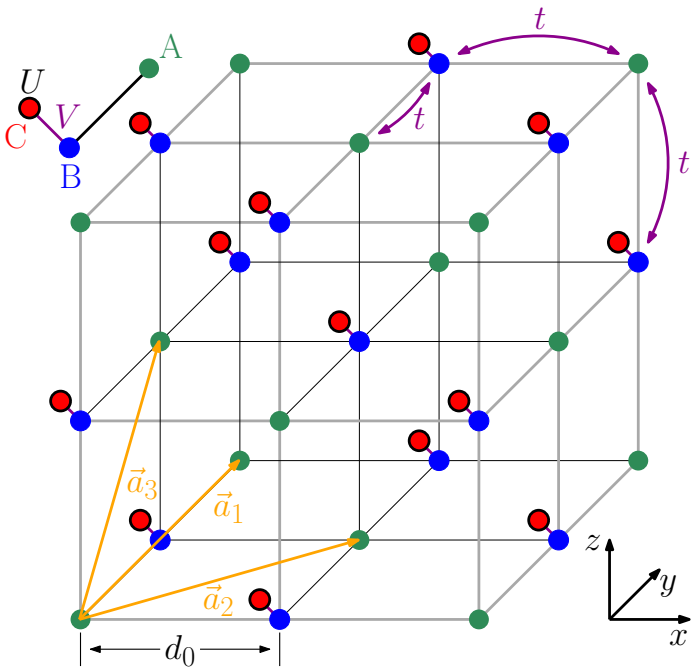

Figure 7.1.: Depleted periodic Anderson model with $R = L/2$ impurities on a $D = 3$-dimensional simple-cubic lattice with L sites ($L \to \infty$). Correlated impurities (C sites, red) with on-site Hubbard interaction U are coupled via a hybridization of strength V to the B sites (blue) of the bipartite lattice. For strong $U, V \gg t$, local Kondo singlets are formed on the half-filled "dimers" consisting of impurity and B sites (if the total electron number N satisfies $2R \leq N \leq 4R$) and strongly confine the motion of the excess conduction electrons on the A-sublattice sites (green). Virtual excitations of the local Kondo singlets induce an effective interaction of the conduction electrons on A sites. The nearest-neighbor hopping t between A and B sites fixes the energy scale: $t = 1$. Periodic boundary conditions are assumed. Figure as printed within [ATP15]. *Copyright (2015) by the American Physical Society. Reproduced with permission.*

At half-filling, $N = L + R = 3R$, one can rigorously show that a ferromagnetic state with fully polarized magnetic moments of the conduction electrons on the A sites is among the ground states [TSP15]. Exact diagonalization of small systems suggests [TSP15] that the model has a ferromagnetically ordered ground state in the filling range $2R < N < 4R$ (for lower or higher fillings, local Kondo singlets are broken up). An inverse indirect magnetic exchange (IIME) where the magnetic moments of A-site electrons are coupled ferromagnetically via virtual excitations of the local Kondo singlets has been identified as the main physical mechanism [STP13; TSP14]. For a one-dimensional depleted Anderson lattice, DMRG calculations have shown [STP13] that the

IIME mechanism gradually crosses over to a *conventional* (RKKY, see section 3.2, page page 27 ff.) indirect magnetic exchange, also favoring ferromagnetism, when varying V from strong to weak hybridization at fixed $U \gg t$. This crossover and the mutual interplay between RKKY and IIME mechanisms for the magnetic ground-state properties has recently been discussed in [SHP14] in the context of SU(N) models of ultracold Fermi atoms trapped in optical lattices.

The purpose of our studies as presented in the following is to study the finite-temperature properties of the depleted Anderson lattice, particularly the stability of the ferromagnetic order against thermal fluctuations. From the RKKY theory, one can expect $T_C \propto J^2 \propto V^4$ for the Curie temperature at weak V and in a parameter regime where the Schrieffer-Wolf transformation [SW66; SN02] (see also eqs. (2.22) and (2.28) in section 2.4, page 18 ff.) applies such that $J = 8V^2/U$ (c.f. eq. (2.24) on page 19). On the other hand, for strong V, the effective model (7.4) suggests that $T_C \propto \alpha \propto V^{-4}$. We therefore expect a pronounced maximum of T_C at an intermediate V. This optimal V but also the absolute value of T_C are interesting from a fundamental theoretical perspective. Not only the strong V dependencies but also the fact that the non-interacting ($U = 0$) depleted Anderson lattice exhibits a flat band at the Fermi energy [TSP14] promise a comparatively high value for the critical temperature. Furthermore, the finite-temperature properties are important for the question whether magnetic correlations and magnetic long-range order induced by the IIME can be verified experimentally. Candidate systems are magnetic nanostructures on non-magnetic surfaces as their geometrical and magnetic properties can be measured, controlled and manipulated to a high degree on a atomic scale [ES90; HLH06; Wie09; Kha+11; Kha+12]. Likewise, ultracold-atom systems come into question, due to the rapidly improving experimental techniques in this field and particularly due to the recent advances to employ fermionic alkaline-earth atoms to efficiently simulate systems with spin and orbital degrees of freedom [Kro+10; Sim+11; PHC13; Str+13; Hil+14; Sca+14; Cap+14].

In the scope of this chapter our study is based on two different types of mean-field methods: To address the strong-V limit, we apply static mean-field theory to the effective spin model eq. (7.4). Since $\mathbf{S}_{i,\mathrm{bond}}$ is not a rigid spin with $S = 1/2$, a fermion mean-field approach must be employed. Using this approximation, a rough estimate of the dependence of the Curie temperature on lattice dimension or coordination number and electron density is obtained. Secondly, we apply our site-dependent dynamical mean-field theory (sdDMFT) ansatz as presented in section 4.3 on page page 44 ff. to the depleted Anderson lattice. For a model with a depleted system of correlated sites, the DMFT can expected to yield reliable results since the electron self-energy is much more local as compared to the dense model. This has been checked for the $D = 1$ dimensional model where essentially exact results are available via the DMRG technique [STP13]. For ground-state properties of local observables as obtained by DMFT even quantitative agreement has been found.

7.2. Static mean-field theory

In the following we will present the mean-field part of this chapter, including the theoretical background, results and according discussion. The data and results presented in this section was

kindly provided by Irakli Titvenidze.

7.2.1. Depleted Anderson lattice revisited

Based on the Hamiltonian of the PAM (2.15) on page page 15 ff., the Hamiltonian of the depleted Anderson lattice is given by

$$\begin{aligned}\mathcal{H} = &-t \sum_{\langle i,j\rangle,\sigma} c^\dagger_{i\sigma} c_{j\sigma} + V \sum_{i\in B,\sigma} \left(c^\dagger_{i\sigma} f_{i\sigma} + \text{h.c.} \right) \\ &+ U \sum_{i\in B} n^{(f)}_{i\uparrow} n^{(f)}_{i\downarrow} - \mu \sum_{i,\sigma} n^{(c)}_{i\sigma} + (\varepsilon - \mu) \sum_{i\in B,\sigma} n^{(f)}_{i\sigma} . \end{aligned} \tag{7.6}$$

It describes a system of electrons hopping over the sites of a bipartite D-dimensional lattice consisting of L sites with periodic boundary conditions. The two sublattices are denoted by A and B. We consider a $D = 3$ simple-cubic lattice (see fig. 7.1) but also the corresponding one- and two-dimensional cases (figs. 7.2 and 7.3). As usually, $c^\dagger_{i\sigma}$ creates a conduction electron in a one-particle orbital with spin projection $\sigma = \uparrow, \downarrow$ at the site $i = 1, \ldots, L$. The nearest-neighbor hopping $t = 1$ sets the energy scale.

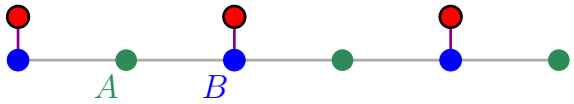

Figure 7.2.: Geometry of the one-dimensional diluted Anderson lattice. Red: "Impurities" with finite Hubbard interaction. Green and blue: sites of the A and of the B sublattice, respectively. Figure as printed within [ATP15]. *Copyright (2015) by the American Physical Society. Reproduced with permission.*

One-particle orbitals at the B sites of the lattice hybridize with orbitals at $R = L/2$ additional "impurity" sites (called C sites) with hybridization strength V. Additionally, $f^\dagger_{i\sigma}$ creates an electron at the impurity site attached to site $i \in B$ of the sublattice B. Furthermore, in the spirit of eq. (2.7) on page 11,

$$n^{(c)}_{i\sigma} = c^\dagger_{i\sigma} c_{i\sigma} \quad \text{and} \quad n^{(f)}_{i\sigma} = f^\dagger_{i\sigma} f_{i\sigma}$$

denote the occupation-number operators for A, B and for C sites, respectively. The f orbitals should be considered as magnetic orbitals: There is a finite repulsive Hubbard interaction U and the one-particle energy is set to $\varepsilon = -U/2$ such that, for strong U, the formation of local magnetic moments at the impurity sites is favored (compare to section 3.1, page 24 ff.).

The Hamiltonian (7.6) contains an overall chemical potential μ, i.e., according to our comments around eq. (3.10) on page 27, we work with the grand canonical ensemble where μ is used to fix the average number of particles $\langle N \rangle$. We will consider the range $2R \leq \langle N \rangle \leq 4R$ for our calculations.

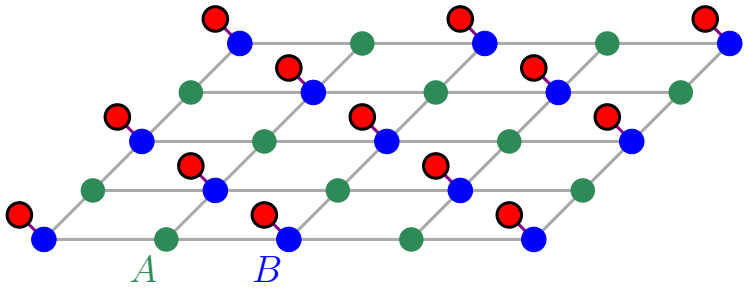

Figure 7.3.: The same as in figs. 7.1 and 7.2 for the two-dimensional case. Figure as printed within [ATP15]. *Copyright (2015) by the American Physical Society. Reproduced with permission.*

Switching off the hopping, i.e. $t = 0$, defines an atomic limit of the model (7.6). The ground state in the atomic limit is highly degenerate. For the considered range of the total electron number, each ground state is characterized by completely local Kondo singlets formed on the B and the attached C sites binding two electrons per singlet. The ground state degeneracy is due to the various configurations of remaining electrons on the A sites. Their density

$$n_{\mathrm{A}} = \sum_{i \in A, \sigma} \langle n_{i\sigma} \rangle / L_{\mathrm{A}} \,,$$

where $L_{\mathrm{A}} = L/2$ is the number of A sites, can vary within the range $0 \leq n_{\mathrm{A}} \leq 2$.

The depleted Anderson lattice (7.6) exhibits the conventional U(1) and SU(2) symmetries corresponding to conservation of the total particle number and the total spin. For $\mu = 0$ the system is half filled, i.e., $\langle N \rangle = 3R$ or $n_{\mathrm{A}} = 1$, and there is an additional SU(2) isospin symmetry [TSU97]. Due to particle-hole symmetry, we can restrict our considerations to the range at and below half-filling.

7.2.2. Strong-coupling limit

For strong $V \gg t$, an effective Hamiltonian $\mathcal{H}_{\mathrm{eff}}$ can be derived by means of fourth-order perturbation theory in t around the degenerate atomic limit [TSP15]. In this limit the ground state is characterized by local Kondo singlets at the B sites and a residual low-energy dynamics of the A-site electrons which is mediated by virtual high-energy excitations of the local Kondo singlets. Hence, $\mathcal{H}_{\mathrm{eff}}$ contains A-site degrees of freedom only. There is a very compact and highly symmetric representation of $\mathcal{H}_{\mathrm{eff}}$ given by eq. (7.4) with the coupling constant α specified by eq. (7.3). Details of the perturbation theory can be found in [TSP15].

Here, we rewrite the effective Hamiltonian such that a static mean-field decoupling, a common application of the mean-field idea as explained in section 4.1 on page 38 ff., can be applied in a straightforward way. To this end, we use the definitions given below (7.4) to express the non-local spin operators in terms of creators and annihilators for electrons on A sites. Furthermore, we

switch to a representation in reciprocal space by means of Fourier transformation in the form

$$c_{i\sigma} = \frac{1}{\sqrt{L_\mathrm{A}}} \sum_{\mathbf{k}\in \mathrm{BZ}_A} \mathrm{e}^{\mathrm{i}\mathbf{k}\mathbf{R}_i} c_{\mathbf{k}\sigma} \qquad (i \in A) \tag{7.7}$$

where $L_\mathrm{A} = L/2$ and where $\mathbf{k}$ is a wave vector in the Brillouin zone BZ_A of the reciprocal A sublattice. Note that the A sublattice is a square lattice for $D = 2$ but a b.c.c. lattice for the $D = 3$ case with a unit cell spanned by the basis vectors $\mathbf{a}_1, \mathbf{a}_2, \mathbf{a}_3$ displayed in fig. 7.1. With this we get:

$$\begin{aligned} \mathcal{H}_\mathrm{eff} = &\sum_{\mathbf{k}} (E(\mathbf{k}) - \mu) c^\dagger_{\mathbf{k}\sigma} c_{\mathbf{k}\sigma} \\ &+ \frac{1}{L_A} \sum_{\mathbf{p},\mathbf{q},\mathbf{k}} U_{\mathbf{pqk}} c^\dagger_{\mathbf{p}\uparrow} c_{\mathbf{p}-\mathbf{k}\uparrow} c^\dagger_{\mathbf{q}\downarrow} c_{\mathbf{q}+\mathbf{k}\downarrow} \,. \end{aligned} \tag{7.8}$$

The effective one-particle dispersion is given by:

$$E(\mathbf{k}) = -\frac{D\alpha}{2} \gamma^2(\mathbf{k}) \tag{7.9}$$

where $\varepsilon_0(\mathbf{k}) = -\gamma(\mathbf{k})t$ is the tight-binding dispersion of the D-dimensional lattice. This also determines the $\mathbf{k}$ dependence of the interaction parameters of the effective Hamiltonian via:

$$U_{\mathbf{p},\mathbf{q},\mathbf{k}} = \frac{\alpha}{2} \gamma(\mathbf{p})\gamma(\mathbf{q})\gamma(\mathbf{p}-\mathbf{k})\gamma(\mathbf{k}+\mathbf{q}) \,. \tag{7.10}$$

Apparently, the effective Hamiltonian describes itinerant electrons on the A sublattice with an interaction, the $\mathbf{k}$ dependence of which corresponds to the non-locality of the quartic parts of the Hamiltonian in real-space representation (7.4).

7.2.3. Mean-field approximation

Note that in the strong-coupling limit both, the one-particle part as well as the interaction, scale with α. Therefore, the standard mean-field decoupling of the interaction term,

$$\begin{aligned} c^\dagger_{\mathbf{p}\uparrow} c_{\mathbf{p}-\mathbf{k}\uparrow} c^\dagger_{\mathbf{q}\downarrow} c_{\mathbf{k}+\mathbf{q}\downarrow} \to &\langle c^\dagger_{\mathbf{p}\uparrow} c_{\mathbf{p}-\mathbf{k}\uparrow} \rangle c^\dagger_{\mathbf{q}\downarrow} c_{\mathbf{k}+\mathbf{q}\downarrow} \\ &+ c^\dagger_{\mathbf{p}\uparrow} c_{\mathbf{p}-\mathbf{k}\uparrow} \langle c^\dagger_{\mathbf{q}\downarrow} c_{\mathbf{k}+\mathbf{q}\downarrow} \rangle \\ &- \langle c^\dagger_{\mathbf{p}\uparrow} c_{\mathbf{p}-\mathbf{k}\uparrow} \rangle \langle c^\dagger_{\mathbf{q}\downarrow} c_{\mathbf{k}+\mathbf{q}\downarrow} \rangle \,, \end{aligned} \tag{7.11}$$

cannot be controlled by a small parameter but must rather be seen as a Hartree-Fock approach neglecting correlation effects in the low-energy sector and assuming a collinear and homogeneous structure of the magnetic moments. The formal advantage is that one obtains a mean-field Hamiltonian which allows for a straightforward study of the temperature dependence of the A-site magnetic moment and therewith gives access to the critical (Curie) temperature T_C. However, typical mean-field artifacts must be expected and tolerated.

Using the decoupling (7.11) in eq. (7.8), we obtain a mean-field Hamiltonian

$$\mathcal{H}_{\text{eff}} = \sum_{\mathbf{k},\sigma} (\eta_\sigma(\mathbf{k}) - \mu) c^\dagger_{\mathbf{k}\sigma} c_{\mathbf{k}\sigma} - \alpha \frac{L_A}{2} Q_\uparrow Q_\downarrow \tag{7.12}$$

which is bilinear in $c^\dagger, c$. The mean-field dispersion

$$\eta_\sigma(\mathbf{k}) = -\frac{\alpha}{2} (D - Q_{-\sigma}) \gamma^2(\mathbf{k}) \tag{7.13}$$

as well as the constant in eq. (7.12) depend on the possibly spin-dependent mean field Q_σ which must be determined self-consistently from the following mean-field equation:

$$Q_\sigma = \frac{1}{L_A} \sum_{\mathbf{k}} \gamma^2(\mathbf{k}) \frac{1}{\mathrm{e}^{\beta(\eta_\sigma(\mathbf{k})-\mu)} + 1} \,. \tag{7.14}$$

Here, according to our unit-conventions (1.1) on page 8, $\beta = 1/T$ and $k_B = 1$. The spin-dependent average A-site occupation number, $n_{\mathrm{A}\sigma} = \sum_{i\in A} \langle n_{i\sigma} \rangle / L_{\mathrm{A}}$ is obtained as

$$n_{\mathrm{A}\sigma} = \frac{1}{L_A} \sum_{\mathbf{k}} \frac{1}{\mathrm{e}^{\beta(\eta_\sigma(\mathbf{k})-\mu)} + 1} \,. \tag{7.15}$$

With this, the order parameter, i.e., the A-sublattice magnetization, is given by

$$m_{\mathrm{A}} = n_{\mathrm{A}\uparrow} - n_{\mathrm{A}\downarrow} \,.$$

Numerical calculations are performed by starting with a guess for the chemical potential and solving the coupled system of eqs. (7.13) and (7.14) self-consistently for each spin projection. From the self-consistent mean field Q_σ, we obtain $n_{\mathrm{A}\sigma}$ via eq. (7.15). In an outer self-consistency loop we then adjust the chemical potential until the total filling $n_{\mathrm{A}\uparrow} + n_{\mathrm{A}\downarrow}$ equals the given filling n_{A}. In the case of half-filling $n_{\mathrm{A}} = 1$, calculations are facilitated by particle-hole symmetry which fixes the chemical potential to $\mu = 0$.

7.2.4. Results of the mean-field approach

Calculations have been performed for lattices with different dimensions $D = 1, 2, 3$ (see figs. 7.1 to 7.3, respectively) as well as for different fillings n_{A} at and below half-filling. fig. 7.4 shows the resulting self-consistent mean fields Q_σ as functions of the temperature. For any D and n_{A}, there is a non-zero critical temperature T_{C} below which we find a spontaneous spin-splitting of the mean field. This supports the above-mentioned exact-diagonalization results of [TSP15] where a fully polarized magnetic ground state has been found for small one-dimensional systems in the filling range considered.

As can be seen in fig. 7.4 there is only a weak dependence of the mean field on the dimension D—after rescaling Q_σ with D or with the coordination number z. For $T = 0$, we have $Q_\downarrow = 0$ and thus the $\sigma = \uparrow$ mean-field dispersion simplifies to $\eta_\uparrow = -\alpha D \gamma^2(\mathbf{k})/2$ resulting in $Q_\uparrow = \max$.

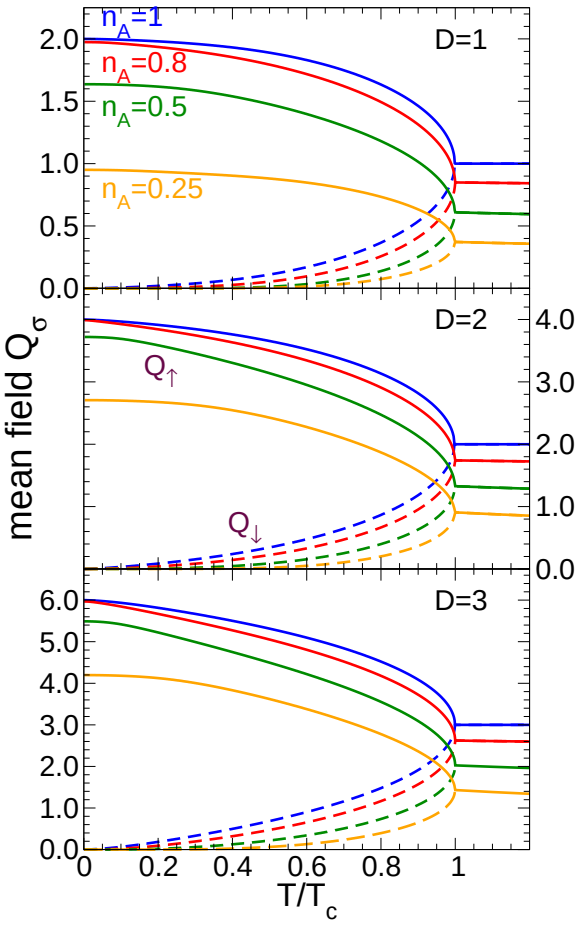

Figure 7.4.: Spin-dependent mean field (see eq. (7.14)) as a function of the reduced temperature T/T_C for different dimensions D (top, middle and bottom panel) and different fillings n_A as indicated (see top panel) at and below half-filling ($n_A = 1$). Solid lines: $\sigma = \uparrow$. Dashed lines: $\sigma = \downarrow$. Figure as printed within [ATP15]. *Copyright (2015) by the American Physical Society. Reproduced with permission.*

and, at half-filling, $Q_\uparrow = z$ since particle-hole symmetry enforces $Q_\uparrow - D = D - Q_\downarrow$. For T higher than the Curie temperature T_C, we have $Q_\uparrow = Q_\downarrow$. The spin-independent mean-field is slightly decreasing with increasing T, except for half-filling where $Q_\uparrow = Q_\downarrow = z/2 = \text{const.}$ above T_C.

The appearance of a symmetry-broken ferromagnetic state at finite temperatures for $D = 1$ and $D = 2$ is a typical mean-field artifact which is at variance with the Mermin-Wagner theorem. This is due to the missing feedback of long-range spin-wave excitations on the local observables within the mean-field approach (c.f. section 3.3.1, page 31 ff.). One therefore has to interpret the finite Curie temperature carefully as the temperature below which there is a formation of ferromagnetic correlations on a short length scale which corresponds to a thermodynamically stable ferromagnet only if the SU(2) symmetry is broken explicitly, e.g., due to the presence of additional anisotropic terms in the Hamiltonian.

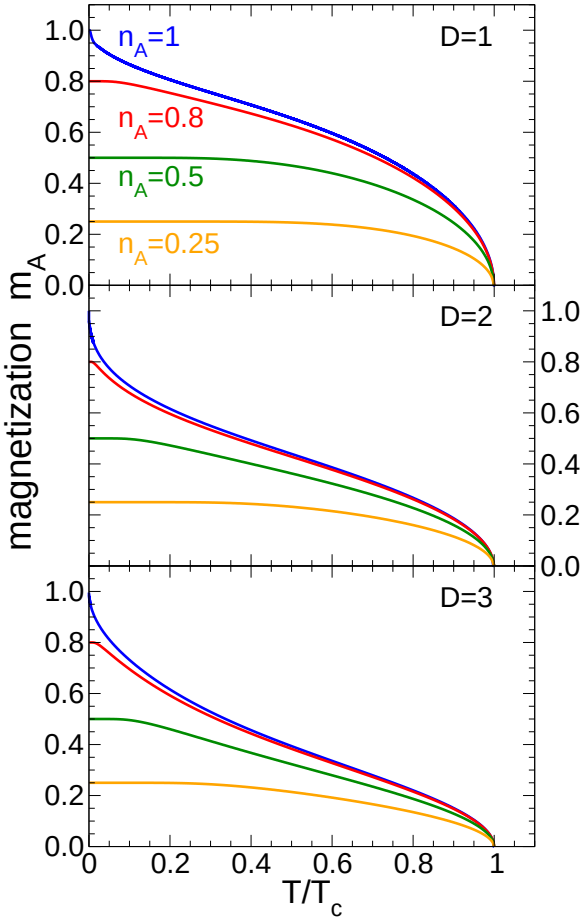

Figure 7.5.: Order parameter $m_A = n_{A\uparrow} - n_{A\downarrow}$ (see eq. (7.15)) as a function of T/T_C for different dimensions D and fillings n_A. Figure as printed within [ATP15]. *Copyright (2015) by the American Physical Society. Reproduced with permission.*

Figure 7.5 shows the temperature-dependent magnetization for the different fillings and dimensions. At zero temperature, the system is always fully polarized, i.e., $n_{A\downarrow} = 0$ and $n_{A\uparrow} = n_A$. Similar to the discussion of the mean fields, after rescaling the temperature with the respective Curie temperature T_C, there is a weak dependence of m_A on the dimension D at finite T. The phase transition from the ferro- to the paramagnetic state at T_C is of second order for any n_A. Close to the Curie point, we find a critical behavior of m_A characterized by the (mean-field) critical exponent for the magnetization $\beta = 0.5$, as expected.

The only unexpected result consists in the unconventional T-dependence of m_A at half-filling. While at low temperatures the missing feedback of long-wavelength spin excitations explains the absence of a power-law T dependence, one would expect, as a typical mean-field behavior, an exponential convergence of $m_A(T)$ for $T \to 0$ with a negative curvature and a vanishing slope $\lim_{T\to 0} dm_A/\mathrm{d}[T] = 0$. However, for $n_A = 1$, fig. 7.5 shows an inflection point of $m_A(T)$ at a finite temperature, which is increasing with increasing D, and an unusual upturn of m_A for

$T \to 0$. Closer inspection of the data shows that the slope is diverging:

$$\frac{dm_A}{d[T]} \sim -\frac{1}{\sqrt{\alpha D T}} \to -\infty \qquad (D = 1, D = 3) \tag{7.16}$$

and

$$\frac{dm_A}{d[T]} \sim \frac{\ln(T/\alpha)}{\sqrt{\alpha D T}} \to -\infty \qquad (D = 2)\,. \tag{7.17}$$

The reason of this behavior is a van Hove singularity of the spin-dependent mean-field local density of states (DOS) at the Fermi edge and is not further discussed, here, but in the Appendix of [ATP15]. From the temperature-dependence of the order parameter we can read off the Curie temperature. This is plotted in fig. 7.6 for different D as functions of the filling n_A. Since $T_C(n_A) = T_C(2 - n_A)$ due to particle-hole symmetry, we restrict ourselves to the range $n_A \leq 1$. Clearly, the Curie temperature must be proportional to the coupling constant α as there is a single energy scale in the effective Hamiltonian eq. (7.4).

Its geometry dependence is more interesting: Namely, T_C is by no means proportional to the coordination number as it typical for many mean-field approaches but is much more rapidly increasing with increasing z (note that the numerical results are scaled by a factor D^3 in fig. 7.6). This finding is not related to singularities in the DOS as it holds for any filling. We attribute the unconventionally high T_C to the non-locality of the interaction in the effective Hamiltonian and to the resulting $\mathbf{k}$-dependent contribution of the mean field to the mean-field dispersion in eq. (7.13).

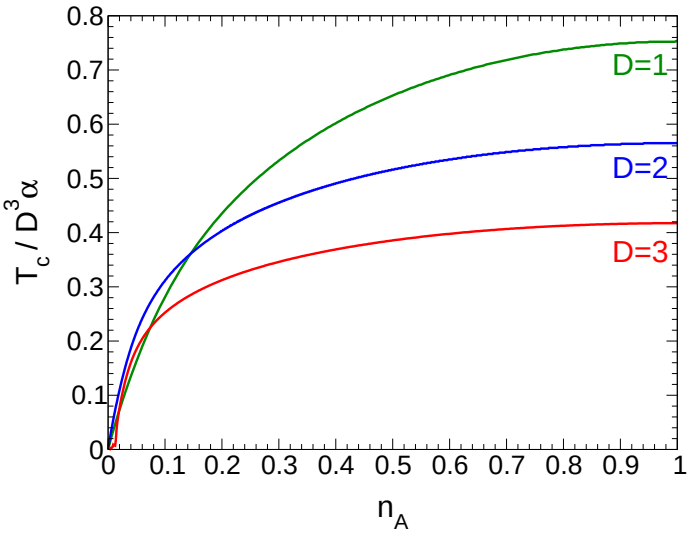

Figure 7.6.: Filling dependence of the Curie temperature for lattices with different dimensions as obtained from the static mean-field theory. Note that T_C is rescaled by D^3 and given in units of the coupling constant α. Figure as printed within [ATP15]. *Copyright (2015) by the American Physical Society. Reproduced with permission.*

7.3. Dynamical mean-field theory

Hereafter we technically will follow up our DMFT calculations of the triangular Anderson lattice as presented in chapter 6 on page 75 ff. by means of an examination of the regularly depleted PAM (7.6). By that, we will partially revisit, hence extend the theoretical background of DMFT in addition to that provided by sections 4.2 and 4.3 on page 40 and the following.

7.3.1. General theory revisited

As was argued in the introduction and additionally in section 4.2 on page 40 ff., DMFT [MV89; Geo+96] neglects the feedback of non-local, e.g. magnetic correlations, on the local self-energy and the local one-particle Green's function but correctly accounts for all local correlations. Particularly, the DMFT is able to describe the formation of local magnetic moments already in the paramagnetic phase of a lattice model of itinerant electrons, such that the phase transition between the paramagnetic and the ferromagnetic phase at T_C can be understood as a transition between well-formed but disordered moments and long-range order. This is opposed to the static theory where the local moments essentially vanish above the Curie point.

It is important to note that the feedback of non-local correlations neglected within single-site DMFT is much weaker for the depleted Anderson lattice considered here as compared to a lattice fermion model with a dense system of correlated sites. This can be understood in the following way: Formally, the only approximation to be tolerated within DMFT is the locality of the self-energy. For a dense lattice model, such as the Hubbard model, for example, the DMFT becomes exact in the limit of infinite spatial dimensions $D \to \infty$ since the nearest-neighbor elements of the self-energy scale as $1/D^{3/2}$ as can be inferred from its diagram expansion [Mül89b]. This is related to the scaling $1/D^{\|i-j\|/2}$ of the bare propagator, where $d \equiv \|i-j\|$ is the Manhattan distance between the orbitals at sites i and j of a hyper-cubic lattice of dimension D (compare to eq. (4.13) on page 42). For a depleted Anderson lattice on a high-dimensional bipartite lattice with a Manhattan distance d between the correlated sites, this also implies that the non-local elements of the self-energy exponentially diminish with increasing d. A completely local self-energy is realized in the single-impurity limit $d \to \infty$. For the Hubbard model ($d = 1$) and the PAM ($d = 3$) and for low dimensions, quantitative studies have been performed within second-order perturbation theory [SC90; SC91; PN97]. The case studied here corresponds to $d = 4$ but there are two, possibly largely different hopping parameters, t and V. For the ground state of the depleted Anderson lattice (with $d = 4$) in $D = 1$ dimension, a direct comparison between DMFT and essentially exact results obtained by the DMRG method has been performed in [STP13], and excellent agreement has been found for static local observables in the entire V/t regime. Comparing with DMRG, a quantitative discussion of the artifacts of the DMFT has been given in [Tit+12] for a $D = 1$ tight-binding model with two Anderson impurities. Concluding, we therefore expect that the DMFT yields reliable results.

Like it was done before in regard to the triangular lattice in section 6.2 according to the general recipe described in section 4.3, DMFT is easily adapted to the depleted model eq. (7.6) by means

of our site-selective extension: For any dimension D, there are three sites in a primitive unit cell of the lattice (see figs. 7.1 to 7.3). Hence, the single-particle Green's function $\mathbf{G}_{\mathbf{k}}(\omega)$ is a 3×3-matrix for any wave vector $\mathbf{k}$ in the first Brillouin zone of the A sublattice and for any one-particle excitation energy ω. Summation over $\mathbf{k}$ provides us with the local Green's function with, say, the (3,3) element referring to the impurity Green's function $\langle\langle f_{i\sigma}; f_{i\sigma}^{\dagger}\rangle\rangle_{\omega}$. Using Dyson's equation, this can be obtained from the local self-energy $\Sigma(\omega)$ in the fashion of eq. (4.27) on page 47 as

$$G_{\mathrm{loc}}^{(\alpha\beta)}(\omega) = \frac{2}{L} \sum_{\mathbf{k}\in \mathrm{BZ}_A} \left[\frac{1}{\omega + \mu - \varepsilon(\mathbf{k}) - \mathbf{\Sigma}(\omega)} \right]_{\alpha\beta} . \tag{7.18}$$

Here, particularly $\alpha, \beta = 1, 2, 3$ label the different sites in the unit cell to be chosen. Furthermore, for the depleted model $\mathbf{\Sigma}(\omega)$ is a 3×3 diagonal matrix with $\Sigma_{33}(\omega) = \Sigma(\omega)$ and $\Sigma_{11}(\omega) = \Sigma_{22}(\omega) = 0$, and

$$\varepsilon(\mathbf{k}) = \begin{pmatrix} 0 & \varepsilon_0(\mathbf{k}) & 0 \\ \varepsilon_0(\mathbf{k}) & 0 & V \\ 0 & V & \varepsilon \end{pmatrix} \tag{7.19}$$

is the lattice Fourier transform of the hopping parameters with $\varepsilon_0(\mathbf{k}) = -\gamma(\mathbf{k})t$.

The DMFT self-energy $\Sigma(\omega)$ is then again obtained as the impurity self-energy of an effective AIM specified by the Hubbard-U and a hybridization function in the fashion of eq. (4.28) on page 47 that is fixed by the self-consistency equation of DMFT. Concretely it reads

$$\Delta(\omega) = \omega + \mu - \varepsilon - \Sigma(\omega) - \frac{1}{G_{\mathrm{loc}}^{(33)}(\omega)} . \tag{7.20}$$

Here, the impurity one-particle energy is given by ε, and $\Sigma(\omega)$ must be determined self-consistently with eq. (7.18).

According to our calculations in chapter 6, we employ our CT-HYB segment code (see chapter 5, page 49 ff.) to compute the self-energy of the effective impurity problem at finite temperature T.

7.3.2. Results of the dynamical mean-field approach

From the results of static mean-field theory for the effective low-energy model eq. (7.4) in the strong V limit (see fig. 7.6) we infer that the Curie temperature is at a maximum for half-filling. More generally, we expect that at half-filling the stability of a ferromagnetically ordered state against thermal fluctuations is the highest not only for strong V but also for weak V, where the period of the RKKY interaction is commensurate with the positions of the correlated sites on the lattice. Furthermore, at half-filing and for the considered lattice geometries, the RKKY interaction is ferromagnetic. We will therefore restrict ourselves to the particle-hole symmetric case with the chemical potential fixed at $\mu = 0$ and with the one-particle energy of the impurities set to $\varepsilon = -U/2$ (see eq. (7.6)). We also fix the Hubbard interaction at an intermediate value $U = 8$ for the rest of the chapter. To discuss the crossover from the RKKY limit to the regime

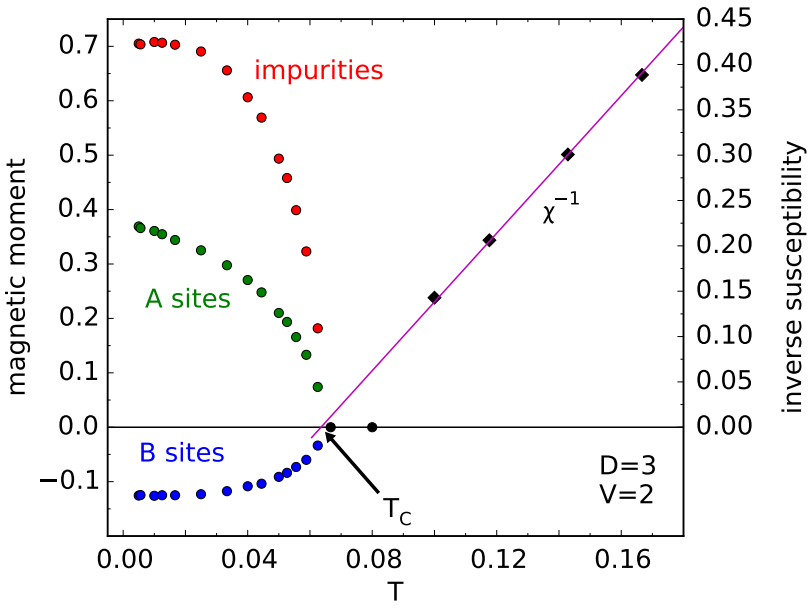

Figure 7.7.: Ordered magnetic moments m_A, m_B, m_{imp} (circles) on the A sites, the B sites and the impurity sites, respectively, and the inverse homogeneous static impurity magnetic susceptibility χ^{-1} (diamonds) as functions of temperature T as obtained by DMFT for the $D = 3$-dimensional depleted Anderson lattice (see fig. 7.1). Hubbard interaction: $U = 8$, hybridization strength: $V = 2$. The line indicates a linear fit to the trend of $\chi^{-1}(T)$. The temperature and energy scales are fixed by the nearest-neighbor hopping $t = 1$ (see eq. (7.6)). Figure as printed within [ATP15]. *Copyright (2015) by the American Physical Society. Reproduced with permission.*

of the inverse indirect magnetic exchange, we consider different hybridization strengths V. Due to relation (A.13) on page 123, by carrying out a sum over Matsubara frequencies in the style of eq. (4.30) that was given on eq. (4.30), one may easily compute the average spin-dependent occupation numbers on the A and B site,

$$n_{A\sigma} = \langle c^\dagger_{A\sigma} c_{A\sigma} \rangle \quad \text{and} \quad n_{B\sigma} = \langle c^\dagger_{B\sigma} c_{B\sigma} \rangle ,$$

from the local Green's function eq. (7.18), once self-consistency has been achieved. The average occupation numbers of the impurity site,

$$n_{imp,\sigma} = \langle f^\dagger_\sigma f_\sigma \rangle ,$$

are obtained in the same way, although could be measured equivalently within the CT-HYB approach directly by means of eq. (5.47) on page 71. We explicitly allow for symmetry-broken states with finite ordered magnetic moments m_A, m_B and m_{imp}, where we have defined

$$m_A = n_{A\uparrow} - n_{A\downarrow} ,$$

and m_B, m_{imp} analogously. It is found that magnetic solutions of the DMFT equations are easily stabilized in the entire range of hybridization strengths V considered (but for sufficiently low

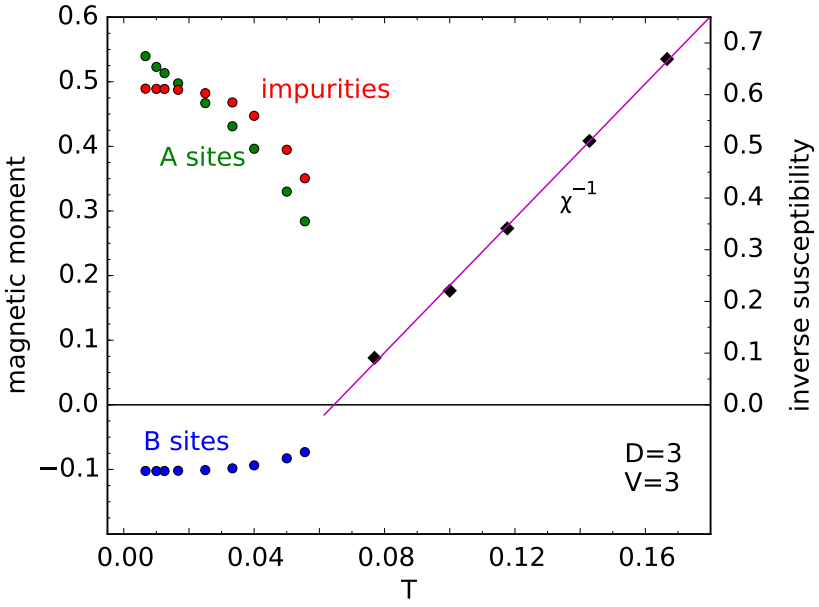

Figure 7.8.: The same as in fig. 7.7 but for $V = 3$. Figure as printed within [ATP15]. *Copyright (2015) by the American Physical Society. Reproduced with permission.*

temperatures) by starting the self-consistency cycle with a slightly spin-asymmetric initial self-energy. In addition, we also compute the homogeneous static impurity spin susceptibility of the paramagnetic state

$$\chi = \partial m_{\mathrm{imp}} / \partial B|_{B=0} \,.$$

Here, B is the strength of a homogeneous magnetic field coupling to the z-component of the total impurity spin as

$$H \longmapsto H - B \sum_{i \in B} (f^\dagger_{i\uparrow} f_{i\uparrow} - f^\dagger_{i\downarrow} f_{i\downarrow})$$

where H is given by eq. (7.6).

Figure 7.7 shows the results of a DMFT calculation at $V = 2$ for the $D = 3$-dimensional lattice with $L = 52^3$ sites, with additional $R = L/2$ impurities and periodic boundary conditions (see fig. 7.1). This is fully sufficient to ensure that the results do not significantly depend on L. Statistical errors of the quantities shown in this and in the following figures are smaller than the size of the symbols. A typical Monte Carlo (MC) run consists of more than 10^7 sweeps, and each sweep of more than k MC steps with k being the average expansion order. Less than 50 DMFT iterations are sufficient for convergence of the results within the statistical error. For high temperatures the system is in a paramagnetic state. The inverse susceptibility χ^{-1} shows a linear Curie-Weiss trend from which one can safely estimate the value for the Curie temperature $T_C \approx 0.064$. χ is calculated from the magnetic moments induced by an explicitly applied homogeneous field for sufficiently weak field strengths in the linear-response regime (typically $B < 0.01$).

The transition to the ferromagnetic state at low temperatures appears to be of second order, and

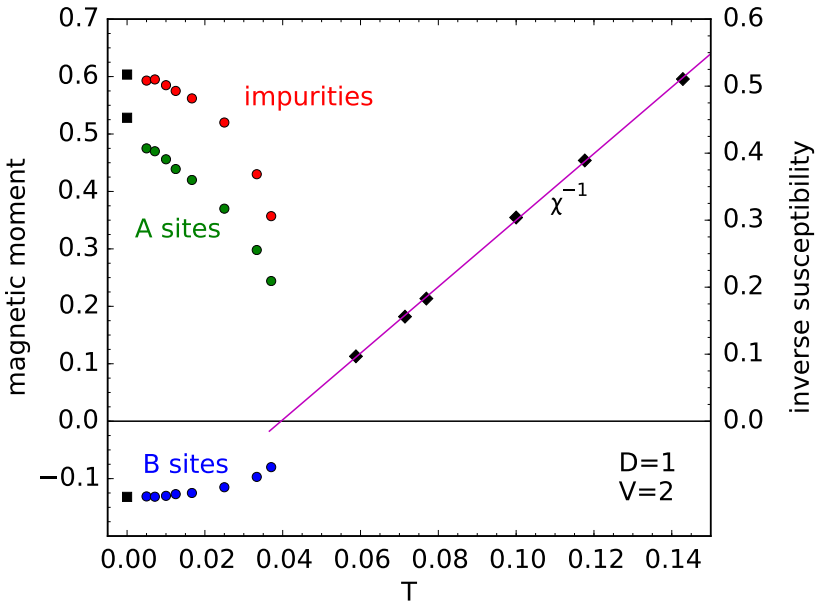

Figure 7.9.: m_A, m_B, m_{imp} (circles) and χ^{-1} (diamonds) as functions of T, as in fig. 7.7 but for the $D = 1$-dimensional depleted Anderson lattice (see fig. 7.2). Hubbard interaction: $U = 8$, hybridization strength: $V = 2$. DMRG data for $T = 0$ (squares) from Ref. [STP13] are included for comparison. Figure as printed within [ATP15]. *Copyright (2015) by the American Physical Society. Reproduced with permission.*

the data for the ordered magnetic moments are consistent with a linear temperature trend of m^2 close to T_C, i.e. $m^2 \propto (T_C - T)$. This implies a critical exponent $\beta = 0.5$ as it must be expected for a DMFT calculation. Note, however, that due to critical slowing down, it becomes progressively more difficult to stabilize symmetry-broken DMFT solutions for temperatures close to T_C. The double occupancy at the impurity site $d_{imp} = \langle n_{imp,\uparrow} n_{imp,\downarrow} \rangle$, and thus the local magnetic moment $\mathbf{S}^2_{imp} = 3(1 - 2d_{imp})/4$ turns out to be almost constant in the entire temperature range considered: $d_{imp} \approx 0.077$. In particular, the moment does not change significantly across the phase transition.

The low-temperature state of the system actually displays ferri-magnetic order since the magnetic moment at the B sites is antiferromagnetically aligned ($m_B < 0$) to the moments at the impurities and the A sites ($m_{imp}, m_A > 0$). This alignment is reminiscent of the antiferromagnetic coupling in the Kondo limit of the model, i.e. for $V \to 0$, where an antiferromagnetic effective exchange interaction (Kondo coupling) of strength $J = 8V^2/U$ emerges between B sites and impurities in the low-energy sector [SW66; SN02]. In the weak-coupling limit $V \to 0$, one furthermore expects that well-formed local magnetic moments appear at the impurity sites since charge fluctuations are strongly suppressed. Ferromagnetic coupling of these moments via the RKKY exchange then implies $|m_{imp}| \to 1$, while $m_A, m_B \to 0$. For $V = 2$, we are still in the RKKY regime since the A-site moment is clearly smaller than the moment on an impurity site.

As fig. 7.8 demonstrates, however, this changes with increasing V. For $V = 3$, we find $m_A > m_{imp}$

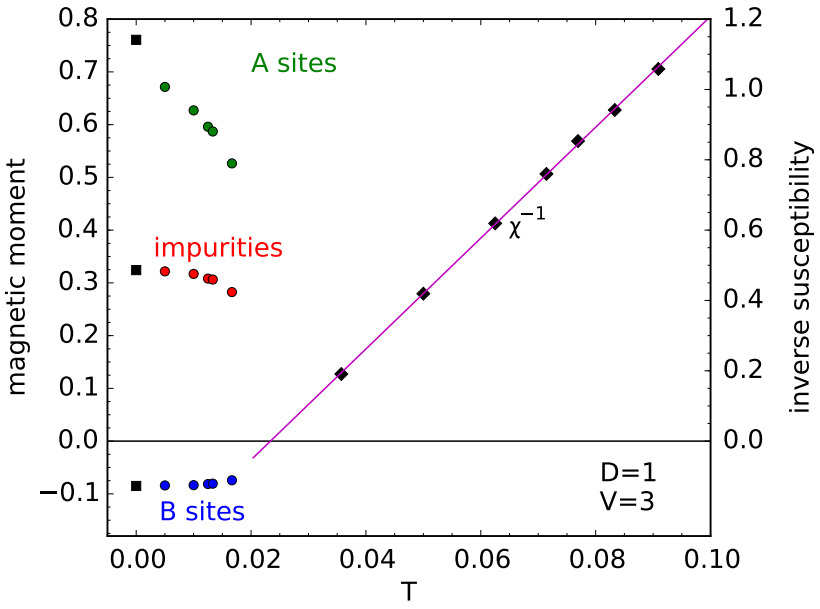

Figure 7.10.: The same as in fig. 7.9 but for $V = 3$. Figure as printed within [ATP15]. *Copyright (2015) by the American Physical Society. Reproduced with permission.*

at low temperatures indicating the crossover from the RKKY regime to the strong-V limit. In the strong-coupling limit $V \gg t$, almost localized "Anderson singlets" are formed by the magnetic moments at B and impurity sites, and thus $m_B, m_{imp} \to 0$. The presence of local singlets at the B sites implies that electrons on the remaining A sites are very efficiently localized such that well-formed local moments emerge. Those moments couple ferromagnetically via the IIME [STP13; TSP14; TSP15], i.e. by virtual excitations of the Anderson singlets, and thus $m_A \to 1$. This picture well explains that $m_A > m_{imp}$ in fig. 7.8.

It is instructive to compare the results for the $D = 3$ lattice with those obtained for $D = 1$ (see fig. 7.2). Figures 7.9 and 7.10 show results for the ordered magnetic moments and the impurity magnetic susceptibility for a chain geometry with $L = 50$ sites with periodic boundary conditions. The overall trends seen in the figures are similar to those found for $D = 3$ but the crossover from the RKKY to the IIME regime appears at lower hybridization strength V as can be inferred from the fact that m_A is considerably higher than m_{imp} already for $V = 3$.

Furthermore, the Curie temperature is seen to *decrease* with increasing V in this regime; T_C drops by about a factor two when increasing the hybridization strength from $V = 2$ to $V = 3$. This can consistently be explained by referring to the strong-V limit where the effective model eq. (7.4) applies and where the only energy scale is given by the coupling α (see eq. (7.3)) which decreases with increasing V.

This also means that the crossover regime shifts to stronger hybridization strengths with increasing lattice dimension or coordination number. This must be kept in mind when comparing T_C

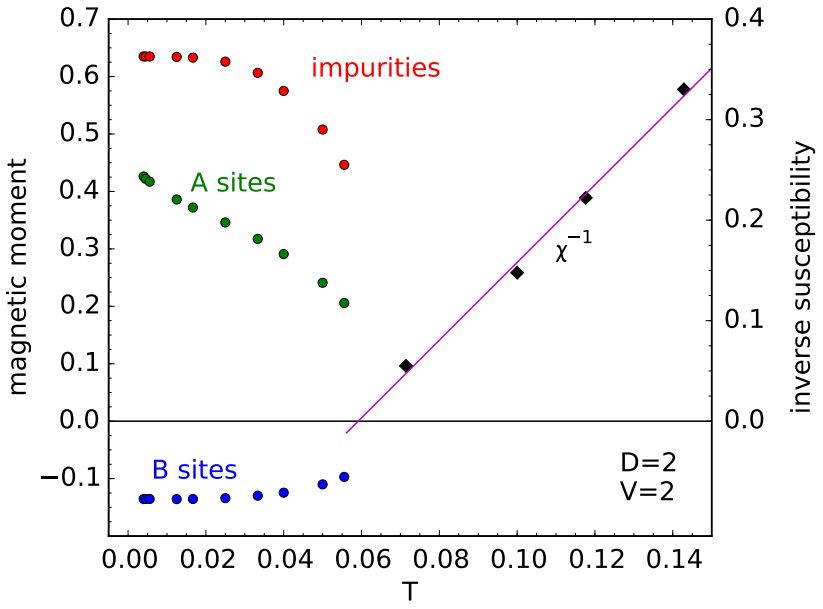

Figure 7.11.: m_A, m_B, m_{imp} (circles) and χ^{-1} (diamonds) as functions of T for the $D = 2$-dimensional depleted Anderson lattice. $U = 8, V = 2$.

obtained for different dimensions D at constant V. At $V = 2$, the Curie temperature does not depend very much on D: We find $T_C = 0.040$ for $D = 1$, $T_C = 0.059$ for $D = 2$ (see fig. 7.11) and $T_C = 0.064$ for $D = 3$. This is easily explained as a balance between two counteracting effects, namely an increase of T_C with increasing D characteristic for a mean-field theory on the one hand and the mentioned shift of the crossover regime resulting in a lower T_C on the other hand.

Obviously, the $D = 1$ and $D = 2$ results are not consistent with the Mermin-Wagner theorem which, as compared to section 3.3.1 on page page 31 and the following, excludes spontaneous breaking of the SU(2) spin rotation symmetry for $D \leq 2$ at finite temperatures. As a matter of course, it *cannot* be satisfied within a static or within dynamical mean-field theory since long wave-length magnetic excitations do not feed back to the single-particle self-energy. We nevertheless expect that the finite T_C predicted by DMFT is physically significant even for $D = 1$ (and $D = 2$) and indicates the onset of ferromagnetic ordering of the magnetic moments on *intermediate* length scales [Ved+11].

For $D = 1$ and in the low-temperature limit the DMFT agrees well with essentially exact data obtained by means of the density-matrix renormalization group (DMRG) method [STP13] at zero temperature. The extrapolation of the DMFT results for the ordered magnetic moments m_{imp} and m_B to $T = 0$ perfectly matches with the DMRG data, see black squares in figs. 7.9 and 7.10. As concerns the magnetic moment on the A sites, we expect the same unconventional T-dependence that has been discussed in the context of static mean-field theory in section 7.2.4, i.e. an upturn of m_A for $T \to 0$, consistent with the $T = 0$ DMRG data, which is induced by the van Hove

singularity of the spin-dependent local density of states at the Fermi edge.

For the $D = 3$ lattice, we have systematically computed T_C as a function of V at fixed $U = 8$. Results as obtained from by linear fits to the temperature trend of the $\chi^{-1}(T)$ are shown in fig. 7.12.

In the weak-coupling limit $V \to 0$, the Curie temperature is expected to be solely determined by the strength of the RKKY interaction and thus to scale as $T_C \propto J_{RKKY} \propto J^2 \propto V^4$ with V. For the strong-coupling or IIME limit, the only energy scale of the effective low-energy theory is given by α and thus $T_C \propto \alpha$ (see solid lines in fig. 7.12). For $U = 8$, a good approximation is $T_C \propto V^{-4}$, see eq. (7.3) and the dashed line in fig. 7.12.

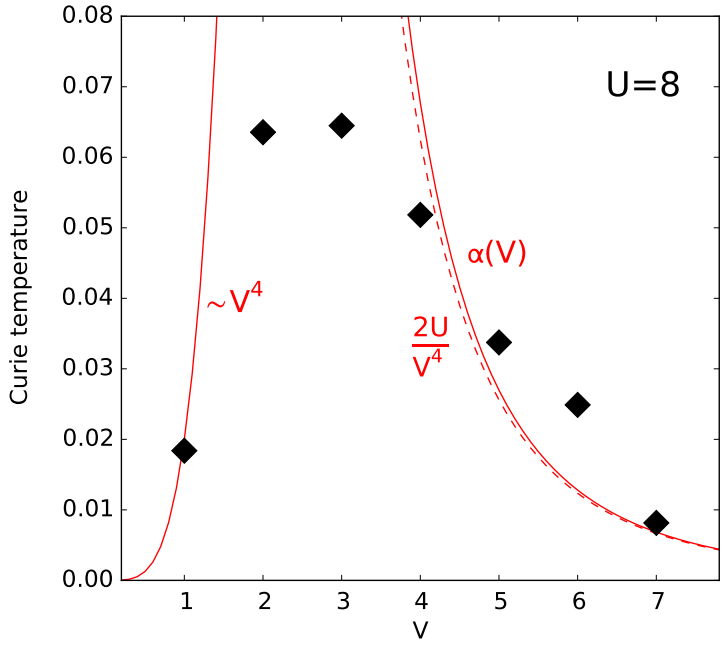

Figure 7.12.: Curie temperature T_C for the $D = 3$-dimensional depleted Anderson lattice at $U = 8$ and half-filling as a function of the hybridization strength V. Points are obtained via $\chi^{-1}(T_C) = 0$ by extrapolating the linear temperature trend of the inverse susceptibility $\chi^{-1}(T)$. Solid lines: a dependence of $T_C(V) \propto V^4$ is expected for $V \to 0$. For strong V, the data are consistent with $T_C(V) \propto \alpha(V)$. Dashed line: $T_C(V) \propto V^{-4}$ represents a good approximation to $\alpha(V)$ at $U = 8$. Figure as printed within [ATP15]. *Copyright (2015) by the American Physical Society. Reproduced with permission.*

The Curie temperature is at its maximum $T_{C,opt} \approx 0.07$ for a hybridization strength of about $V_{opt} \approx 2.5$. $T_{C,opt}$ is almost an order of magnitude smaller than the maximum Néel temperature of the $D = 3$ Hubbard model at half-filling [Ken+05] and also an order magnitude smaller than typical Curie temperatures of the Hubbard model with asymmetric free density of states, as obtained for lower fillings by DMFT [Ulm98]. The same holds if compared with DMFT estimates for the Curie temperature of the standard periodic Anderson model [MN00].

7.4. Summary

Our study presented within this chapter has demonstrated that the Anderson-lattice model with a regularly depleted system of localized orbitals at every second site supports ferromagnetic long-range order which exhibits, depending on the hybridization strength V, a high stability against thermal fluctuations. The temperature-dependent magnetism has been investigated systematically for different coupling strengths and electron densities.

We have taken into account two different types of mean-field approaches:

1. static mean-field theory of the effective low-energy model that emerges at strong couplings V within fourth-order perturbation theory, and

2. site-dependent dynamical mean-field theory (sdDMFT) of the full model using the CT-HYB segment variant as impurity solver, we have employed in terms of our numerical apparatus as described in section 4.3.

The Curie temperature is obtained by computing the temperature dependence of the magnetic moments as well as by the divergence of the homogeneous static magnetic susceptibility. The maximal T_C is found at half-filling and for intermediate hybridization strengths:

For weak V, magnetic order is induced by the standard effective RKKY interaction between the local magnetic moments formed at the correlated impurity sites. For the geometry considered and at half-filling, the RKKY interaction is ferromagnetic. The Curie temperature scales with V^4 in this limit. For strong V, on the other hand, the recently proposed IIME also leads to ferromagnetic order. In this limit the impurity magnetic moments are Kondo screened and form almost local Kondo singlets on a high-energy scale V which localize the fraction of conduction electrons not taking part in the screening. Those conduction electrons develop local magnetic moments which are ferromagnetically coupled by virtual excitations of the local Kondo singlets on an energy scale α (see eq. (7.3)). Therefore, T_C scales with $\alpha \sim V^{-4}$ for fixed U in this limit.

While the numerical data obtained for different V appear to be consistent with the expected trends, it turned out to be very difficult to reach the extreme limits $V \to 0$ and $V \to \infty$ with pure RKKY or IIME coupling, respectively, as the energy scale given by T_C becomes too small. On the other hand, the maximum $T_{C,opt} \approx 0.07$ found for intermediate V is well accessible and surprisingly high, in view of the fact that the magnetic coupling is mediated indirectly only. Compared to DMFT estimates [Ken+05; Ulm98; MN00] of critical (Néel or Curie) temperatures in the Hubbard or periodic Anderson model with a dense system of correlated impurities, it is about an order of magnitude lower. The optimal intermediate hybridization strength where T_C is at its maximum is given by $V_{\text{opt}} \approx 2.5$, i.e., clearly stronger than the nearest-neighbor hopping $t = 1$.

8. Final conclusions

In this thesis we have documented and discussed our successfully performed simulations of magnetic phase transitions in the periodic Anderson model (PAM) on two different lattice geometries: The $D = 2$-dimensional triangular lattice on the one hand and a diluted lattice scheme at dimensions $D = 1, 2, 3$ on the other hand.

We close this thesis by summarizing the main contents and results. Furthermore, we want to provide some outlook where experienced as necessary throughout our argumentation. We started with the basics, the general construction of model Hamiltonians of many-particle systems. Based on that we explicitly derived the construction of the model Hamiltonian of the—for our concerns most important—Anderson lattice in chapter 2 from the Hubbard Hamiltonian in its role of the basic model of correlated many-particles on a lattice. The Anderson impurity model (AIM) was modeled as the little brother of the PAM. In addition, we introduced the Kondo lattice models as effective low-energy models of the Anderson impurity models.

By that we were able to focus on the formation of local magnetic moments as the initial requirement for the emerging of phase transitions in regard to itinerant magnetism in chapter 3. Here, we followed tradition and primarily used the AIM before extending the theories towards the Anderson lattice. The lattice offered the possibility to direct the discussion towards order among the local magnetic moments in terms of Ruderman-Kittel-Kasuya-Yosida (RKKY) interaction. In addition we introduced the Kondo effect as purely local effect that operates against the establishing of magnetic order. As both phenomena take place in the local-moment regime of the PAM, we reviewed them on the Kondo lattice for reasons of simpler demonstration. Besides having a look, each on its own, on the purely local Kondo effect and the long-ranging itinerant exchange, we merged both together to a rival which manifests in the Doniach phase diagram. The physics behind this famous phase diagram was emphasized as the basic theoretical environment for our concrete studies in chapters 6 and 7 to come. Chapter 3 was closed by an outlook on specific context-relevant phenomena that may negatively influence order between local magnetic moments: The Mermin-Wagner theorem that prohibits the existence of magnetic long-range order in systems of dimension $D < 3$ at finite temperature and the phenomena of geometric frustration that takes place on triangular lattices. The review of the prior one was additionally used to recapitulate the basic theory behind a magnetic phase transition, in concrete terms of a transition from a ferro- towards a paramagnetic phase at a critical temperature T_C.

Chapter 4 led us to the framework of our numerical apparatus intended to be used to simulate quantum magnetic phase transitions on the Anderson lattice in chapters 6 and 7. In essence, this was a site-dependent dynamical mean-field approach. Before the concrete presentation of the site-selective extension, we first recapitulated the practical as well as formal basics of stan-

dard mean-field theory (MFT) and afterwards the dynamical mean-field theory (DMFT). We concluded chapter 4 by means of fig. 4.3 with a sketch of the full self-consistency circle in regard to our actually used implementation of the corresponding numerics. This was implemented from scratch as part of the research activities that were reported on in this thesis.

In chapter 5 we proceeded with the description of the numerical background of this thesis: We went on with the review and discussion of the segment variant of the continuous-time hybridization expansion (CT-HYB) algorithms as a special representative of the continuous-time quantum Monte Carlo (CT-QMC) impurity solvers. As already emphasized there, this solver was also implemented in addition to the site-dependent dynamical mean-field theory (sdDMFT) implementation from scratch in terms of the research work presented by this thesis. In similarity to the outline of chapter 4 we reported on the quantum Monte Carlo (QMC) and CT-QMC method in general before we went into detail with the CT-HYB method. Thereby, we reviewed a general sampling procedure and included important topics like a correct advanced error estimation and the fermionic sign problem. In regard to the CT-HYB algorithm we fully derived the underlying hybridization expansion and extended the sampling procedure towards that of a segment picture. Accordingly, the sophisticated measurement scheme in terms of "improved estimators" was motivated and explained. Content main results out of literature could be verified by results of our own calculations and were especially presented in figs. 5.2 and 5.5. By that, we entirely recapitulated and understood the CT-HYB approach at a level that enables for a full implementation by oneself.

With the full numerical setup at hand, we finally were able to perform simulations of magnetic order and magnetic phase transitions of the triangular (see chapter 6) and the regularly depleted (compare to chapter 7) Anderson lattice. As motivated in the introduction, page 1 ff., both lattices posed different main attempts on our investigations by means of our sdDMFT. To the end this approach turned out to be very suitable for our concerns. It was easily adaptable to the given models and we could achieve our aims:

Within the framework of DMFT in regard to the triangular Anderson lattice, we could adapt the sdDMFT easily to the given model geometry and managed to stabilize a frustration alleviating partial Kondo screening (PKS) phase, embedded into a surprisingly feature-rich U-n phase diagram, impressively shown in fig. 6.3 and extensively discussed in sections 6.3 and 6.4. Here, the PKS phase arises in the local-moment regime for fillings slightly off half-filling in terms of the transition from a competing RKKY induced "collinear" ("↑, ↑, ↓") antiferromagnetic (AFM) phase towards a metallic heavy-fermion Kondo singlet (KS) state. At half-filling $n = 1$, the hybridization band gap in the non-interacting density of states results in a band insulator for $U = 0$, while with increasing U this develops into a correlated Kondo insulator (KI). At low fillings, we additionally observed a metallic ferromagnetic (FM) phase in the mixed-valence regime where the f local moments are no longer well defined.

Two main results of our study might be relevant for the understanding of PKS in real materials, such as CePdAl [Oya+08], UNi_4B [Men+94] or even artificial geometries of magnetic atoms on metallic surfaces, [Wie09; Kha+12] and for corresponding electronic-structure models:

1. The PKS state appears at non-integer fillings and thus spin-only models may be question-

able, and

2. the PKS state exclusively shows up at the border between the paramagnetic heavy-fermion and the magnetically ordered phase.

This could be tested experimentally by steering the system through this border, either by controlling the temperature or by means of chemical substitution [Fri+14]. There are several lines along which our study could be continued in the future: First, non-collinear, i.e. "120°" phases are in principle accessible by an SU(2)-symmetric formulation of the sdDMFT. This may lead to a certain refinement of the magnetic phase diagram, with non-collinear (or even incommensurate) AFM phases partially replacing the "↑, ↑, ↓" phase but we do not expect a further qualitative change as the relevant energy scale is still set by the effective RKKY-exchange coupling constant. Second, it would be interesting to make contact with the corresponding phase diagram of the Kondo model on the triangular lattice, either by applying DMFT to the Kondo model directly [OKK09] or by using a solver which allows to resolve the Kondo scale, such as the numerical renormalization group [BCP08].

Finally, one may address the effect of non-local correlations beyond the single-site DMFT. The Kondo effect results from correlations between a single correlated f orbital and the conduction-band system and is, therefore, captured correctly by a dynamical mean-field theory which treats those correlations exactly. DMFT also provides an accurate description of the non-local indirect exchange but the feedback of non-local magnetic correlations on the self-energy is missing. Those missing fluctuations must result in mean-field artifacts. Typically, the (site-dependent) DMFT approach is therefore, to some extent, biased towards the formation of magnetic order and tends to favor a symmetry-broken state $|\uparrow\rangle|\downarrow\rangle$ at the expense of a non-local singlet $(|\uparrow\rangle|\downarrow\rangle - |\downarrow\rangle|\uparrow\rangle)/\sqrt{2}$ [Tit+12; ATP15]. One might speculate that, compared to the PKS state, the AFM phase is overestimated and that both, the PKS and the AFM phases are overestimated as compared to the KS state.

As recent follow-ups of our studies two references should be mentioned: Firstly the attempt of Peschke, Rausch, and Potthoff in [PRP17] to simulate a $D = 2$-dimensional triangular Kondo lattice by visiting a $D = 1$-dimensional zigzag Kondo model in terms of the density matrix renormalization group (DMRG). Here, the search for a PKS phase factually was not successful. Instead, alleviation of the installed frustration could be achieved by a mechanism of dimerization. Secondly there was a publication of Sato, Assaad, and Grover [SAG18] that reports on the application of a sign-free auxiliary-field QMC approach on a hybrid model that couples spins to fermions on the frustrated Honeycomb lattice. In addition to the conventional Kondo insulator and anti-ferromagnetically ordered phases, relevant investigations actually yield a partial Kondo screened state where spins are selectively screened so as to alleviate frustration, and the lattice rotation symmetry is broken nematically. In comparison to our numerical setup, this ansatz has the sheer unbeatable charme that it operates exactly and thus even leaves behind possible artifacts due to approximations as e.g. tolerated by means of DMFT per definition.

For the case of the regularly depleted Anderson lattice, our sdDMFT implementation succeeded in verifying the general support for ferromagnetic long-range order of high stability against ther-

mal fluctuations, in dependence on the hybridization strength V. Thus we could verify the V-dependence of the critical temperature to be consistent with the predicted rivaling energy scales of RKKY at weak and of inverse indirect magnetic exchange (IIME) at strong hybridization strength (see fig. 7.12). The maximal T_C is found at half-filling and for intermediate hybridization strengths. This was presented and discussed in detail in sections 7.3.2 and 7.4.

Concluding in this matter, one should note that DMFT applied to the depleted Anderson lattice can be expected to be much more reliable than for the dense case. In fact, perfect agreement with numerically exact DMRG data is observed in the low-temperature limit. We are therefore convinced that our study of the depleted Anderson lattice provides quantitative insight into the physics and contributes to the fundamental understanding of magnetic order of correlated orbitals coupled indirectly by conduction electrons.

A. Remarks

A.1. Mathematical notation and definitions

In regard to the mathematical notation this thesis tries to be conform with common standard notation used and introduced in textbooks like e.g.[GBL08; Hig15; LS90]. In that spirit it was tried to note **vectors** and **matrices** as bold symbols like $\mathbf{v}$ and $\mathbf{M}$, whereas the capital letters may not necessarily be used to distinguish between vectors and matrices. In contrast to that, **operators** will not be marked in special and so it depends on the context whether one deals with an operator or already with its eigen-value. However, there should not be any danger of confusion for the intent reader.

Numbers will be categorized within the common **sets**:

- The set of natural numbers $\mathbb{N}$,
- the set of integers $\mathbb{Z}$,
- the set of real numbers $\mathbb{R}$,
- and the set of complex numbers $\mathbb{Z}$.

Inside formulas one often meets the following **mathematical constants** and constant expressions:

- If not defined otherwise, π marks the mathematical constant that is equal to a circle's circumference divided by its diameter.
- The base of the natural logarithm ln, also called **Euler's number** is marked by e, like in e^x.
- In order to deal with complex numbers like $z = x + \mathrm{i}y$, we use the **imaginary unit** i.

Concerning the last point, let again $z = x+\mathrm{i}y$ be a complex number, then its **complex conjugate** is given by $z^* = x - \mathrm{i}y$.

Shorthand notation of mathematical statements implies the two logical **quantifiers**:

- The universal quantifier ∀, read “for all”,
- and the existential quantifier ∃, read “there exists”.

In conformity to [BF04], the following definitions are adopted:

- **Kronecker’s delta** for discrete variables i and j as

$$\delta_{ij} = \begin{cases} 0, & \text{if } i \neq j\,, \\ 1, & \text{if } i = j\,; \end{cases} \tag{A.1}$$

- **Dirac’s delta distribution** for a continuous variable x as

$$\delta(x) = 0 \quad \forall\, x \neq 0\,, \quad \text{while } \int \mathrm{d}x\, \delta(x) = 1\,; \tag{A.2}$$

- The **Heaviside step function** is meant to be

$$\theta(x) = \begin{cases} 1, & \text{if } x \geq 0\,, \\ 0, & \text{if } x < 0\,; \end{cases} \tag{A.3}$$

- The **sign function**

$$\operatorname{sgn}(x) = \begin{cases} 1, & \text{if } x \geq 0\,, \\ -1, & \text{if } x < 0\,. \end{cases} \tag{A.4}$$

Quantum theory generally lives on (anti-)commutator relations. In that sense the **commutator** between two arbitrary operators A and B is defined as

$$[A, B]_- = AB - BA\,, \tag{A.5}$$

whereas the **anti-commutator** of the same operators in analogy is given by

$$[A, B]_+ = AB + BA\,. \tag{A.6}$$

Any further general mathematical expressions are explained where introduced or needed.

A.2. Perturbation theory (at finite temperature)

In quantum theory, perturbation theories belong to the *approximative methods*. The basic idea is to write a Hamiltonian H as

$$H = H_0 + H_1\,, \tag{A.7}$$

where H_0 is the unperturbed part of H for which all energy eigenvalues and eigenstates are known exactly and H_1 contains the hopefully small perturbation. The latter is then approximated by an expansion. Clearly, for small perturbations this has only to be performed up to low perturbation orders in order to get a recently good approximation.

In quantum many-body theory, as one might look up in very detail in standard textbooks on the topic like [NO98; Mah00; FW03; AGD65; BF04] to only mention a few, perturbation theory of many-particle systems at finite temperatures $T > 0$ are formally handled within the so-called *Matsubara formalism* [Mat55]. Following this formalism, all arising times t are considered as purely imaginary owning the dimension of an inverse energy. Mathematically the prior is put into practice by a Wick rotation of t into the complex plane, hence

$$t \in \mathbb{R} \to t = -\mathrm{i}\tau \,. \tag{A.8}$$

This substitution in addition to the identification of the inverse temperature β as an inverse energy like τ allows for a very elegant unification of the thermal averages and the time-evolution, hence dynamics of a given system with a general but time-independent Hamiltonian H. That is just because for $\tau = \beta$ the already structurally similar time-evolution operator $U(t) = \mathrm{e}^{-\mathrm{i}tH}$ and the density operator $\rho = \mathrm{e}^{-\beta H}$ of the system become the same and by that may be perturbatively treated, i.e. expanded in one go.

As a consequence, the dynamics of all imaginary-time dependent operators are described within a *modified Heisenberg picture*. Concretely for fermionic single-particle creation and annihilation operators $a_\alpha^\dagger$ and a_α as introduced in 2.1, regardless of any indices, this means[1]

$$a^\dagger(\tau) = \mathrm{e}^{\tau H}\, a^\dagger\, \mathrm{e}^{-\tau H} \,, \tag{A.9}$$

$$a(\tau) = \mathrm{e}^{\tau H}\, a\, \mathrm{e}^{-\tau H} \,. \tag{A.10}$$

The application of this representation then formally evolves further on to the construction of electronic *Green's functions*, generally defined as time-ordered correlation functions, hence expectation values of two electronic operators, in imaginary time. In this context, a *fermionic single-particle imaginary time Green's function* may be written as

$$G_{\alpha\beta}(\tau, \tau') \equiv -\left\langle T_\tau \left[a_\alpha(\tau) a_\beta^\dagger(\tau') \right] \right\rangle \,. \tag{A.11}$$

Thereby, necessarily an appropriate *imaginary time-order operator* T_τ is usually defined as

$$T_\tau \left[a(\tau) a^\dagger(\tau') \right] = \theta(\tau - \tau')\, a(\tau)\, a^\dagger(\tau') - \theta(\tau' - \tau)\, a^\dagger(\tau')\, a(\tau) \tag{A.12}$$

what implies a *Heaviside step function* θ as defined by eq. (A.3) on page 122. Here, by considering operators of the same spin flavor σ, hence $\alpha = \beta \equiv \sigma$ at zero times, one may derive

$$\begin{aligned} G_{\sigma\sigma}(0, 0^+) &= -\left\langle T_\tau \left[a_\sigma(0) a_\sigma^\dagger(0^+) \right] \right\rangle \\ &= \left\langle a_\sigma^\dagger(0^+) a_\sigma(0) \right\rangle = n_\sigma^{(a)}(0) \,, \end{aligned} \tag{A.13}$$

[1] Here, admittedly a consistent notation concerning physical aspects is preferred in contrast to a correct mathematical one as *modified Heisenberg operators* like those given by eqs. (A.9) and (A.10) are definitely not hermitian conjugate. Therefore, the "†" in eq. (A.9) physically marks the corresponding operator as creator, but is mathematically incorrect. For a quick reminder on the mathematical definition of *hermitian conjugates*, return to the footnote on page 10.

where in the last step the definition of the particle number operator according to eq. (2.7) on page 11 was used.[2] Thus, in this case the single-particle imaginary time Green's function could be identified as the average single occupation number. It is crucial to note that imaginary-time Green's functions like $G_{\alpha\beta}(\tau,\tau')$ (A.11) generally do not depend on the times τ and τ' explicitly but rather on the time difference.[3] Hence, it is

$$G_{\alpha\beta}(\tau,\tau') = G_{\alpha\beta}(\tau-\tau')\,, \quad (\tau-\tau') \in [-\beta,\beta]\,. \tag{A.14}$$

Furthermore imaginary-time Green's functions like $G_{\alpha\beta}(\tau,\tau')$ (A.11) characteristically behave 2β-*periodic* and particularly in the fermionic case β-*antiperiodic*. From the latter follows the property

$$G_{\alpha\beta}(\tau) = -G_{\alpha\beta}(\tau+\beta)\,, \quad -\beta < \tau < 0\,. \tag{A.15}$$

Naturally this indicated periodicity allows for a Fourier expansion of the imaginary-time on to the Matsubara Green's functions which leads to the following corresponding Fourier transforms [Col15b]:

$$G_{\alpha\beta}(\mathrm{i}\omega_n) = \int_0^\beta \mathrm{d}\tau\, \mathrm{e}^{\mathrm{i}\omega_n\tau} G_{\alpha\beta}(\tau)\,, \tag{A.16}$$

$$G_{\alpha\beta}(\tau) = \sum_{n=-\infty}^{\infty} \mathrm{e}^{-\mathrm{i}\omega_n\tau} G_{\alpha\beta}(\mathrm{i}\omega_n)\,. \tag{A.17}$$

The ω_n arising thereby are called *Matsubara frequencies* that in the fermionic case are defined as odd multiples of π/β in the fashion of

$$\omega_n = \frac{(2n+1)\,\pi}{\beta}\,, \quad n \in \mathbb{Z}\,. \tag{A.18}$$

From that, one may derive the relation

$$\omega_{-m-1} = -\omega_m\,. \tag{A.19}$$

A.3. Representations of the grand canonical partition function

Given a model in the grand canonical ensemble, its corresponding grand canonical partition function $\mathcal{Z}$ may be formally constructed in two different ways [AS10; NO98; Mah00; Wip13; FW03; BF04]:

[2] The infinitely small time shift 0^+ was necessary in order to formally get the imaginary times into the right order when applied to T_τ.

[3] This directly contrasts with Green's functions in Keldysh's real-time formalism to describe dynamics of quantum systems in non-equilibrium. There, the defined Keldysh Green's functions explicitly depend on two real time arguments. See e.g. [Wag91; Ram07] for details.

1. Within the context of statistical quantum physics in a purely imaginary formulation as time ordered trace over time-integrated Boltzmann-like weights:

$$\mathcal{Z} = \mathrm{Tr}\left[T_\tau \mathrm{e}^{-\int_0^\beta \mathrm{d}\tau\, \mathcal{H}\{a^\dagger(\tau),a(\tau)\}}\right] . \tag{A.20}$$

   Here, $\mathcal{H}$ is the given model Hamiltonian in the grand canonical ensemble. It depends on adequate fermionic creation $a^\dagger(\tau)$ and annihilation operators $a(\tau)$ in the modified Heisenberg representation as defined by eqs. (A.9) and (A.10) on page 123. Those are ordered with increasing times from right to left positions by means of the time-order operator for fermionic single-particle creation and annihilation operators T_τ as given by eq. (A.12) on page 123.

2. Within the context of condensed matter field theory as a functional integral over conjugated fermionic Grassmann fields $\bar{\psi}(\tau)$ and $\psi(\tau)$ that are in direct correspondence to the creation and annihilation operators $a^\dagger(\tau)$ and $a(\tau)$ of the first notation

$$\mathcal{Z} = \int \mathrm{D}[\bar{\psi}(\tau), \psi(\tau)] \mathrm{e}^{-\mathcal{S}[\bar{\psi}(\tau),\psi(\tau)]} , \tag{A.21}$$

   where particularly the *abstract measure*

$$\mathrm{D}[\bar{\psi}(\tau), \psi(\tau)] = \lim_{M\to\infty} \prod_{m=1}^{M} \mathrm{d}[\bar{\psi}^m(\tau), \psi^m(\tau)] \tag{A.22}$$

   and the generally *anti-commuting* fields satisfy the *anti-periodic* boundary condition

$$\bar{\psi}(0) = -\bar{\psi}(\beta) , \quad \psi(0) = -\psi(\beta) , \tag{A.23}$$

   hence allow for the definition of an appropriate Fourier transform into the space of Matsubara frequencies already introduced by means of eq. (A.18). Here, $\mathcal{H}$ enters $\mathcal{Z}$ implicitly by means of the action $\mathcal{S}$ that in more detail reads:

$$\mathcal{S}\left[\bar{\psi}(\tau), \psi(\tau)\right] = \int_0^\beta \mathrm{d}\tau \left\{\bar{\psi}(\tau)\, \partial_\tau \psi(\tau) + \mathcal{H}\left[\bar{\psi}(\tau), \psi(\tau)\right]\right\} , \tag{A.24}$$

   where typically the Grassmann fields arise in direct correspondence to the imaginary-time dependent creation and annihilation operators inside $\mathcal{H}(\tau)$ in operator notation. Formally, this *Lagrangian approach* is a direct result of the theory of *fermionic coherent states* [NO98; Zin04; AS10].

Both representations allow for the definition of respective thermal averages $\langle ... \rangle$. From eq. (A.21) follows

$$\langle \bullet \rangle := \frac{1}{\mathcal{Z}} \cdot \int \mathrm{D}[\bar{\psi}(\tau), \psi(\tau)]\, \mathrm{e}^{-\mathcal{S}[\bar{\psi}(\tau),\psi(\tau)]} \bullet , \tag{A.25}$$

whereas eq. (A.21) invites for

$$\langle \hat{\bullet} \rangle := \frac{1}{\mathcal{Z}} \mathrm{Tr}\left[\mathrm{e}^{-\beta\mathcal{H}\{a^\dagger(\tau),a(\tau)\}} \cdot T_\tau\, \hat{\bullet}\right] . \tag{A.26}$$

Here, $\hat{\bullet}$ represents an observable in "operator", $\bullet$ marks the same observable but in corresponding "Grassmann" notation, i.e. representation. Then, it is an important matter of fact, that it is

$$\langle \hat{\bullet} \rangle = \langle \bullet \rangle \,, \tag{A.27}$$

hence, both averages are equal in value.

Bibliography

[AAP15] M. W. Aulbach, F. F. Assaad, and M. Potthoff. “Dynamical mean-field study of partial Kondo screening in the periodic Anderson model on the triangular lattice”. In: *Phys. Rev. B* 92 (23 2015), p. 235131 (cit. on pp. 37, 75, 79, 82–85, 87, 89, 91, 143).

[AE08] F. Assaad and H. Evertz. “World-line and Determinantal Quantum Monte Carlo Methods for Spins, Phonons and Electrons”. In: *Computational Many-Particle Physics*. Springer Berlin Heidelberg, 2008. Chap. 10, pp. 277–356 (cit. on pp. 53, 54).

[Aff09] I. Affleck. “The Kondo screening cloud: what it is and how to observe it”. In: *ArXiv e-prints* (2009) (cit. on p. 29).

[AGD65] A. A. Abrikosov, L. P. Gorkov, and I. E. Dzyaloshinski. *Quantum field theoretical methods in statistical physics*. Pergamon Press, 1965 (cit. on p. 123).

[AI10] V. Anisimov and Y. Izyumov. *Electronic Structure of Strongly Correlated Materials*. Vol. 163. Springer Berlin Heidelberg, 2010 (cit. on pp. 17, 18).

[Amu+15] M. Y. Amusia, K. G. Popov, V. R. Shaginyan, and V. A. Stephanovich. *Theory of Heavy-Fermion Compounds*. Vol. 182. Springer International Publishing, 2015 (cit. on p. 17).

[And12] F. B. Anders. “The Kondo Effect”. In: *Correlated electrons: from models to materials*. Vol. 2. Forschungszentrum Jülich GmbH, 2012. Chap. 11, pp. 11.1–11.27 (cit. on pp. 40, 44).

[And61] P. W. Anderson. “Localized Magnetic States in Metals”. In: *Phys. Rev.* 124 (1 1961), pp. 41–53 (cit. on pp. 3, 17, 24).

[Aok+14] H. Aoki, N. Tsuji, M. Eckstein, M. Kollar, T. Oka, and P. Werner. “Nonequilibrium dynamical mean-field theory and its applications”. In: *Rev. Mod. Phys.* 86 (2 2014), pp. 779–837 (cit. on p. 40).

[Ari10] Aristotle. *De Anima: On the Soul (Focus Philosophical Library)*. Focus, 2010 (cit. on p. 1).

[AS10] A. Altland and B. D. Simons. *Condensed Matter Field Theory*. Cambridge University Press, 2010 (cit. on pp. 1, 9, 48, 124, 125).

[Ass02] F. F. Assaad. “Quantum Monte Carlo Methods on Lattices:The Determinantal Approach”. In: *Quantum Simulations of Complex Many-Body Systems: From Theory to Algorithms*. Vol. 10. John von Neumann Institute for Computing, 2002. Chap. 6, pp. 99–156 (cit. on p. 53).

[Ass14] F. F. Assaad. “Continuous-time QMC Solvers for Electronic Systems in Fermionic and Bosonic Baths”. In: *DMFT at 25: Infinite Dimensions*. Vol. 4. Forschungszentrum Jülich Zentralbibliothek, Verlag, 2014. Chap. 7, pp. 7.1–7.40 (cit. on pp. 5, 54–56, 60, 63).

[ATP15] M. W. Aulbach, I. Titvinidze, and M. Potthoff. “Crossover from conventional to inverse indirect magnetic exchange in the depleted Anderson lattice”. In: *Phys. Rev. B* 91 (17 2015), p. 174420 (cit. on pp. 37, 95, 98, 100, 101, 104–106, 109–112, 114, 119, 143).

[Bac11] M. Bachmann. “Monte Carlo Simulations”. In: *ArXiv e-prints* (2011) (cit. on p. 63).

[Bal10] L. Balents. “Spin liquids in frustrated magnets”. In: *Nature* 464 (2010), p. 199 (cit. on pp. 4, 33).

[BB06] S. Blundell and K. Blundell. *Concepts in Thermal Physics*. Oxford University Press, USA, 2006 (cit. on p. 12).

[BB09] S. J. Blundell and K. M. Blundell. *Concepts in Thermal Physics*. Oxford University Press, 2009 (cit. on p. 8).

[BBG02] C. D. Batista, J. Bonca, and J. E. Gubernatis. “Segmented Band Mechanism for Itinerant Ferromagnetism”. In: *Phys. Rev. Lett.* 88 (18 2002), p. 187203 (cit. on p. 92).

[BCP08] R. Bulla, T. A. Costi, and T. Pruschke. “Numerical renormalization group method for quantum impurity systems”. In: *Rev. Mod. Phys.* 80 (2 2008), pp. 395–450 (cit. on pp. 72, 119).

[BDN01] K. Baberschke, M. Donath, and W. Nolting. *Band-Ferromagnetism*. Vol. 580. Springer Berlin Heidelberg, 2001 (cit. on p. 90).

[Bel06] M. L. Bellac. *Quantum Physics*. Cambridge University Press, 2006 (cit. on pp. 1, 10, 14).

[Ben+15] G. Bengel, C. Baun, M. Kunze und K.-U. Stucky. *Masterkurs Parallele und Verteilte Systeme*. Springer Fachmedien Wiesbaden, 2015 (siehe S. 61).

[BF04] H. Bruus and K. Flensberg. *Many-body quantum theory in condensed matter physics : an introduction*. Oxford Univ. Press, 2004 (cit. on pp. 1, 9, 27, 38, 39, 48, 58, 122–124).

[BFV11] A. Benlagra, L. Fritz, and M. Vojta. “Kondo lattices with inequivalent local moments: Competitive versus cooperative Kondo screening”. In: *Phys. Rev. B* 84 (7 2011), p. 075126 (cit. on p. 4).

[BH10] K. Binder and D. W. Heermann. *Monte Carlo Simulation in Statistical Physics*. Vol. 0. Springer Berlin Heidelberg, 2010 (cit. on p. 50).

[BHP98] R. Bulla, A. C. Hewson, and T. Pruschke. “Numerical renormalization group calculations for the self-energy of the impurity Anderson model”. In: *Journal of Physics: Condensed Matter* 10.37 (1998), p. 8365 (cit. on p. 72).

[BJ03] B. H. Bransden and C. J. Joachain. *Physics of Atoms and Molecules*. Prentice Hall, 24, 2003 (cit. on p. 1).

[BLN91] R. Ballou, C. Lacroix, and M. D. Nunez Regueiro. “Frustration-induced vanishing of magnetic moments in $R\,Mn_2$ systems”. In: *Phys. Rev. Lett.* 66 (14 1991), pp. 1910–1913 (cit. on p. 4).

[Blu01] S. J. Blundell. *Magnetism in Condensed Matter*. Oxford University Press, USA, 2001 (cit. on pp. 24, 28, 32).

[Blü11] N. Blümer. “Hirsch-Fye Quantum Monte Carlo Method for Dynamical Mean-Field Theory”. In: *The LDA+DMFT approach to strongly correlated materials*. Vol. 1. Forschungszentrum, Zentralbibliothek, 2011. Chap. 9, pp. 9.1–9.35 (cit. on p. 53).

[Bon13] M. Bonamente. *Statistics and Analysis of Scientific Data*. Springer New York, 2013 (cit. on p. 51).

[Bra14] S. Brandt. *Data Analysis*. Springer International Publishing, 2014 (cit. on p. 51).

[BSS81] R. Blankenbecler, D. J. Scalapino, and R. L. Sugar. “Monte Carlo calculations of coupled boson-fermion systems. I”. In: *Phys. Rev. D* 24 (8 1981), pp. 2278–2286 (cit. on p. 53).

[Bul12] R. Bulla. “The Numerical Renormalization Group”. In: *Correlated electrons: from models to materials*. Vol. 2. Forschungszentrum Jülich GmbH, 2012. Chap. 12, pp. 12.1–12.23 (cit. on p. 72).

[Cah13] K. Cahill. *Physical Mathematics*. Cambridge University Press, 2013 (cit. on pp. 51, 56).

[Cal85] H. B. Callen. *Thermodynamics and an Introduction to Thermostatistics*. Wiley, 1985 (cit. on p. 38).

[Cap+14] G. Cappellini, M. Mancini, G. Pagano, P. Lombardi, L. Livi, M. Siciliani de Cumis, P. Cancio, M. Pizzocaro, D. Calonico, F. Levi, C. Sias, J. Catani, M. Inguscio, and L. Fallani. “Direct Observation of Coherent Interorbital Spin-Exchange Dynamics”. In: *Phys. Rev. Lett.* 113 (12 2014), p. 120402 (cit. on p. 99).

[Cap87] *Magnetic Magnetism*. Vol. 42. Springer Berlin Heidelberg, 1987 (cit. on p. 90).

[Coe10] J. M. D. Coey. *Magnetism and Magnetic Materials*. Cambridge University Press, 2010 (cit. on p. 32).

[Col02] P. Coleman. “Local moment physics in heavy electron systems”. In: *AIP Conference Proceedings* 629.1 (2002), pp. 79–160 (cit. on pp. 17, 20, 31).

[Col15a] P. Coleman. *Introduction to Many-Body Physics*. Cambridge University Press, 2015 (cit. on pp. 20, 31).

[Col15b] P. Coleman. *Introduction to Many-Body Physics*. Cambridge University Press, 2015 (cit. on p. 124).

[Com07] A.-B. Comanac. “Dynamical Mean Field Theory of Correlated Electron Systems: New Algorithms and Applications to Local Observables”. PhD thesis. Columbia University, 2007 (cit. on p. 48).

[Cor+09] T. H. Cormen, C. E. Leiserson, R. L. Rivest, and C. Stein. *Introduction to Algorithms*. The MIT Press, 2009 (cit. on p. 52).

[Don77] S. Doniach. “The Kondo lattice and weak antiferromagnetism”. In: *Physica B+C* 91.0 (1977), pp. 231–234 (cit. on pp. 3, 23, 27, 30, 31, 88).

[DR84] P. J. Davis and P. Rabinowitz. *Methods of Numerical Integration*. Elsevier Inc, Academic Press, 1984 (cit. on p. 52).

[DS98] R. Doradzi ski and J. Spaek. “Mean-field magnetic phase diagram of the periodic Anderson model with the Kondo-compensated phases”. In: *Phys. Rev. B* 58 (6 1998), pp. 3293–3301 (cit. on p. 92).

[Dze+10] M. Dzero, K. Sun, V. Galitski, and P. Coleman. "Topological Kondo Insulators". In: *Phys. Rev. Lett.* 104 (10 2010), p. 106408 (cit. on p. 2).

[Efr82] B. Efron. *The Jackknife, the Bootstrap and Other Resampling Plans*. Society for Industrial and Applied Mathematics, 1982 (cit. on p. 51).

[EK16] L. Edelhäuser and A. Knochel. *Tutorium Quantenfeldtheorie: Was Sie schon immer über QFT wissen wollten, aber bisher nicht zu fragen wagten*. Springer Berlin Heidelberg, 2016 (cit. on p. 8).

[ES90] D. M. Eigler and E. K. Schweizer. "Positioning single atoms with a scanning tunnelling microscope". In: *Nature* 344.6266 (1990), pp. 524–526 (cit. on pp. 6, 99).

[Ess+05] F. H. L. Essler, H. Frahm, F. Göhmann, A. Klümper, and V. E. Korepin. *The One-Dimensional Hubbard Model*. Cambridge University Press, 2005 (cit. on p. 12).

[Faz99] P. Fazekas. *Lecture Notes on Electron Correlation and Magnetism*. World Scientific, 1999 (cit. on pp. 12, 19).

[Fel68] W. Feller. *An Introduction to Probability Theory and Its Applications, Volume 1*. John Wiley & Sons, 1, 1968 (cit. on p. 51).

[Fer56] E. Fermi. *Thermodynamics*. Dover Publications, 1956 (cit. on p. 38).

[Fis+86] Z. Fisk, H. R. Ott, T. M. Rice, and J. L. Smith. "Heavy-electron metals". In: *Nature* 320.6058 (1986), pp. 124–129 (cit. on pp. 2, 17).

[Fou+01] W. M. C. Foulkes, L. Mitas, R. J. Needs, and G. Rajagopal. "Quantum Monte Carlo simulations of solids". In: *Rev. Mod. Phys.* 73 (1 2001), pp. 33–83 (cit. on pp. 50, 51).

[Fri+14] V. Fritsch, N. Bagrets, G. Goll, W. Kittler, M. J. Wolf, K. Grube, C.-L. Huang, and H. v. Löhneysen. "Approaching quantum criticality in a partially geometrically frustrated heavy-fermion metal". In: *Phys. Rev. B* 89 (5 2014), p. 054416 (cit. on p. 119).

[FW03] A. L. Fetter and J. D. Walecka. *Quantum Theory of Many-particle Systems*. Dover Publications, 2003 (cit. on pp. 1, 123, 124).

[Gan99] F. Gantmacher. *The Theory of Matrices*. Volume One. American Mathematical Society, 1999 (cit. on p. 59).

[GBL08] T. Gowers, J. Barrow-Green, and I. Leader. *The Princeton companion to mathematics*. Princeton University Press, 2008 (cit. on pp. 52, 121).

[Geb97] F. Gebhard. *The Mott Metal-Insulator Transition*. Vol. 137. Springer Berlin Heidelberg, 1997 (cit. on p. 12).

[Gen60] P. G. de Gennes. "Effects of Double Exchange in Magnetic Crystals". In: *Phys. Rev.* 118 (1 1960), pp. 141–154 (cit. on p. 90).

[Geo+96] A. Georges, G. Kotliar, W. Krauth, and M. J. Rozenberg. "Dynamical mean-field theory of strongly correlated fermion systems and the limit of infinite dimensions". In: *Rev. Mod. Phys.* 68 (1 1996), pp. 13–125 (cit. on pp. 5, 40, 107).

[Geo11] H.-O. Georgii. *Gibbs Measures and Phase Transitions*. De Gruyter, 2011 (cit. on p. 59).

[Geo14] A. Georges. “Dynamical Mean-Field Theory: Materials from an Atomic Viewpoint Beyond the Landau Paradigm”. In: *DMFT at 25: Infinite Dimensions*. Vol. 4. Forschungszentrum Jülich Zentralbibliothek, Verlag, 2014. Chap. 3, pp. 3.1–3.21 (cit. on pp. 41, 43).

[GLS14] W. Gropp, E. Lusk, and A. Skjellum. *Using MPI: Portable Parallel Programming with the Message-Passing Interface*. The MIT Press, 2014 (cit. on p. 61).

[GM12] R. Gross and A. Marx. *Festkörperphysik*. München: Oldenbourg Verlag, 2012 (cit. on p. 25).

[GN01] A. Gelfert and W. Nolting. “The absence of finite-temperature phase transitions in low-dimensional many-body models: a survey and new results”. In: *Journal of Physics: Condensed Matter* 13.27 (22 2001), R505 (cit. on p. 32).

[GRH91] E. Gross, E. Runge, and O. Heinonen. *Many-particle theory*. A. Hilger, 1991 (cit. on p. 32).

[Gro+14] W. Gropp, T. Hoefler, R. Thakur, and E. Lusk. *Using Advanced MPI: Modern Features of the Message-Passing Interface*. The MIT Press, 2014 (cit. on p. 61).

[Gro13] C. Gros. *Complex and Adaptive Dynamical Systems*. Springer Berlin Heidelberg, 2013 (cit. on p. 51).

[GRS96] W. Gilks, S. Richardson, and D. Spiegelhalter. *Markov Chain Monte Carlo in Practice*. Chapman & Hall, 1996 (cit. on p. 50).

[GS97] C. M. Grinstead and J. L. Snell. *Introduction to Probability*. American Mathematical Society, 1997 (cit. on pp. 50, 59).

[Gul+08] E. Gull, P. Werner, O. Parcollet, and M. Troyer. “Continuous-time auxiliary-field Monte Carlo for quantum impurity models”. In: *EPL (Europhysics Letters)* 82.5 (2008), p. 57003 (cit. on p. 50).

[Gul+11] E. Gull, A. J. Millis, A. I. Lichtenstein, A. N. Rubtsov, M. Troyer, and P. Werner. “Continuous-time Monte Carlo methods for quantum impurity models”. In: *Rev. Mod. Phys.* 83 (2 2011), pp. 349–404 (cit. on pp. 5, 50, 53, 72).

[Gul08] E. Gull. “Continuous-Time Quantum Monte Carlo Algorithms for Fermions”. PhD thesis. ETH Zürich, 2008 (cit. on p. 65).

[Häg02] O. Häggström. *Finite Markov Chains and Algorithmic Applications*. Cambridge University Press, 2002 (cit. on p. 59).

[Has70] W. K. Hastings. “Monte Carlo sampling methods using Markov chains and their applications”. In: *Biometrika* 57.1 (1970), pp. 97–109 (cit. on p. 61).

[Hau07] K. Haule. “Quantum Monte Carlo impurity solver for cluster dynamical mean-field theory and electronic structure calculations with adjustable cluster base”. In: *Phys. Rev. B* 75 (15 2007), p. 155113 (cit. on pp. 66, 70).

[HE88] D. A. Huse and V. Elser. “Simple Variational Wave Functions for Two-Dimensional Heisenberg Spin-¡ Antiferromagnets”. In: *Phys. Rev. Lett.* 60 (24 1988), pp. 2531–2534 (cit. on p. 34).

[Hew93] A. C. Hewson. *The Kondo Problem to Heavy Fermions*. Cambridge University Press, 1993 (cit. on pp. 17, 20, 97).

[HF86] J. E. Hirsch and R. M. Fye. "Monte Carlo Method for Magnetic Impurities in Metals". In: *Phys. Rev. Lett.* 56 (23 1986), pp. 2521–2524 (cit. on p. 53).

[Hig15] *The Princeton Companion to Applied Mathematics*. Princeton University Press, 2015 (cit. on pp. 52, 121).

[Hil+14] S. Hild, T. Fukuhara, P. SchauSS, J. Zeiher, M. Knap, E. Demler, I. Bloch, and C. Gross. "Far-from-Equilibrium Spin Transport in Heisenberg Quantum Magnets". In: *Phys. Rev. Lett.* 113 (14 2014), p. 147205 (cit. on p. 99).

[HLH06] C. F. Hirjibehedin, C. P. Lutz, and A. J. Heinrich. "Spin Coupling in Engineered Atomic Structures". In: *Science* 312.5776 (2006), pp. 1021–1024 (cit. on pp. 6, 99).

[HPW12] H. Hafermann, K. R. Patton, and P. Werner. "Improved estimators for the self-energy and vertex function in hybridization-expansion continuous-time quantum Monte Carlo simulations". In: *Phys. Rev. B* 85 (20 2012), p. 205106 (cit. on pp. 68, 72).

[Hub63] J. Hubbard. "Electron Correlations in Narrow Energy Bands". In: *Proceedings of the Royal Society of London. Series A, Mathematical and Physical Sciences* 276.1365 (1963), pp. 238–257 (cit. on pp. 11, 42).

[HUM11] S. Hayami, M. Udagawa, and Y. Motome. "Partial Disorder in the Periodic Anderson Model on a Triangular Lattice". In: *Journal of the Physical Society of Japan* 80.7 (2011), p. 073704 (cit. on pp. 4, 76, 77, 80, 84, 88).

[HUM12] S. Hayami, M. Udagawa, and Y. Motome. "Partial Disorder and MetalInsulator Transition in the Periodic Anderson Model on a Triangular Lattice". In: *Journal of the Physical Society of Japan* 81.10 (2012), p. 103707 (cit. on pp. 4, 76, 77, 80, 85, 88).

[Ida15] N. Ida. *Engineering Electromagnetics*. Springer International Publishing, 2015 (cit. on p. 1).

[IT15] M. Iazzi and M. Troyer. "Efficient continuous-time quantum Monte Carlo algorithm for fermionic lattice models". In: *Phys. Rev. B* 91 (24 2015), p. 241118 (cit. on p. 54).

[Jac98] J. D. Jackson. *Classical Electrodynamics*. John Wiley & Sons Inc, 27, 1998 (cit. on p. 1).

[Jan02] W. Janke. "Statistical analysis of simulations: Data correlations and error estimation". In: *Quantum Simulations of Complex Many-Body Systems: From Theory to Algorithms* 10 (2002), pp. 423–445 (cit. on pp. 63, 64).

[Jän08] K. Jänich. *Lineare Algebra*. Springer Berlin Heidelberg, 2008 (cit. on p. 57).

[Jar95] M. Jarrell. "Symmetric periodic Anderson model in infinite dimensions". In: *Phys. Rev. B* 51 (12 1995), pp. 7429–7440 (cit. on p. 5).

[Kas56] T. Kasuya. "Electrical Resistance of Ferromagnetic Metals". In: *Progress of Theoretical Physics* 16.1 (1956), pp. 58–63 (cit. on pp. 3, 27, 86).

[Kat09] H. G. Katzgraber. "Introduction to Monte Carlo Methods". In: (2009) (cit. on p. 52).

[Ken+05] P. R. C. Kent, M. Jarrell, T. A. Maier, and T. Pruschke. "Efficient calculation of the antiferromagnetic phase diagram of the three-dimensional Hubbard model". In: *Phys. Rev. B* 72 (6 2005), p. 060411 (cit. on pp. 114, 115).

[Kha+11] A. A. Khajetoorians, J. Wiebe, B. Chilian, and R. Wiesendanger. “Realizing All-SpinBased Logic Operations Atom by Atom”. In: *Science* 332.6033 (2011), pp. 1062–1064 (cit. on pp. 6, 99).

[Kha+12] A. A. Khajetoorians, J. Wiebe, B. Chilian, S. Lounis, S. Blugel, and R. Wiesendanger. “Atom-by-atom engineering and magnetometry of tailored nanomagnets”. In: *Nat Phys* 8.6 (2012), pp. 497–503 (cit. on pp. 6, 99, 118).

[Kit05] C. Kittel. *Introduction to Solid State Physics*. Wiley, 2005 (cit. on p. 32).

[Kle08] A. Klenke. *Probability Theory*. Springer London, 2008 (cit. on p. 50).

[KMR13] K. E. h. Küpfmüller, W. Mathis, and A. Reibiger. *Theoretische Elektrotechnik: Eine Einführung*. Springer Berlin Heidelberg, 2013 (cit. on p. 1).

[Koc12] E. Koch. “Exchange Mechanisms”. In: *Correlated electrons: from models to materials*. Vol. 2. Forschungszentrum Jülich GmbH, 2012, pp. 7.1–7.31 (cit. on pp. 28, 90).

[Kol11] M. Kollar. “Introduction to Dynamical Mean-Field Theory”. In: *The LDA+DMFT approach to strongly correlated materials*. Vol. 1. Forschungszentrum, Zentralbibliothek, 2011. Chap. 5, pp. 5.1–5.20 (cit. on p. 42).

[Kon64] J. Kondo. “Resistance Minimum in Dilute Magnetic Alloys”. In: *Progress of Theoretical Physics* 32.1 (1964), pp. 37–49 (cit. on pp. 3, 18, 27, 29).

[Kra06] W. Krauth. *Statistical Mechanics: Algorithms and Computations*. Oxford University Press, UK, 2006 (cit. on p. 50).

[Kro+10] J. Kronjäger, C. Becker, P. Soltan-Panahi, K. Bongs, and K. Sengstock. “Spontaneous Pattern Formation in an Antiferromagnetic Quantum Gas”. In: *Phys. Rev. Lett.* 105 (9 2010), p. 090402 (cit. on p. 99).

[KS83] J. G. Kemeny and J. L. Snell. *Finite Markov Chains: With a New Appendix "Generalization of a Fundamental Matrix"*. Springer, 1983 (cit. on p. 59).

[Kuz15] A. L. Kuzemsky. “Variational principle of Bogoliubov and generalized mean fields in many-particle interacting systems”. In: *International Journal of Modern Physics B* 29.18 (2015), p. 1530010 (cit. on p. 38).

[LB14] D. P. Landau and K. Binder. *A Guide to Monte Carlo Simulations in Statistical Physics*. Cambridge University Press, 2014 (cit. on p. 50).

[Lec11] F. Lechermann. “Model Hamiltonians and Basic Techniques”. In: *The LDA+DMFT approach to strongly correlated materials*. Vol. 1. Forschungszentrum, Zentralbibliothek, 2011. Chap. 3, pp. 3.1–3.29 (cit. on pp. 12, 18).

[Li08] G. Li. “Non-Local Correlations within Dynamical Mean Field Theory”. PhD thesis. Rheinische Friedrich-Wilhelms-Universität Bonn, 2008 (cit. on p. 40).

[LM15] J. Liesen and V. Mehrmann. *Linear Algebra*. Springer International Publishing, 2015 (cit. on p. 57).

[Löh+07] H. v. Löhneysen, A. Rosch, M. Vojta, and P. Wölfle. “Fermi-liquid instabilities at magnetic quantum phase transitions”. In: *Rev. Mod. Phys.* 79 (3 2007), pp. 1015–1075 (cit. on pp. 3, 31).

[LP16] C. B. Lang and N. Pucker. *Mathematische Methoden in der Physik*. Springer Berlin Heidelberg, 2016 (cit. on p. 52).

[LS90] L. H. Loomis and S. Sternberg. *Advanced Calculus*. Jones and Bartlett Publishers, 1990 (cit. on p. 121).

[LSA12] M. Lewenstein, A. Sanpera, and V. Ahufinger. *Ultracold Atoms in Optical Lattices: Simulating quantum many-body systems*. Oxford University Press, 2012 (cit. on p. 6).

[LW09] A. M. Läuchli and P. Werner. "Krylov implementation of the hybridization expansion impurity solver and application to 5-orbital models". In: *Phys. Rev. B* 80 (23 2009), p. 235117 (cit. on p. 66).

[Mag04] M. Maggiore. *A Modern Introduction to Quantum Field Theory*. OUP Oxford, 2004 (cit. on p. 11).

[Mah00] G. D. Mahan. *Many-particle physics*. Kluwer Academic/Plenum Publishers, 2000 (cit. on pp. 48, 123, 124).

[Mat55] T. Matsubara. "A New Approach to Quantum-Statistical Mechanics". In: *Progress of Theoretical Physics* 14.4 (1955), pp. 351–378 (cit. on pp. 40, 42, 47, 53, 55, 73, 123–125).

[Men+94] S. A. M. Mentink, A. Drost, G. J. Nieuwenhuys, E. Frikkee, A. A. Menovsky, and J. A. Mydosh. "Magnetic Ordering and Frustration in Hexagonal UNi_4B". In: *Phys. Rev. Lett.* 73 (7 1994), pp. 1031–1034 (cit. on p. 118).

[Met+53] N. Metropolis, A. W. Rosenbluth, M. N. Rosenbluth, A. H. Teller, and E. Teller. "Equation of State Calculations by Fast Computing Machines". In: *The Journal of Chemical Physics* 21.6 (1953), pp. 1087–1092 (cit. on p. 61).

[Mey01] C. D. Meyer. *Matrix analysis and applied linear algebra. With solutions to problems*. SIAM: Society for Industrial and Applied Mathematics, 2001 (cit. on pp. 59, 60, 70).

[Min+14] C.-H. Min, P. Lutz, S. Fiedler, B. Y. Kang, B. K. Cho, H.-D. Kim, H. Bentmann, and F. Reinert. "Importance of Charge Fluctuations for the Topological Phase in SmB_6". In: *Phys. Rev. Lett.* 112 (22 2014), p. 226402 (cit. on p. 2).

[MMJ09] K. Mikelsons, A. Macridin, and M. Jarrell. "Relationship between Hirsch-Fye and weak-coupling diagrammatic quantum Monte Carlo methods". In: *Phys. Rev. E* 79 (5 2009), p. 057701 (cit. on p. 53).

[MN00] D. Meyer and W. Nolting. "Dynamical mean-field study of ferromagnetism in the periodic Anderson model". In: *Phys. Rev. B* 62 (9 2000), pp. 5657–5666 (cit. on pp. 92, 114, 115).

[MN98] M. Matsumoto and T. Nishimura. "Mersenne Twister: A 623-dimensionally Equidistributed Uniform Pseudo-random Number Generator". In: *ACM Trans. Model. Comput. Simul.* 8.1 (1998), pp. 3–30 (cit. on p. 61).

[MNR12] T. Müller-Gronbach, E. Novak, and K. Ritter. *Monte Carlo-Algorithmen*. Springer Berlin Heidelberg, 2012 (cit. on p. 50).

[MO95] N. Matsumoto and F. J. Ohkawa. "Kondo-lattice model in infinite dimensions". In: *Phys. Rev. B* 51 (7 1995), pp. 4110–4121 (cit. on p. 19).

[Mor85] T. Moriya. *Spin Fluctuations in Itinerant Electron Magnetism*. Vol. 56. Springer Berlin Heidelberg, 1985 (cit. on p. 90).

[Mot+10] Y. Motome, K. Nakamikawa, Y. Yamaji, and M. Udagawa. “Partial Kondo Screening in Frustrated Kondo Lattice Systems”. In: *Phys. Rev. Lett.* 105 (3 2010), p. 036403 (cit. on pp. 4, 76, 93).

[Mot68] N. F. Mott. “Metal-Insulator Transition”. In: *Rev. Mod. Phys.* 40 (4 1968), pp. 677–683 (cit. on p. 12).

[Mül89a] E. Müller-Hartmann. “Correlated fermions on a lattice in high dimensions”. In: *Zeitschrift für Physik B Condensed Matter* 74.4 (1989), pp. 507–512 (cit. on p. 42).

[Mül89b] E. Müller-Hartmann. “The Hubbard model at high dimensions: some exact results and weak coupling theory”. In: *Zeitschrift für Physik B Condensed Matter* 76.2 (1989), pp. 211–217 (cit. on p. 107).

[MV89] W. Metzner and D. Vollhardt. “Correlated Lattice Fermions in $d = \infty$ Dimensions”. In: *Phys. Rev. Lett.* 62 (3 1989), pp. 324–327 (cit. on pp. 5, 40, 42, 107).

[MW66] N. D. Mermin and H. Wagner. “Absence of Ferromagnetism or Antiferromagnetism in One- or Two-Dimensional Isotropic Heisenberg Models”. In: *Phys. Rev. Lett.* 17 (22 1966), pp. 1133–1136 (cit. on pp. 6, 24, 31).

[MW93] B. Möller and P. Wölfle. “Magnetic order in the periodic Anderson model”. In: *Phys. Rev. B* 48 (14 1993), pp. 10320–10326 (cit. on p. 92).

[MZ91] G. Marsaglia and A. Zaman. “A new class of random number generators”. In: *The Annals of Applied Probability* (1991), pp. 462–480 (cit. on p. 61).

[NB80] P. Nozières and A. Blandin. “Kondo effect in real metals”. In: *J. Phys. France* 41.3 (1980), pp. 193–211 (cit. on p. 96).

[Ner16] F. Neri. *Linear Algebra for Computational Sciences and Engineering*. Springer International Publishing, 2016 (cit. on p. 52).

[Neu+07] M. Neumann, J. Nyéki, B. Cowan, and J. Saunders. “Bilayer 3He: A Simple Two-Dimensional Heavy-Fermion System with Quantum Criticality”. In: *Science* 317.5843 (2007), pp. 1356–1359 (cit. on pp. 2, 17).

[NO98] J. W. Negele and H. Orland. *Quantum Many-Particle Systems*. Westview Press, 1998 (cit. on pp. 9–11, 123–125).

[Nor98] J. Norris. *Markov chains*. Cambridge University Press, 1998 (cit. on p. 59).

[Noz74] P. Nozières. “A “fermi-liquid” description of the Kondo problem at low temperatures”. In: *Journal of Low Temperature Physics* 17.1 (1974), pp. 31–42 (cit. on p. 96).

[NOZ76] P. NOZIÈRES. « APPLICATIONS DE L’IDÉE DE RENORMALISATION EN PHYSIQUE DU SOLIDE ». In : *Le Journal de Physique Colloques* 37.C1 (1976), p. C1–271–C1-282 (cf. p. 96).

[NR09] W. Nolting and A. Ramakanth. *Quantum Theory of Magnetism*. Springer Berlin Heidelberg, 2009 (cit. on pp. 12, 20, 28, 32).

[OKK09] J. Otsuki, H. Kusunose, and Y. Kuramoto. “The Kondo Lattice Model in Infinite Dimensions: I. Formalism”. In: *Journal of the Physical Society of Japan* 78.1 (2009), p. 014702 (cit. on p. 119).

[Orú14] R. Orús. “A practical introduction to tensor networks: Matrix product states and projected entangled pair states”. In: *Annals of Physics* 349 (2014), pp. 117–158 (cit. on p. 6).

[Oya+08] A. Oyamada, S. Maegawa, M. Nishiyama, H. Kitazawa, and Y. Isikawa. “Ordering mechanism and spin fluctuations in a geometrically frustrated heavy-fermion antiferromagnet on the Kagome-like lattice CePdAl: A ^{27}Al NMR study”. In: *Phys. Rev. B* 77 (6 2008), p. 064432 (cit. on pp. 4, 118).

[Par+13] N. Parragh, G. Sangiovanni, P. Hansmann, S. Hummel, K. Held, and A. Toschi. “Effective crystal field and Fermi surface topology: A comparison ofd- anddp-orbital models”. In: *Physical Review B* 88.19 (2013) (cit. on p. 5).

[PBJ00] T. Pruschke, R. Bulla, and M. Jarrell. “Low-energy scale of the periodic Anderson model”. In: *Phys. Rev. B* 61 (19 2000), pp. 12799–12809 (cit. on p. 5).

[PE] I. Peschel and V. Eisler. “The Conceptual Background of Density-Matrix Renormalization”. In: *Computational Many-Particle Physics*. Springer Berlin Heidelberg, pp. 581–596 (cit. on p. 6).

[Pes14] M. Peschke. “From Polarons to Magnetism in the depleted Kondo Lattice”. MA thesis. Universität Hamburg, 2014 (cit. on p. 49).

[PHC13] C. V. Parker, L.-C. Ha, and C. Chin. “Direct observation of effective ferromagnetic domains of cold atoms in a shaken optical lattice”. In: *Nat Phys* 9.12 (2013), pp. 769–774 (cit. on p. 99).

[PN66] D. Pines and P. Nozieres. *The Theory of Quantum Liquids: Normal Fermi Liquids*. Vol. 1. WA Benjamin, 1966 (cit. on pp. 2, 16).

[PN97] M. Potthoff and W. Nolting. “Surface magnetism in the strongly correlated Hubbard model”. In: *Phys. Rev. B* 55 (5 1997), pp. 2741–2744 (cit. on pp. 5, 45, 107).

[Pot+98] M. Potthoff, T. Herrmann, T. Wegner, and W. Nolting. “The Moment Sum Rule and Its Consequences for Ferromagnetism in the Hubbard Model”. In: *physica status solidi (b)* 210.1 (1998), pp. 199–228 (cit. on p. 90).

[PP09] R. Peters and T. Pruschke. “Magnetic phase diagram of the Hubbard model with next-nearest-neighbour hopping”. In: *New Journal of Physics* 11.8 (2009), p. 083022 (cit. on p. 90).

[Pre+07] W. H. Press, S. A. Teukolsky, W. T. Vetterling, and B. P. Flannery. *Numerical Recipes 3rd Edition: The Art of Scientific Computing*. Cambridge University Press, 2007 (cit. on pp. 52, 70).

[PRP17] M. Peschke, R. Rausch, and M. Potthoff. “Frustrated quantum magnetism in the Kondo lattice on the zig-zag ladder”. In: (17, 2017) (cit. on p. 119).

[Pru08] T. Pruschke. “Dynamical Mean-Field Approximation and Cluster Methods for Correlated Electron Systems”. In: *Computational Many-Particle Physics*. Vol. 739. Springer Berlin Heidelberg, 2008. Chap. 16, pp. 473–503 (cit. on p. 42).

[PTK13] R. Peters, Y. Tada, and N. Kawakami. “Kondo effect in f-electron superlattices”. In: *Phys. Rev. B* 88 (15 2013), p. 155134 (cit. on p. 5).

[Ram07] J. Rammer. *Quantum field theory of non-equilibrium states*. Cambridge University Press, 2007 (cit. on p. 124).

[RF94] H. Römer and T. Filk. *Statistische Mechanik*. Vol. 3. VCH Weinheim, New York, Basel, Cambridge, Tokyo, 1994 (cit. on p. 51).

[RHJ98] S. Rombouts, K. Heyde, and N. Jachowicz. "A discrete Hubbard-Stratonovich decomposition for general, fermionic two-body interactions". In: *Physics Letters A* 242.45 (1998), pp. 271–276 (cit. on p. 50).

[RHJ99] S. M. A. Rombouts, K. Heyde, and N. Jachowicz. "Quantum Monte Carlo Method for Fermions, Free of Discretization Errors". In: *Phys. Rev. Lett.* 82 (21 1999), pp. 4155–4159 (cit. on p. 50).

[RK07] R. Y. Rubinstein and D. P. Kroese. *Simulation and the Monte Carlo Method*. John Wiley & Sons, Inc., 2007 (cit. on p. 60).

[RK54] M. A. Ruderman and C. Kittel. "Indirect Exchange Coupling of Nuclear Magnetic Moments by Conduction Electrons". In: *Phys. Rev.* 96 (1 1954), pp. 99–102 (cit. on pp. 3, 27, 86).

[RSL05] A. N. Rubtsov, V. V. Savkin, and A. I. Lichtenstein. "Continuous-time quantum Monte Carlo method for fermions". In: *Phys. Rev. B* 72 (3 2005), p. 035122 (cit. on p. 50).

[SAG18] T. Sato, F. F. Assaad, and T. Grover. "Quantum Monte Carlo Simulation of Frustrated Kondo Lattice Models". In: *Physical Review Letters* 120.10 (2018) (cit. on p. 119).

[Sak94] J. J. Sakurai. *Modern Quantum Mechanics*. Addison-Wesley, 1994 (cit. on pp. 1, 10, 19, 24, 25, 38).

[SB17] L. Savary and L. Balents. "Quantum spin liquids: a review". In: *Reports on Progress in Physics* 80.1 (2017), p. 016502 (cit. on p. 34).

[SC90] H. Schweitzer and G. Czycholl. "The second order U-perturbation approach to the Anderson Lattice model in one, two and three dimensions". In: *Solid State Communications* 74.8 (1990), pp. 735–742 (cit. on p. 107).

[SC91] H. Schweitzer and G. Czycholl. "Weak-coupling treatment of the Hubbard model in one, two and three dimensions". In: *Zeitschrift für Physik B Condensed Matter* 83.1 (1991), pp. 93–103 (cit. on p. 107).

[Sca+14] F. Scazza, C. Hofrichter, M. Hofer, P. C. De Groot, I. Bloch, and S. Folling. "Observation of two-orbital spin-exchange interactions with ultracold SU(N)-symmetric fermions". In: *Nat Phys* 10.10 (2014), pp. 779–784 (cit. on p. 99).

[Sch05] U. Schollwöck. "The density-matrix renormalization group". In: *Rev. Mod. Phys.* 77 (1 2005), pp. 259–315 (cit. on p. 6).

[Sch08] F. Schwabl. *Quantenmechanik für Fortgeschrittene (QM II)*. Springer Berlin Heidelberg, 2008 (cit. on p. 24).

[Sch11] U. Schollwöck. "The density-matrix renormalization group in the age of matrix product states". In: *Annals of Physics* 326.1 (2011), pp. 96–192 (cit. on p. 6).

[Sch12] F. Scheck. *Classical Field Theory*. Springer Berlin Heidelberg, 2012 (cit. on p. 11).

[Sch13] U. Schollwöck. "DMRG: Ground States, Time Evolution, and Spectral Functions". In: *Emergent Phenomena in Correlated Matter*. Vol. 3. Forschungszentrum Jülich Zentralbibliothek, Verlag, 2013. Chap. 16, pp. 16.1–16.34 (cit. on p. 6).

[SGP12] A. Schwabe, D. Gütersloh, and M. Potthoff. "Competition between Kondo Screening and Indirect Magnetic Exchange in a Quantum Box". In: *Phys. Rev. Lett.* 109 (25 2012), p. 257202 (cit. on p. 6).

[SHP14] A. Schwabe, M. Hänsel, and M. Potthoff. "Cooperation of different exchange mechanisms in confined magnetic systems". In: *Phys. Rev. A* 90 (3 2014), p. 033615 (cit. on pp. 5, 99).

[Sim+11] J. Simon, W. S. Bakr, R. Ma, M. E. Tai, P. M. Preiss, and M. Greiner. "Quantum simulation of antiferromagnetic spin chains in an optical lattice". In: *Nature* 472.7343 (2011), pp. 307–312 (cit. on p. 99).

[SM02] P. Schmidt and H. Monien. "Nonequilibrium dynamical mean-field theory of a strongly correlated system". In: *eprint arXiv:cond-mat/0202046* (2002) (cit. on p. 40).

[SN02] P. Sinjukow and W. Nolting. "Exact mapping of periodic Anderson model to Kondo lattice model". In: *Phys. Rev. B* 65 (21 2002), p. 212303 (cit. on pp. 18–20, 27, 99, 111).

[STP13] A. Schwabe, I. Titvinidze, and M. Potthoff. "Inverse indirect magnetic exchange". In: *Phys. Rev. B* 88 (12 2013), p. 121107 (cit. on pp. 6, 98, 99, 107, 111–113).

[Str+13] J. Struck, M. Weinberg, C. Olschlager, P. Windpassinger, J. Simonet, K. Sengstock, R. Hoppner, P. Hauke, A. Eckardt, M. Lewenstein, and L. Mathey. "Engineering Ising-XY spin-models in a triangular lattice using tunable artificial gauge fields". In: *Nat Phys* 9.11 (2013), pp. 738–743 (cit. on p. 99).

[SW66] J. R. Schrieffer and P. A. Wolff. "Relation between the Anderson and Kondo Hamiltonians". In: *Phys. Rev.* 149 (2 1966), pp. 491–492 (cit. on pp. 3, 18, 83, 99, 111).

[Tay97] J. R. Taylor. *An Introduction Error Analysis: The Study of Uncertainties in Physical Measurements*. University science books, 1997 (cit. on p. 51).

[Tit+12] I. Titvinidze, A. Schwabe, N. Rother, and M. Potthoff. "Dynamical mean-field theory of indirect magnetic exchange". In: *Phys. Rev. B* 86 (7 2012), p. 075141 (cit. on pp. 107, 119).

[TJF97] A. N. Tahvildar-Zadeh, M. Jarrell, and J. K. Freericks. "Protracted screening in the periodic Anderson model". In: *Phys. Rev. B* 55 (6 1997), R3332–R3335 (cit. on p. 92).

[TO15] T. Tomé and M. J. de Oliveira. *Stochastic Dynamics and Irreversibility*. Springer International Publishing, 2015 (cit. on p. 59).

[TSP14] I. Titvinidze, A. Schwabe, and M. Potthoff. "Ferromagnetism of magnetic impurities coupled indirectly via conduction electrons: Insights from various theoretical approaches". In: *Phys. Rev. B* 90 (4 2014), p. 045112 (cit. on pp. 6, 98, 99, 112).

[TSP15] I. Titvinidze, A. Schwabe, and M. Potthoff. "Strong-coupling limit of depleted Kondo- and Anderson-lattice models". In: *The European Physical Journal B* 88.2, 9 (2015) (cit. on pp. 6, 96, 98, 101, 103, 112).

[TSU97] H. Tsunetsugu, M. Sigrist, and K. Ueda. “The ground-state phase diagram of the one-dimensional Kondo lattice model”. In: *Rev. Mod. Phys.* 69 (3 1997), pp. 809–864 (cit. on pp. 2, 14, 17, 26, 27, 101).

[TW05] M. Troyer and U.-J. Wiese. “Computational Complexity and Fundamental Limitations to Fermionic Quantum Monte Carlo Simulations”. In: *Phys. Rev. Lett.* 94 (17 2005), p. 170201 (cit. on p. 52).

[Ulm98] M. Ulmke. “Ferromagnetism in the Hubbard model on fcc-type lattices”. In: *The European Physical Journal B - Condensed Matter and Complex Systems* 1.3 (1998), pp. 301–304 (cit. on pp. 90, 114, 115).

[VBK12] D. Vollhardt, K. Byczuk, and M. Kollar. “Dynamical Mean-Field Theory”. In: *Strongly Correlated Systems*. Vol. 171. Springer Berlin Heidelberg, 2012, pp. 203–236 (cit. on pp. 40–42).

[Ved+11] E. Y. Vedmedenko, N. Mikuszeit, T. Stapelfeldt, R. Wieser, M. Potthoff, A. I. Lichtenstein, and R. Wiesendanger. “Spin-spin correlations in ferromagnetic nanosystems”. In: *European Physical Journal B* 80 (2011), pp. 331–336 (cit. on p. 113).

[Vol+99] D. Vollhardt, N. Blümer, K. Held, M. Kollar, J. Schlipf, M. Ulmke, and J. Wahle. “Metallic ferromagnetism: Progress in our understanding of an old strong-coupling problem”. In: *Advances in Solid State Physics* 38 (1999), pp. 383–396 (cit. on p. 90).

[Vol10] D. Vollhardt. “Dynamical Mean-Field Theory of Electronic Correlations in Models and Materials”. In: *American Institute of Physics Conference Series*. Vol. 1297. 2010, pp. 339–403 (cit. on p. 42).

[Vol11] D. Vollhardt. “Dynamical Mean-Field Approach for Strongly Correlated Materials”. In: *The LDA+DMFT approach to strongly correlated materials*. Vol. 1. Forschungszentrum, Zentralbibliothek, 2011. Chap. 1, pp. 1.1–1.29 (cit. on p. 39).

[WA13] J. Werner and F. F. Assaad. “Interaction-driven transition between topological states in a Kondo insulator”. In: *Phys. Rev. B* 88 (3 2013), p. 035113 (cit. on p. 5).

[WA14a] J. Werner and F. F. Assaad. “Dynamically generated edge states in topological Kondo insulators”. In: *Phys. Rev. B* 89 (24 2014), p. 245119 (cit. on pp. 2, 5).

[WA14b] J. Werner and F. F. Assaad. “Ring-exchange periodic Anderson model for ^{3}He bilayers”. In: *Phys. Rev. B* 90 (20 2014), p. 205122 (cit. on pp. 2, 17).

[Wag91] M. Wagner. “Expansions of nonequilibrium Green’s functions”. In: *Phys. Rev. B* 44 (12 1991), pp. 6104–6117 (cit. on p. 124).

[Wah+98] J. Wahle, N. Blümer, J. Schlipf, K. Held, and D. Vollhardt. “Microscopic conditions favoring itinerant ferromagnetism”. In: *Phys. Rev. B* 58 (19 1998), pp. 12749–12757 (cit. on pp. 91, 92).

[Wei00] S. Weinzierl. “Introduction to Monte Carlo methods”. In: *ArXiv High Energy Physics - Phenomenology e-prints* (2000) (cit. on p. 52).

[Wer+06] P. Werner, A. Comanac, L. de’Medici, M. Troyer, and A. J. Millis. “Continuous-Time Solver for Quantum Impurity Models”. In: *Phys. Rev. Lett.* 97 (7 2006), p. 076405 (cit. on pp. 5, 50, 56, 72).

[Wer+08] P. Werner, E. Gull, M. Troyer, and A. J. Millis. "Spin Freezing Transition and Non-Fermi-Liquid Self-Energy in a Three-Orbital Model". In: *Physical Review Letters* 101.16 (2008) (cit. on p. 5).

[Wer11] P. Werner. "Continuous-Time Impurity Solvers". In: *The LDA+DMFT approach to strongly correlated materials*. Vol. 1. Forschungszentrum, Zentralbibliothek, 2011. Chap. 10, pp. 10.1–10.17 (cit. on pp. 65, 72).

[Wer15] J. Werner. „Numerical Simulations of Heavy Fermion Systems: From He-3 Bilayers to Topological Kondo Insulators". Diss. Julius-Maximilians-Universität Würzburg, 2015 (siehe S. 20).

[Wie09] R. Wiesendanger. "Spin mapping at the nanoscale and atomic scale". In: *Rev. Mod. Phys.* 81 (4 2009), pp. 1495–1550 (cit. on pp. 6, 99, 118).

[Wil75] K. G. Wilson. "The renormalization group: Critical phenomena and the Kondo problem". In: *Rev. Mod. Phys.* 47 (4 1975), pp. 773–840 (cit. on p. 97).

[Wip13] A. Wipf. *Statistical Approach to Quantum Field Theory*. Vol. 100. Springer Berlin Heidelberg, 2013 (cit. on p. 124).

[WM06] P. Werner and A. J. Millis. "Hybridization expansion impurity solver: General formulation and application to Kondo lattice and two-orbital models". In: *Phys. Rev. B* 74 (15 2006), p. 155107 (cit. on pp. 5, 50).

[WM07] P. Werner and A. J. Millis. "High-Spin to Low-Spin and Orbital Polarization Transitions in Multiorbital Mott Systems". In: *Physical Review Letters* 99.12 (2007) (cit. on p. 5).

[Wol+13] S. Wolgast, C. Kurdak, K. Sun, J. W. Allen, D.-J. Kim, and Z. Fisk. "Low-temperature surface conduction in the Kondo insulator SmB_6". In: *Phys. Rev. B* 88 (18 2013), p. 180405 (cit. on p. 2).

[Yeo92] J. M. Yeomans. *Statistical Mechanics of Phase Transitions*. Clarendon Press; Oxford University Press, 1992 (cit. on p. 38).

[Yos57] K. Yosida. "Magnetic Properties of Cu-Mn Alloys". In: *Phys. Rev.* 106 (5 1957), pp. 893–898 (cit. on pp. 3, 27, 86).

[Yos96] K. Yosida. *Theory of magnetism*. Springer, 1996 (cit. on pp. 24, 28).

[You12] P. Young. "Everything you wanted to know about Data Analysis and Fitting but were afraid to ask". In: (2012) (cit. on pp. 51, 63).

[YS93] T. Yanagisawa and Y. Shimoi. "Itinerant ferromagnetism in strongly correlated electron systems". In: *Phys. Rev. B* 48 (9 1993), pp. 6104–6110 (cit. on p. 92).

[Zen51] C. Zener. "Interaction between the *d*-Shells in the Transition Metals. II. Ferromagnetic Compounds of Manganese with Perovskite Structure". In: *Phys. Rev.* 82 (3 1951), pp. 403–405 (cit. on p. 90).

[Zin04] J. Zinn-Justin. *Path integrals in quantum mechanics*. Oxford University Press, 2004 (cit. on p. 125).

[Zin07] J. Zinn-Justin. *Phase Transitions and Renormalisation Group*. Oxford University Press, USA, 2007 (cit. on p. 32).

[ZW15] Z. Zhu and S. R. White. “Spin liquid phase of the $S = \frac{1}{2}$ $J_1 - J_2$ Heisenberg model on the triangular lattice”. In: *Phys. Rev. B* 92 (4 2015), p. 041105 (cit. on p. 34).

List of publications

The research relating to this thesis led to the following publications:

- M. W. Aulbach, F. F. Assaad, and M. Potthoff. "Dynamical mean-field study of partial Kondo screening in the periodic Anderson model on the triangular lattice". In: *Phys. Rev. B* 92 (23 Dec. 2015), p. 235131

- M. W. Aulbach, I. Titvinidze, and M. Potthoff. "Crossover from conventional to inverse indirect magnetic exchange in the depleted Anderson lattice". In: *Phys. Rev. B* 91 (17 May 2015), p. 174420

Eidesstattliche Versicherung / *Declaration on oath*

Hiermit erkläre ich an Eides statt, dass ich die vorliegende Dissertationsschrift selbst verfasst und keine anderen als die angegebenen Quellen und Hilfsmittel benutzt habe.

I hereby declare upon oath that I have written the present dissertation independently and have not used further resources and aids than those stated.

Hamburg, den 18.01.2021

Maximilian Aulbach

Danksagung

Der Weg hin zum Abschluss dieser Arbeit glich einer Odyssee, die ich alleine nicht durchstehen bzw. bestreiten hätte können. Es sei an dieser Stelle all jenen gedankt, die mich hier begleitet und unterstützt haben.

Meinem Doktorvater Prof. Dr. Michael Potthoff danke ich nicht nur für die Bereitschaft, mich als Doktoranden anzunehmen, zu betreuen und vieles aus der Physik zu lehren. Vielmehr danke ich ihm für seine unglaubliche Freundlichkeit und Geduld mit mir während meiner Odyssee.

Darüber hinaus danke ich meinen ehemaligen Kollegen aus der Arbeitsgruppe für eine lockere und dennoch knackig kompetente Arbeitsatmosphäre. Besonders hervorheben möchte ich hier Dr. Andrej Schwabe und Dr. Mohammad Sayad.

Prof. Dr. Fakher Assad danke ich nicht nur für den Großteil meiner Expertise in Sachen Monte Carlo Simulation, sondern auch für eine konstruktive Zusammenarbeit bis hin zu einer kooperativen Publikation, die ohne die unkomplizierte Bereitstellung von Rechenzeit aus Fakhers Kontingent am Leibniz Rechenzentrum nicht realisierbar gewesen wäre.

Eine Arbeit wie diese kann nicht gänzlich aus dem privaten Leben heraus gehalten werden, vielmehr stellt sie temporär einen Großteil desselbigen dar. Ich danke herzlichst meiner Familie, besonders meiner unglaublichen Frau Kathrin, mir diese Zeit geschenkt zu haben.

Auch im „post-universitären“ Lebensabschnitt in der Freien Wirtschaft gibt es zum Glück Kollegen, die nicht müde werden einen anzuhalten, endlich die eigene Promotion abzuschließen, trotz aller anderen Umstände. Hierfür danke ich besonders Dr. Bernd Herkert, der stets an die Fertigstellung dieser Zeilen geglaubt hat.

Last but not least, danke ich Axel Schwind fürs beeindruckend gründliche Korrekturlesen dieser Arbeit mit Blick auf ein passables Englisch.